Développements de nouveaux détecteurs cryogéniques bas seuils pour la recherche de matière noire légère et la physique des neutrinos de basse énergie

Dimitri Misiak

N°d'ordre NNT :
2021LYSE1025

THESE de DOCTORAT DE L'UNIVERSITE DE LYON
opérée au sein de
l'Université Claude Bernard Lyon 1

Ecole Doctorale N° 52
(Physique et Astrophysique de Lyon)

Spécialité de doctorat : **Physique des Astroparticules**

Soutenue publiquement le 12/02/2021, par :
Dimitri Misiak

Développements de nouveaux détecteurs cryogéniques bas seuils pour la recherche de matière noire légère et la physique des neutrinos de basse énergie

-

Development of new cryogenic low-threshold detectors for the search of light dark matter and low-energy neutrino physics

---

Devant le jury composé de :

DAVESNE Dany	Professeur des Universités	UCBL	Président
FORMAGGIO Joseph	Professeur	MIT, Cambridge	Rapporteur
MARNIEROS Stefanos	Chargé de Recherche	CNRS, IJCLab	Rapporteur
NONES Claudia	Chercheure	CEA Saclay	Examinatrice
AUGIER Corinne	Professeure des Universités	UCBL	Directrice de thèse
BILLARD Julien	Chargé de Recherche	CNRS IP2I	Co-directeur de thèse

UNIVERSITÉ CLAUDE BERNARD LYON 1

Abstract

École Doctorale de Physique et Astrophysique de Lyon - ED52 PHAST
Institut de Physique des deux Infinis de Lyon

Doctor of Philosophy in Physics

Development of a new generation of low-threshold cryogenic detectors for the search of low-mass dark matter and low-energy neutrino physics

by Dimitri MISIAK

The Coherent Elastic Neutrino-Nucleus Scattering (CENNS) is a process predicted nearly 40 years ago. In August 2017, the COHERENT experiment reported the first keV-scale detection at the 6.7 sigma level of this process, which is a probe for the new low energy physics, opening a window on a myriad of new physics opportunities.

The RICOCHET experiment aims at measuring with high accuracy the CENNS process in order to probe various exotic physics scenarios in the electroweak sector. Using cryogenic bolometers operated in a cryostat 8 meters away from the core of the ILL research nuclear reactor, the experiment will benefit from an intense neutrino flux, allowing the results of COHERENT to be reproduced in a single week. The objective of an accurate measurement will be achieved after one year of data collection, by 2024. The CRYOCUBE is a compact cubic array of cryogenic detectors with the following specifications: a very low energy threshold of $\mathcal{O}(10)$ eV on the thermal signal, an electromagnetic background rejection of at least 10^3 and a total target mass of 1 kg distributed among 27 germanium crystals of about 30 g each.

The objective of this thesis is to propose an optimized detector design for the CRYOCUBE, inspired by the cryogenic germanium detectors equipped with charge and temperature readings of the direct dark matter search experiment EDELWEISS. This joint R&D program is based on event discrimination realized in germanium semiconductor crystals. The recoil energy of an incident particle is derived either from the increase of the crystal temperature measured by a GeNTD thermistor (heat channel) or from the excited electric charges collected by electrodes on its surface (ionization channel). This double energy measurement makes it possible to distinguish the nuclear recoils produced by the CENNS or the dark matter from the electronic radioactive background. As these recoils are of the order of $\mathcal{O}(100)$ eV, this thesis work is focused on the development of a new generation of cryogenic low threshold germanium detectors with particle identification. It explores how to improve the resolution in heat and ionization energy up to $\mathcal{O}(10)$ eV while maintaining a good rejection of background events. This study is based on the testing of prototype detectors in the IP2I cryostat, which are compared to theoretical predictions from electro-thermal and electrostatic modeling of the detectors.

This manuscript begins with the definition of the CENNS process, its scientific importance and the objectives of the RICOCHET experiment. It then presents the cryogenic installation allowing the surface operation of the detectors at 20 mK in optimal conditions. An electro-thermal model of the bolometers, compared with experimental data, is developed and applied to the simulation of the noise associated with the electronics of the heat signal. The thesis then formalizes the generation of the ionization signals arising from excited charge carriers drifting in the germanium crystal under the influence of the applied electric field. The expected resolution from a future low-noise electronics is modeled based on two detector designs. They are optimized by their electrostatic simulation in a finite element calculation software. A comparison of the theoretical and experimental performance of ionization is performed on the basis of the RED80 and REDN1 prototype detectors. This work ends with the characterization of the radioactive background in the cryogenic laboratory with the analysis of the data from RED80, and in particular its neutron component, used to estimate the expected background at the ILL site for RICOCHET.

UNIVERSITÉ CLAUDE BERNARD LYON 1

Résumé

École Doctorale de Physique et Astrophysique de Lyon - ED52 PHAST
Institut de Physique des deux Infinis de Lyon

Docteur en Physique

Développement de nouveaux détecteurs cryogéniques bas seuils pour la recherche de matière noire légère et la physique des neutrinos de basse énergie

par Dimitri MISIAK

La diffusion élastique cohérente neutrino-noyau (CENNS) est un processus prédit il y a près de 40 ans. En août 2017, l'expérience COHERENT a rapporté la première détection à l'échelle du keV au niveau 6,7 sigma, de ce processus qui est une sonde pour la nouvelle physique à basse énergie, ouvrant une fenêtre sur une myriade de nouvelles possibilités en matière de physique.

L'expérience RICOCHET vise à mesurer avec une grande précision le processus CENNS afin de sonder divers scénarios de physique exotique dans le secteur électrofaible. En utilisant des bolomètres cryogéniques installés dans un cryostat à 8 mètres du cœur du réacteur nucléaire de recherche de l'ILL, l'expérience bénéficiera d'un flux intense de neutrinos, permettant de reproduire les résultats de COHERENT en une semaine. L'objectif de mesure précise sera atteint après un an de collecte de données, d'ici 2024. Le CRYOCUBE est un ensemble compact cubique de détecteurs cryogéniques présentant les spécifications suivantes : un seuil en énergie très faible de $\mathcal{O}(10)$ eV sur le signal thermique, un rejet du fond électromagnétique d'au moins 10^3 et une masse totale de la cible de 1 kg répartie entre 27 cristaux de germanium d'environ 30 g chacun.

L'objectif de cette thèse est de proposer une conception optimisée des détecteurs pour le CRYOCUBE, inspirée des détecteurs cryogéniques en germanium équipés de lecture de charge et de températures de l'expérience de détection directe de matière noire EDELWEISS. Ce programme conjoint de R&D est basé sur la discrimination d'événements réalisée dans des cristaux de germanium semi-conducteurs. L'énergie de recul d'une particule incidente est dérivée soit de l'augmentation de la température du cristal mesurée par une thermistance GeNTD (voie chaleur), soit des charges électriques excitées collectées par des électrodes à sa surface (voie ionisation). Cette double mesure d'énergie permet de distinguer les reculs nucléaires produits par le CENNS ou la matière noire, du fond radioactif électronique. Ces reculs étant de l'ordre de $\mathcal{O}(100)$ eV, ce travail de thèse est axé sur le développement d'une nouvelle génération de détecteurs cryogéniques au germanium à faible seuil avec identification des particules. Il explore comment améliorer la résolution en énergie chaleur et ionisation jusqu'à $\mathcal{O}(10)$ eV tout en conservant un bon rejet des événements de fond. Cette étude est basée sur l'essai de prototypes de détecteurs dans le cryostat IP2I, qui sont comparés aux prévisions théoriques issues de la modélisation électro-thermique et électrostatique des détecteurs.

Ce manuscrit commence par la définition du processus CENNS, son importance scientifique et les objectifs de l'expérience RICOCHET. Il présente ensuite l'installation cryogénique permettant le fonctionnement en surface des détecteurs à 20 mK dans des conditions optimales. Un modèle électro-thermique des bolomètres, comparé à des données expérimentales, est développé et appliqué à la simulation du bruit associé à l'électronique du signal chaleur. La thèse formalise ensuite la génération des signaux d'ionisation résultant de la dérive, sous l'influence du champ électrique exercé, de porteurs de charge excités dans le cristal de germanium. La résolution attendue d'une future électronique bas-bruit est modélisée à partir de deux designs de détecteurs. Ils sont optimisés par leur simulation électrostatique dans un logiciel de calculs aux éléments finis. Une comparaison des performances théoriques et expérimentales de l'ionisation est effectuée sur la base des prototypes de détecteurs RED80 et REDN1. Ces travaux se terminent par la caractérisation du bruit de fond radioactif dans le laboratoire cryogénique avec l'analyse des données de RED80, et notamment sa composante neutronique, utilisée pour estimer le fond attendu sur le site ILL pour RICOCHET.

Remerciements

J'aimerais remercier toutes les personnes qui m'ont entouré lors de ces trois ans et demi de thèse. Elles ont toutes contribué à leur manière, plus ou moins directement et plus ou moins consciemment, à la création de cette thèse.

Je voudrais tout d'abord remercier mes deux directeurs de thèses, Julien Billard et Corinne Augier pour m'avoir épaulé si remarquablement tout au long de la thèse et pour leur soutien indéfectible pourtant mis à rude épreuve. Julien, je suis honoré d'avoir été ton premier doctorant. Je te suis reconnaissant pour ta présence, ton partage de ta culture scientifique et ta vison toujours optimiste, audacieuse et éclairée qui a pavé mon travail. Corinne, ma directrice 10%, je te remercie d'avoir toujours trouvé le temps de me conseiller et guider dans mes projets de thèse et d'enseignement. Tu t'es donnée sans compter pour organiser et bonifier cette thèse, tu as tout fait pour garder mon esprit libre de s'adonner à la recherche. Pour ça, tu as toute ma gratitude.

J'adresse ensuite mes remerciements aux membres de mon jury de soutenance pour l'intérêt qu'ils ont porté à mon sujet de thèse et le temps qu'ils ont consacré à l'évaluation de mon travail. Je remercie Stefanos Marnieros et Joseph Formaggio qui m'ont fait l'honneur d'être rapporteurs de cette thèse ainsi que Claudia Nones et Dany Davesne qui ont accepté d'en être les examinateurs.

J'aimerais ensuite remercier tous les membres du groupe de recherche MANOIR avec qui j'ai partagé mon quotidien de doctorant : d'expérimentateur au cryostat, d'analyste dans nos bureaux, de conférencier autour du monde et de bons vivants autour de crêpes, raclettes et autres prétexte à se retrouver ensemble. Je prends conscience de la chance d'avoir effectuer ma thèse à vos côtés. J'ose espérer que j'emmène avec moi dans mes futurs aventures une petite étincelle de la bienveillance et la joie de vivre ensemble qui anime ce groupe. J'ose espérer pouvoir célébrer avec vous d'ici quelques années les prochains résultats de EDELWEISSet RICOCHET. Un grand merci donc à tous les permanents: Maryvonne, Alex, Lionel, Véronique, Antoine, Jules, Corinne et Julien. Ainsi qu'aux un-peu-moins-permanents : Romain, Emeline, Eva, Quentin, Thomas, Valérian, Hugues, Jean-Baptiste et Jules.

Je remercie ma famille, mes parents, mes grands-parents, tantes, oncles, cousins, petit-cousins pour les bons moments partagés ensemble, votre soutien et votre curiosité toujours renouvelée qui ont agrémenté mes quelques années dans la physique fondamentale.

Je remercie tout particulièrement mon frère, Vladimir, qui m'a supporté, plus que je n'oserai l'admettre (j'y arriverai jamais Vlad !), tout au long de l'aventure qu'est la thèse ! Je suis ravi d'avoir vécu en ta compagnie d'avoir débattu, joué, ragé, dompté des fauves , rigolé, tout ça depuis notre repaire (sur l'équateur penché Mont-Blanc/centrale nucléaire !). J'ai été témoin de tes études à Lyon, de ton évolution au cours de ces années et j'ai hâte du spectacle que nous offrira ton épanouissement certain lors de ta thèse !

J'aimerais également exprimer de la gratitude pour mes amis, ceux que j'ai croisé et qui m'ont accompagné tout au long de cette période de vie mouvementée. Merci à Emeline, tu as accepté un petit sauvage dans ton bureau et il est presque devenu doctorant civilisé le bougre, à part quand tu l'invites pour jouer et manger ! Merci à Romain, partenaire inestimable de montage-démontage de cryostat sur chant de Franconie, de grandes choses nous attendent ! Merci à la grande Eva et notre maître absolu le chichissimme Gribouille, que nos discussions méta-physiques soient toujours entrecoupées des meilleurs bêtises ! Merci à Hughes, second à la villicus E. pour l'hospitalité et les notes de sagesses. Merci à Danny pour avoir présidé ma

soutenance de thèse, et m'avoir poussé et accompagné dans des expériences marathonienne et dansantes hors-normes. Merci à Jean-Baptiste qui me laisse l'embêter et faire mon intéressant, courage à toi pour la suite de ta thèse. Merci (en vrac mais tout aussi pensé) à Beatrice, Sihem, Valérie, David, Pauline, Katia, Adriana, Marine, Emma. Merci à ceux que j'aurais invariablement oublié de citer.

Merci à toi qui aura pris le temps de lire jusqu'ici, et qui s'apprête (sait-on jamais) à approfondir ses connaissances dans les bolomètres cryogéniques en lisant les quelques pages suivantes, tu verras c'est fun :)

Contents

Introduction

The Coherent Elastic Neutrino-Nucleus Scattering (CENNS) is a process predicted nearly 40 years ago. In August 2017, the COHERENT experiment reported the first keV-scale detection at the 6.7 sigma level of this process opening a window on a myriad of new physics opportunities. The RICOCHET experiment aims at measuring with high accuracy the CENNS process at low energy in order to probe various exotic physics scenarios in the electroweak sector. Using cryogenic bolometers operated in a cryostat 8 meters away from the core of the ILL research nuclear reactor, the experiment will benefit from an intense neutrino flux, allowing the results of COHERENT to be reproduced in a single week. The objective of an accurate measurement will be achieved after one year of data collection, by 2024. The CryoCube is a compact cubic array of cryogenic detectors developed for RICOCHET, with the following specifications: a very low energy threshold of $\mathcal{O}(10)$ eV on the thermal signal, an electromagnetic background rejection of at least 10^3 and a total target mass of 1 kg distributed among 27 germanium crystals of about 30 g each. The objective of this thesis is to propose an optimized detector design for the CryoCube, inspired by the cryogenic germanium detectors equipped with charge and temperature readouts of the direct dark matter search experiment EDELWEISS.

The first chapter of this manuscript introduces the CENNS process in the framework of the Standard Model. It then presents multiple exotic physics scenarios that would emerge from the measure of the CENNS at low energy range. Different low energy neutrino sources as well as detector technologies are discussed in order to realize this precision measurement. We discuss the R&D program of the nuclear reactor experiment RICOCHET, joint with one of the direct detection dark matter search experiment EDELWEISS, based on event discrimination realized in germanium semiconductor crystals. Their specificity is their intrinsic ability to distinguish the nuclear recoils produced by the CENNS or the dark matter from the electronic radioactive background. As these recoils are of the order of $\mathcal{O}(100)$ eV, this thesis work is focused on the development of a new generation of cryogenic low threshold germanium detectors with particle identification.

The second chapter describes the working principles of these detectors featuring a double measurement of the recoil energy of an incident particle as a temperature increase measured by a GeNTD thermistor (heat channel) and as the collection of electric charges by electrodes on the surface of the crystal (ionization channel). It presents the IP2I cryogenic facility allowing the surface operation of prototype detectors at 20 mK in optimal conditions, thanks to the mitigation of the cryostat mechanical vibrations. The data collected from the RED series of prototype detectors drive the studies of the heat and ionization channels in all the later chapters, exploring how to improve the resolution in heat and ionization energies up to $\mathcal{O}(10)$ eV while maintaining a good rejection of background events.

The third chapter is dedicated to the study of the heat channel based on experimental data of RED detectors of simple design with one GeNTD thermal sensor and no electrodes. These bolometers are modeled with a system of electro-thermal equations. The noise affecting two readout electronics is characterized by adjusting this model in the frequency domain using Monte Carlo Markov Chain analysis. Similarly, a new detector is characterized based on its steady-state and the shape of heat signals. The strategy for improving the heat channel performance is then discussed based on simulation of the energy resolutions.

The fourth chapter introduces the ionization channel of the cryogenic detectors. The processes of ionization and charge drift in the semiconducting germanium crystal are described along with the theory of the signal generation on the electrodes. The electrostatic simulation of detectors in the finite element calculation software COMSOL® is explained. It is used to characterize two detector designs candidate for the CryoCube by estimating their electric field, electric capacitance and fiducial volume. This chapter ends on the estimation of the ionization energy resolution from a future low-noise HEMT-based electronics for the two detector designs.

The fifth chapter describes the optimization of the detector designs introduced in the previous chapter. It presents a methodology based on the electrostatic simulations for studying the influence of each of the design parameters on the projected ionization channel performance.

The sixth chapter concludes this series of three chapters dedicated to the ionization channel, by comparing the projected performance from electrostatic simulations and experimental results for two prototype detectors operated in the IP2I cyrostat. It starts with the description of the simulations. It then follows with an explanation of the analysis pipeline applied to the raw experimental data. The last section discusses the comparison between experimental and simulated results, especially regarding the optimization of the designs proposed in chapter 5.

The seventh chapter is dedicated to the measurement of the neutron background at the IP2I cryogenic facility with the prototype detector RED80. It describes the specific experimental setup used to calibrate the detector with a neutron source. An advanced analysis in order to discriminate the nuclear and electronic recoils is presented using analytical pulse simulation to estimate their associated event rate spectrum. The characterization of the IP2I neutron background is then used to estimate the expected fast neutron background component at the ILL site for RICOCHET.

Chapter 1

Measurement of the CENNS with Cryogenic Bolometers in the RICOCHET experiment

1.1 CEνNS and the new physics

1.1.1 Coherent Elastic Neutrino-Nucleus Scattering

A scattering phenomenon occurs when two particles interacts during a collision. An elastic scattering is a process where the kinetic energy of a particle is conserved in the center-of-mass frame, but its direction of propagation is modified (by interaction with other particles and/or potentials). Furthermore, while the particle's kinetic energy in the center-of-mass is constant, its energy in the lab frame is not. This work especially focuses on the elastic scattering between neutrinos and atomic nuclei. Even though the nucleus is an assembly of nucleons, a coherent scattering occurs when the neutrino can interact with the nucleus as a whole, as if it was a uniform object. When the scattering of a neutrino on a nucleus is coherent and elastic, it is defined as a Coherent Elastic Neutrino-Nucleus Scattering, shortened to CEνNS or CENNS. This physical phenomenon, described by Freedman in 1973 within the framework of the Standard Model, was measured for the first time in august of 2017 by the COHERENT collaboration, with an experiment installed near the spallation source at the Oak Ridge National Laboratory in the United States. Before presenting the scientific context of this work, a brief recall is done on nucleus and neutrino. We will therefore discuss the CENNS equations and the various experiments aimed at measuring this process.

1.1.2 The Atomic Nucleus

Rutherford's experience with gold leaf in 1909 provided valuable information for the development of Bohr's atomic model in 1913. Rutherford understood that the electrically positively charged of an atom is concentrated in the middle of the atom. Indeed, knowing that the matter is electrically neutral and that an atom has electrons (charged negatively) there are necessarily positive charges "somewhere". Bohr then designed an atomic model for the hydrogen that reminds us of a planetary system. There would be the nucleus at the center and the electrons around it, only allowed to be on specific circular orbitals. Theoretical and experimental developments show us today that the electrons are not really on circular orbits but rather have a probability of presence described by combinations of spherical harmonics. Bohr's model for hydrogen is not fundamentally questioned and is still taught. Electrons are considered to orbit around the nucleus of positive charge. The latter can be either stable or unstable in the case of radioactive elements. This is an important fact, that an atom is not a fundamental object of modern physics: it is composed of nucleons (neutrons and protons), which are themselves composed of three quarks held together by to the strong nuclear interaction mediated by gluons. The size of an

atom is of the order of 0.1 nm $= 10^{-10}$ m which is five orders of magnitude larger than the size of its nucleus 1 fm $= 10^{-15}$ m.

1.1.3 The Neutrino

The neutrino is one of the elementary particles of the Standard Model (SM) of particles physics, which is an electrically neutral lepton. There are three flavors of neutrinos each associated with a charged lepton: the electronic neutrino ν_e is coupled to the electron e^-, the muonic neutrino ν_μ with the muon μ^- and the tauic neutrino ν_τ with the tau τ^-. The physicist Wolfgang Pauli was the first to postulate the existence of the neutrino in 1930. This new particle (at the time) helped to explain the continuous spectrum of the beta disintegration, which is a radioactive decay in which a radionucleide emits an electron (or positron) and an antineutrino (or neutrino). The experimental confirmation was obtained by Cowan and Reines in 1956 based on an idea by Wang Ganchang (1942) and Reines was awarded the Nobel Prize for physics in 1995 for this discovery. A neutrino is only sensitive to the electroweak and gravitational interactions. The later is negligible in particle physics but hold impact on the larger scale of cosmology. The neutrino has a very low probability of interaction with matter, which is formalized in particle physics as a weak cross-section. To have an order of magnitude in mind we can show that out of 10 billion neutrinos of 1 MeV that cross the Earth, only 1 will interact with its components. In the study of the CENNS process, no particular attention is brought on distinguishing neutrinos from antineutrinos as well as different flavors. Indeed, this scattering process is insensitive to these differences.

1.1.4 CENNS and Standard Model

It was in 1973 that Daniel Z. Freedman, a physicist currently at MIT, proposed the coherent elastic neutrino-nucleus scattering as a probe for weak interaction [29]. In its description based on the Standard Model still under development at that time (it will take its current form in the mid-1970s), Freedman expresses the evolution rate of the effective cross-section of the neutrino-nucleus interaction as a function of the recoil energy of the nucleus:

$$\frac{\mathrm{d}\sigma(E_\nu, E_R)}{\mathrm{d}E_R} = \frac{G_f^2}{4\pi} Y_w^2 m_A \left(1 - \frac{m_A E_R}{2E_\nu^2}\right) F^2(E_r) \tag{1.1}$$

This equation shows that the evolution of the effective cross-section noted $\sigma(E_\nu, E_R)$ depends on the neutrino energy E_ν and recoil energy E_r of the nucleus as well as of the mass of the target nucleus m_A. Without going into the details of the theoretical calculations to obtain this expression, one can try to explain simply the different terms.

The Fermi coupling constant G_f is measured experimentally by studying the life time of the muon (inversely proportional to G_f^2) [24]. We can express G_f with the coupling constant of the weak interaction g_W , the mass m_W of the boson W, the speed of light c and the reduced Planck constant $\hbar$ according to the equation:

$$G_f = \frac{\sqrt{2}}{8}\left(\frac{g_W}{m_W c^2}\right)^2 (\hbar c)^3 \sim 1.17 \times 10^{-5}\,\mathrm{GeV}^{-2} \tag{1.2}$$

The weak nuclear hypercharge Y_w is given by:

$$Y_w = N - Z(1 - 4\sin^2\theta_w) \tag{1.3}$$

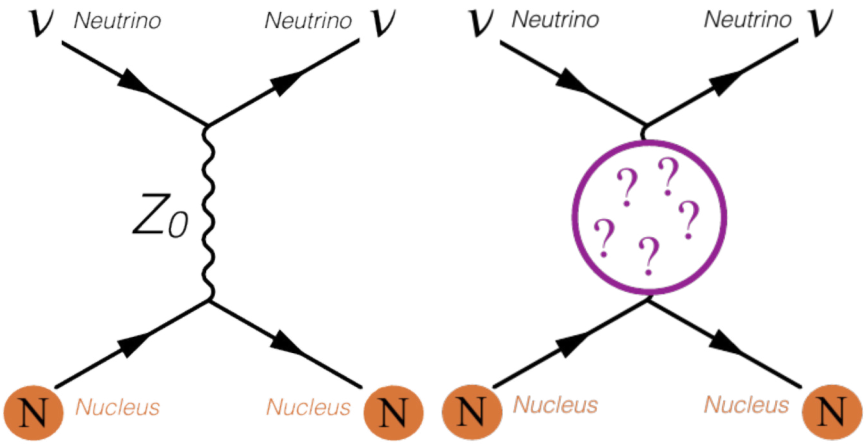

Figure 1.1: Feynman diagrams of the CEvNS. On the left in the case of the Standard Model. On the right the same process within the framework of alternative theories.

It depends on the number of neutrons N and protons Z composing the nucleus. The term θ_w is the mixing angle which is a parameter of the Weinberg-Salam theory of the electroweak interaction (reunification of the theory of electromagnetism and weak interaction). The value of $\sin^2\theta_w$ is close to 0.24 [23]. Thus, in practice, the hypercharge simplifies to $Y_w \simeq N$. As described later in this work, the measurement of the $\sin^2\theta_w$ value as a function of the transferred momentum would permit to probe for new physics in the electroweak sector.

The form factor F is a function of the recoil energy that characterizes the loss of coherence at high transferred momentum. It is equal to 1 for low recoil energies, so it is often neglected in very low energy regimes, and decreases with the recoil energy E_R.

The effective cross-section σ associated with the CENNS is obtained by integrating the equation 1.1 from $E_R = 0$ to $E_R^{max} = 2E_\nu^2/(m_A + 2E_\nu)$, the maximum recoil energy of the nucleus accessible for a given neutrino energy E_ν [51]. Its expression is:

$$\sigma \sim \frac{G_f^2 N^2}{4\pi} E_\nu^2 \tag{1.4}$$

which is proportional to the square of the number of neutrons N in the target nucleus and the energy of the neutrino thanks to the coherence of the interaction in case $m_N \gg E_\nu$.

The detection of CENNS is not done by directly measuring the cross-section of the particles that interact with the atomic nuclei of the detector. We measure the number of neutrinos having interacted with a nucleus according to the recoil energy of the latter. By doing this on a fairly wide range of recoil energy, we end up with what is called an energy spectrum of CENNS events. In this case, we will speak of CENNS spectrum, and of energy spectrum in the general case for different scattering processes. The expected differential CENNS event rate R is calculated from the differential cross-section by convolving with the incoming neutrino flux Φ:

$$\frac{\mathrm{d}R}{\mathrm{d}E_r} = \mathcal{N} \int_{E_\nu^{min}} \Phi(E_\nu) \frac{\mathrm{d}\sigma(E_\nu, E_r)}{\mathrm{d}E_r} \mathrm{d}E_\nu \tag{1.5}$$

In this equation, $\mathcal{N}$ represents the number of target nuclei per mass unit. The minimum energy of a neutrino to induce a nuclear recoil is given by the relation $E_\nu^{min} = \sqrt{m_N E_R/2}$.

A common representation of this type of interaction in particle physics is done with the help of Feynman diagrams. In this representation, the time flows from left to right and the distance between the particles is represented along the vertical axis. The mediator bosons are indicated with wavy lines. The figure 1.1 displays two Feynman diagrams for the CENNS. The

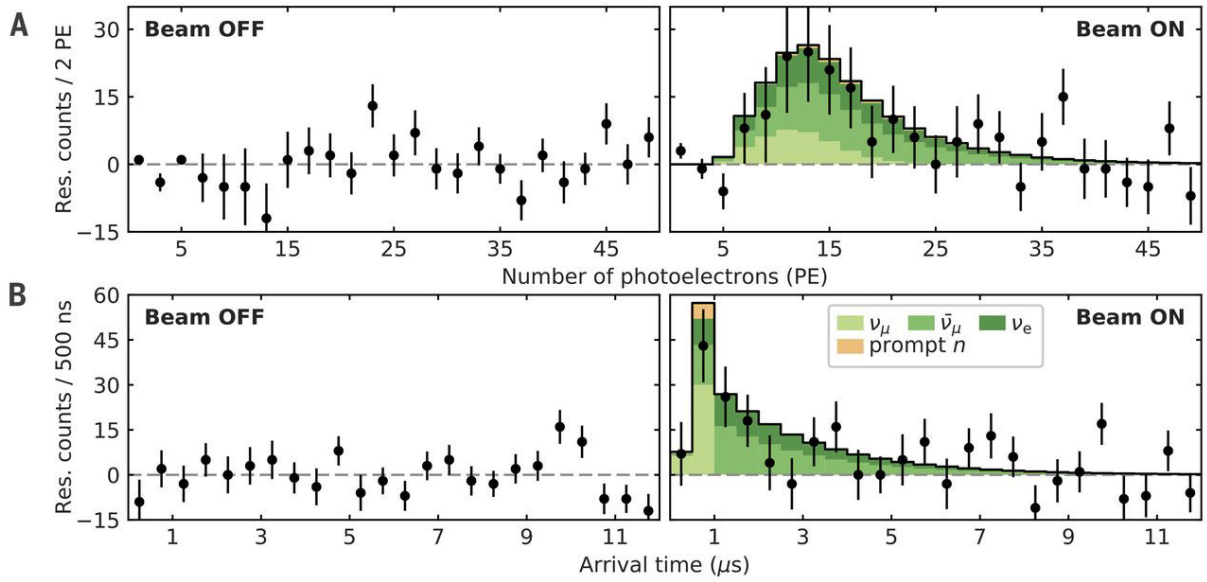

Figure 1.2: Experimental result of the COHERENT experiment at the SNS demonstrating unambiguously the existence of the CENNS. Figure taken from [7].

left diagram corresponds to the CENNS process in the SM framework, by having the Z_0 boson as the mediator of the weak interaction between the neutrino and the nucleus. The right diagram presents the CENNS in the framework of alternative theories.

1.1.5 First Detection of CEνNS

The COHERENT collaboration was the first to observe experimentally and unambiguously the signature of the CENNS in August 2017 [7]. The technology used at that time was a 14.6 kg sodium-doped cesium iodide (CsI[Na]) scintillator instrumented with photo-multipliers. The detector was located at a distance of 19.3 m from the neutrino source and had an energy detection threshold of 4.5 keV. The neutrino flux of average energy $E_\nu = 30$ MeV used for this detection was produced with the so-called "pion-at-rest" method. It consists in taking advantage of the decay of positive pions, obtained after a controlled collision of a mercury atom with a proton, which leads to the production of neutrinos and antineutrinos. The proton source comes from the SNS (Spallation Neutron Source) located at the Oak Ridge National Laboratory in Oak Ridge, Tennessee (USA).

Scientists in the collaboration have detected an excess of CENNS-like events, shown in Figure 1.2, with a confidence level of 6.7σ compatible at 1σ with the SM prediction. The statistical uncertainty of this study is estimated to 16 %. This result proves the existence of the CENNS process which has been considered for years as purely hypothetical.

It would be now possible to constrain models of new physics [7]. Nevertheless current data do not allow to study predictions in the low-energy region such as the existence of new mediating bosons [21]. This requires a source of lower energy neutrinos, which in turn requires detectors with lower energy threshold.

1.2 Search for New Low Energy Physics

In the framework of beyond Standard Model physics, the measure of the CENNS process at low-energy could be associated with:

- the existence of new massive bosons,

- the existence of an anomalously large magnetic moment of the neutrino,
- the existence of non-standard interactions.

There is an important scientific stake in making these low energy measurements to provide additional elements in the understanding of fundamental interactions but also to provide additional constraints for a large number of neutrino research projects. A precise measurement of the CENNS would, for example, make it possible to constrain the previously mentioned theoretical models.

However, to do new physics research with the CENNS process, the use of a suitable neutrino source is required. This source should have a known and adapted neutrino energy spectrum (typically $E_\nu \approx 10\,\text{MeV}$). This will result in lowered recoil energies E_R in the detector requiring lower energy threshold. This upgrade in detector performances can only be reached by diminishing the volume of the detectors resulting in a loss of exposure. As such, the neutrino source should produce a very high flux of neutrinos as to counter the inevitable loss of detector mass and obtain an equivalently high CENNS event rate.

Additionally, various technical and practical considerations are taken into account: possibility of interruption of the flow (or pulsed flow) for background rejection (as in the case of COHERENT for example), minimum accessible source/detector distance, ease of access and installation, regulations and availability of infrastructure.

1.2.1 Neutrino Sources

There are many sources of neutrinos because the radioactive decay processes that generate them are very common in nature. This subsection discusses some common low-energy neutrino sources and their characteristics regarding the search for CENNS. Neutrinos out of experimental range such as those composing the cosmic neutrino background (the analogue of the cosmic microwave background for neutrinos) or the diffuse supernovae neutrino background will not be discussed. The resting pion method used by COHERENT will not be recalled as it has already been presented and is not a viable solution for the search for new low energy physics because of the too large energy of the emitted neutrinos and too low integrated flux.

Solar Neutrinos

Thermonuclear fusion reactions take place in the heart of stars. During these reactions, low energy neutrinos (a few MeV) are emitted. They escape from their original star without great difficulty thanks to their low effective cross-section. The process responsible for most of the neutrino emission of the Sun, is the fusion of two protons p into a ^{2}H deuterium (heavy hydrogen) nucleus, an anti-electron e^+ (otherwise known as positron) and an electronic neutrino ν_e:

$$p + p \longrightarrow {}^2H + e^+ + \nu_e \tag{1.6}$$

For this specific reaction the energy of the emitted neutrinos is in the order of $\mathcal{O}(100)$ keV. It should be noted, however, that there are other reactions of a different nature producing neutrinos within the Sun. The figure 1.3 displays on the left, the simulated spectrum of the neutrino flux as seen from Earth associated with these different processes. Despite of the rather large neutrino flux of the order of $7 \times 10^{10}\,\text{cm}^{-2}\text{s}^{-1}$, their small interaction cross-section with matter makes their detection very difficult.

Despite this difficulty, large experiments, such as Borexino located in the underground laboratory of the Gran Sasso in Italy, are able to measure this solar neutrino spectrum as seen on the right subplot of figure 1.3. However, for a CENNS precision measurement experiment, the Sun is clearly not a relevant source because even if the energy of some neutrinos is low enough for

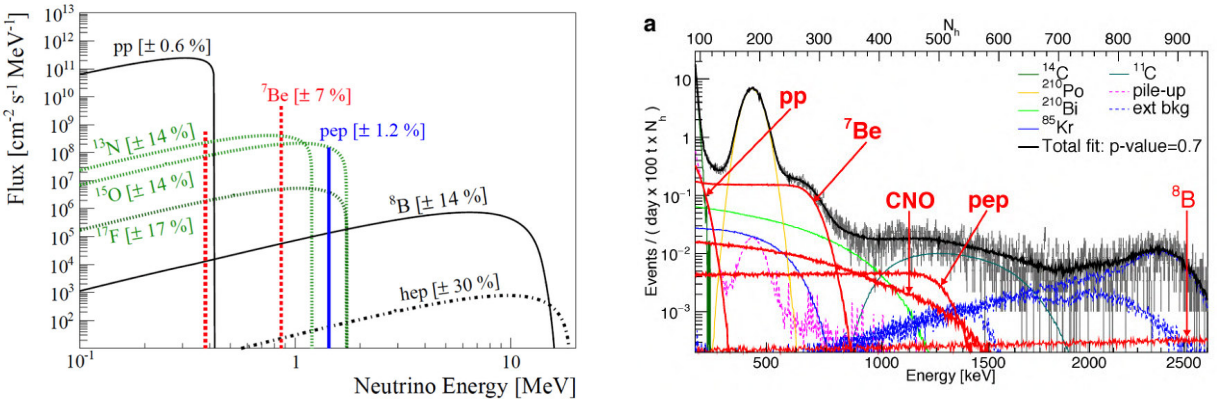

Figure 1.3: Solar neutrino spectrum. On the left, simulated spectra of solar neutrinos seen from the Earth associated with the different fusion reactions, taken from [25]. On the right, solar neutrino spectrum and its components measured by the Borexino experiment at the Gran Sasso in Italy, taken from [49].

probing new physics, the neutrino flux is too low and would require a huge volume (mass) of detector as used by solar neutrino experiments as SNO [13]. Another negative point is that it is not possible to turn off the source to identify the background noise. Indeed, the solar neutrino flux is constant and crosses the Earth to reach the detector without difficulty.

Terrestrial Neutrinos (geo-neutrinos)

Our own planet, the Earth, emits neutrinos through natural radioactivity processes. Geo-neutrinos are emitted by the Earth's core through natural radioactivity processes, resulting in a flux at the Earth's surface estimated to be $1 \times 10^{6}\,\mathrm{cm}^{-2}\mathrm{s}^{-1}$ [14]. This flux of geo-neutrinos is low and is coupled with a wide distribution in energy. Consequently, they are very difficult to detect because of the background of neutrinos from extraterrestrial and human origin. Nevertheless some experiments try to carry out geo-neutrino measurements for the information they would allow us to obtain on the Earth and in particular at the level of the Earth's core. The same large-scale experiment Borexino claims to have recently detected events attributable to geo-neutrinos [5]. For reasons similar to solar neutrinos, geo-neutrinos are not relevant in view of the current knowledge for CENNS precision measurement.

Production from Human Activity

Humans are capable of producing neutrinos in controlled physical processes. In particle accelerators, for example, it is not uncommon to produce neutrinos with energies of up to 100 GeV. The most intense man-made source of low-energy neutrinos are the nuclear fission power plants. However, the main objective of these power generation plants is not the production of neutrinos, which consists in a very abundant by-product of the electricity production. The flow of neutrinos emitted by a standard nuclear power plant 10 m from the reactor is approximately equal to $2 \times 10^{15}\,\mathrm{cm}^{-2}\mathrm{s}^{-1}$, for an average neutrino energy of 4 MeV. Nuclear fission reactors offer a range of energy compatible with the research of new physics, the neutrino flux is among the most important and in addition to that it is possible to take advantage of unit outages to measure background noise. For this last point the subtraction background noise is not as optimal as with a pulsed source if the background noise is not stationary on the time scales represented by the combustion of a fuel rod but it is always an interesting plus to gain in measurement accuracy.

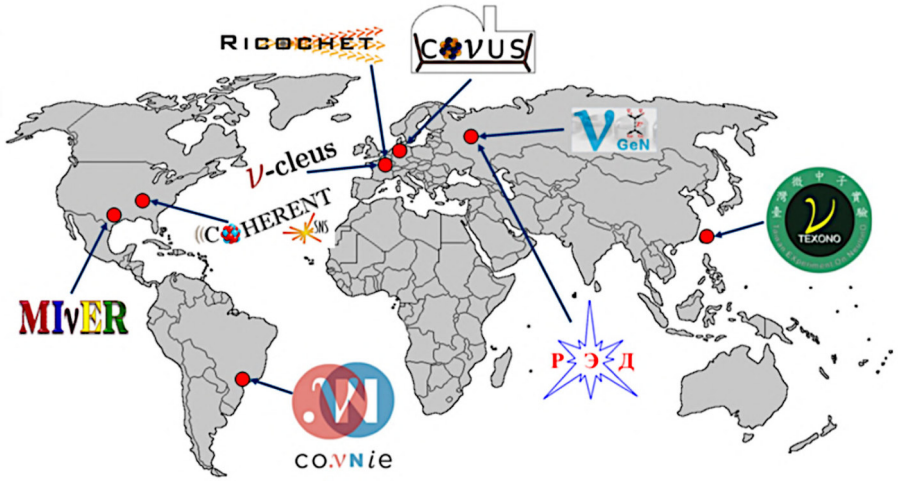

Figure 1.4: Main experiences of CEvNS in the world today (2020).

Experiment	(Detector Material) @ Location	Reference
NuGEN	(Ge) @ Kalinin Reactor (Russia)	[15]
CONUS	(Ge) @ Brokdorf (Germany)	[37]
TEXONO	(Ge) @ Kuo-Sheng Reactor (Taiwan)	[54]
CONNIE	(Si) @ Angra Reactor (Brazil)	[6]
RED100	(Xe) @ Kalinin Reactor (Russia)	[8]
MINER	(GeSi) @ Nuclear Science Center (USA)	[4]
NU-CLEUS	($CaWO_4$, Al_2O_3) @ Chooz (France)	[55]
RICOCHET	(Ge, Zn, Al, (Si)) @ ILL (France)	[18]

Table 1.1: Presentation of CENNS experiments associated with a nuclear reactor: materials used for detection @ localization. In red are represented the cryogenic experiments with a very low detection threshold for the research of new physics. The RICOCHET experiment is the only one to propose a detector capable of discriminating between nuclear and electronic recoils.

1.2.2 Reactor Experiments

The strong potential of nuclear power plants as sources of neutrinos has led a small number of CENNS experiments to be installed close to a reactor core around the world. The main experiments searching for the CENNS near nuclear reactors are identified on the atlas displayed in figure 1.4 and listed in the table 1.1 with their detector material and their localization.

The CENNS experiments near a reactor would allow the estimation of the Weinberg angle θ_w at low energies. Figure 1.5 shows the SM prediction (blue line) for this parameter and the zone of the parameter space accessible by the CENNS experiments (green zone) which still remains largely unexplored. The estimation of this parameter with different physical processes is also very important to identify incompatibilities and allows the scientific community to go beyond the Standard Model.

In view of the number of CENNS experiments, we can expect this precision measurement within a few years. What is uncertain is whether this scientific result will deviate from the Standard Model at low-energy scale or confirm this theory. The "cooperation" at work between all these collaborations and with dark matter direct detection experiments such as EDELWEISS favors rapid developments and technological improvements.

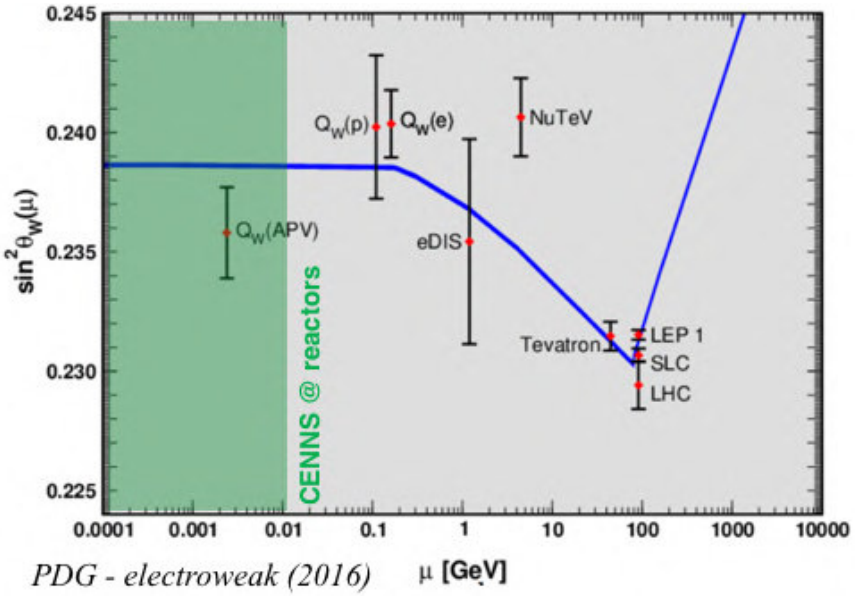

Figure 1.5: Scale dependence of the weak mixing angle, adapted from [46]. The blue curve is the prediction of the Standard Model for different processes and experiments. The green area shows the area accessible with a precision measurement of the CENNS spectrum near a nuclear reactor.

1.2.3 RICOCHET

RICOCHET is a CENNS experiment based on an international collaboration of some fifty researchers, technicians and engineers through various laboratories and universities in France, Russia and the United States. RICOCHET aims at measuring the CENNS spectrum with a statistical accuracy of 1 % after one year of data taking. With this objective, the CENNS detection with low energy neutrinos (a few MeV) with an accuracy of at least 5σ, like the COHERENT experiment, will be reached within a week of operation. It should be noted that the targeted accuracy is far superior to that obtained by COHERENT. To achieve these scientific objectives the RICOCHET device is composed of a cryogenic system, a shielding to limit sources of unwanted background, and the CryoCube and QArray detector arrays. It will be installed in 2022 at the Laue Langevin Institute (ILL) in Grenoble, France. The ILL hosts a 58 MW fission research nuclear reactor. A numerical modeling of RICOCHET at ILL and the implementation scheme near the reactor core are presented in figure 1.6.

The CryoCube detector will be at only 8 m from the core of the nuclear reactor which will produce a neutrino flux of $10^{12}\,\mathrm{cm}^{-2}\mathrm{s}^{-1}$. The CryoCube will be cooled down close to the absolute zero at cryogenic temperatures around 10 mK, in order to be able to measure minute temperature rises caused by the neutrinos following their interaction with the nuclei that make up the detector's target material.

The cryogenic detector load will be protected from external radiations by a thick layer of lead and borated polyethylene shielding weighting more than 15 tons and an active cosmic particle rejection device designated as "veto muon". The objective of this shielding strategy is to prevent as much as possible any unwanted diffusion processes in the experimental data which would reduce the signal-to-noise ratio and significantly hurt the chances of detecting signs of new physics.

The incident neutrino flux at the location of the CryoCube at on ILL site was estimated and the collaboration has precisely simulated the expected CENNS spectrum according to different theoretical models considered and taking into account the different background contributions.

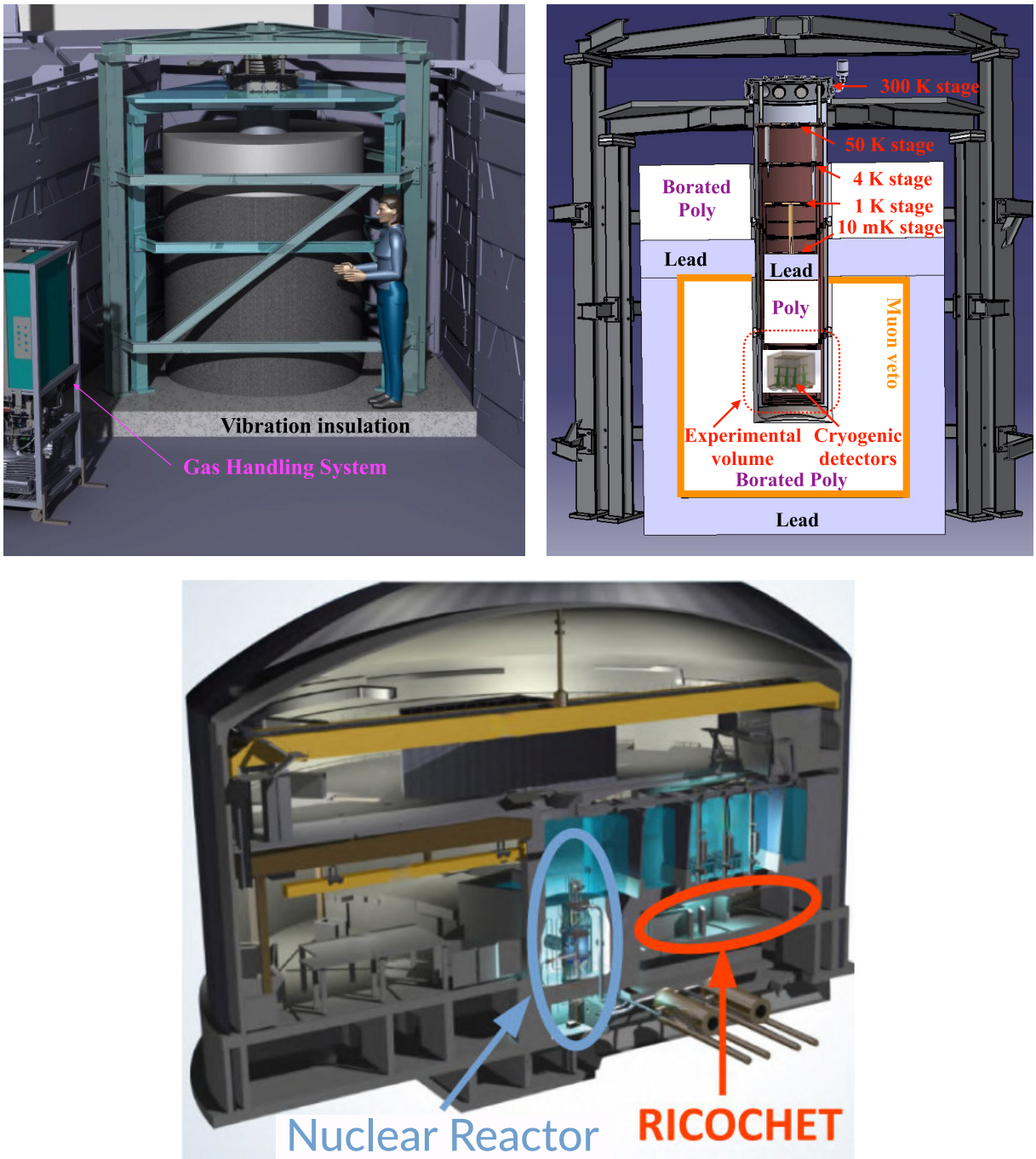

Figure 1.6: On the top left, Installation of RICOCHET at ILL, 3D modeling. On the top right, view in cryostat cut. At the bottom, location of the RICOCHET cryostat within the ILL nuclear reactor. The water pool above the location of RICOCHET provides protection against cosmic particles. Images adapted from [20].

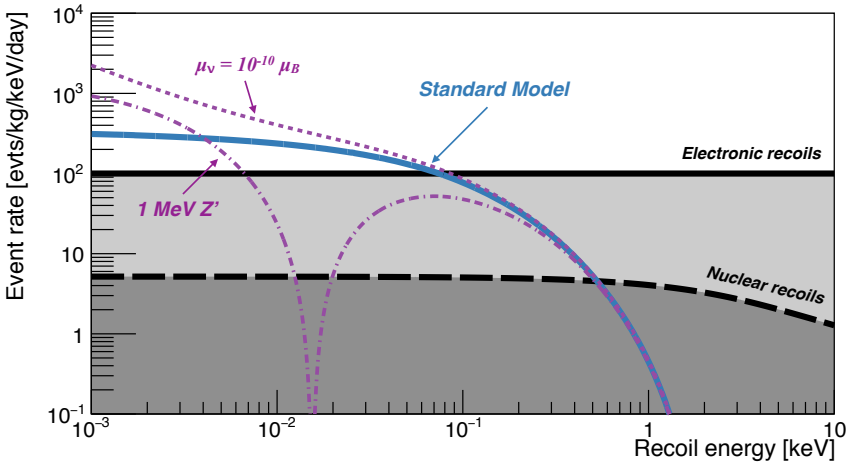

Figure 1.7: Simulation of the background noise on the CENNS spectrum for RICOCHET at the ILL. The radioactive background noise is represented as its two components inducing electronic recoils in light grey and inducing nuclear recoils in dark gray. Figure taken from [21].

In figure 1.7, we see the prediction of the Standard Model (in blue) and the assumed effect of two alternative theories: the existence of an anormally high magnetic moment of neutrino (violet, fine dotted line) or of a new Z' boson (violet, dashed line). The background noise, of electronic or nuclear origin, is represented in grey and is for both almost uniform in the energy range considered.

This numerical simulation allows to define the specifications of RICOCHET so that the CENNS spectrum is measured specifically in the region of interest for new physics search. From the spectra associated with two exotic physics scenarios in figure 1.7, we see that we need a low enough detection threshold in recoil energy. Otherwise, we will not be able to see the deviations from the Standard Model or even the CENNS itself.

We can notice that the spectrum is given in events/keV/kg/d and therefore to have a sufficient statistic it is necessary to find an interesting ratio of detector mass over data acquisition time.

Having an ultra massive detector near the nuclear core represents a real technical challenge, and it is hardly possible to achieve significantly lower energy thresholds. The exposure of the detector, which is its mass multiplied by the experiment time in kg · d, is not the only parameter to be considered, it is necessary to have sufficient sensitivity to measure the minute energy deposition generated by the interaction of a neutrino with matter. This is the reason why the RICOCHET collaboration chose to use low-threshold cryogenic bolometers. To carry out the identification of neutrino recoils, the material of the target for coherent neutrino scattering is semiconductor germanium which features an intrinsic discrimination ability thanks to a recoil heating and ionizing this material. The double energy measurement, described later in the section 2.3, leads to difference in signal signature between nuclear recoils, produced by CENNS, and electronic recoils generated by the electronic component of the background.

Specifically, a detector with the following characteristics would be required:

- detection threshold / energy resolution: $E_R \sim 50\,\text{eV}$ / $\sigma(E_R) \sim 10\,\text{eV}$,

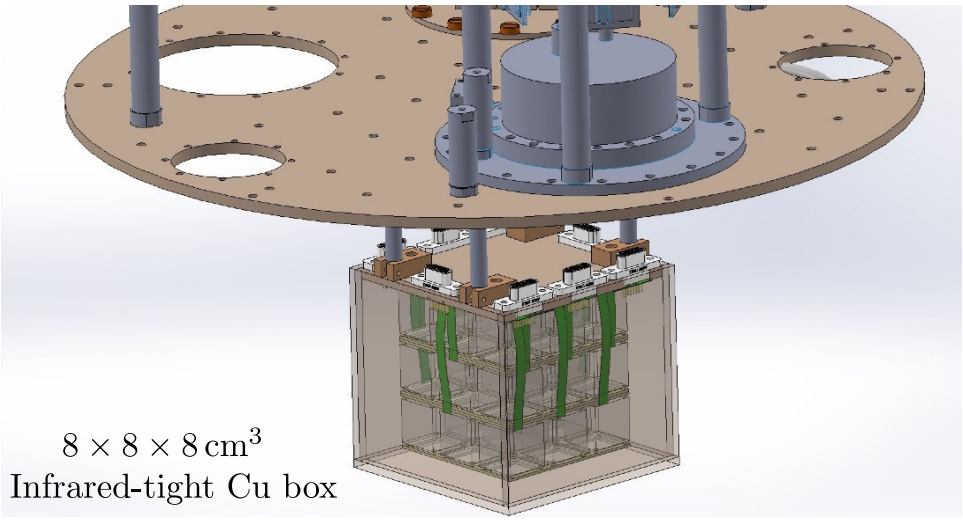

Figure 1.8: 3D model of the CryoCube installed at the coldest stage of its cryostat. We can see by transparency the 27 germanium crystals of 38g electrically connected to the systems of acquisition by the green cables.

- ability to discriminate between electronic and nuclear recoils with thermometer + electrodes for electronic background rejection with semiconductor material ,
- mass of the detector: $m_d \sim 1\,\mathrm{kg}$ with a flux of $10^{12}\,\mathrm{cm}^{-2}\mathrm{s}^{-1}$ to have about ten of CENNS events per day.

To meet these specifications, the members of the RICOCHET collaboration are developing an innovative detector called CryoCube which is presented in the figure 1.8. It will be composed of 27 germanium crystals of 38 g each equipped with a heat measurement channel and an ionization measurement channel for discrimination purpose. The goal of my thesis is the design of the elementary cryogenic detectors.

Chapter 2

Experimental Setup at the IP2I cryogenic facility

This chapter describes the IP2I Cryostat Facility in which the cryogenic germanium detectors presented in this work were operated. It explains how cryogenic conditions are obtained, presents the cryogenic germanium detectors and their principle of operation.

2.1 The IP2I cryogenic facility

The particle detectors studied in this work are cryogenic germanium bolometers. The term "cryogenic" indicates that these detectors are operated at cryogenic temperatures below 1 K $=$ $-272.15\,^{\circ}$C. In order to reach such temperatures, the detectors are placed inside of a ^{3}He/^{4}He dilution cryostat.

The experimental results discussed in this work were obtained by running germanium detectors in the dry dilution cryostat of the *Institut de Physique des 2 Infinis de Lyon* (IP2I). The IP2I cryogenic facility is located in the basement of the IP2I Haefely building (see figure 2.1). With an almost negligible overburden roughly estimated to be about 1.5 m $\cdot$ w $\cdot$ e (meter water equivalent), the cryogenic detectors are operated in an above-ground (or surface) experiment as opposed to the underground operation of the EDELWEISS detectors at the LSM.

In order to reduce the environmental gamma background, the cryostat is surrounded by a 10 cm thick cylindrical lead shield covering a solid angle of $\sim 70\,\%$ of 4π around the detectors. A reduction of about a factor of 10 is estimated on the triggering rate of our detectors with this lead shield. There is no lead shield inside the cryostat. The materials used for the cryostat construction were not selected for low radioactivity, with the exception of the replacement of the standard glass fiber rods [1] by stainless steel ones, shown to have much less radioactive contamination. While the radioactive background is high as a consequence of the above-ground operation, it is very similar to what is expected from the ILL site for the RICOCHET experiment. The neutron and gamma components of this background are characterized down to 1 keV in Chapter 7.

The total surface area of the facility is about a 100 m^2 and encompasses the main cryogenic lab (80 m^2), a technical room for pumps and gas handling system (6 m^2), an ISO-5 clean room for detector mounting (9 m^2), and a room hosting a chemical bench also related to detector fabrication (5 m^2). A photo of the cryogenic laboratory is displayed in figure 2.2 with the open cryostat in the corner of the room next to the lead shield on the left and the acquisition electronics and computers on the right.

[1] used by the Cryoconcept company which built the cryostat

Figure 2.1: Photo of the IP2I Haefely building. The cryogenic facility is located in the basement, at the same height as the parking lot.

2.1.1 Presentation of the IP2I R&D Dry Cryostat

The cryostat is a Hexadry-200 commercially available from Cryoconcept, which has been upgraded to reduce the vibration levels at the mixing chamber. The cryostat assures a cryogenic temperature with low fluctuations and a temperature setpoint of about 10 mK for the bolometer operation. It provides a steady cooling power over several weeks for standard R&D runs which can be extended to several months for physic runs.

The structure of the cryostat is illustrated with annotated photo and scheme displayed in the figure 2.3. This cryostat is built with several cooling stages at different temperatures which allow the transition from the exterior ambient temperature $\sim$ 300 K to the lowest cryogenic temperature $\sim$ 10 mK on the mixing chamber. During operation, the cryostat is maintained hermetically shut with the Outer Volume Casing (OVC) mounted on the feedtrough of the cryostat. The whole inner volume is immersed in a medium vacuum, the air is pumped out to reach a pressure less than 10^{-5} mbar). As such, there is no gas to conduct heat between the different stages. The thermal conduction between stages can only occur though the metal structure of the cryostat, the cooling circuit and the thermal radiation. Each stage is surrounded by gold-plated copper casings to block the infrared radiation from various stages.

The IP2I cryostat is a Dry Dilution Refrigerators (DDR). It runs solely on electric power as opposed to the Wet Dilution Refrigerators (WDR) of the EDELWEISS experiment which consumes liquid helium to cool down. Dry cryostats are particularly adapted to R&D work as the operating cost is low and it is possible to descend very quickly to cryogenic temperatures (24 hours to reach 4 K, compared to one week for the EDELWEISScryostat at the LSM[2]). They provide a similar low temperature environment as the one obtained with WDR at the cost of increased vibration levels. The IP2I cryostat was equipped with vibration mitigation solutions described in the next section 2.2.

[2]Laboratoire Souterrain de Modane, France

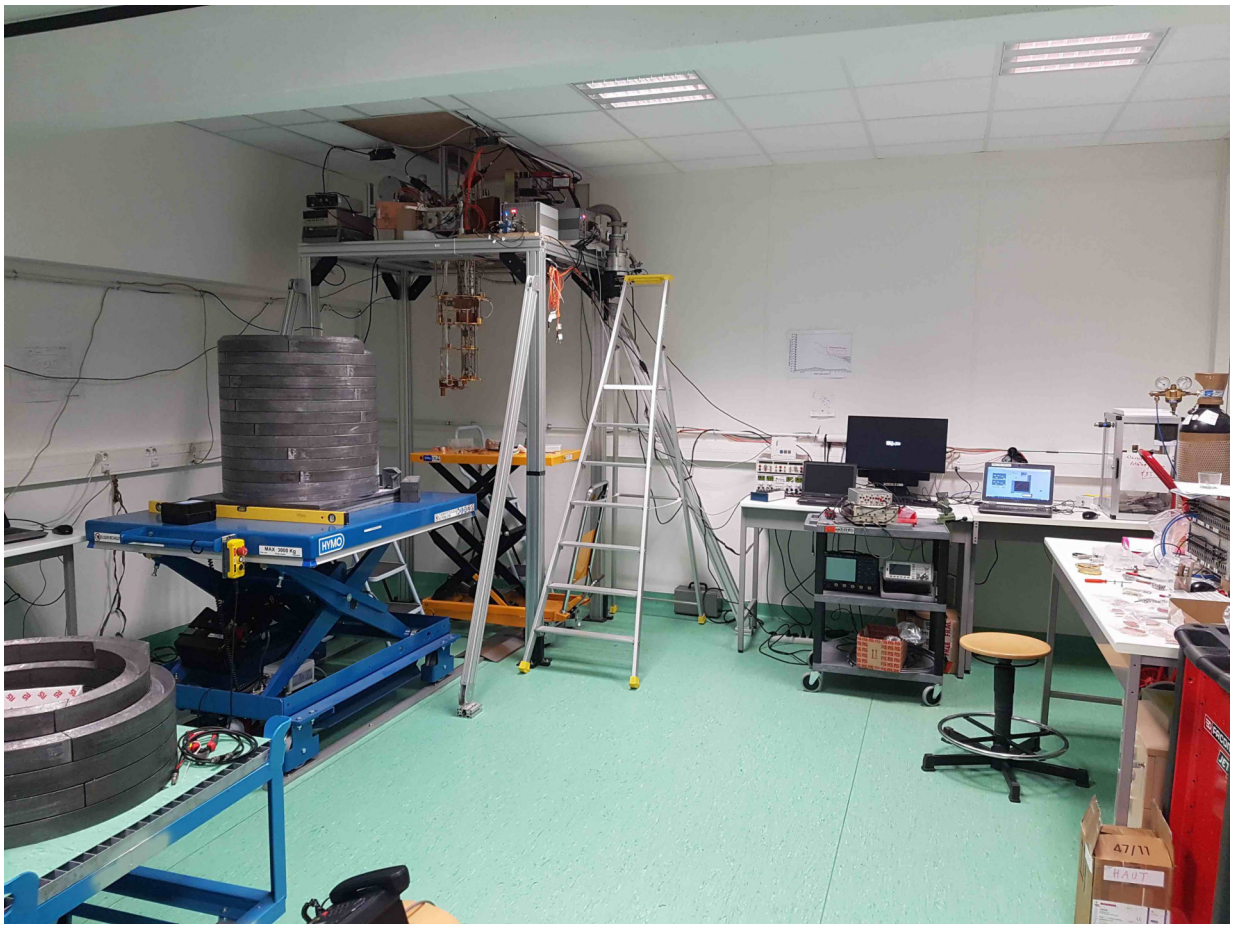

Figure 2.2: Photo of the cryogenic lab, where the dry dilution cryostat (opened) and its lead shield are clearly visible. On the right side are the computers and outside electronics in charge of the detector readout and polarization.

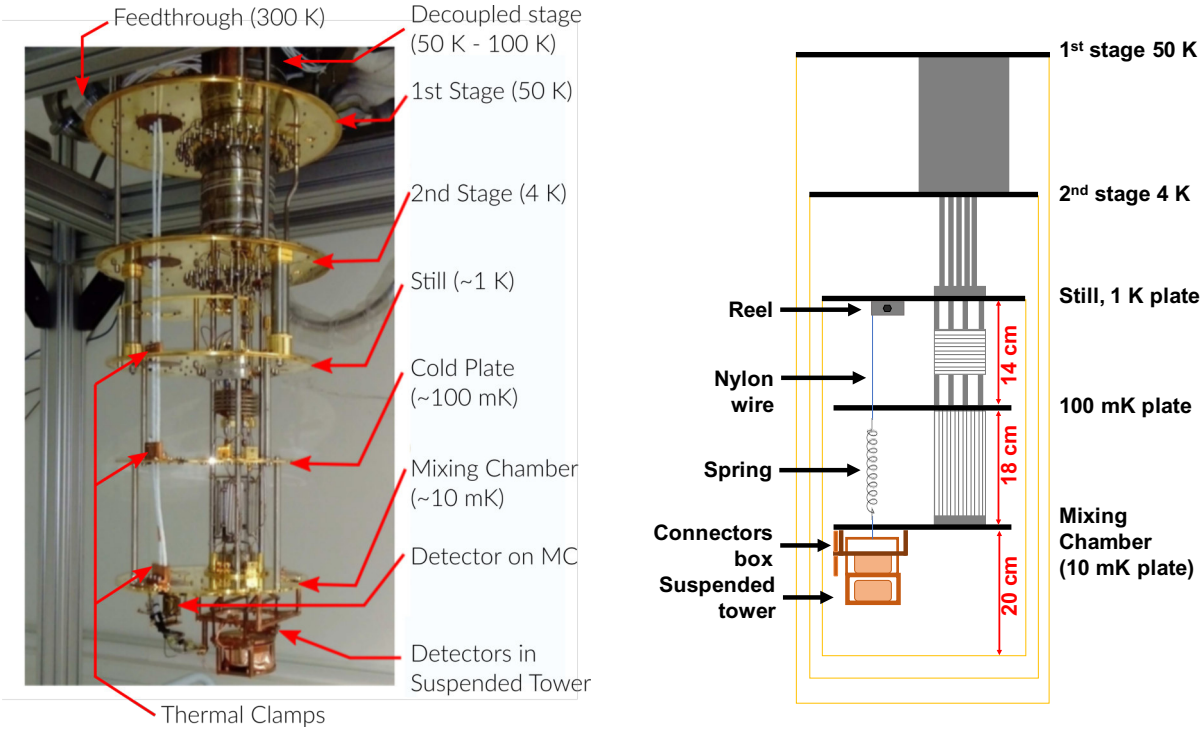

Figure 2.3: On the left, annotated photo of the open cryostat. On the right, annotated scheme of the cryostat. The copper screens blocking the infrared radiations are represented as the orange rectangles separating each cooling stage. Figures taken from [39].

The IP2I dry cryostat has one closed cooling circuit using as cooling fluid a mixture of 75 % ^{4}He and 25 % ^{3}He. This cooling circuit is separated in two cycles: the "Pulse Tube" cycle and the dilution cycle. The pulse tube cycle is in charge of cooling the first stage and second stage to reach the temperatures 50 K and 4 K respectively. The "Pulse Tube" applies Stirling cycles between 9 and 18 bars at a frequency of 1.6 Hz, which allows the ^{4}He fluid to reach a temperature of 4 K. The dilution cycle extends the cooling circuit to the three other stages and cools them to their operating temperatures: the still at $\sim$ 1 K, the cold plate at $\sim$ 100 mK and the mixing chamber (MC) at $\sim$ 10 mK. In this cycle, the helium mixture is cooled by passing through fine capillaries located on the first and second stages, benefiting from the cooling of the pulse tube cycle. As the cooling fluid reaches 4 K, it condensates in its liquid phase. A succession of Joule-Thompson expansions and heat exchangers allows the mixture to reach a temperature of 800 mK at the still. It is near this temperature that a phase separation occurs within the mixture: the first phase is concentrated in ^{3}He and floats on the surface of the second phase diluted in ^{3}He and rich in ^{4}He. This phenomenon can be explained by the Fermi-Dirac statistic followed by the ^{3}He atoms: they cannot simultaneously occupy the same energy state and the same position. Thus, for a sufficiently low temperature, the phase separation becomes energetically favorable. This phase separation takes place within the mixing chamber. The phase with low ^{3}He is then pumped out. The thermodynamic equilibrium of the two phases is broken and there is a transfer of ^{3}He from the concentrated phase to the diluted phase in ^{3}He. This process is endothermic, which decreases the temperature of the mixture and thus of the mixing chamber. The pumped helium ^{3}He is then re-injected into the dilution circuit. To this end, the dilution cycle allows a minimum temperature of 9 mK to be reached on the mixing chamber for this cryostat. The detector load is thermally linked to the mixing chamber in order to reach the lowest temperatures and the best performances.

Once the cryostat is cooled down, it continues to operate at full power until the end of the run. The power of the cooling circuit is in constant equilibrium with the thermal heat coming

from the exterior of the cryostat or from the operation of the detectors. Consequently, in this state, the exact temperature of the mixing chamber would fluctuate near its minimal equilibrium value. As a mean to operate the cryogenic detectors with constant performances and at a chosen temperature, the latter is regulated at higher temperatures usually superior to 14 mK. The regulation is assured by the Joule effect of a heating resistor. Its heat power is set by a Proportional-Integrate-Derivative controller (PID controller) reading the temperature with a RuO_2 thermistance close to the detectors in the suspended tower.

2.1.2 Standard Operation of the Detectors

We want to operate the bolometers at the coldest temperature possible. We may want to attach the detectors directly on the mixing chamber stage as seen on left photo of figure 2.3. However, the "dry" cryostat creates a lot of mechanical vibration especially due to the pulse tube operation. These vibrations propagate to the detectors, causing thermal noise (parasitic phonons), electric noise (triboelectricity) as well as heat power on the mixing chamber which prevents a good cooldown [45]. To tackle this issue, the cryostat is mechanically decoupled from the ceiling/pulse tube with a bellow (external decoupling). This external decoupling was done in partnership with Cryoconcept by mechanically decoupling the cold head of the pulse tube cryocooler from the dilution unit. The vibrations at the detector level were further mitigated by placing the bolometers inside a suspended tower (internal decoupling) developed by the MANOIR group [39]. The suspended tower is a copper chassis solely linked to the cryostat by a spring providing mechanical support and mechanical decoupling. This device makes it possible to avoid a significant low-frequency noise on the heat measurement while ensuring thermal conduction to the cryostat thanks to thin copper braids. This suspended tower is described in the paragraph 2.2.

The detectors are cabled to the acquisition computer on the outside of the cryostat through the cold and warm electronics. The cold electronics transports the voltage signal of the detectors located near the mixing chamber to a first Bi-FET preamplifier stage at 100 K and a second stage amplifier at 300 K [9]. The white cables of this cold electronic are visible on the left photo of figure 2.3. The cabling comes from the top of the cryostat and goes down to the dilution and is thermalized at each stage thanks to thermal clamps. As such, there is only minimal heat transfer from the hotter stages on the mixing chamber due to the electronics. Once the signal is amplified, it is transported to the acquisition computer with optical fiber. The detector signals are recorded as continuous time series called data streams. These data streams are then processed with a dedicated pipeline based on the NEPAL software developed by the MANOIR group in order to ensure high quality data processing. The stream processing and analysis is described in Chapter 6. Once the processing is done at the CC-IN2P3, monitoring plots are transferred automatically to a monitoring website allowing us to follow the performance and behavior of the detectors as a function of time.

2.2 Vibration mitigation and cryogenic suspension

The cool-down process of the two first stages within DDR is ensured by the technology of pulse-tube cryocoolers. However, the mechanical vibrations they induce can drastically affect the performance of cryogenic detectors. This effect has been reported by several cryogenic experiments using such bolometers (see [39] and references there in).

The IP2I cryostat was upgraded with an external vibration mitigation solution. Its first two stages (50K and 4K) are thermally coupled to the highly vibrating pulse-tube cold head thanks to low-pressure gas exchangers (Hexagas^{TM}), hence avoiding any mechanical contact and vibration propagation to the dilution unit. In 2016, one year after its delivery to IP2I, the cold head has

been mechanically anchored to the ceiling hence providing two independent and maximally decoupled frames. As shown in the figure 2.2, the metallic framework surrounding the cryostat supports and anchors the dilution unit to the ground, while the cold-head is fixed to the ceiling of the laboratory (hidden by a wooden panel on the photo).

This upgrade led to the reduction of the vibration levels by about two orders of magnitude between 0.5 Hz and 20 Hz hence achieving world-leading vibration levels in a dry cryostat of few-$\mu g/\sqrt{Hz}$ below 20 Hz [45]. At the time, the impact on our detectors has been tremendous. Indeed, before the decoupling, due to the high vibration levels, the detectors were not able to operate due to the significant vibration-induced frictional heat power dissipation.

With the improvement of our detector sensitivity and resolution, we found that the cold-head decoupling was not enough to ensure optimal operation of the new generation of detectors. Indeed, it was found that the large radial stiffness of the edge-welded below connecting the cold-head to the dilution unit still allowed for some vibration propagation down to the detectors. A second vibration mitigation system at the mixing chamber level, where the detectors are installed, had to be implemented.

2.2.1 Internal Mitigation Solution: the Suspended Tower

This internal vibration mitigation solution is the suspended tower which can be considered as a simple elastic pendulum. The 3-D dynamical description of the elastic-pendulum can be divided into two pseudo-independent equations in the approximation of small perturbations. The natural frequency for vertical modes is then given by:

$$f_{0,\text{vertical}} = \frac{1}{2\pi}\sqrt{\frac{k}{M}} = \frac{1}{2\pi}\sqrt{\frac{g}{l_{\text{eq}} - l_0}} \tag{2.1}$$

where M corresponds to the total mass of the suspended tower, k, l_0, and l_{eq} are the elastic constant, the rest length, and the length at equilibrium of the spring, respectively. The vertical resonance frequency can either be expressed in terms of k and M simultaneously or by the spring elongation alone $|l_{\text{eq}} - l_0|$. The natural frequency for radial oscillations of the pendulum, which are related to its total length l_{tot}, is given by:

$$f_{0,\text{ radial}} = \frac{1}{2\pi}\sqrt{\frac{g}{l_{\text{tot}}}}. \tag{2.2}$$

From these approximations, we can estimate the theoretical resonance frequencies of the elastic pendulum depending on the spring constant, the pendulum length and the total mass of the detector assembly. Interestingly, one can notice that as $l_{\text{tot}} \geq (l_{\text{eq}} - l_0)$, the natural frequency in the radial direction is necessarily lower than in the vertical direction: $f_{0,\text{ radial}} < f_{0,\text{vertical}}$.

Thanks to the use of a single spring holding system, we avoid any transverse momentum related natural frequencies which could populate the vibration spectrum at high frequencies. Therefore, the system is expected to have a transfer function response under the form of a 2^{nd} order low-pass filter with a single resonance frequency in both directions $i = \{\text{vertical, radial}\}$:

$$H(\omega_i) = \frac{\omega_{0,i}^2}{\omega_{0,i}^2 - \omega_i^2}, \tag{2.3}$$

where $\omega_{0,i}$ is the natural pulsation of the suspended tower, with $\omega_{0,i} = 2\pi f_{0,i}$. The natural frequencies of the suspended tower in both vertical and radial directions have been tuned to be as low as possible in order to attenuate all vibrations above 1.4 Hz, corresponding to the frequency of the pulse-tube cryocooler. According to equation 2.1, we obtain a vertical resonance frequency $f_{0,\text{vertical}} \leq 1$ Hz for a spring elongation of at least $(l_{\text{eq}} - l_0) \geq 25$ cm. The same

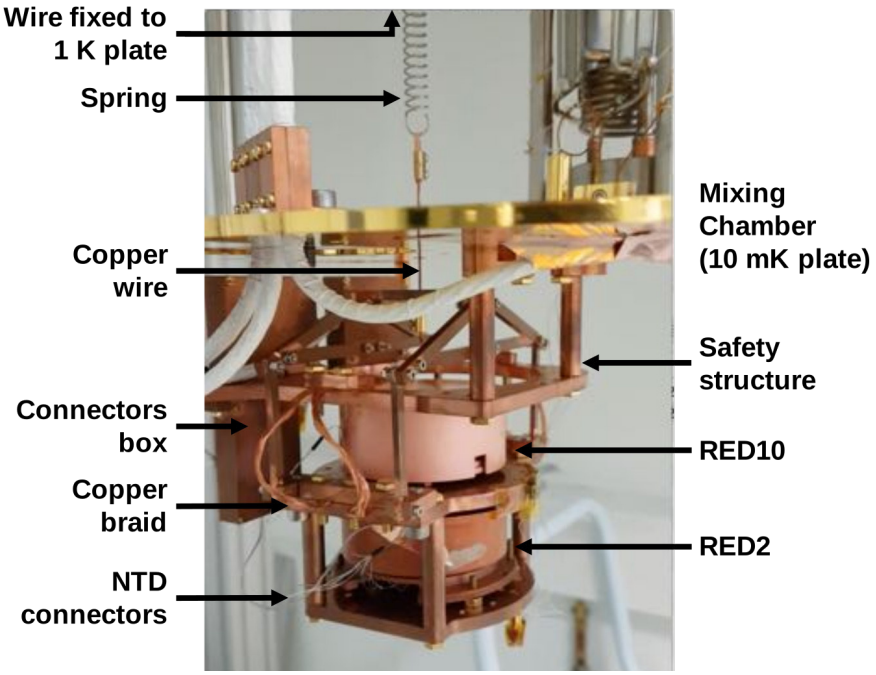

Figure 2.4: Photo of the suspended tower containing the two 200 g bolometers RED10 and RED2. This device mechanically decouples the detector load from the mixing chamber while assuring its thermalization. Figure taken from [39].

condition applied to the radial frequency, $f_{0,\text{radial}} \leq 1\,\text{Hz}$ results in a total pendulum length of at least $l_{tot} \geq 25\,\text{cm}$ using equation 2.2.

The challenge then comes from accommodating with the constraints imposed by the cryostat geometry. As the distance between the mixing chamber plate and the inner thermal screen is only of about 18 cm, the pendulum had to be attached to the still plate and not directly to the mixing chamber. The scheme of the figure 2.3 and the photo 2.4 illustrate the holding strategy of the suspended tower in the cryostat. A Kevlar wire is fixed below the still plate at 1 K and running without contact through the cold plate at 100 mK. A stainless steel spring with an elastic constant of $k = 240\,\text{N}\cdot\text{m}^{-1}$ is attached to the wire between the cold plate and the MC at 10 mK. The elastic constant k has to be carefully chosen, taking into account the total mass of the detector assembly M, as its elongation is constrained by the $\sim$ 18 cm distance between the 100 mK stage and the MC. Finally, the suspended tower is connected to the spring via a thick ($\sim$ 2 mm in diameter) 5 cm long copper wire through the MC plate. This copper wire ensures the thermalization of the stainless steel spring, so that it does not emit infrared radiation damaging the detector performance. With this approach, the total pendulum length from the still plate to the center of mass of the detector assembly is $l_{\text{tot}} = 25\,\text{cm}$.

The detector tower is shown in the figure 2.4 holding the two detectors RED2 and RED10. This module has a total height of 13 cm and can hold two cryogenic detectors based on 200 g germanium crystal or lighter. During the installation, before attaching the spring, the tower is firmly held by a copper frame screwed under the MC plate. This structure remains as a safety structure during cool-down and operation in case the wire should break. Connector boxes are placed close to the detector on the external side of the safety structure. They are used to connect the sensors of the detectors to the readout electronics at the warmer stages. Both the suspended tower and the safety structure are made of radiopure CuC_2 copper. During operation, the suspended tower is floating and its thermalization is realized by four 10 cm long ultra-supple flat copper braids linking the safety structure and the tower.

2.2.2 Characterization of the Vibration Levels

This subsection quickly presents the impact of the suspended tower on the vibration level and the noise of the heat channel of the bolometer RED10. All the results are published in the paper [39] in which the suspended tower was demonstrated to attenuate the transmission of both vertical and radial vibrations, with a particular emphasis on the radial modes as these are less efficiently damped from our pulse-tube cold head decoupling.

The vibration level is characterized by measuring the movement of the detectors [45]. The set-up is composed of a high sensitivity seismic accelerometer from *PCB Piezotronics*. We used the high sensitivity accelerometer *PCB-393B05* which has a gain of 10 V/g and an intrinsic noise limit of [0.5-0.07] $g/\sqrt{Hz}$ within [1-1000] Hz frequency range.

The accelerometer is fixed on a U-shaped workpiece allowing to measure the vibrations along either the radial or the vertical direction. The accelerometer can be fixed below the MC stage of the cryostat, or below the bottom stage of the suspended tower in order to compare their respective vibration level. The elastic constant k and Young's modulus E values of the stainless steel and copper, composing the majority of the rigid strucutre of the cryostat, have small variations between ambient and cryogenic temperatures. As such, all vibration measurements are performed at room temperature [12]. The output signal of the accelerometer is sampled at 10 kHz, well beyond the signal bandwidth of the accelerometer of 1 kHz. The vibration levels is obtained as LPSD expressed in $g/\sqrt{Hz}$ from a Fast Fourier Transform (FFT) analysis using Hanning windowing over 5 s time windows. Figure 2.5 displays the vibration levels on the MC plate and in the suspended tower comparing the measurements with the pulse-tube (PT) cryocooler switched on (PT ON), emulating the normal cryostat operation, or off (PT OFF). The intrinsic noise limit of the accelerometer is plotted as dashed lines as reference.

The main differences observed between these two PT configurations are coming from few pick-up lines which are mostly at high frequencies and arise from the acoustic noise generated by the operation of the pulse-tube cooling cycle. At low frequencies (< 40 Hz), in the detector bandwidth, the impact of turning the PT ON is very small on the suspended tower, merely being expressed as resonance peaks of low amplitudes. As a matter of fact, by comparing the vibration level of the MC plate in the PT OFF case (purple solid line) to the level of the suspended tower in the PT ON case (orange solid line), one can further conclude that the suspended tower is not only efficient at reducing the PT-induced noises but also most of the whole setup-related vibrations from the building, the cryostat holding structure, and so on. This demonstrates that vibration-wise, our detectors are largely insensitive to their surrounding environment, suggesting that they should run in optimal conditions inside the IP2I cryostat.

This optimal operation condition can be checked by comparing the noise level affecting the signal measurement of a detector either installed on the mixing chamber plate or in the suspended tower. In this paragraph, this comparison is made with the 200 g detector RED10 whose heat channel is later characterized in the chapter 3. With a heat sensitivity of about $100\,nV \cdot keV^{-1}$ at around 18 mK, RED10 is sensitive to perturbative displacements and vibrations.

The noise levels are presented as LPSD expressed in $V \cdot \sqrt{Hz}^{-1}$. These LPSD were measured as presented in section 3.2.3 dedicated to the characterization of the electronics noise affecting the heat channel of the bolometers.

Figure 2.6 shows the LPSDs obtained for RED10 on the MC plate as dashed lines, and on the suspended tower as solid lines. The 1 V normalized heat signal template power spectrum and the theoretical noise calculations based on the full electro-thermal modeling of the detectors (see Sec.3.2.3) are also plotted as a reference. Measurements of the LPSDs were made with and without polarizing the heat sensor (called NTD and described in section 2.3) of RED10 in order to estimate the effect of the vibrations on the cabling, such as microphonics. Note that

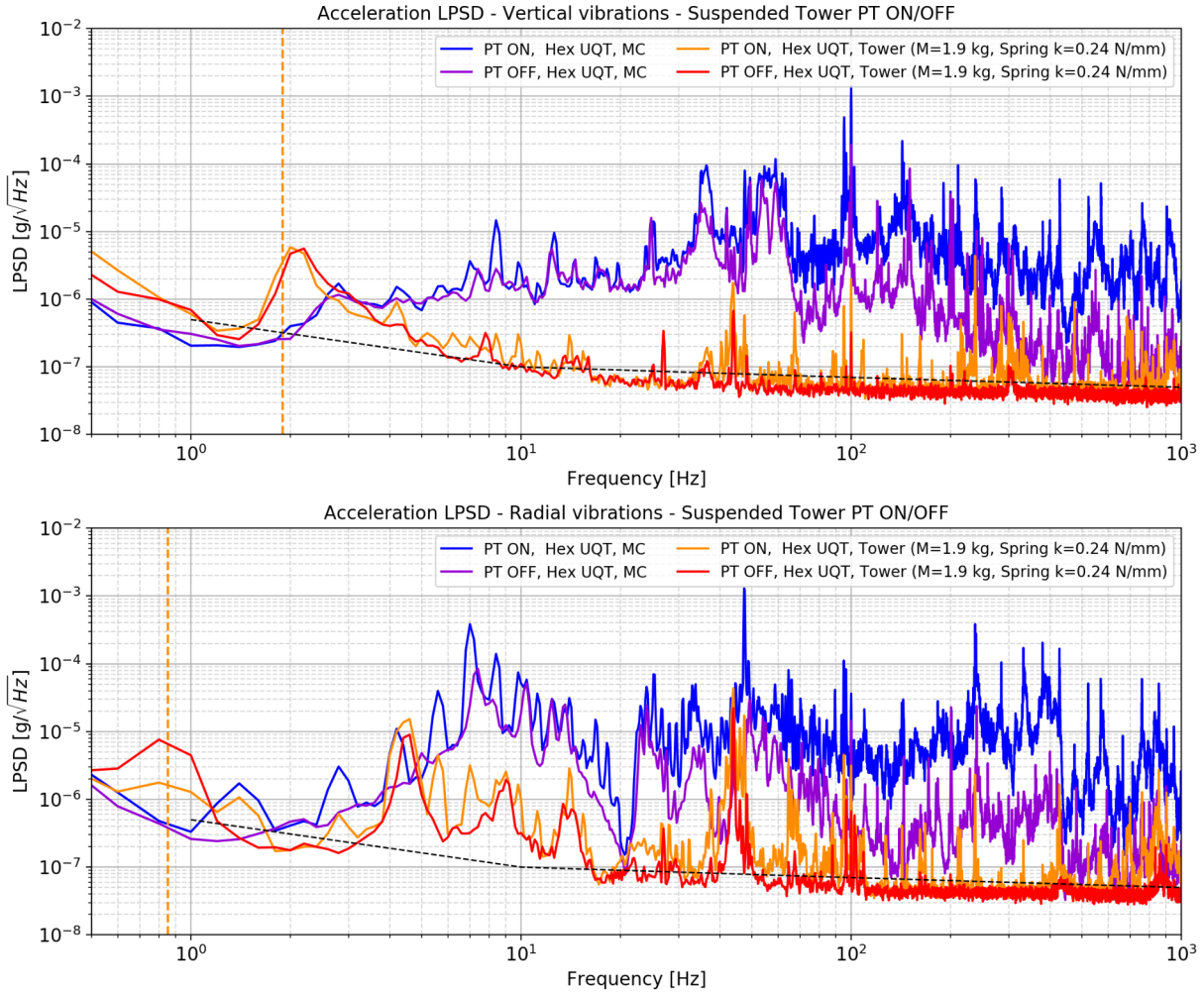

Figure 2.5: Comparison of the vertical (top subplot) and radial (bottom subplot) vibration levels of the MC plate and the suspended tower in both PT ON and OFF configurations. The dashed black line is the accelerometer sensitivity, and the orange vertical dashed lines represent the position of the natural frequencies of the suspended tower derived from equations 2.1 and 2.2. Figures taken from [39].

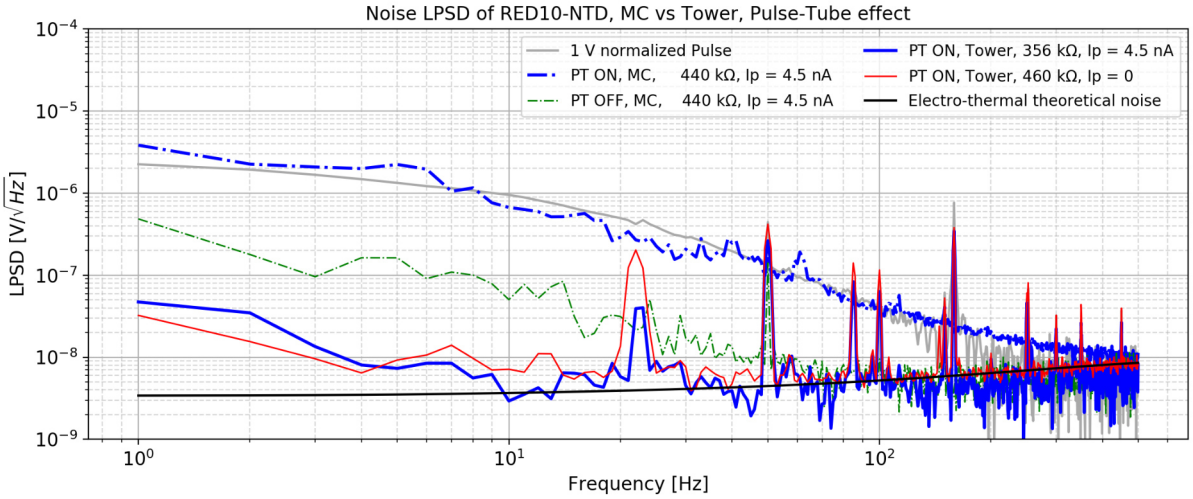

Figure 2.6: Noise power spectra density for the NTD of RED10 mounted on the MC plate (dashed lines) and on the suspended tower (solid lines). Measurements were performed at optimal NTD polarization currents with PT ON and PT OFF at 16 mK. The black solid line refers to the expected noise level derived from the electro-thermal model described in section 3.2.3, while the grey solid line shows the unit normalized pulse template illustrating the signal bandwidth. Figures taken from [39].

the discussion will mostly focus on the frequency range of interest, from 1 Hz to 40 Hz, as it corresponds to the detector signal bandwidth.

From comparing the various voltage PSD presented in Figure 2.6, we can extract a few major conclusions regarding the effectiveness of the suspended tower at mitigating the vibration-induced noise on bolometers.

The first obvious comparison is between the cases where the detectors are optimally polarized (blue curves) and either on the mixing chamber (dashed lines) or on the suspended tower (solid lines). The LPSD at the lowest frequencies is reduced by almost two orders of magnitude. Furthermore, we observe that the noise levels obtained PT ON and with the NTD optimally polarized (blue solid lines) are almost identical to the case where the NTDs are not polarized and the pulse-tube OFF (red dashed lines), suggesting that we are limited by both the electronics and the intrinsic thermal noise from the detector, and not by the vibrations when the detectors are mounted on the tower. This is confirmed by the fact that the resulting noise levels are very close to the theoretical expectations obtained with the electro-thermal model illustrated by the black solid lines.

Interestingly, we do not see on the NTD a 1.8 Hz pick-up noise as was potentially suggested from the vertical acceleration measurements shown as the red (PT OFF) and orange (PT ON) solid lines from Figure 2.5. This suggests that such frequency vibrations within the detector bandwidth do not limit the detector performance.

Finally, one can derive from Figure 2.6 that the noise PSD obtained with the NTDs optimally polarized on the suspended tower with PT ON (blue solid lines) are below the ones obtained with the detectors running on the mixing chamber with the PT OFF (green dashed lines). This observation confirms what was suggested from the vibration measurements shown in figure 2.6: the suspended tower damps very efficiently the vibration-induced noise from the pulse-tube cryocooler, but makes the detectors insensitive to any residual vibrations from the surrounding environment of the experiment

The improvement on RED10 performance can be appreciated by computing its energy resolution. It was found that the heat resolution of RED10 improved from 14 keV, when installed on the mixing chamber, to 400 eV when installed in the suspended tower. This impressive gain

of almost two orders of magnitude on the energy resolution can be explained by the detector RED10 being especially susceptible to vibrations. This detector would have been discarded due to poor performances without this internal mitigation solution.

Following the publication of this work [39], similar improvement factors were found, between a factor of a few up to one order of magnitude, on all of the detector prototypes of the RED series. The detectors operated in the IP2I cryostats are no longer limited by vibrations, but only by the intrinsic JFET-based electronic noise limiting us from reaching the ultimate thermal fluctuation noise floor. Based on this success, a new suspended tower that can host up to 5 RED detectors was installed in the IP2I cryostat in early 2020. Though a similar elastic pendulum approach would not be feasible in the RICOCHET cryostat for the CryoCube, a slightly different three-spring pendulum approach is currently being investigated for optimal operation of the CryoCube detector at ILL.

2.3 Cryogenic Particle Detectors

2.3.1 Semiconductor Crystals for Particle Detection and Discrimination

The use of cryogenic semiconductor crystals has been pioneered by the direct dark matter detection experiments searching for low-mass dark matter. A wide variety of crystal materials can be used, but in recent years the leading materials have been: $CaWO_4$ in CRESST [1], Ge and Si in (Super)CDMS [3], and Ge in EDELWEISS [9].

These crystalline detectors, also designated as bolometers, aim at measuring the heat signals, in the form of thermal or athermal phonons, induced by a particle interaction. Several temperature sensing techniques exist, but the most widely and mature ones are the (low-impedance) Transition Edge Sensors (TES) and neutron transmutation dopped germanium (NTD-Ge) thermistors. In both cases, the heat increase is measured via a change in resistance which is either measured as a current or voltage drop at the front-end of the readout electronics.

While their operation at cryogenic temperatures $\mathcal{O}(100)$ mK is challenging and expensive, cryogenic detectors feature a precise energy measurement with excellent energy resolution and background rejection down to recoil energies of $\mathcal{O}(1)$ keV. Indeed, the specificity of these detectors based on semiconductor crystal lies in the simultaneous measurement of a second observable, such as ionisation in semiconductors (Ge, Si) or scintillation in scintillating crystals ($CaWO_4$). This allows for the discrimination of the electronic recoils, induced by the radioactive background from the nuclear recoils, potentially generated by dark matter candidates, as in both cases the ionization/scintillation yields vary with the recoiling particle type.

Similarly to these dark matter candidates, a neutrino interacting with an atom of the semiconductor crystal of the detector through the CENNS process results in a nuclear recoil, giving access to the discrimination of the backgrounds signals. For this reason, the RICOCHET experiment aims at adapting this technology, in particular the germanium detectors of EDELWEISS, for the precise measurement of the CENNS process with the development of the CryoCube detector array.

2.3.2 Working Principle of Cryogenic Germanium Bolometers

This work is focused on cryogenic germanium bolometers equipped with an ionization readout. Their working principles are illustrated with the scheme of figure 2.7.

An ultra-pure semiconductor germanium crystal acts as an absorber: it is the element that serves as a target for the elastic collision of the incident particle. This interaction, called a recoil, deposits a recoil energy E_R in the crystal which is expressed as thermal energy E_{ph} (phonons)

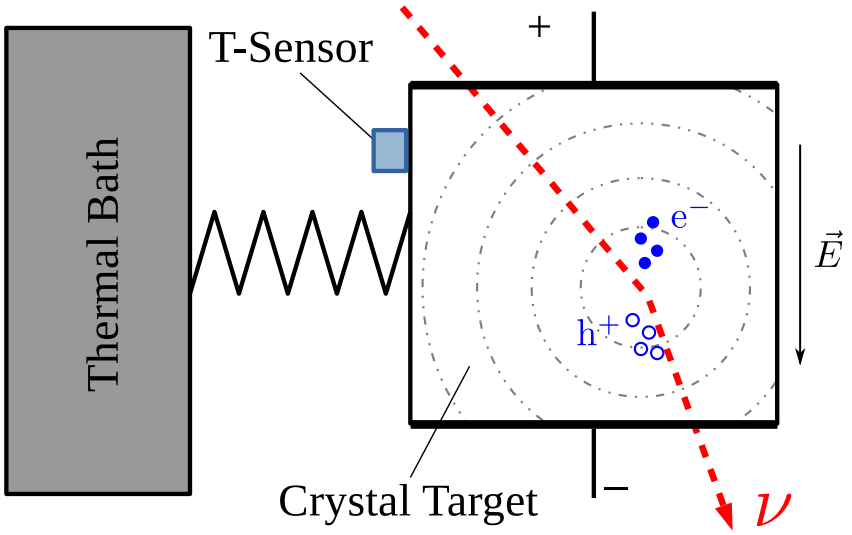

Figure 2.7: Working principle of a crystalline bolometer (here with additional charge-readout) for particle detection. The induced recoil from an interacting particle (here a nuclear recoil from an incident neutrino) on the atom of the germanium crystal release its recoil energy E_R by creating phonons (illustrated as dashed concentric circles) and excited charge carriers (electron e^- and holes h^+). The heat channel measures the increase in temperature ΔT from the phonons with a GeNTD thermal sensor. The ionization channel consists in the electrodes collecting the drifting charges by applying an electric field $\vec{E}$. Image adapted from [52].

and ionization energy $E_{Ion.}$ (electron-hole pairs):

$$E_R = E_{ph} + E_{Ion.} \tag{2.4}$$

The fraction of the recoil energy going into the phonon and ionization energies is formalized with the quenching factor Q such that:

$$E_{Ion.} = QE_R \quad \text{and} \quad E_{ph} = (1-Q)E_R \tag{2.5}$$

This quenching factor depends on the type of recoil induced by the incident particle interacting with the germanium crystal. The two major types of recoils considered in this work are the nuclear and the electronic recoils. The electronic recoils (ER) are generated by incident photons or charged particles. In this case, the particle interacts with the electronic cloud of a germanium atom of the crystal. As a result, the entirety of the recoil energy E_R is expressed in the excitation of the electrons, such that the associated quenching factor is $Q_{ER} = 1$ with $E_{Ion.} = E_R$. The nuclear recoils (NR), induced by the CENNS process and neutrons, have the incident particle interacting with the nucleus of the atom. The transmitted recoil energy E_R is immediately expressed as gain in momentum of the germanium nucleus. The movement of the nucleus generates vibrations of the crystal lattice, the phonons. The moving nucleus also disturbs the electronic cloud of its atom, thus creating some electron-hole pairs. The quenching factor Q_{NR} associated with the nuclear recoils is an increasing function of the recoil energy E_R. It is comprised between 0 and 0.3 for E_R between 0 and 20 keV. The intrinsic difference in heat and ionization energies between the nuclear and electronic recoils is the key aspect of the discrimination for the germanium detectors.

The term ionization designates the creation of electron-hole pairs by a recoil. These excited charge carriers are the sole agents of the electric conduction in the semiconducting germanium, each carrying a positive or negative elementary charge $q_e = 1.6 \times 10^{-19}$ C. The ionization energy

E_{e-h} determines the number N_p of electron-hole pairs created in the crystal as:

$$E_{Ion.} = N_p \epsilon_{e^- - h^+} \tag{2.6}$$

with $\epsilon_{e^- - h^+} \approx 3\,\text{eV}$ the average energy of a pair in Germanium. Several electrodes applying an electric field $\vec{E}$ in the crystal will collect the drifting electrons and holes. The ionization signal is registered as voltage ΔV in Volt on the electrodes such that:

$$Q = N_p q_e = C_{el} \Delta V \tag{2.7}$$

with Q the total collected electric charge in Coulomb and C_{el} the electric capacitance of the electrode in Farad. The ionization energy $E_{Ion.}$ is deduced from the measured voltage signal ΔV:

$$E_{Ion.} = \frac{C_{el} \Delta V}{q_e} \epsilon_{e^- - h^+} \tag{2.8}$$

and is used to access the recoil energy E_R with knowledge of the quenching in equation 2.5. This measure of the recoil energy through the ionization energy is defined as the ionization channel of the detector.

Phonons are vibrations of the crystal lattice which eventually thermalize with a global increase in temperature of the germanium crystal. The original thermal energy E_{ph} is contained in the phonons created by the recoil and the recombination of the electron-hole pairs, such that $E_{ph} = E_R$. Additional phonons are produced by the drifting of the charge carriers across the crystal under the influence of the voltage bias V_{bias} imposed by the electrodes. This process is the Neganov-Trofimov-Luke effect which can be considered as the equivalent of the Joule effect in semiconductors [38, 44]. The boost to the thermal energy is defined as the Luke-Neganov energy expressed as:

$$E_{NL} = N_p q_e V_{bias} = E_{Ion.} \frac{V_{bias}}{\epsilon_{e^- - h^+}} \tag{2.9}$$

Hence, the total thermal energy E_{heat} induced by the recoil is expressed:

$$E_{heat} = E_{ph} + E_{NL} = E_R \left(1 + Q \frac{V_{bias}}{\epsilon_{e^- - h^+}} \right) \tag{2.10}$$

It is linked to the increase in crystal temperature ΔT in Kelvin with the thermal capacity of germanium crystal C_{Ge} in $\text{J} \cdot \text{K}^{-1}$ such that:

$$E_{heat} = C_{Ge} \Delta T \tag{2.11}$$

In time, the absorber cools down thanks to the thermal leakage, assured with gold wires between the detector and its copper chassis maintained at constant cryogenic temperature. This thermal signal can be measured with a very sensitive thermometer. In our case, the thermal sensor is a Neutron transmutation dopped germanium thermistor (GeNTD or NTD) glued on the surface of the crystal. The electric resistance R_{NTD} of this thermistance depends very strongly on its temperature T_{NTD} following the law from Efros and Shllovskii [42]:

$$R_{NTD}(T_{NTD}) = R_0 \exp\left(\sqrt{\frac{T_0}{T_{NTD}}}\right) \tag{2.12}$$

where R_0 and T_0 are a characteristic resistance $\mathcal{O}(1)\ \Omega$ and temperature $\mathcal{O}(1)$ K of the NTD used. They depend on the geometry of the NTD and its doping [42]. Although this thermistor is made of germanium, it is doped and its physical properties are changed: it is conductive and thus

has a free electron system in addition to a phonon system. The phonon system has a thermal capacity evolving like the cube of the temperature of the absorber (low thermal capacity), while the capacity of the electron system is linear with the temperature (high thermal capacity). We can therefore understand the usefulness of having an absorber-sensor couple: one serves as a target for the deposition of energy with low thermal capacity, while the other allows the measurement of the temperature rise through the epoxy glue assuring the thermal coupling such that $T_{NTD} \simeq T$. Therefore, the GeNTD allows the measurement of temperature variations of the germanium crystal with its decreases in resistivity following a particle interaction. This R_{NTD} resistivity is measured with the polarization of the NTD: a constant direct current I of a few nA is applied to the thermistance. The Ohm's law gives:

$$V_{NTD} = R_{NTD} I \tag{2.13}$$

so that the resistance is deduced from its measured voltage V_{NTD}.

Cryogenic temperatures are necessary to be in a temperature range where the NTD thermistor becomes sufficiently sensitive to temperature variations. The exponential relation 2.12 allows to obtain the largest variation of voltage ΔV_{NTD} for a small temperature variation ΔT at the lowest temperature of the detector T:

$$\Delta V_{NTD} = I \left. \frac{\mathrm{d}R_{NTD}}{\mathrm{d}T} \right|_T \Delta T \tag{2.14}$$

In the end, the heat energy E_{heat} is derived from the measured voltage signal ΔV_{NTD} as:

$$E_{heat} = C_{Ge} \frac{\Delta V_{NTD}}{I} \left(\left. \frac{\mathrm{d}R_{NTD}}{\mathrm{d}T} \right|_T \right)^{-1} \tag{2.15}$$

It is used to calculate the recoil energy E_R with the knowledge of the quenching Q in equation 2.5. This measure of the recoil energy through the heat energy is defined as the heat channel of the detector.

In the end, the cryogenic germanium detectors studied in this work have a double measurement of the recoil energy: the heat channel and the ionization channel. The double read-out is used to discriminate background-induced electron recoils from potential CENNS-induced nuclear recoils on an event-by-event basis.

An illustration of this discrimination is displayed in figure 2.8. The graphic consists in the ionization energy $E_{Ion.}$ versus the heat energy E_{heat} of simulated recoils of different types. Due to their difference in quenching factor $Q_{NR} < Q_{ER}$, the electronic recoils form the red band which is easily separated from the blue band of the nuclear recoils at sufficiently high energy (here for $E_{heat} \geq 0.1\,\mathrm{keV}$).

Hence, the combination of the heat and ionization energies allows a highly efficient rejection of the dominant gamma backgrounds as well as the majority of beta-backgrounds. It is worth highlighting that, in addition to the event-by-event discrimination, the simultaneous heat and ionization energy measurements also provides a direct measurement of the true nuclear recoil energy, hence avoiding any assumptions on the quenching factor Q to be made.

2.3.3 RED Prototype Detectors

This thesis is inscribed in the R&D program for the development of the detectors of the CryoCube array. In order to meet its specification presented in paragraph 1.2.3, the modelization of the detectors and the subsequent optimization of their design are tested and validated with experimental measurements in the IP2I R&D cryostat. These studies are carried out in collaboration with the EDELWEISS collaboration with the operation of the RED detector series. The RED

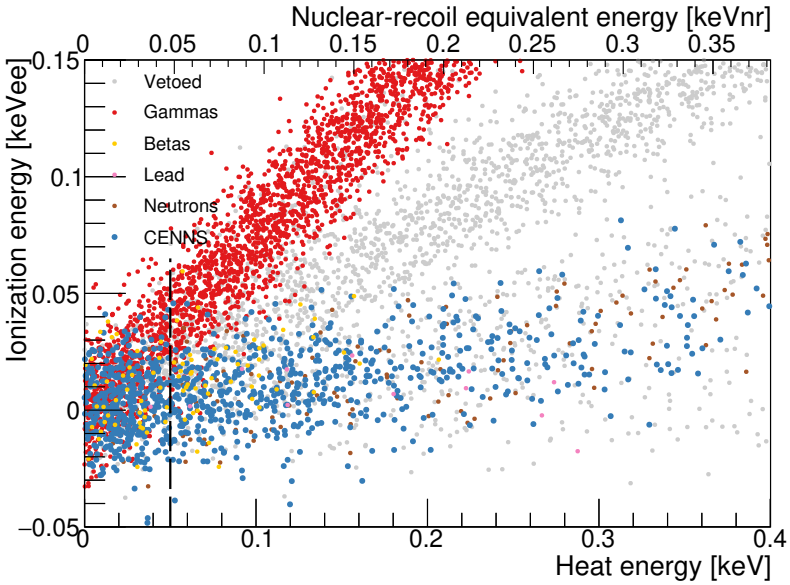

Figure 2.8: Illustration of the discrimination of simulated nuclear (blue) and electronic (red) recoils thanks to the simultaneous double-energy measurement with the ionization and heat channels of the CryoCube detectors. Other type of recoils with negligible event rate are also visible. (Courtesy of J. Billiard)

series are R&D-focused bolometers aiming at a full understanding and optimization of the heat and ionization channels. Eventually, the prototypes become very similar to the future element of the CryoCube detector. All of the bolometers discussed hereafter in this work were fabricated by our collaborators at IJCLab, CEA Saclay, and Institut Néel.

A RED prototype detector is based on cylindrical high-purity Ge crystal weighting between 32 g and 200 g. The crystal is maintained in a copper chassis with Teflon clamps whose heat conduction is negligible compared to the thermal leakage. Every RED detector has a heat channel consisting in one GeNTD thermal sensor glued on the surface of the crystal with gold wires assuring the electric cabling of the NTD and the thermal leakage of the whole detector.

In particular, early R&D detectors such as RED10 and RED20, studied in Chapter 3 were assembled with a very simple and clear design and do not possess an ionization channel. This permits to test thermal models and to better understand the physical processes involved in the thermal response of the detector.

Only the most recent RED prototypes, such as RED80 and REDN1 studied in Chapter 6 are equipped with an ionization channel. The electrodes of these RED detectors are made by evaporating aluminium on the surface of the target material with various shape. It is possible to shape the electric field in the crystal with more complex designs of electrodes. In particular, the detector design FID38, studied in Chapter 4 and inspired by the FID detectors of EDELWEISS-III, has two main collecting electrodes and two auxiliary veto electrodes allowing the tagging of surface events.

2.3.4 Calibration Sources

The detectors are calibrated with particles inducing recoils of known heat (E_{heat}) and the ionization ($E_{Ion.}$) energies. For the first RED detectors, cosmic muons of high energy were used as calibration source. This natural source, available due to the very low overburden of the cryogenic facility, would generate a large ionization peak at 18 MeV. This calibration source has

significant uncertainty on the position of the peak due to the wide cosmic muon energy distribution. Also, due to the non-linearity of the heat response, the measurements at low energies are severely underestimated with this calibration at high energy.

The muon calibration was quickly replaced with the use of radioactive iron sources. An ^{55}Fe calibration source was glued on the inner part of the detector's copper housing and facing the crystal surface opposite to the side on which is glued the GeNTD. It generates electronic recoils from a doublet peak of X-ray emission at 5.90 keV and 6.49 keV. This calibration method was mainly used for the operation of the RED detectors equipped solely with a heat channel (RED10 and RED20 in this work).

The newest and most advantageous calibration method used in the current runs at IP2I is based on the activation of the germanium atoms in the crystal of the detectors with thermal neutrons. The detectors are activated with an intense AmBe neutron source, inducing the neutron capture by the stable ^{70}Ge:

$$^{70}\mathrm{Ge} + \mathrm{n} \longrightarrow {}^{71}\mathrm{Ge} \tag{2.16}$$

The ^{70}Ge isotope decays [2] through electron capture with the half-life $t_{1/2} = 11.43$ d as:

$$^{71}\mathrm{Ge} + \mathrm{e}^{-} \longrightarrow {}^{71}\mathrm{Ga}^{*} + \nu_e \tag{2.17}$$

The daughter nucleus ^{71}Ga* is in an excited state due to the hole left in one of its electronic shell. When relaxing, a photon is emitted which produces an electronic recoil in the germanium crystal of the detector. The energy of this photon is equal to the binding energy of the electron associated with the K/L/M shells of the ^{71}Ga: 10.37 keV, 1.3 keV and 160 eV respectively [56]. All these calibration peaks are in the exact energy range for the CENNS signal search $\mathcal{O}(1)$keV while yielding a uniform distribution of the recoils in the whole detector volume. A direct application of this property is the experimental estimation of the fiducial volume and efficiency of the RED detectors as described in Chapter 6.

Chapter 3

Study of the Heat Channel

This chapter is dedicated to the study of the heat channel of the cryogenic germanium bolometers. For this purpose, several prototype RED detectors were operated for the collection of experimental data upon which is based this work.

The first section explains the development of an electro-thermal model to simulate a detector. This is followed by a description of the analysis used to characterize the electronics from experimental data obtained with the already characterized RED1 detector. Then is presented the characterization of a new RED10 detector based on the constructed model and new experimental measurements. Finally, the comparison between the resolutions of the experiment and the simulation allows to verify the validity of the model and to define the next research tracks.

RED1 and RED10 have the same clear design with only one heat channel. A picture of the RED10 detector is presented in figure 3.1. Each of these detector is based on a polished 200 g Ge crystal which is devoid of any electrode. The crystal is held fixed inside the copper chassis with six insulating Teflon clamps. A single NTD thermistance is glued near the center of the top planar surface. This thermal sensor is cabled to the polarization and readout electronics with 8 gold wires of width 25 µm which also act as the thermal leak of the detector.

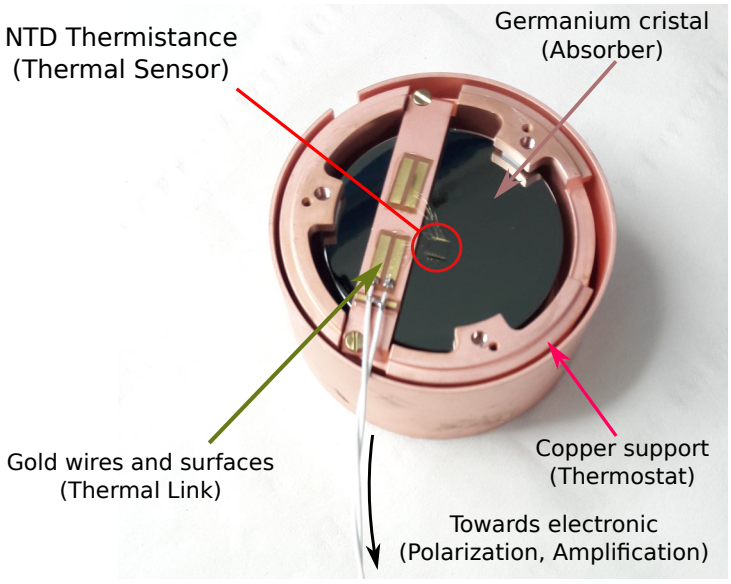

Figure 3.1: Annotated photo of the prototype detector RED10.

The major difference between these detectors lies in the thermal sensor. The NTD of RED1 has already been characterized with the parameters $R_0 = 1.04\,\Omega$ and $T_0 = 4.77\,\mathrm{K}$ from the expression 2.12 of its resistivity. The NTD of RED10 is characterized later in this work thanks to experimental data.

3.1 Electro-Thermal Modelization of the RED Dectectors

In this part, the theoretical calculations used to build the detector model are presented. The study focused on the first-order resolution of the system of coupled differential equations using a linear algebra method [27, 17]. It is then possible to simulate the behavior of a detector in the steady state, in the time domain and in the frequency domain, which gives access to the complete characterization of the detector.

3.1.1 Describing the Detector with a System of Equation

In this subsection, we define the system of equations ruling a RED10 like detector with a single NTD thermal sensor. The detector is considered as a thermal system composed of multiple thermal baths of homogeneous temperature T, each characterized by a thermal capacity C in $\mathrm{J \cdot K^{-1}}$. This approximation of thermal baths with homogeneous temperature is motivated by the cryogenic temperature of few tens of mK of the detector: in this situation, all the differences in temperature are located on the interfaces between each of the thermal components of the detector. The thermal scheme of the detector RED10 is presented in the figure 3.2 which features four thermal baths:

- in orange, the germanium crystal acting as an absorber (T_a, C_a),
- in yellow, the thermal bath of the phonons in the NTD resistor (T_p, C_p),
- in blue, the thermal bath of electrons in the NTD resistor (T_e, C_e).
- the cryostat thermostat of fixed temperature T_b (and infinite thermal capacity).

They are connected by thermal links characterized by thermal conductivity G in $\mathrm{W \cdot K^{-1}}$, which allows a power transfer P between the baths. At cryogenic temperatures, all heat powers are modeled using the non-linear conduction formula for non-diffusive processes [30]. The heat power from a thermal bath "1" to a thermal bath "2" is expressed as:

$$P_{12} = g_{12}\left(T_2^{n_{12}} - T_1^{n_{12}}\right) \tag{3.1}$$

with g_{12} the conductance in $\mathrm{W/K^{-n_{12}}}$ and n_{12} an exponent. Both parameters depend on the interface between the thermal baths and were mainly determined experimentally.

The NTD thermistance is modeled as two separate thermal baths: the phonon bath (index p) and the electron bath (index e). Indeed at ambient temperature, the phonons and conduction electrons are in constant thermal equilibrium with the same apparent temperature $T_p = T_e$. However, at cryogenic temperature, this thermal equilibrium is reached much later and has significant impact on the thermal response of the detector. The heat power transferred from the electron bath to the phonon bath depends on their temperatures as:

$$P_{ep} = \mathcal{V}_{NTD} g_{ep}(T_e^n - T_p^n) \tag{3.2}$$

where $\mathcal{V}_{NTD}$ is the volume of the NTD sensor in $\mathrm{mm^3}$, g_{ep} is the electron-phonon coupling constant per volume unit and n is a material dependent exponent that is typically equal to 6 for thermistors such as GeNTDs.

The thermal bath associated with the absorber (index a) represents the phonon system of the germanium crystal. Indeed, since this material is a semiconductor at these operating temperatures, there are no free electrons in the conduction band. The absorber only exchanges heat power with the phonon system of the NTD through the thin layer of epoxy glue (with negligible thermal capacity). The heat power transferred from the absorber bath to the phonon bath is

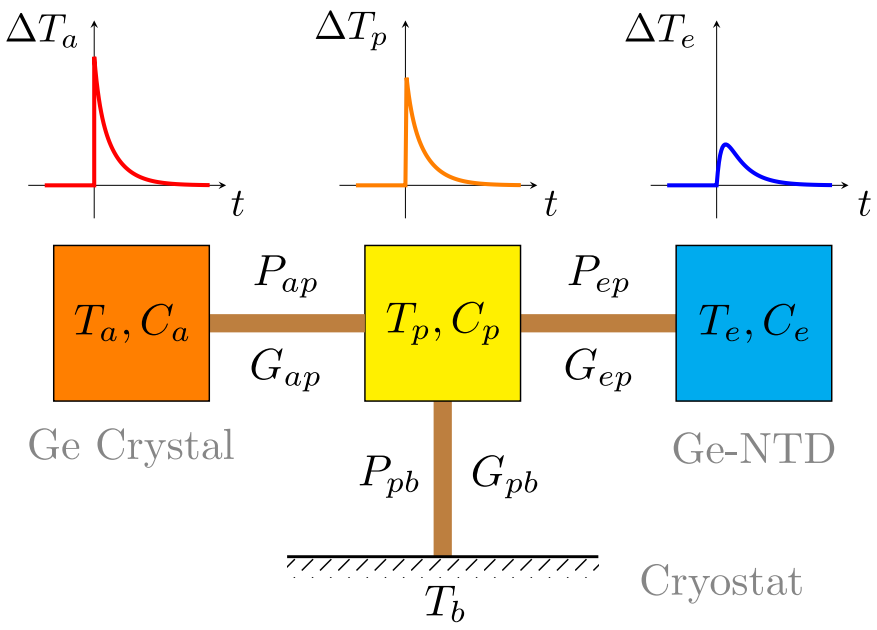

Figure 3.2: Thermal diagram of RED1 and RED10 with representation of the diffusion of a signal created by an event in the germanium crystal on top. Each thermal bath is characterized by a temperature T and a thermal capacity C. Each thermal link is associated with a thermal conductivity G and a thermal power transfer P. The NTD sensor is modeled as a system of thermally coupled phonons (index p) and elecrons (index e). The absorber bath (index a) and the cryostat (index b) are both connected to the NTD phonon bath.

expressed as:

$$P_{ap} = g_{glue} S_{NTD} \left(T_p^{n_g} - T_a^{n_g} \right) \tag{3.3}$$

with S_{NTD} the surface of the NTD facing the absorber in mm^2, g_{glue} the surface thermal conductivity constant of the glue and n_g an exponent.

The thermal leakage of the detector is assured by the cabling gold wires on the gold-plated electrodes of the NTD. The heat power transferred from the phonon bath to the cryostat thermostat is:

$$P_{pb} = S_{Au} g_k (T_p^{n_k} - T_b^{n_k}) \tag{3.4}$$

with g_k the Kapitza conductance per unit area and the exponent $n_k = 4$. The term S_{Au} corresponds to the effective gold surface connecting the NTD to the copper chassis.

The heat channel derives the heat energy E_{heat} created by a recoil in the absorber from a variation of the voltage ΔV of the NTD thermistance. In order to maintain the proportionality between the voltage V and the resistivity R of the NTD in the Ohm's law 2.13, it is polarized with a constant current I_P. This is realized by adding a very high load resistance R_L in series with a constant voltage source V_B. The electronics schematic that allows the polarization and the measurement of the voltage at the terminals of the NTD resistor is shown in figure 3.3.

On the left is the schematic of the polarization electronics with voltage and current noise sources represented in red. The capacity of the cabling $C_{cabling}$ of the electronics is taken into account. The right scheme corresponds to the simplification with multiple Thevenin-Norton transformation [41] in the context of the frequency study, which is addressed later. A constant

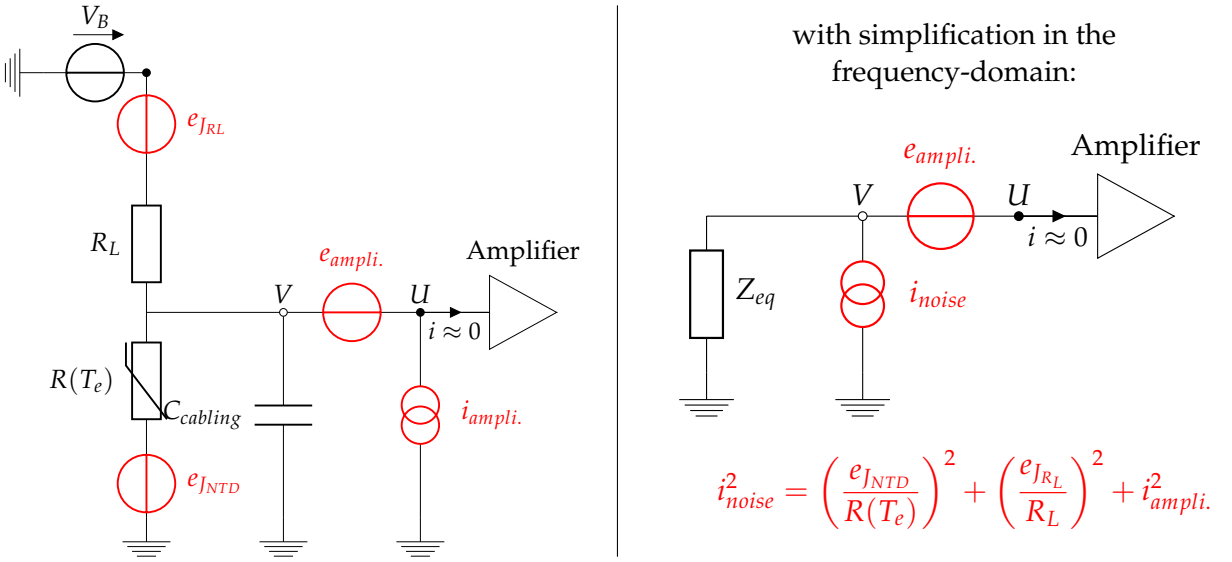

Figure 3.3: On the left, diagram of the polarization and readout electronics. On the right, simplified diagram in the frequency-space with the use of Thevenin-Norton transformation. The NTD resistor $R(T_e)$, the load resistor R_L and the cabling capacitance $C_{cabling}$ become the equivalent complex impedance Z_{eq}. Noise sources appear in red. Johnson noise, $e_{J_{RL}}$ and $e_{J_{NTD}}$, and amplifier current noise $i_{ampli.}$ are grouped into a current noise i_{noise} whose expression is specified.

bias voltage V_B is applied to the load resistance R_L, of a few GΩ, in series with the NTD resistance $R(T_e)$ depending on the temperature of the electron bath T_e according to the law:

$$R(T_e) = R_0 \exp\left(\sqrt{\frac{T_e}{T_0}}\right) \tag{3.5}$$

with R_0 and T_0 a characteristic resistivity and temperature of the NTD [42].

The electrical system takes into account the variation of the polarization current (second-order effect as $R_L \gg R_{NTD}$). The differential equation associated with the voltage of the NTD is:

$$C_{cabling}\frac{\mathrm{d}V}{\mathrm{d}t} = \frac{V_B - V}{R_L} - \frac{V}{R(T_e)} \tag{3.6}$$

Due to the polarization of the NTD, a Joule effect is present, coupling the electron thermal bath and the electronics:

$$P_J = I_P^2 \cdot R(T_e) = \frac{V^2}{R(T_e)} \tag{3.7}$$

The heat equations associated with each thermal bath is derived from all the previously defined heat powers. The thermal equation for the electron bath is obtained from the NTD Joule heating (eq. 3.7) and the thermal coupling to the phonon bath (eq. 3.2) such that:

$$C_e\frac{\mathrm{d}T_e}{\mathrm{d}t} = \frac{V^2}{R(T_e)} - \mathcal{V}_{NTD}g_{ep}\left(T_e^n - T_p^n\right) \tag{3.8}$$

For the NTD phonon system, we have the power from the phonon-electron coupling P_{ep}, the power transfer with the absorber (eq. 3.3), and the thermal leakage (eq. 3.4) to the cryostat. This phonon bath is described by the heat equation:

$$C_p\frac{\mathrm{d}T_p}{\mathrm{d}t} = -g_{glue}S_{NTD}\left(T_p^{n_g} - T_a^{n_g}\right) + V_{NTD}g_{ep}\left(T_e^n - T_p^n\right) - g_kS_{Au}\left(T_p^{n_k} - T_b^{n_k}\right) \tag{3.9}$$

The thermal equation for the absorber bath is simply derived from the heat conduction through the glue (eq. 3.3):

$$C_a \frac{\mathrm{d}T_a}{\mathrm{d}t} = g_{glue} S_{NTD} \left(T_p^{n_g} - T_a^{n_g} \right) \tag{3.10}$$

By bringing together the three heat equations 3.10, 3.8 and 3.9 as well as the differential equation 3.6 associated with the polarization electronics, we can compose a system of coupled differential equations that completely describes the electro-thermal model of the detector RED10 schematized in the figures 3.2 and 3.3:

$$\begin{cases} C_a \dfrac{\mathrm{d}T_a}{\mathrm{d}t} & = g_{glue} S_{NTD} \left(T_p^{n_g} - T_a^{n_g} \right) \\ C_p \dfrac{\mathrm{d}T_p}{\mathrm{d}t} & = -g_{glue} S_{NTD} \left(T_p^{n_g} - T_a^{n_g} \right) + \mathcal{V}_{NTD} g_{ep} \left(T_e^n - T_p^n \right) - g_k S_{Au} \left(T_p^{n_k} - T_b^{n_k} \right) \\ C_e \dfrac{\mathrm{d}T_e}{\mathrm{d}t} & = \frac{V^2}{R(T_e)} - \mathcal{V}_{NTD} g_{ep} \left(T_e^n - T_p^n \right) \\ C_{cabling} \dfrac{\mathrm{d}V}{\mathrm{d}t} & = \frac{V_B - V}{R_L} - \frac{V}{R(T_e)} \end{cases} \tag{3.11}$$

3.1.2 Steady State Solution

The study of the steady state allows to obtain the physical quantities around which the disturbances of the system will occur. It is essential to calculate it in order to obtain the values of the NTD resistance, thermal capacities and thermal conductivities. It is also necessary to perform a linearization step afterwards. The steady state is experimentally defined by the cryostat temperature T_b and the bias voltage V_B.

It is sufficient to cancel the time derivative terms in the system of equations 3.11 to obtain the system of equations in the stationary state with $(\bar{T}_a, \bar{T}_p, \bar{T}_e, \bar{V})$ being the solutions of the stationary state:

$$\begin{cases} 0 & = g_{glue} S_{NTD} \left(\bar{T}_p^{n_g} - \bar{T}_a^{n_g} \right) \\ 0 & = -g_{glue} S_{NTD} \left(\bar{T}_p^{n_g} - \bar{T}_a^{n_g} \right) + \mathcal{V}_{NTD} g_{ep} \left(\bar{T}_e^n - \bar{T}_p^n \right) - g_k S_{Au} \left(\bar{T}_p^{n_k} - \bar{T}_b^{n_k} \right) \\ 0 & = \frac{V^2}{R(\bar{T}_e)} - \mathcal{V}_{NTD} g_{ep} \left(\bar{T}_e^n - \bar{T}_p^n \right) \\ 0 & = \frac{V_B - V}{R_L} - \frac{V}{R(\bar{T}_e)} \end{cases} \tag{3.12}$$

These algebraic equations are non-linear due to the expressions of the heat power (eq. 3.1) and of the NTD resistance 2.12. It is therefore necessary to use a numerical resolution to solve this system.

3.1.3 Response in the Time Domain

Solving the system of equations 3.11 would give the exact expressions of the temporal evolution of the temperatures of the different baths $T_a(t), T_p(t), T_e(t)$ and of the voltage at the terminals of the NTD $V(t)$. However, the very strong non-linearity of the system does not allow an analytical resolution. Nevertheless, only the response of the system to an event is of interest. As reference, a particle depositing a heat energy of 1 keV in the absorber induces a temperature increase of the order of $\mathcal{O}(100)$ µK, which in turn, gives a voltage variation at the terminals of the NTD of the order of $\mathcal{O}(100)$ nV. It is thus a question of studying the response of the system to small signals.

We propose to apply a first-order perturbation theory [47] to the system of equations 3.11 with:

$$\begin{cases} T_a(t) & \simeq \bar{T}_a + \Delta T_a(t) \\ T_p(t) & \simeq \bar{T}_p + \Delta T_p(t) \\ T_e(t) & \simeq \bar{T}_e + \Delta T_e(t) \\ V(t) & \simeq \bar{V} + \Delta V(t) \end{cases} \tag{3.13}$$

With this linearization of the physical quantities, it is possible to define thermal conductivities G for the different thermal links :

- glue crystal-NTD:

$$G^a_{ap} = n_g g_{glue} S_{NTD} \bar{T}_a^{n_g - 1} \qquad \text{and} \qquad G^p_{ap} = n_g g_{glue} S_{NTD} \bar{T}_p^{n_g - 1} \tag{3.14}$$

- electrons-phonon coupling:

$$G^e_{ep} = n g_{ep} \mathcal{V}_{NTD} \bar{T}_e^{n-1} \qquad \text{and} \qquad G^p_{ep} = n g_{ep} \mathcal{V}_{NTD} \bar{T}_p^{n-1} \tag{3.15}$$

- thermal leakage through gold wires:

$$G_{pb} = n_k g_k S_{Au} \bar{T}_p^{n_k - 1} \tag{3.16}$$

By subtracting the steady state equation 3.12 from the original system 3.11, we then obtain a system of coupled linear equations:

$$\begin{cases} C_a \dfrac{d\Delta T_a}{dt} & = -G^a_{ap}\Delta T_a + G^p_{ap}\Delta T_p \\ C_p \dfrac{d\Delta T_p}{dt} & = G^a_{ap}\Delta T_a - G^p_{ap}\Delta T_p + G^e_{ep}\Delta T_e - G^p_{ep}\Delta T_p - G^p_{pb}\Delta T_p \\ C_e \dfrac{d\Delta T_e}{dt} & = -G^e_{ep}\Delta T_e + G^p_{ep}\Delta T_p + 2\frac{\bar{V}}{R(\bar{T}_e)}\Delta V - \frac{\bar{V}^2}{R(\bar{T}_e)^2}\left.\frac{dR}{dT}\right|_{T_e}\Delta T_e \\ C_{cabling} \dfrac{d\Delta V}{dt} & = -\left(\frac{1}{R_L} + \frac{1}{R(\bar{T}_e)}\right)\Delta V + \frac{\bar{V}}{R(\bar{T}_e)^2}\left.\frac{dR}{dT}\right|_{\bar{T}_e}\Delta T_e \end{cases} \tag{3.17}$$

This can be simplified to:

$$\begin{cases} \dfrac{d\Delta T_a}{dt} & = -\frac{G^a_{ap}}{C_a}\Delta T_a + \frac{G^p_{ap}}{C_a}\Delta T_p \\ \dfrac{d\Delta T_p}{dt} & = \frac{G^a_{ap}}{C_p}\Delta T_a - \frac{G^p_{ap}+G^p_{ep}+G^p_{pb}}{C_p}\Delta T_p + \frac{G^e_{ep}}{C_p}\Delta T_e \\ \dfrac{d\Delta T_e}{dt} & = \frac{G^p_{ep}}{C_e}\Delta T_p - \frac{1}{C_e}\left(G^e_{ep} + \frac{\bar{V}^2}{R(\bar{T}_e)^2}\left.\frac{dR}{dT}\right|_{\bar{T}_e}\right)\Delta T_e + 2\frac{1}{C_e}\frac{\bar{V}}{R(\bar{T}_e)}\Delta V \\ \dfrac{d\Delta V}{dt} & = \frac{1}{C_{cabling}}\frac{\bar{V}}{R(\bar{T}_e)^2}\left.\frac{dR}{dT}\right|_{\bar{T}_e}\Delta T_e - \frac{1}{C_{cabling}}\left(\frac{1}{R_L} + \frac{1}{R(\bar{T}_e)}\right)\Delta V \end{cases} \tag{3.18}$$

A system of linear equations is now being studied. It is thus possible to solve them analytically. For this purpose, this system of equations can be rewritten in matrix form to facilitate the

calculations. The vector $\boldsymbol{\phi}$ containing the temperature and voltage perturbations is introduced:

$$\boldsymbol{\phi} = \begin{pmatrix} \Delta T_a \\ \Delta T_p \\ \Delta T_e \\ \Delta V \end{pmatrix} \tag{3.19}$$

The simplified system of equations 3.18 is now simply expressed as the matrix equation:

$$\frac{d\boldsymbol{\phi}}{dt} = -\boldsymbol{M}\boldsymbol{\phi} + \boldsymbol{F}(t - t_0) \tag{3.20}$$

where $\boldsymbol{M}$ is the matrix regrouping the electro-thermal coupling terms. It is directly derived from the previous equations 3.18, and is expressed as:

$$\boldsymbol{M} = \begin{pmatrix} \frac{G^a_{ap}}{C_a} & -\frac{G^p_{ap}}{C_a} & 0 & 0 \\ -\frac{G^a_{ap}}{C_p} & \frac{G^p_{ap}+G^p_{ep}+G^p_{pb}}{C_p} & -\frac{G^e_{ep}}{C_p} & 0 \\ 0 & -\frac{G^p_{ep}}{C_e} & \frac{1}{C_e}\left(G^e_{ep} + \frac{\bar{V}^2}{R(T_e)^2}\left.\frac{dR}{dT}\right|_{\bar{T}_e}\right) & -\frac{2}{C_e}\frac{\bar{V}}{R(T_e)} \\ 0 & 0 & -\frac{1}{C_{cabling}}\frac{\bar{V}}{R(T_e)^2}\left.\frac{dR}{dT}\right|_{\bar{T}_e} & \frac{1}{C_{cabling}}\left(\frac{1}{R_L} + \frac{1}{R(T_e)}\right) \end{pmatrix} \tag{3.21}$$

A source term $\boldsymbol{F}$ has also been added to contain the energy perturbation in the detector and the various sources of interference noise. In the case of a particle depositing a heat energy E in the absorber, this term is expressed as,

$$\boldsymbol{F}(t - t_0) = \begin{pmatrix} E/C_a \\ 0 \\ 0 \\ 0 \end{pmatrix} \delta(t - t_0) \tag{3.22}$$

The deposition of the recoil energy, the relaxation of the phonons created in the absorber, and the temperature rise of the absorber are considered instantaneous processes, hence the use of the Dirac function $\delta(t - t_0)$. A variant of this model consists in assigning a relaxation time to the phonons and taking into account the temperature rise of the thermal baths during phonon relaxation.

The general solution of the equation 3.21 is a linear combination of N exponentials, with $N = 4$ corresponding to the dimensions of the system, each characterized by a characteristic time constant. Their expressions are obtained by diagonalizing the coupling matrix $\boldsymbol{M}$, which shifts the framework to the basis formed by the eigenvectors of the system solutions. We consider, for $i \in \{1, 2, 3, 4\}$, the eigenvectors $\boldsymbol{v}_i$ and the associated eigenvalues λ_i to write these solutions:

$$\boldsymbol{f}_i(t) = f_i(t)\boldsymbol{v}_i \tag{3.23}$$

Without considering the source term, we introduce these expressions into the matrix equation 3.20 to give

$$\frac{d\boldsymbol{f}_i(t)}{dt} = -f_i(t)\boldsymbol{M}\boldsymbol{v}_i = -\lambda_i f_i(t)\boldsymbol{v}_i \tag{3.24}$$

Solving this equation leads to the expression of the solutions in the basis of the eigenvectors:

$$\boldsymbol{f}_i(t) = A_i e^{-t/\tau_i}\boldsymbol{v}_i \tag{3.25}$$

with A_i the normalization constant and $\tau_i = 1/\lambda_i$ the characteristic time constant of the solution. The general solution of 3.21 is then expressed in the new basis as

$$\boldsymbol{f}(t) = \sum_i A_i e^{-t/\tau_i} \boldsymbol{v}_i \tag{3.26}$$

To make the link between the basis of the eigenvectors and the temperature and voltage fluctuations, the $\boldsymbol{f}$ solution must be projected onto the 4 orthogonal vectors forming the vector $\boldsymbol{\phi}$ such that :

$$\phi_j = \boldsymbol{f} \cdot \boldsymbol{\phi}_j = \sum_i^4 f_i(t) \boldsymbol{v}_i \cdot \boldsymbol{\phi}_j = \sum_i P_{ij} f_i(t) = \sum_i P_{ij} A_i e^{-t/\tau_i} \tag{3.27}$$

where P_{ij} designates the vectors composing the transfer matrix satisfying $\boldsymbol{M} = \boldsymbol{PDP}^{-1}$.

To set the normalization constants A_i, the initial conditions of the system are considered:

$$\boldsymbol{\phi}(0) = \boldsymbol{F}(0) = \begin{pmatrix} \sum_i P_{ai} A_i \\ \sum_i P_{pi} A_i \\ \sum_i P_{ei} A_i \\ \sum_i P_{vi} A_i \end{pmatrix} = \boldsymbol{PA} \qquad \longrightarrow \qquad \boldsymbol{A} = \boldsymbol{P}^{-1} \boldsymbol{\phi}(0) \tag{3.28}$$

with $\boldsymbol{A}$ the vector containing the constants A_i.

The study of a detector in time is equivalent to solving the matrix equation 3.21 and thus to find the eigenvalues and eigenvectors of the coupling matrix $\boldsymbol{M}$. The electro-thermal model is now completely described in the time domain.

3.1.4 Response in Frequency Domain

The study of noise leading to the calculation of the resolution of the detector requires to describe now the behavior in frequency domain. Indeed, the noises of a system are characterized from their power spectral densities (PSD). We consider the Fourier transform of the matrix equation 3.20:

$$\boldsymbol{C}(i\omega + \boldsymbol{M}) \tilde{\boldsymbol{\phi}}(\omega) = \boldsymbol{Z}(\omega) \tilde{\boldsymbol{\phi}}(\omega) = \boldsymbol{C} \tilde{\boldsymbol{F}}(\omega) \qquad \text{with} \qquad \boldsymbol{C} = \begin{pmatrix} C_a & 0 & 0 & 0 \\ 0 & C_p & 0 & 0 \\ 0 & 0 & C_e & 0 \\ 0 & 0 & 0 & C_{cabling} \end{pmatrix} \tag{3.29}$$

where we introduce the matrix $\boldsymbol{Z}$ containing the electro-thermal coupling terms expressed in the Fourier space. The equation is rewritten by explaining the terms of the matrices and vectors:

$$\boldsymbol{Z}(\omega) \tilde{\boldsymbol{\phi}}(\omega) = \begin{pmatrix} \frac{1}{a} & -g & 0 & 0 \\ -b & \frac{1}{c} & -h & 0 \\ 0 & -d & \frac{1}{e} - k & -l \\ 0 & 0 & -f & Z_{eq}^{-1} \end{pmatrix} \begin{pmatrix} \Delta T_a \\ \Delta T_p \\ \Delta T_e \\ \Delta V \end{pmatrix} = \begin{pmatrix} W - P_{ap} \\ P_{ap} + P_{ep} + P_{bp} \\ -P_{ep} \\ i_{noise} \end{pmatrix} = \boldsymbol{C} \tilde{\boldsymbol{F}}(\omega) \tag{3.30}$$

The terms of the vector $\boldsymbol{C}\tilde{\boldsymbol{F}}(\omega)$ corresponds to the perturbation sources in the form of heat power or current source. The heat power W comes from the recoil induced by an interacting particle. All the red terms corresponds to the various noise sources affecting the detector performance. The heat powers P_{xy} with $x, y \in \{a, p, e, b\}$ are generated by the thermodynamic fluctuation noise (TFN) at the interface between two thermal baths. The current source i_{noise} corresponds to the propagation of all the electronics noise sources propagated to the terminals of the NTD.

The coefficients of the matrix $\boldsymbol{Z}$ are derived from the system of linearized equations 3.18 such as :

$$\begin{aligned} a &= (iC_a\omega + G^a_{ap})^{-1} & g &= G^p_{ap} \\ b &= G^a_{ap} & h &= G^e_{ep} \\ c &= (iC_p\omega + G^p_{ap} + G^p_{ep} + G_{pb})^{-1} & k &= -\frac{(dR/dT)V^2}{R^2} \\ d &= G^p_{ep} & \ell &= \frac{2V}{R} \\ e &= (iC_e\omega + G^e_{ep})^{-1} & & \\ f &= \frac{(dR/dT)V}{R^2} & & \end{aligned} \tag{3.31}$$

and with the complex impedance Z_{eq}, containing the electrical components of the bias circuit according to the figure 3.3, expressed as:

$$Z_{eq} = \left(\frac{1}{R_L} + \frac{1}{R(T_e)} + i\omega C_{cabling}\right)^{-1} \tag{3.32}$$

The expression of the vector of fluctuations $\tilde{\boldsymbol{\phi}}$ is obtained by inverting the coupling matrix $\boldsymbol{Z}$ as:

$$\tilde{\boldsymbol{\phi}}(\omega) = \begin{pmatrix} \Delta\tilde{T}_a \\ \Delta\tilde{T}_p \\ \Delta\tilde{T}_e \\ \Delta\tilde{V} \end{pmatrix} = \begin{pmatrix} Z^{-1}_{aa} & Z^{-1}_{ap} & Z^{-1}_{ae} & Z^{-1}_{av} \\ Z^{-1}_{pa} & Z^{-1}_{pp} & Z^{-1}_{pe} & Z^{-1}_{pv} \\ Z^{-1}_{ea} & Z^{-1}_{ep} & Z^{-1}_{ee} & Z^{-1}_{ev} \\ Z^{-1}_{va} & Z^{-1}_{vp} & Z^{-1}_{ve} & Z^{-1}_{vv} \end{pmatrix} \begin{pmatrix} \Delta\tilde{P}_a \\ \Delta\tilde{P}_p \\ \Delta\tilde{P}_e \\ \Delta\tilde{I} \end{pmatrix} = \boldsymbol{Z}^{-1}(\omega)\tilde{\boldsymbol{F}}(\omega) \tag{3.33}$$

We note here that the matrix formalism coupled with a numerical calculation tool allows an easy access to the temperature and voltage perturbations from the coupling matrix $\boldsymbol{M}$ and external power sources contained in the $\tilde{\boldsymbol{F}}(w)$ vector.

In spite of this simplification of the calculations, the understanding of the couplings between the different physical quantities is not so easy. A better understanding is possible by converting the system of equations 3.21 into a block diagram formalism. An illustration of the matrix equation is displayed in figure 3.4 as a block diagram. This representation is useful to understand the localization of the different signal-induced or noise-induced perturbations in the electro-thermal system. We find there the coupling coefficients used in the coupling matrix $\boldsymbol{Z}$ as well as the external power sources. It is easier to visualize the coupling between the different baths as well as the diffusion of the power deposited by a particle in the absorber W.

By reading the block diagram from left to right, we can follow the propagation of the signal in the detector and the different feedback mechanisms between each node. The power W is injected in the absorber bath from the heat energy E_{heat} released by a recoil. This bath is also affected with the TFN heat power $-P_{ap}$, associated with its thermal link with the NTD phonon bath, and the heat transfer $g\Delta T_p$ coming from the NTD phonon bath. The term a converts all the heat powers incoming in the absorber bath (first node on the block diagram) into the temperature fluctuation ΔT_a. The latter is in turn converted back with the term b into a heat power incoming on the NTD phonon bath (second node of the block diagram). The subsequent propagation of the signal and noises in the system eventually reaches the end node on the right of the block diagram corresponding to the measured voltage signal ΔU amplified by the electronics (see the circuit scheme 3.3 for reference).

The response of the system to an event is characterized by the sensitivity s_V. In the case of a particle interaction depositing all the recoil energy in the absorber, the sensitivity is expressed as $s_V(\omega) = Z^{-1}_{va}\hat{p}(\omega)$ with $\hat{p}(\omega)$ the Fourier transform of the signal into power W. The approximation of an instantaneous recoil energy deposit gives $\hat{p}(\omega) = \hat{\delta} = 1$, which tremendously simplifies the calculations. The variant where we consider the phonon relaxation time requires

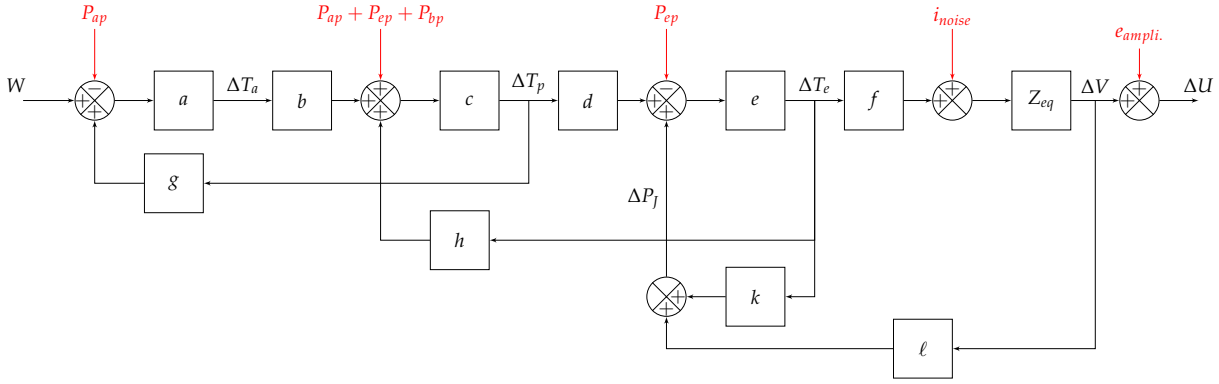

Figure 3.4: Block diagram of the electro-thermal model with the power injection of an event W, power noise P_{ap}, P_{ep}, P_{pb}, current noise i_{noise} and voltage noise $e_{ampli.}$. The block coefficients are specified in (3.31). Block diagram formalism and matrix formalism are equivalent and result in identical expressions for sensitivity and noise calculations.

to multiply by the low-pass function $\hat{p}(\omega) = 1/(1 + i\omega\tau_P)$ with τ_P the time constant corresponding to the phonon relaxation time within the detector. Other direct detection experiments, such as CDMS [19], work by detecting athermal phonons that can transfer between the different components of the detector before relaxing. Thus, it is possible to have a fraction ϵ of the phonons, produced during an event, leaving the absorber to the NTD and relax there. We would then observe a temperature rise directly in the NTD sensor, in addition to the temperature rise in the absorber. Taking this possibility into account, the sensitivity of the system is rewritten:

$$\hat{s}_V(\omega) = \left[(1-\epsilon)Z_{va}^{-1} + \epsilon Z_{ve}^{-1}\right]\hat{p}(\omega) \qquad [V/W] \tag{3.34}$$

The ϵ fraction of so-called "athermal" phonons depends very strongly on the geometry of the germanium crystal, its polishing, the glue used between the absorber and the NTD, and surely other parameters of the experiment that are not yet identified. The presence of athermal phonons is detected thanks to the signal shape: the temperature rise of the NTD is faster and an exponential contribution appears characterized by the time constant τ_P. We will see later in this chapter that the RED10 detector has a relatively large fraction of athermal phonons which is estimated by the signal shape.

The resolution of the block-diagram 3.4 ensures that the feedback loop associated with the Joule power ΔP_J is negative, allowing the stability of the NTD resistor polarization. Indeed, the temperature rise ΔT_e created by the bias current in the NTD decreases its resistance R due to its resistivity characteristic (eq. 2.12) being monotically decreasing. This, in turn, reduces the Joule effect $P_J \propto R$ assuming the bias current I_P being almost constant. This negative feedback is characteristic from the thermal sensor technology used: the resistance of the NTDs decreases with temperature. The other main thermal sensor technology used in cryogenic bolometers, the Transition Edge Sensors (TES) based on the superconductive transition of a material have an increasing resistance with the temperature [19] [27]. In this situation, this would result in a positive feedback which would eventually lead to the thermal sensor heating itself out of its sensitivity range. To obtain negative feedback and polarization stability, these experiments use voltage polarization and not current polarization. Indeed, we are in the case $P_J = V^2/R$ with V kept constant.

Another advantage of this negative feedback is the attenuation of some disturbances: we can then reduce the impact of noise in general and in particular thermal noises [41]. The thermal noises are the intrinsic limiting phenomenon interfering with the measurement. Generally

speaking, the only way to reduce them is to lower the temperature of the cryostat further, which is difficult because we then come up against the limit of cryogenic technology.

It is now possible to access the noise spectral density referred to the voltage at the terminals of the NTD by quadratically summing the different noise sources, considering that they are not correlated with each other. The total noise power spectral density is expressed in V^2/Hz as,

$$S_{V,total} = \sum_{i}^{sources} \left| \sum_{j}^{a,p,e,v} Z_{v,j}^{-1}(\omega)\tilde{F}_j(\omega) \right|^2 \tag{3.35}$$

where the quadratic summation is performed on all noise sources, and the v index refers to the coefficients of the inverted coupling matrix relative to the voltage across the NTD.

The different noise sources and the level at which they occur are shown in red on the figure 3.4. First of all we have the presence of TFN heat power presents for each thermal link in the system: P_{ap}, P_{pb}, P_{ep}. The PSD of these power fluctuations in the link connecting a bath at T_i and a bath at T_j is expressed in W^2/Hz as [36] [57] :

$$S_{P,ij} = 2k_B(T_i^2 + T_j^2)G_{ij} \tag{3.36}$$

with the thermal conductivity of the link G_{ij}. Thanks to the perturbation theory, we have obtained expressions of the conductivities (eq. 3.14,3.15 and 3.16) depending on the direction of heat transfer considered. Since the behavior of TFN noise with such conductivities is not properly defined, an effective thermal conductivity for TFN noise is approximated as the average of these two conductivities relative to the thermal link. Since TFN noise is associated with a thermal bond, it affects two thermal baths. In order to respect the principle of energy conservation, the anti-correlation of the contributions of a TFN noise in the two baths must be taken into account. By adapting the equation 3.35, one can obtain an intermediate PSD in V^2/Hz that includes all the TFN noise terms:

$$\begin{aligned} S_{V,TFN} = 2k_B \times \Big[& (T_a^2 + T_p^2)G_{ap} \left| Z_{vp}^{-1} - Z_{va}^{-1} \right|^2 \\ & + (T_e^2 + T_p^2)G_{ep} \left| Z_{vp}^{-1} - Z_{ve}^{-1} \right|^2 + (T_p^2 + T_b^2)G_{pb} \left| Z_{vp}^{-1} \right|^2 \Big] \end{aligned} \tag{3.37}$$

Following the noises indicated on the block diagram 3.4, we now have the intervention of a current noise i_{noise} which comes from the Thevenin-Norton transformation of the electric circuit presented on the figure 3.3. It corresponds to the quadratic sum of the Johnson noises $e_{J_{R_L}}, e_{J_{NTD}}$ related to the load and NTD resistors and the current noise introduced by the amplification electronics $i_{ampli.}$ which is expressed in A^2/Hz as:

$$i_{noise}^2 = i_{ampli}^2 + \left(\frac{e_{J_{R_L}}}{R_L} \right)^2 + \left(\frac{e_{J_{NTD}}}{R(T_e)} \right)^2 \tag{3.38}$$

An electrical resistance of value R at temperature T has its terminal voltage fluctuating randomly due to the Johnson noise whose PSD is expressed in V^2/Hz:

$$e_{J_R}^2 = 4k_B TR \tag{3.39}$$

This gives the contribution of the Johnson noises to the total noise PSD:

$$S_{V,R(T_e)} = \frac{4k_B T_e R(T_e)}{R(T_e)^2} \left| Z_{vv}^{-1} \right|^2 \tag{3.40}$$

$$S_{V,R_L} = \frac{4k_B T_{R_L} R_L}{R_L^2} \left| Z_{vv}^{-1} \right|^2 \tag{3.41}$$

The contribution of the Johnson noise is weighted by the corresponding resistance, which is ultimately a voltage divider. Thus, the voltage fluctuations at the terminals of the load resistor R_L are 2 to 3 orders higher than the voltage fluctuations at the terminals of the NTD sensor $R(T_e)$ but the division by R_L allows the Johnson noise of the NTD to dominate in the calculation.

The last two current noise terms i_{ampli} and e_{ampli} come from the amplification electronics simply represented by an amplifier follower on the figure 3.3. They are dependent on the type of electronics used and must be determined experimentally. Their contribution to the total PSD is expressed in V^2/Hz as :

$$S_{V,i_{ampli.}} = i_{ampli.}^2 \left| Z_{vv}^{-1} \right|^2 \tag{3.42}$$

$$S_{V,e_{ampli.}} = e_{ampli.}^2 \tag{3.43}$$

Indeed, there is no current leakage to the amplifier electronics, so the amplifier voltage noise term $e_{ampli.}$ affects the measurement independently of the upstream circuit.

Now that we have expressed the spectral noise density on the measured voltage and the sensitivity of the system to the signal, it is possible to perform the calculation of the detector resolution. To do this, we introduce the Noise-Equivalent Power (NEP). This value corresponds to the PSD of the noise produced in the absorber (and the electron system, if athermal phonons are considered) which would induce a voltage noise PSD identical to the total noise PSD already calculated by the formula 3.35. In a simpler way, it is a "tool" to compare the sensitivity of the system and the spectral density of noise affecting the measurement, independently of the signal and noise sources. In this system with the signal being a power, the NEP is expressed in $W \cdot \sqrt{Hz}^{-1}$. Its expression is given by the formula:

$$NEP^2(\omega) = \frac{S_{V,total}}{|\hat{s}_V|^2} \tag{3.44}$$

The NEP can be interpreted as the inverse of the signal-to-noise ratio, taking into account the system bandwidth. It can therefore be expected that the energy resolution σ_E of the detector will be related to this value. Calculations described in [26] gives the expression of the energy resolution in Joules as a function of the NEP:

$$\sigma_E^2 = \left(\int_0^\infty \frac{d\omega}{2\pi} \frac{4}{|NEP(\omega)|^2} \right)^{-1} \qquad [J^2] \tag{3.45}$$

The integration on the pulsation ω from 0 to infinity is only theoretical. Experimentally, these integration bounds are limited by the duration of the measurement, which sets the lower bound, and the Nyquist frequency, which sets the upper bound. Considering the recoil energy range associated with the recoils in a cryogenic detectors, it is customary to reason in eV and therefore to multiply the resolution by the conversion factor $u = (1.602 \times 10^{-19})^{-1} = 6.241 \times 10^{18}\,eV \cdot J^{-1}$.

3.2 Application of the Model to Experimental Data

In the previous section, we have set up the electro-thermal model of a RED detector with a single thermal sensor, like RED1 and RED10. Thus this model can now be applied to characterize the noise affecting the measurement of the heat channel as well as to the characterization of the RED10 detector. It will thus be possible to compare the constructed model with the experimental data from the RED1 and RED10 detector acquisitions.

3.2.1 Presentation of the two Electronics

The electro-thermal model gives access to the calculation of the resolution from the sensitivity to the signal and the power spectral densities of the various noise sources. Among the sources of noise in the system are the current and voltage noises coming from the amplification electronics (eq. 3.42). Indeed, this is the noise resulting from all the components contained in the amplification assembly, and there are no associated theoretical expressions. This part focuses on the characterization of two amplification electronics available to the laboratory. It will thus be possible to evaluate the total noise PSD and to obtain numerical values for the resolution.

The two available electronics are:

- a warm "JFET-based" polarization and readout electronics,
- an "EDELWEISS" polarization and readout electronics, also using J-FET but at 100 K.

These two electronics are based on the action of a field effect transistor called FET (Field Effect Transistor). The major difference between JFET-based and EDELWEISS comes from the difference in the FET used. In the case of JFET-based, the operating temperature of the FET corresponds to the ambient temperature. For EDELWEISS, the FET needs to be placed in the cryostat to reach its optimum operating temperature of 100 K. In addition, a capacity of 10 pF replaces the load resistor in the polarization circuit of the EDELWEISS electronics. This component was already present from the previous use of EDELWEISS electronics and does not add any additional noise. It only slightly increases the capacity of the cabling $C_{cabling}$ which does not hinder the characterization and comparison of the two electronics.

3.2.2 Noise Characterization

Although there are no precise expressions for the PSDs of current and voltage noise, several models have already been proposed to describe different transistor technologies [43] [36]. Based on PSD measurements and the literature, the following noise model is proposed for the current and voltage sources associated with the amplification electronics:

$$i^2_{ampli.} = i^2_A + (i_B\sqrt{f})^2 + (i_C f)^2 \qquad \text{in A}^2/\text{Hz} \tag{3.46}$$

$$e^2_{ampli.} = e^2_A + e^2_{BF} = e^2_A + \left(\frac{e_B}{\sqrt{f}}\right)^2 + \left(\frac{e_C}{f}\right)^2 \qquad \text{in V}^2/\text{Hz} \tag{3.47}$$

with $i_{A,B,C}$ and $e_{A,B,C}$ coefficients whose unit allows the homogeneity of the formulas. The term e_{BF} is relative to the predominant noise at low frequency.

The objective is to fit the proposed model to experimental PSD measurements in order to obtain constraints on the coefficients of the formulas 3.46 and 3.47. In addition to these coefficients, we will also want to constrain the capacity of the cabling $C_{cabling}$. We thus have a set of free parameters noted,

$$\Theta = (C_{fil}, i_A, i_B, i_C, e_A, e_B, e_C) \tag{3.48}$$

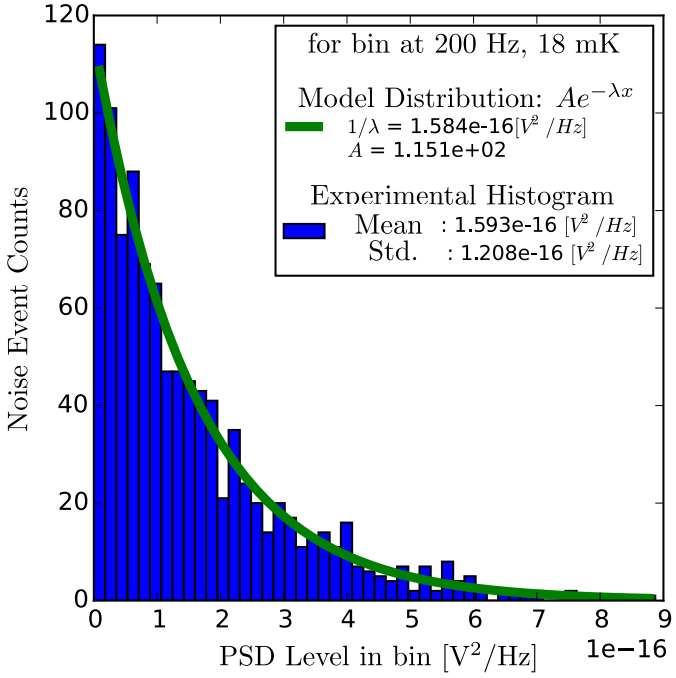

Figure 3.5: Histogram of the noise PSD level in the frequency bin at 200 Hz adjusted by an exponential model.

We want to implement a likelihood function analysis to fit the model to the experimental data. This requires knowledge of the noise distribution. It is necessary to make a measurement of the noise of the system. To do this, we do not polarize the NTD resistor ($I_P = 0$ A), and we remove the load resistor R_L from the circuit shown in figure 3.3 so as not to be dominated by its Johnson noise. We choose to work with a 1 s time windows with a sampling frequency $f_s = 10$ kHz. A Welch algorithm is applied to these windows to estimate the PSD of the noise affecting the measure. Acquisitions of 120 s allow us to perform an average of the measured noise PSD.

In a first step, the histogram of the measured PSD value for different frequencies is plotted. Such a histogram is presented as an illustration for a bin in frequency at 200 Hz on the figure 3.5. Regardless of the frequency probed, the temperature of the cryostat, or the electronics used, a similar distribution pattern is observed. An exponential distribution is successfully fitted to these histograms. A property of the exponential distribution can be applied to the noise: the mean PSD level $\mathcal{D}_i$ in the i-th frequency bin is equal to its standard deviation $\sigma_{\mathcal{D}_i}$. Indeed, the experimental values of the mean and the standard deviation are close to the term $1/\lambda$. Thus, on a measure averaged over $N = 120$ windows of 1 second, the Central Limit Theorem expresses the standard deviation on the averaged measure $\sigma_{\bar{\mathcal{D}}_i}$ such that:

$$\sigma_{\bar{\mathcal{D}}_i} = \frac{\sigma_{\mathcal{D}_i}}{\sqrt{N}} = \frac{\bar{\mathcal{D}}_i}{\sqrt{120}} \tag{3.49}$$

This information on the noise PSD allows to rigorously construct a likelihood function based on the χ^2 function related to the noise model with the set of parameters Θ and the experimental

data $\mathcal{D}$.The expression of the χ^2 function is:

$$\chi^2(\Theta|\mathcal{D}) = \sum_{j}^{N_{Temp}} \sum_{i}^{N_{bin}} \left[\frac{\bar{\mathcal{D}}_{ij} - \mathcal{M}(f_{ij};\Theta)}{\sigma_{\bar{\mathcal{D}}_{ij}}} \right]^2 \tag{3.50}$$

where we sum over all the frequency bins N_{bin} and over the set of measurement temperatures N_{Temp}. Indeed, the model is simultaneously adjusted on several PSD measurements carried out for temperatures ranging from 18 mK to 40 mK. We thus hope to obtain better constraints on the parameters, firstly because more points are analyzed, but above all because the change in temperature modifies the system parameters (in particular the resistance of the NTD $R(T_e)$) and removes the problems of degeneration between the different free parameters.

Motivated by a Bayesian approach [19], the likelihood function to be maximized with the model adjustment to the experimental data is expressed as,

$$\mathcal{L}(\Theta|\mathcal{D}) = \exp\left(\frac{-\chi^2(\Theta|\mathcal{D})}{2}\right) \tag{3.51}$$

3.2.3 Monte Carlo Markov Chain Analysis

We look for the set of parameters Θ that maximizes the likelihood function $\mathcal{L}(\Theta|\mathcal{D})$. To do this, we apply a Markov Chain Monte Carlo (MCMC) analysis with the use of the Python module "emcee" [28]. It is a method based on a random walk of one (or more) Markov chain, a set containing the free parameters, in the dimensional space $N = 7$ corresponding to the number of free parameters. It has been shown that with a correct likelihood function, the Markov chain allows to sample this function in a neighborhood of the optimal solution. The advantages of the MCMC method are that it can probe a large part of the free parameter space and converges quickly to the neighborhood of the optimal solution which can then be explored and analyzed with histograms of Markov chain positions. Figure 3.6 displays such histograms in the case of the adjustment to the noise PSD of the EDELWEISS electronics. From the position histogram, the mean position is extracted as an estimate of the set of optimal free parameters as well as the 1σ error bars on this estimate from the 0.16 and 0.84 quantiles of the distributions. The shape of the distributions also informs us about the quality of the constraint imposed on the considered parameter. Indeed, a narrow distribution indicates a well constrained parameter (like parameter i_B) with small error bars contrary to a distribution with wide spread which induces large error bars (like parameter i_A). Two parameters whose projection in 2 dimensions is elongated indicates their correlation (parameter i_C and e_{DAC}).

After MCMC analysis, we obtain the fit of the experimental data related to JFET-based and EDELWEISS electronics presented in the figure 3.7. The adjustment was performed on the PSD envelope, the parasitic peaks were ignored for the analysis. For the JFET-based electronics, a cut-off above 2 kHz is observed: this comes from a low-pass filter integrated in the electronics. It has been taken into account and therefore does not affect the convergence of the MCMC for this electronics. We also note the appearance of two additional free parameters. The f_B parameter corresponds to the order of the low-pass filter for JFET-based measurements. The parameter e_{DAC} corresponds to the noise of a power supply connected in series with the capacitance of the EDELWEISS electronics.

We check that the fit is excellent over all frequencies, with some slight difference in behavior for the low frequencies of the JFET-based electronics. Indeed, the function of χ^2 weighted by the number of degrees of freedom *ddl* is equal to 2.556 for JFET-based and 2.0 for EDELWEISS, which is close to the value 1 corresponding to a perfect modeling. The optimal solutions, indicated in the table 3.52, for the electronics allow to simulate the noise of the electronics from the proposed model of electronics noise (eq. 3.46 and 3.47). Different behaviors are observed depending on

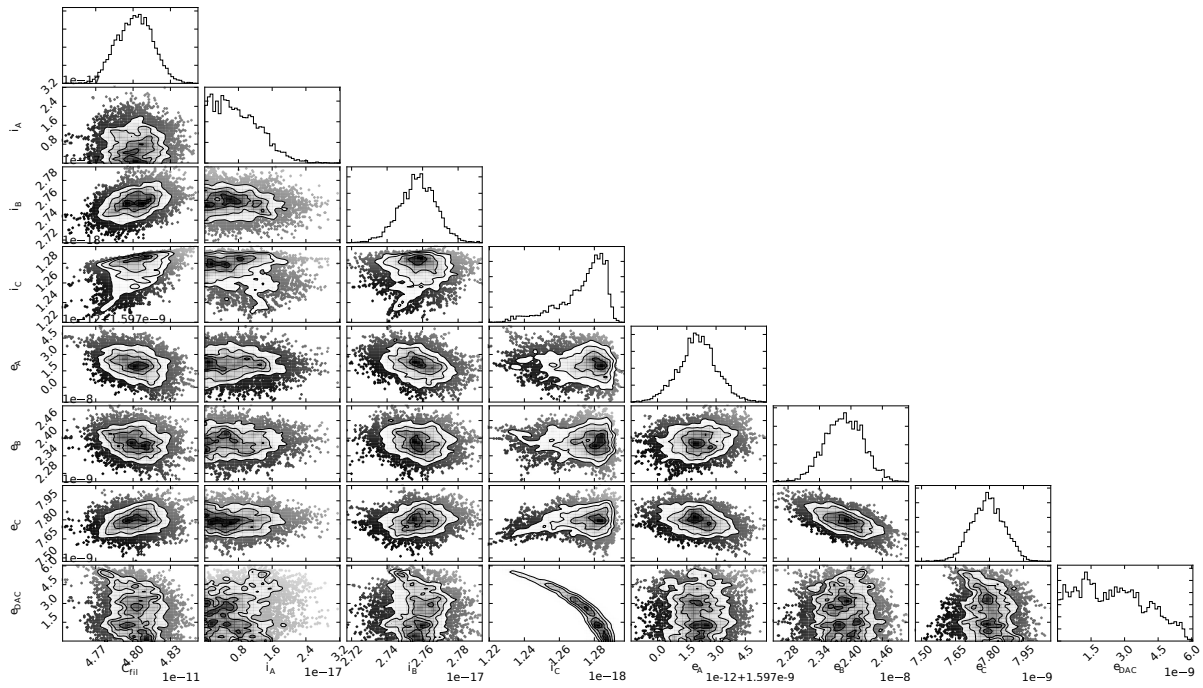

Figure 3.6: Histogram of Markov chain positions with 2-dimensional projections, during MCMC analysis for EDELWEISS electronics. The free parameters presented are from top to bottom, and from left to right: $C_{cabling}, i_A, i_B, i_C, e_A, e_B, e_C, e_{DAC}$.

.

the temperature of the cryostat: the PSD levels are globally larger at low temperatures. This can be explained by the contribution of the current noise i_{noise} increasing with the norm of the complex impedance Z_{eq}. Indeed, the NTD resistance $R(T_e)$ increases very strongly when the temperature of the cryostat decreases, so the complex impedance Z_{eq} also increases.

JFET-based		**EDELWEISS**	
$C_{fil} = (2.94 \pm 0.01) \times 10^{-10}$	$[F]$	$C_{fil} = (4.80 \pm 0.02) \times 10^{-11}$	$[F]$
$i_A = (1.9 \pm 0.03) \times 10^{-15}$	$[A/\sqrt{Hz}]$	$i_A = (6.17 \pm 4.8) \times 10^{-18}$	$[A/\sqrt{Hz}]$
$i_B = (6.11 \pm 0.01) \times 10^{-16}$	$[A/Hz]$	$i_B = (2.76 \pm 0.01) \times 10^{-19}$	$[A/Hz]$
$i_C = (1.16 \pm 0.01) \times 10^{-17}$	$[A/Hz^{3/2}]$	$i_C = (1.28 \pm 0.02) \times 10^{-18}$	$[A/Hz^{3/2}]$
$e_A = (3.28 \pm 0.01) \times 10^{-9}$	$[V/\sqrt{Hz}]$	$e_A = (1.60 \pm 0.00) \times 10^{-9}$	$[V/\sqrt{Hz}]$
$e_B = (3.03 \pm 0.04) \times 10^{-8}$	$[V]$	$e_B = (2.39 \pm 0.04) \times 10^{-8}$	$[V]$
$e_C = (1.08 \pm 0.02) \times 10^{-8}$	$[V \cdot \sqrt{Hz}]$	$e_C = (7.81 \pm 0.07) \times 10^{-9}$	$[V \cdot \sqrt{Hz}]$
$f_B = (2.70 \pm 0.01)$	$[u.a.]$	$e_{DAC} = (2.02 \pm 1.9) \times 10^{-9}$	$[V/\sqrt{Hz}]$

(3.52)

The low-frequency behavior of the two electronics is very similar: one observes a strong rise at low frequencies associated with the parameters $e_{B,C}$. At higher frequencies, we note that the JFET-based electronics noise PSDs are much more sensitive to temperature than for the EDELWEISS electronics. For all temperatures, the noise level of the JFET-based electronics is higher than that of EDELWEISS. We simply have a factor of 2 at 40 mK while we have almost an order of magnitude difference at 18 mK. The fitting parameters listed in table 3.52 show a difference of two orders of magnitude between the current noise i_A of the two electronics. For

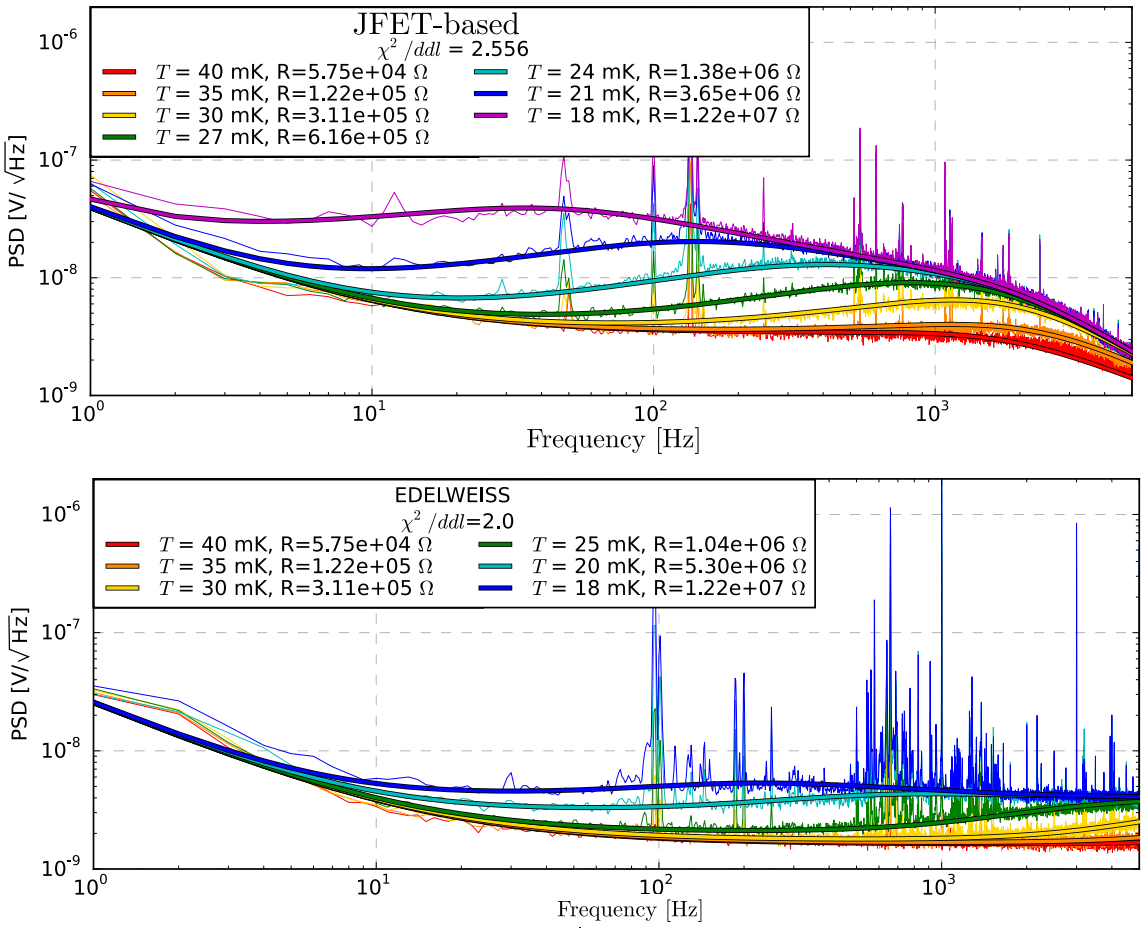

Figure 3.7: Averaged measurements (thin lines) and adjustment by MCMC analysis (thick lines) of noise linear PSD for different temperatures on both electronics: JFET-based and EDELWEISS. It is important to note that these are noise measurements performed without polarization current. For each cryostat temperature T is specified the value of the thermistor R. The term χ^2/ddl indicates the value of the function χ^2 divided by the number of points (degrees of freedom) of the fit. For a perfect modeling of the experimental data: $\chi^2/ddl \to 1$

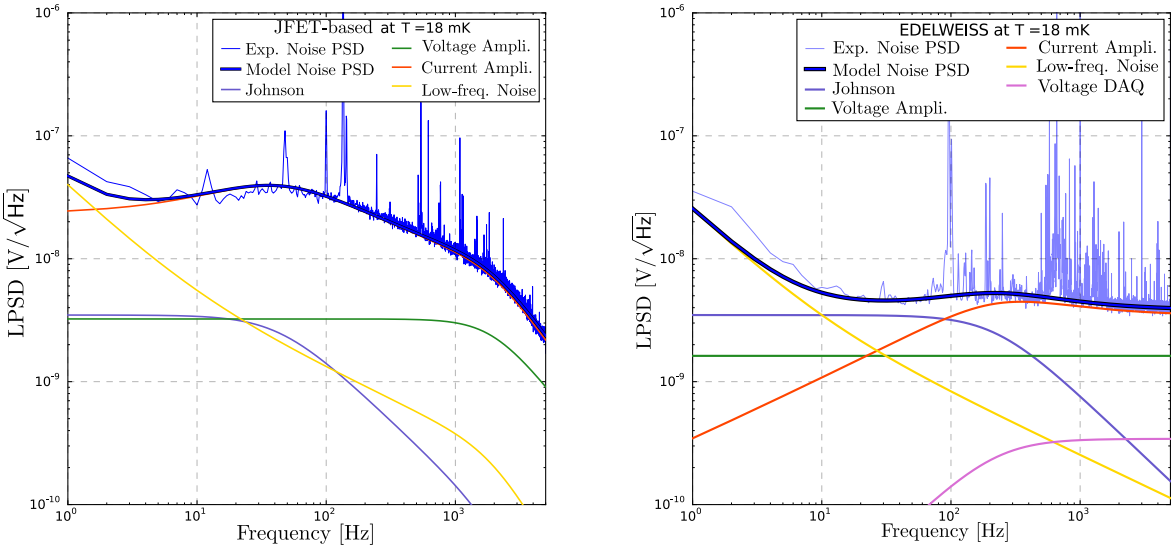

Figure 3.8: Experimental measurement and model of a noise spectral density at 18 mK for JFET-based (left) and EDELWEISS (right) electronics with visualization of the contributions of the different noise sources.

the EDELWEISS, the current noise is coupled to the complex impedance Z_{eq} which explains the measured noise level.

It therefore appears that the least noisy is the EDELWEISS electronics. It is thus with this electronics that it is agreed to optimize the resolution of the detectors.

Using the optimal solution found with the MCMC analysis, it is possible to visualize the contributions of the different noise sources to the total noise PSD, an example at 18 mK is shown in figure 3.8 for the two electronics. It can be seen that the current noise of JFET-based is very high and dominates almost the whole frequency range. The Johnson noise cut-off frequency, which is different for the two electronics, illustrates the influence of the cabling capacitance $C_{cabling}$. Indeed, we have $f_{cut} = 2\pi/(R_{NTD}C_{cabling})$ considering $R_L \gg R_{NTD}$. A higher cut-off frequency is found in the case of EDELWEISS which has a lower cabling capacitance according to the fitting parameters (eq. 3.52). It is also possible to study the predominance of noise sources as a function of frequency. For the electronics of EDELWEISS:

- below 10 Hz, the noise is dominated by the low-frequency contributions of noise in voltage $e_{B,C}$. From 10 Hz to 100 Hz, the total noise is based on the intrinsic noise of the detector (TFN noise and Johnson noise of the NTD). This is exactly what is sought: one seeks to be limited by these detector thermal noises which sets the ultimate attainable limit.

- above 100 Hz, the current noise of the amplification electronics characterized by the coefficients $i_{A,B,C}$ becomes predominant.

3.2.4 Calculation of the NEP and Resolution

Now that we have constrained all the parameters of the noise model, it is possible to finalize the computation of the resolution (eq. 3.45) with the computation of the NEP (eq. 3.44). Figure 3.9 shows the simulated sensitivity and NEP graphs of the detector for the EDELWEISS electronics at 18 mK for a bias current $I_P = 1$ nA. The sensitivity is consistent with the transfer function of a thermal system: it is indeed a low-pass. The simulation of the NEP is obtained from the sensitivity and the total noise PSD according to the formula 3.44. It presents its lowest values between 1 Hz and 100 Hz.

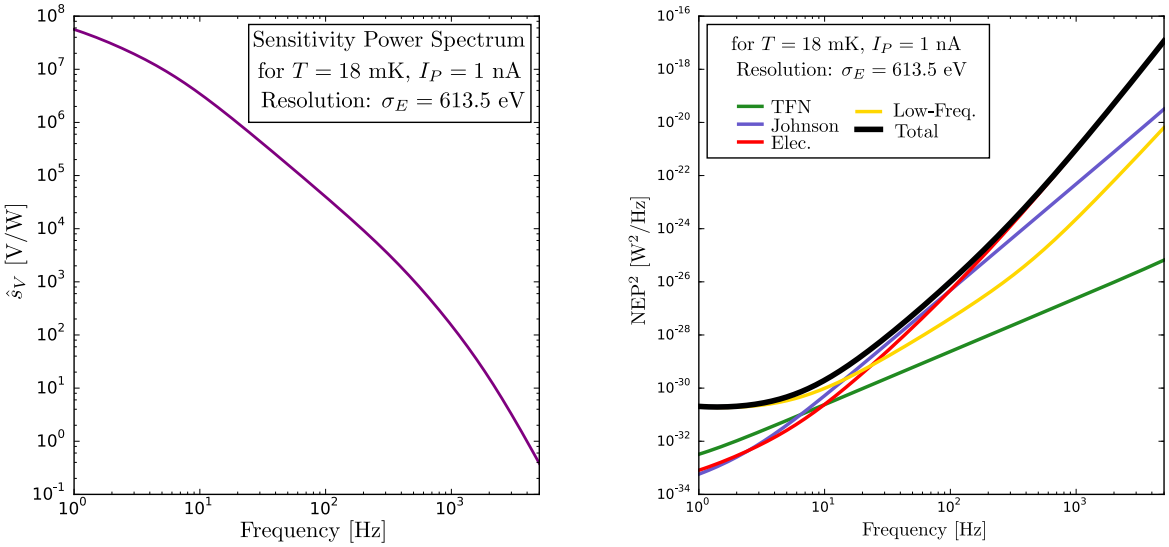

Figure 3.9: Simulation of sensitivity (left) and NEP (right) with contributions of different noise sources for EDELWEISS electronics at a cryostat temperature of $T = 18$mK and a bias current of 1nA.

It is now possible to access the resolution of this experimental configuration with the associated formula 3.45. We calculate here a heat energy resolution of $\sigma_E = 613.5$ eV for EDELWEISS, and a resolution of 1061 eV with the JFET-based electronics, with a temperature of 18 mK and a bias current of 1 nA. A lower value is obtained with the EDELWEISS electronics, which further confirms the choice of this electronics for the optimization of the resolution.

The formula 3.45 used for calculating the resolution indicates that the lowest NEP values contribute the most to the resolution. Although integrating over a wider frequency range results in lower resolution, the gain becomes negligible as the NEP value increases. Note that the NEP takes its minimum values around 10 Hz: most of the heat measurement information is contained in a frequency range from 0 Hz to about 50 Hz. The gain in resolution by integrating beyond 50 Hz is marginal. The frequency range of interest for the study of the signal is then identified. By observing the contributions of the different noise sources to the NEP in figure 3.9, we can see that it is the low frequency (LF) noise that dominates in this frequency range of interest, followed by the Johnson noise of the NTD resistor. We understand that to further decrease the resolution of these detectors, we should increase the sensitivity of the system to an event or reduce this low-frequency noise.

3.2.5 Thermal Characterization of the RED10 Detector

At the time of this study of the heat channel, the RED10 detector had only recently come into the possession of the MANOIR group. It shares its design with the prototype RED1. The difference with the latter lies in the glue composition used and the dimensions of the NTD used. Some thermal parameters are therefore modified compared to RED1. It is thus necessary to characterize these thermal parameters for this new detector. One will be able to study its response to an event as it was done with RED1 in the previous section.

3.2.6 Current-Voltage Characteristic and Signal Shape

The characterization of the thermal parameters uses the electro-thermal model that was built in the section 3.1. We want to adjust the unconstrained parameters to the experimental data with an MCMC analysis similarly to the characterization of the electronics in the subsection 3.2.3. This time, the set of free parameters is:

$$\Theta = (R_0, T_0, g_{ep}, g_k, g_{glue}, \epsilon, \tau_P) \tag{3.53}$$

Indeed, the new glue has a different conductivity g_{glue}. The new geometry of the NTD (and also its uncertainty of neutron doping) will lead to a modification of the resistance R_0 and characteristic temperature T_0 present in the equation 2.12. The change in dimension also impacts the electron-phonon coupling g_{ep} and the Kapitza conduction coefficient g_k. In principle, the volumetric thermal capacities of the absorber and the NTD remain unchanged, which makes it possible to recalculate the new thermal capacities from the known dimensions of the NTD. It would have been possible to include these in the free parameters, but the choice to fix them was favored in order to avoid degeneration problems and thus better constrain the set of parameters Θ.

A preliminary study of the signal shape (shown on the right of figure 3.10) of RED10 reveals that the pulse decay has two characteristic time constants. This type of signal has never been observed on signal measurements performed with RED1: there is only one characteristic decay time explained by the thermal leakage to the cryostat from the electron bath with a recoil energy deposit in the absorber. The presence of a second characteristic time for RED10 can only be explained by the presence of athermal phonons as introduced in section 3.1.4. These are phonons that do not immediately relax in the absorber, pass into the NTD sensor before relaxing. They thus create a temperature rise directly within the NTD. The source term $\boldsymbol{F}$ in the equation 3.21 is then rewritten:

$$\boldsymbol{F}(t - t_0) = \begin{pmatrix} (1-\epsilon)E/C_a \\ 0 \\ \epsilon E/C_e \\ 0 \end{pmatrix} \delta(t - t0) \tag{3.54}$$

with ϵ the fraction of recoil energy converted into athermal phonons, and C_a and C_e the thermal capacity of the absorber and the electron bath respectively.

The normalization constants of the general time solution (eq. 3.26) depend on the source term $\boldsymbol{F}$ according to formula 3.28 and therefore differ from the case of RED1, devoid of athermal phonons. This has the effect of better expressing a new exponential, and thus a new characteristic time, contained in the general solution. This observation of two characteristic times for the signal motivates the addition of the fraction of athermal phonons ϵ and their characteristic relaxation time τ_P to the free parameters of the model.

The electro-thermal model is adjusted to the experimental data collected with RED10. The detector RED10 is polarized with a fixed bias current $I_P = 4\,\text{nA}$ for different temperatures ranging from 18 mK to 30 mK. We study the behavior of RED10 in the steady state (see section 3.1.2), with its experimental current-voltage characteristic, and its temporal response (section 3.1.3) with experimental heat signals generated by electronic recoils induced by the natural radioactivity. The likelihood function analysis is performed with the MCMC method as in section 3.2.3. Experimental data with the adjusted models are presented in the figure 3.10.

The fit seems good for both types of measurement with a $\chi^2/ddl = 1.612$. However, the model has some difficulty in adjusting the pulse at a temperature of 30 mK. The current-voltage characteristic, also called V(I) curve, makes it possible to constrain the free parameters involved in the steady state equations 3.12: R_0, T_0, g_{ep}, g_k. The experimental points in the linear part of the V(I) curves below 1 nA mainly constrains the resistance value of the NTD, and thus R_0, T_0.

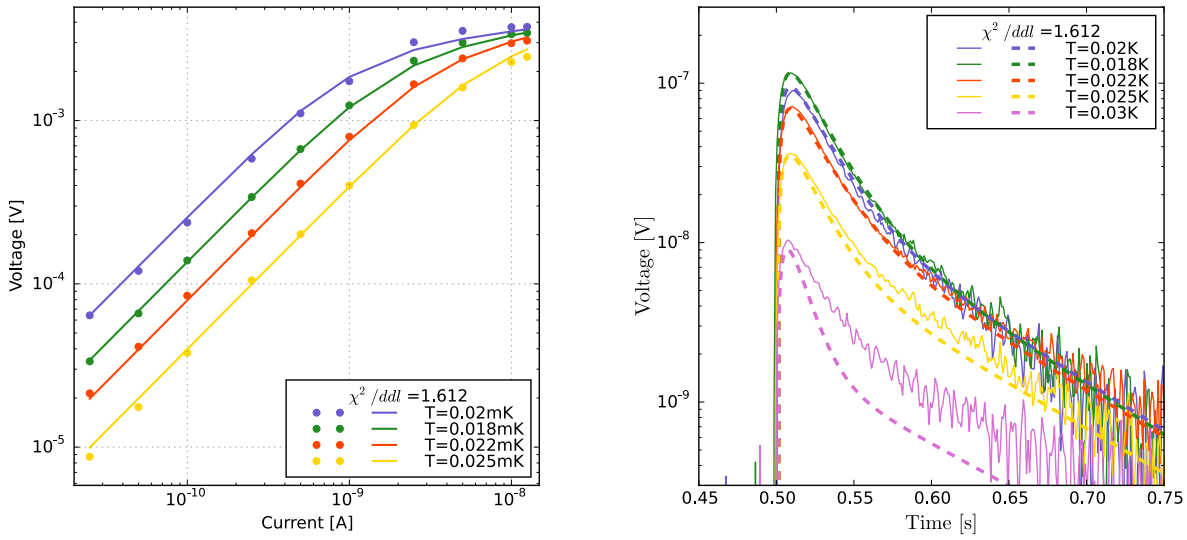

Figure 3.10: Experimental measurements and model fittings of the current-voltage characteristic (left) and normalized heat signals (right) for the RED10 detector.

The voltage plateau at higher bias current above 1 nA comes from an excessive Joule effect in the NTD which is then no longer compensated by the thermal leakage to the cryostat. The temperature of the NTD increases and its resistivity decreases with constant bias current I_P, which causes the voltage plateau to appear. Its adjustment thus constrains the values of conductivity g_k and electron-phonon coupling g_{ep}.

As for the shape of the signal, the model shows two slopes and thus two characteristic times. The adjustment of these two decay slopes constrains the athermal phonon fraction ϵ, and more generally, all the parameters involved in the calculation of the normalization constants of the time dependent solutions 3.23. The rise in tension allows to constrain the relaxation time of the phonons τ_P. Indeed, for an immediate relaxation of the phonons, the rise time would be infinitely large (modulo the cutoff frequency $(RC_{cabling})^{-1}$).

The MCMC method then gives the fitting parameters for RED10:

$$R_0 = (11.6 \pm 0.4) \quad [\Omega] \tag{3.55}$$
$$T_0 = (2.72 \pm 0.01) \quad [K] \tag{3.56}$$
$$g_{ep} = (21.1 \pm 4.4) \quad [W/K^6/cm^3] \tag{3.57}$$
$$g_k = (2.77 \pm 0.1) \times 10^{-4} \quad [W/K^4/mm^2] \tag{3.58}$$
$$g_{glue} = (7.46 \pm 1.67) \times 10^{-4} \quad [W/K^{n_g}/mm^2] \tag{3.59}$$
$$\epsilon = (0.202 \pm 0.001) \quad [fraction] \tag{3.60}$$
$$\tau_P = (4.03 \pm 0.03) \times 10^{-3} \quad [s] \tag{3.61}$$

These values are of the same order of magnitude as those corresponding to RED1. It is important to highlight the high portion heat energy expressed as athermal phonons of about 20 % which is to be compared to their complete absence within the RED1 detector. This is a new observation for this type of detector. Their high proportion results in an acceleration of the voltage signal and thus an increase of the frequency range of interest of the signal introduced in section 3.2.4. In addition, athermal phonons are not affected by the capacity of the absorber, and

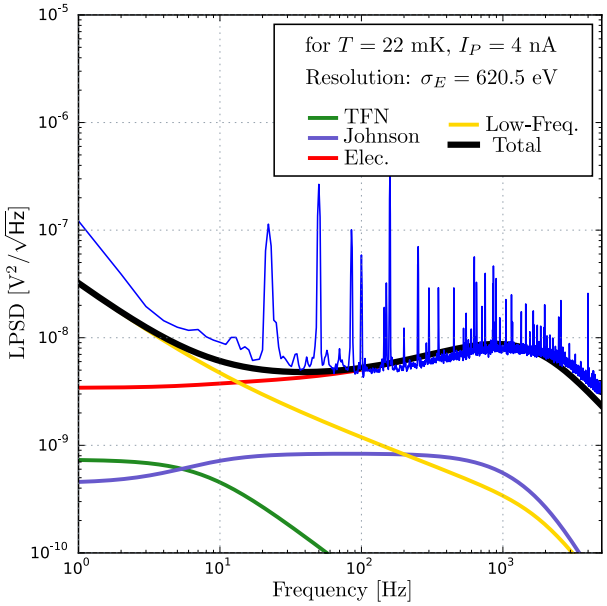

Figure 3.11: Experimental measurement of the noise PSD at 22mK with RED10 compared to its simulation with the electro-thermal model.

transmit all their energy directly to the NTD. Understanding and increasing the rate of athermal phonons will thus allow to increase the sensitivity leading to lowered energy resolution of the detector. A new way of optimizing the detectors has been discovered, which has not yet been considered within the R&D program.

3.2.7 Noise Levels and Energy Resolution of RED10

Since RED10 is fully characterized from the thermal point of view, and the JFET-based electronics used for the measurements is also characterized, we are able to simulate the noise spectrum related to RED10 compared to the experimental measurement. Figure 3.11 shows the adjusted model and the experimental measurement of the noise PSD of RED10 for a bias current of 4 nA and an operating temperature of 22 mK. Note that a Bessel filter is applied to the measurement, and to the model, which explains the cutoff appearing from 2 kHz.

The model and the measurement describe very similar developments. We do find the presence of a low frequency noise of high level dominating the total noise PSD up to 15 Hz. It is then the current noise that predominates over the rest of the frequency range. It should be noted that this PSD measurement is performed with the polarization of the NTD as opposed to the characterization of the noise of the JFET-based and EDELWEISS electronics which was done with $I_P = 0$ A. As such, it would be incorrect to compare the presented current noise of RED10 with the current noise of RED1 obtained without bias current. There is a slight shift in the model from the experimental data to the low frequencies. This can be explained by the underestimation of the low-frequency noise already observed for the JFET-based electronics in the figure 3.7. The excess of low-frequency noise also comes from the high rate of muon events during the measurements: despite the cuts made in the analysis, part of the signal decay is always recovered, which helps to amplify the low frequencies of the measured spectrum.

The experimental resolution measurement is carried out from the noise PSD and the measurement of a heat signal. Indeed, renormalizing the amplitude of the signal and applying a Welch method allows to estimate the signal power spectrum, equivalent to the sensitivity s_V of the RED10 detector. The renormalization also requires to know the conversion between the

energy deposited in the absorber by an event and the amplitude of the measured signal. This calibration is performed using the interaction of cosmic muons with the absorber. The energy they deposit in the absorber is equal to 18 MeV. Measuring the voltage amplitude of a muon signal therefore allows to deduce the conversion factor necessary for the renormalization of a signal. The experimental heat energy resolution σ_E is calculated using the discrete analogue of the formula 3.45.

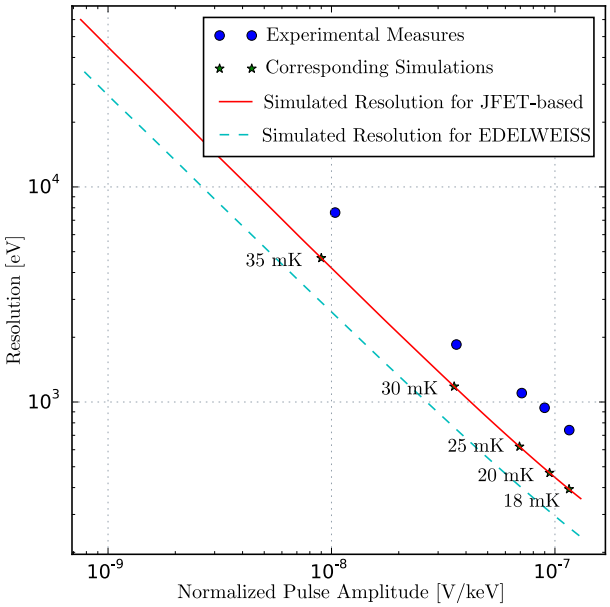

Figure 3.12: Heat resolution σ_E versus the normalized signal amplitude for the detector RED10 polarized with a bias current of 4 nA with temperatures ranging from 18 mK to 30 mK.

Figure 3.12 shows the energy resolutions σ_E as a function of the normalized heat signal amplitudes in $\mathrm{nV} \cdot \mathrm{keV}^{-1}$ for different temperatures at a fixed bias current. The experimental resolutions are higher than the simulated resolutions. This is explained by the deviation between model and noise measurement observed in figure 3.11: the modeled low-frequency noise is lower than in reality, hence the simulation of lower resolutions. The pulse amplitude is used to estimate the sensitivity of RED10 to the signal. Except for the 30 mK measurement where the signal was already poorly modeled, the simulated and real amplitude values are almost identical. Moreover, since the two sets of dots show a very similar evolution of the resolution as a function of amplitude, it is deduced that the model is in good adequacy with the experimental reality. A study of the noise difference is still necessary to obtain a complete adequacy of model and experiment.

It should be noted that the measurements were performed with the JFET-based electronics. The simulation of the resolution-amplitude characteristic is plotted for both the JFET-based and the EDELWEISS electronics. It should be noted that the latter makes it possible to gain almost a factor of 2 on the value of the resolution as the amplitude remains unchanged. This is consistent with the low noise level of EDELWEISS compared to the noise level of the common JFET-based electronics.

3.2.8 Optimization of the RED10 Detector and Perspectives

An electro-thermal model was built and tested with RED10. Even if some parameters need to be further refined to have a better fit, we can perform a preliminary optimization of the RED10 detector. A simulation of the resolution of RED10 as a function of the bias current I_P in the NTD

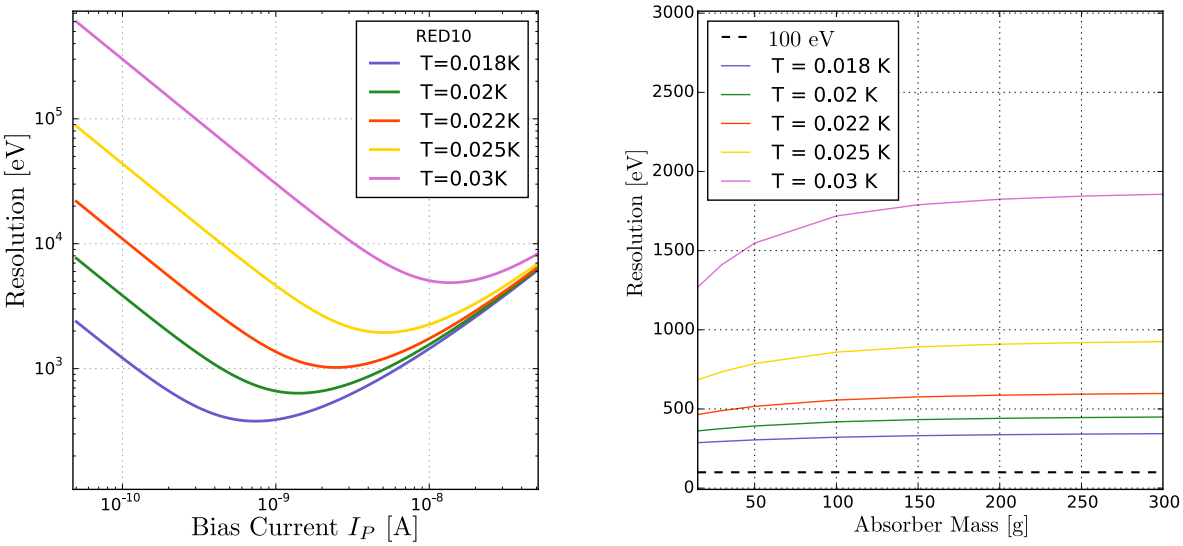

Figure 3.13: On the left, Simulation of the resolution of RED10 as a function of the bias current for different temperatures. On the right, Simulation of the resolution with optimized bias current as a function of the absorber mass for different temperatures. The design considered is the same as that of RED10, only the mass of the absorber is changed by adjusting the bias current to obtain the lowest resolution.

thermistance for different cryostat temperatures is presented in figure 3.13. The simulation is performed with the EDELWEISS electronics which has the lowest noise level, and the temperature of the load resistor is lowered to the temperature of the mixing chamber to reduce its Johnson noise.

It is observed that there is an optimal bias current I_P corresponding to each temperature to minimize the energy resolution σ_E. Indeed, if the NTD thermistor is polarized too much, the heat produced by Joule effect can no longer be evacuated efficiently by the thermal leakage. The temperature of the NTD becomes high and therefore its value drops, which affects the sensitivity of the system. This effect is observed in the current-voltage characteristic as the plateau at high bias current in figure 3.10. At too low bias current, the NTD sensor is no longer polarized enough to efficiently convert the heat signal into a voltage signal: the sensitivity drops as well.

No matter what bias current is used, the lowest resolution is always obtained at the lowest temperature. The NTD resistivity formula 2.12 explains why the signal is more sensitive at low temperatures: the derivative of the resistance with respect to the temperature takes its maximum values there. Moreover, lowering the temperature reduces all TFN noises, and the Johnson noise of the NTD thermistor, which further improves the energy resolution.

The RED10 study was fully realized for a bias current of 4 nA, which corresponds to the optimal current at a temperature of about 24 mK. It would therefore have been possible to obtain better resolution values by adjusting the bias current for each temperature. Thus, it will be important, in the future, to properly determine the optimal polarization current of a detector according to the measurement conditions.

The precision measurement of the CENNS requires the development of a new generation of detectors with very low detection threshold. For this, it is necessary to work on the design of the detectors. For example, it is necessary to study the behavior of the detector according to the geometry of the NTD or the mass of the absorber. A simulation of the resolution of a detector as a function of the absorber mass is shown in the graph on the right side of figure 3.13. Note that the polarization current is adjusted for each point to draw an already optimized

resolution curve. According to the formula 3.54, it would be interesting to reduce the thermal capacity of the absorber C, by lowering its mass, in order to increase the temperature pulse ΔT, and thus amplify the heat signal. According to the simulation, this amplification of the heat signal would appear only for very small detector masses, and would remain very modest for low temperatures.

The result of this study motivated the optimization of the RED detector mass. The mass of the germanium crystals went from 200 g for RED10 to 37.6 g, like for the detectors RED80 and REDN1 with electrodes described in the Chapter 6, and 33.4 g for RED detectors with no ionization channel. Based on five 33.4 g prototype detectors, an average energy resolution 22 eV is reliably obtained, with the best performance being attributed to the detector RED20 [10] with an heat energy resolution of 16.5 eV. The specification of the CryoCube on the energy resolution $\sigma(E_R) = 10$ eV is therefore within reach.

Chapter 4

Electrodes Design with Electrostatic Simulation

4.1 Electrodes as Sensors for the Ionization Channel

4.1.1 Basics of the Ionization channel

The ionization channels aims at converting the ionization of the germanium into a voltage signal. This is done with the use of aluminium electrodes forming a capacitor characterized by its capacitance C in the range of $\mathcal{O}(100\,\mathrm{pF})$. When collecting an electric charge ΔQ on its two plates, a voltage ΔU is created across the capacitor according to the equation:

$$\Delta Q = C \cdot \Delta U \quad \Leftrightarrow \quad \Delta U = \frac{Q}{C} \tag{4.1}$$

A high sensitivity of the ionization channel means that the created voltage ΔU is maximized. The equation 4.1 shows that a low capacitance C of the electrodes and a high collection of electric charge ΔQ increase the ionization channel response. While the amount of electric charge ΔQ can depend of the electric field shape, in the case of a theoretically perfect charge collection, the number of electron-hole pairs created and collected only depends on the part of the recoil energy E_R going into the ionization channel deemed the ionization energy $E_{Ion.}$. The capacitance depends on the design of the detector, and is the one of the main quantities used to quantify the performance of a detector design.

4.1.2 Reference detector designs

The reference detector designs are used to illustrate the different concepts of the ionization channel. They are the result of the optimization of the ionization channel (presented later in this chapter) and thus presents very good performances. There are two reference designs based on a 38 g cylindrical Germanium crystal of height 10 mm and diameter 30 mm. The figure 4.1 presents the simulated geometry of these designs.

The geometry on the left corresponds to the "Planar 38 g" design (PL38). Its ionization channel consists in two collecting electrodes fully covering the planar faces and extending on the lateral face. The geometry on the right corresponds to the "Fully Inter-Digitized 38 g" design (FID38). This design is an adaptation of the electrode design of the 200 g and 800 g FID detectors from the EDELWEISS-III experiment. It possesses four interleaved electrodes made out of concentric circular aluminium rings. Contrary to the simpler PL38 design, the FID38 is able to tag surface events thanks its more complex electrodes shaping the electric field. Both designs are extensively described in section 4.2.

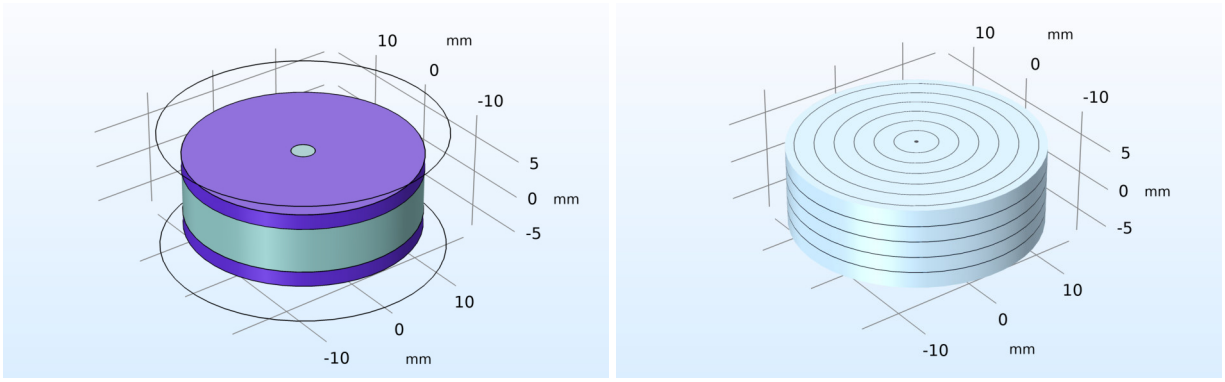

Figure 4.1: 3D views of the simulated designs PL38 (on the left) and FID38 (on the right). The bare germanium crystal is colored in grey while the aluminium deposits are purple.

4.1.3 Ionization in Semiconducting Germanium Crystals

The ionization channel is based on the semi-conducting germanium crystal of high purity acting as absorber of the detectors. Along with an increase in temperature assessed in the previous chapter 3, the semi-conducting Ge crystal also features a phenomenon of ionization caused by a recoil. This section describes this process of ionization creating electron-hole pairs in the germanium crystal and the subsequent collection of these electric charges by the electrodes.

The pure germanium is a semi-conducting material. In order to understand the physical properties of a semi-conductor, we can consider the theory of electronic energy bands. In a solid material at rest, electrons are occupying the lowest state of energy according to a Fermi-Dirac distribution. This lowest state of energy is strongly linked to the nucleus, forming the valence electronic band of energy. Higher energy states are able to interact with neighboring atoms, carry the electric charges in the material and compose the conduction electronic band of energy. A conducting material has overlapping valence and conduction bands and boasts a very high number of electric charge carriers. On the contrary, insulators presents a separation of the two bands by such high energy gap that its conduction bands is empty. Semiconductors stands as a middle point between conductors and insulators. Semiconducting material features a small energy gap E_g between the valence and conduction bands. This energy gap is low enough that the thermal energy at rest is sufficient to excite charges and creates carriers in the conduction band. As such, the electronic properties of a semiconductor depends on its energy gap and its temperature, these parameters controlling the number of charge carriers presents in the material. The amount of impurities present in the semiconducting crystal is also of importance and is discussed later in this section.

At cryogenic temperatures in the order of $\mathcal{O}(100\,\mathrm{mK})$, no charge in the Ge crystal crosses the Fermi level. This results in a freeze-out of the electronics charge carriers with all the electron in rest state. The process called ionization described the carriers being excited by an external source of energy such as the deposit of a recoil energy by an event in the crystal. A recoil excites an electron into the conduction band leaving a hole in the valence band, an electron-hole pair is created and assure charge conduction in the crystal.

When interacting with the atoms of a germanium crystal, a particle deposits a recoil energy E_R in the crystal lattice. The word "recoil" references to the elastic scattering of the incoming particle on in the germanium crystal. If the particle scattering happens on the nucleus of a Ge atom, the event is called a nuclear recoil (NR). If the particle scatters on an electronic cloud of Ge atom, the event is defined as an electronic recoil (ER). The deposited recoil energy E_R manifests in the crystal lattice in two ways: as heat energy E_{heat} with the creation of phonons and as ionization energy $E_{Ion.}$ with creation of electron-hole pairs through the ionization process. The fraction of recoil energy E_R attributed to the ionization channel is the ionization quenching

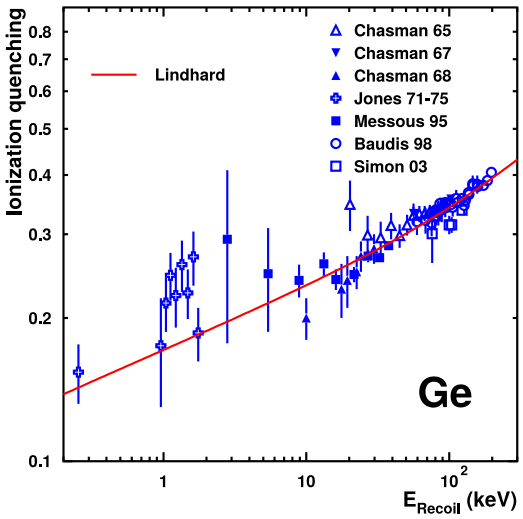

Figure 4.2: Lindhard model of the ionization quenching factor in germanium (in red). Experimental results of direct measurements of the quenching factor from multiples experiments are displayed in blue. Figure taken from [16].

factor Q:

$$Q = \frac{E_R}{E_{Ion.}} \tag{4.2}$$

The expression of the quenching factor Q depends on the recoil type. For an electronic recoil, the entirety of the recoil energy goes into the ionization process with $E_R = E_{Ion.}$ such that the associated quenching is:

$$Q_{ER} = 1 \tag{4.3}$$

For nuclear recoils, the electron cloud is excited indirectly through the movement of the Ge nuclei in the crystal lattice. The quenching factor Q_{NR} associated with the nuclear recoils is a function of the recoil energy E_R which is defined by the Lindhard model [34] applied to the germanium:

$$Q_{NR}(E_R) = \frac{k \cdot g(E_R)}{1 + k \cdot g(E_R)} \tag{4.4}$$

The k, g terms depends on the germanium atomic number $Z = 32$ and average number of nucleon $A = 72.63$ such that:

$$\begin{cases} k & = 0.133 \cdot Z^{\frac{2}{3}} \cdot A^{\frac{-1}{2}} \\ \epsilon(E_R) & = 11.5 \cdot E_R \cdot Z^{\frac{-7}{3}} \\ g(E_R) & = 3 \cdot \epsilon(E_R)^{0.15} + 0.7 \cdot \epsilon(E_R)^{0.6} + \epsilon(E_R) \end{cases} \tag{4.5}$$

The figure 4.2 (extracted from [16]) presents the Lindhard model of the quenching factor of nuclear recoils in germanium as a function of the recoil energy. The parameters of the Lindhard model are adjusted to experimental measurements of the quenching factor displayed as blue points with error bars.

Immediately following the ionization process, electrons can be excited with energies much greater than the germanium band gap energy E_g. However, such electrons relaxes by phonon emission and creation of new electron-hole pairs. After the relaxation, we can consider that there

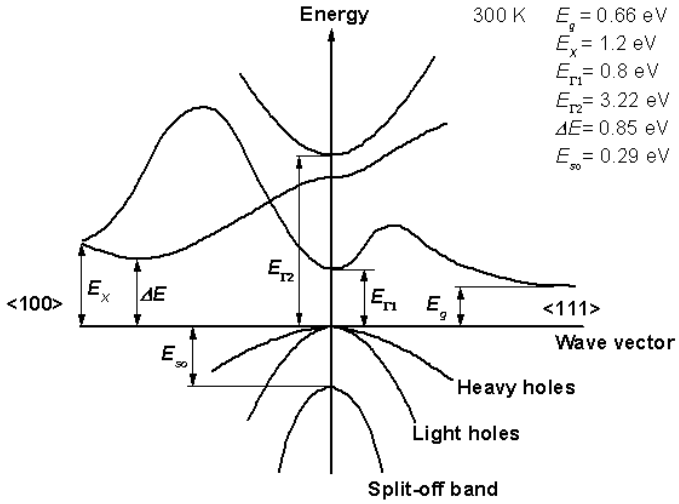

Figure 4.3: Electronic band structure of the Germanium in the energy versus momentum space. Below the origin are the valence bands, above are the conduction bands. The minimum energy gap $E_g = 0.67\,\text{eV}$ is set between the lowest-energy excited states in the valence bands at $\vec{k} \in$ <000> and conduction bands at $\vec{k} \in$ <111>. Figure taken from [33].

is in the Ge crystal a number of pairs N_p:

$$N_p = \frac{E_{Ion.}}{\epsilon_{e^- - h^+}} = Q \cdot \frac{E_R}{\epsilon_{e^- - h^+}} \tag{4.6}$$

with $\epsilon_{e^- - h^+}$ the average energy of the relaxed electron-hole pairs. This equation demonstrates the key property of the semiconducting Ge crystal: the number of pairs N_p is linked to the recoil energy E_R. Thus, its measurement yields an estimation of the recoil energy.

This estimation requires to know the average energy of the pairs $\epsilon_{e^- - h^+}$. A naive approach is to consider the band gap of the germanium E_g. It can be extracted from the electronic band structure of the germanium displayed in the figure 4.3 (extracted from [33]). The valence and conduction bands are plotted in the energy versus momentum space. The Germanium crystal possesses diamond cubic lattices. These repeating spacial pattern affects the electrons so that an available electronic states is defined by its energy and its momentum in respect to the crystal lattice. The momentum space is expressed using the Miller indices which define the directions in the Ge crystal lattice.

In the figure 4.3, the valence bands are situated below the origin while the conduction bands are above the origin. The minimal band gap $E_g = 0.67\,\text{eV}$ of the germanium is derived from the lowest-energy states of excited carriers. Excited electrons, carrying a negative charge $-e$ are promoted to the conduction bands while the holes, carrying a positive charge $+e$, are created in the valence bands. The maximum of the valence bands corresponds to the <000> directions signifying a null momentum. The minimum of the conduction bands is obtained along the <111> directions. Excited electrons and holes have different momenta. As such, the germanium gap is defined as indirect: the transition of an electron to an excited state of the conduction band necessitate the transfer of a momentum $\vec{k}$ in addition to the gap energy E_g. The average energy $\epsilon_{e^- - h^+}$ contained in an electron-hole pair consists in the germanium gap band of energy E_g added to the energy of the phonon of momentum $\vec{k} \in$ <111> associated with the pair. The

average energy of an electron-hole pair in germanium is measured:

$$\epsilon_{e^- - h^+} = 2.96\,\text{eV/pair} \tag{4.7}$$

The relation 4.6 between the number of pairs N_p and the recoil energy E_R is now applicable in the germanium.

The number of created pairs N_p is subject to fluctuation and thus imposes itself as an intrinsic limit to the resolution of the ionization channel. The number of pairs N_p should be expected to follow a Poisson distribution of standard deviation $\sigma(N_p) = \sqrt{N_p}$. However, experiments observed these fluctuations to be lower than expected. This can be explained by a correlation of the relaxation process of the phonons and electron-hole pairs. The empirical standard deviation is expressed as:

$$\sigma(N_p) = \sqrt{F \cdot N_p} = \sqrt{F \frac{Q \cdot E_R}{\epsilon_{e^- - h^+}}} \tag{4.8}$$

with an introduced Fano factor F of about 0.1 for the germanium. Considering the current range of ionization channel resolution, the fluctuation of the number of pairs created by ionization could be limiting with $\sigma(N_p) \approx 300\,\text{eV}$ which could be obtained for electronic recoil energies greater than 300 keV. As we are interested in the lowest energy range and the experiments presented in this work use calibration peaks of energy in the order of $\mathcal{O}(10)$ keV, the impact of these fluctuation are negligible. This is especially true considering other effects with opposite impact on the ionization resolution such as the electronic noise of the electronic readout and incomplete charge collection.

The semi-conducting properties of a germanium crystal heavily depends on the impurities affecting it. These impurities creates intermediary energy states in the semi-conducting germanium band gap accessible to electric charges (as seen in figure 4.3). The presence of these intermediate energy states has several consequences on the ionization channel. It reduces the energy necessary to create an electron-hole pair, thus creating additional noise and biasing for the ionization channel. Then, it creates a trapping phenomenon which prevents electric charge carriers from reaching the electrodes. With trapped charges in the crystal, a counter electric field slowly generates, reducing the sensitivity of the electrodes. The semi-conducting germanium is used as an absorber thus should contain the lowest amount of impurities in order to have a detector with good performances. We define N_a and N_d as the number of acceptor and donor impurities respectively. As a result, the EDELWEISS and RICOCHET experiment use High-Purity Germanium (HPGe) with a low impurity concentration:

$$10^9 < |N_a - N_d| < 10^{10} \quad \text{in atoms/cm}^3 \tag{4.9}$$

which corresponds to less than one impurity atom for 10^{12} germanium atoms. As reference, a common germanium crystal possesses a concentration of about $10^{23}\,\text{atoms/cm}^3$. With this material, low leakage currents of few fA can be achieved for the usual operating electric field range of a $\text{V} \cdot \text{cm}^{-1}$.

4.1.4 Electric Charge Drifting in Crystal

The charge collection defines the drift of the electric charge in the crystal under the influence of an electric field $\vec{E}$. The objective of this drift is for the charge to reach electrodes on the surface of the germanium crystal leading to a voltage signal measurable with an electronic readout. In this work, the magnitude of the electric field is of the order of $1\,\text{V} \cdot \text{cm}^{-1}$.

Following a recoil at a position $\vec{r}$ in the crystal, a high number N_p of electron-holes pairs are created in the immediate vicinity of $\vec{r}$. This vicinity can be considered as a sphere of radius in the range of $\mathcal{O}(1\,\mu\text{m})$ in which the electric charges are evenly distributed due to an initial diffusion

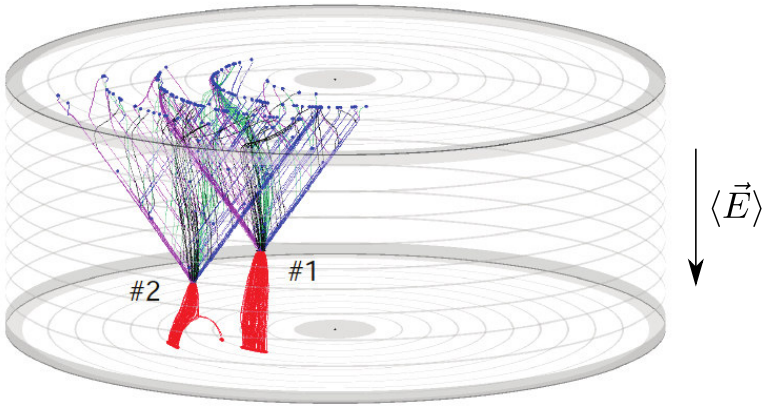

Figure 4.4: Simulation of the drift of the electron-hole pairs in a semi-conducting germanium crystal of an EDELWEISS FID detector. The red trajectories of the holes h^+ follow the electric field lines. The electrons e^- show an oblique propagation in blue along the <111> crystal directions. The direction of the average electric field $\langle \vec{E} \rangle$ imposed in the crystal is indicated on the right.

of the charges. From these initial positions, the electric charges propagate in the crystal under the influence of the electric field $\vec{E}$ and slightly by the presence of neighboring exited charges of same charges.

The equations of motion of a single charge depends on the band structure of the germanium. As described earlier with the band structure of the germanium in figure 4.3, the excited state of the electrons and holes are associated with momentum directions. On the one hand, the holes with $\vec{k} \in$ <000> presents an isotropic behavior in the crystal lattice as no momentum is in its excited state. They are thus free to propagate along the electric field lines. On the other hand, the excited states of the electrons are constrained with a momentum $\vec{k} \in$ <111>. As such, the electrons undergo a strongly anistropic propagation in the crystal.

At low field strength, inferior to $10\,\mathrm{V \cdot cm^{-1}}$, the electrons are moving along the <111> valleys in the crystal. In practice, the direction of the electric field $\vec{E}$ corresponds to the vertical axis $\hat{z}$ of the cylindrical crystal which is along the <100> lattice directions. As such, the trajectories of the electrons are oblique forming a 33° with the vertical axis towards the higher electric potentials. At high field strength, superior to $10\,\mathrm{V \cdot cm^{-1}}$, the probability of electrons scattering in the crystal and switching in another <111> valley is heightened. These inter-valley scattering are so common that the macroscopic trajectory of the electrons corresponds to the electric field lines. This behavior is observable in the vicinity of the FID electrodes where the electric field is increased due to the electric point effect.

The figure 4.4 displays the simulated [22] trajectories of electrons and holes drifting inside the semi-conducting Ge crystal of a 200 g EDELWEISS FID detector under the influence of an electric field. The holes drifts along the electric field lines and draw in red directs trajectories to the bottom collecting electrode. The electrons propagates towards the top collecting electrode following oblique trajectories in blue in the <111> directions. The charge drift lasts less than one microsecond (of the order of few 100 ns).

The transversal motion of the electrons in the Ge crystal is problematic for the charge collection. Whereas the trajectories of the holes are predicted from the electric field lines, the electrons deviates from expectations. As such, there is more error on forecasting the position of the electrons at the end of their drift and the resulting signal induced on the electrodes.

Several processes can lead to an incomplete charge collection. An incomplete collection means the number of electron-hole pairs measured is lower than the actual number of pair created by a recoil. This happens when an electric charge does not reach its associated collecting

electrode. These three phenomenon are: the bulk trapping, the surface trapping and the crystal neutralization.

The bulk trapping corresponds to electric charge getting stuck in the crystal due to intermediate energy state induced by impurities in the crystal. This trapping is countered with the use of High Purity germanium crystals. The amount of charge lost is proportional to the initial number created by the ionization process. As such, assuming a constant rate of bulk trapping, the sensitivity of the ionization channel is lowered but the measurement of the ionization energy $E_{Ion.}$ is feasible. In this work, the bulk trapping rate is estimated to 2 % at a standard magnitude of $2\,\mathrm{V}\cdot\mathrm{cm}^{-1}$. The bulk trapping rate depends on the electric field magnitude: while low magnitude $\mathcal{O}(0.1\,\mathrm{V}\cdot\mathrm{cm}^{-1})$ boasts a high rate of bulk trapping, the application of a high electric field $\mathcal{O}(10\,\mathrm{V}\cdot\mathrm{cm}^{-1})$ drastically reduces this rate.

The surface trapping is happening when electric charges reach the bare surface of the Ge crystal. As opposed to the interior of the crystal with a controlled electronic band structure due to the periodic lattice, the germanium lattice stops on the surface creating irregularities in the band structure due to edge effects. These surface irregularities easily trap in place the electrons or holes. As such any charge reaching a surface is considered to have been surface trapped. This effect can be avoided for the holes: the detector are designed as to avoid electric field lines leaving the crystal. However, this counter has mitigated efficiency for the electrons due to their oblique propagation.

The crystal neutralization refers to the progressive weakening of the electric field in the Ge crystal. All the electric charges trapped in the crystal produce a counter electric field. Depending on the crystal crystallography and the design of the electrodes, the electric field can lose in magnitude or can be warped, effectively becoming neutralized. This neutralization further boost the bulk trapping rate and can lead to unexpected surface trapping. This phenomenon gains in intensity with the trapping rate, the event rate and the operation time of the detector. It usually becomes noticeable within hours to days. The crystal neutralization is countered by a "regeneration" procedure. It consists in grounding all the electrodes of the detector and submitting it to an intense event rate in order to neutralize the trapped charges. These events are generally originating from a LED or a radioactive source. Stuck charges are excited out of their traps and recombines under the influence of their own counter electric field. As the detector is not available for data taking in this condition, the period between two regeneration procedures should be empirically adjusted to the measured charge accumulation while not too frequent to avoid supplementary dead times. For the above-ground operation at IP2I, a regeneration is realized ever two days. A radioactive cesium source (^{137}Cs) of high activity of about 4×10^{10} Bq is placed on the outside of the closed cryostat at about 20 cm from the detector load.

4.1.5 Electrode Deposition on the Germanium Crystal Surface

The electrodes of the ionization channel consists in aluminium deposits on the surface of the germanium crystal [40]. The germanium crystal is placed in a vacuum chamber where its surface can be processed with beams of vaporized atoms. These atoms are radicals, atoms with unpaired valence electrons, with high chemical reactivity. As such, these radicals reacts with any material in place. This technology is used in the creation of thin layers and for the precise alteration of the germanium surface. A solid mask can be set between the beam source and the crystal in order to shape the altered surface. In the case of the cylindrical crystal of this work, the top and bottom planar faces as well as the lateral surface can be faced towards the beam source. The crystal is usually rotated around its vertical axis to assure the homogeneity of the aluminium deposition.

Before depositing aluminium, it is necessary to prepare the germanium surface meant to host the aluminium layer. The preparation step is the creation of the amorphous layer meant to host the aluminium deposits. The germanium surface is locally altered with a beam of vaporized hydrogen atoms to form a layer about 80 nm deep of hydrogenated germanium. As mentioned

is the previous section, this compound is highly resistive preventing an early recombination of the electron-hole pairs. Another advantage of this layer is to reduce leakage current between the electrodes through the surface of the germanium.

The next step is the actual deposition of the aluminium using a beam of vaporized aluminium atoms. An aluminium layer is estimated to be about 50 nm. A layer with a continuous shape is called an aluminium deposit. For cylindrical germanium crystal, we call "full planar electrode" an aluminium deposit covering the entirety of the planar surface. Two techniques are used to form shapes with the deposits. The most straightforward method is the evaporation of aluminium with a mask. This technique is precise and quick but is limited to simple pattern respecting the cylindrical symmetry of the crystal. The most remarkable deposit shape in use for the FID detectors of the EDELWEISS-III experiment is the concentric circular rings. The mask consists in several curved slits which allow the passage of vaporized aluminium. By rotating the mask during the process, the aluminium is deposited in a ring pattern on the germanium. The electrodes of the FID38 design would likely be produced in the same way. The other technique is called the photolitography. First, the whole surface of the crystal is covered with a layer of aluminium. Then, the aluminium is coated with a chemically-protective wax. The negative of the electrode pattern is carved in the wax coating with the use of lasers, hence the name photolitography. Once done, the germanium crystal face is immersed in a chemical solution reactive with aluminium. Only the aluminium protected by the wax (patterned as the desired electrode design) is left on the surface. Finally, the wax coating is removed with an other chemical. The process has some drawbacks compared to the use of mask: it is longer and can be less precise due to the chemical attack of the aluminium. However, this method can produced any pattern desired such as square grids and holes useful for hosting the NTD thermal sensor on the germanium surface. An inevitable constraints on the shape of the aluminium deposits is the minimum width of thin deposits (such as rings) of about 50 µm.

We now describe how these thin aluminium deposits can be cabled to the electronics and considered as electrodes. The fragility of the germanium and the shallow aluminium layers motivate the use of wire-bonding as cabling technique. It consists in soldering 25 µm thin metal wires on the aluminium deposits. Wedge bonding is used to solder the metal to the aluminium using ultrasonic power and force the bonding. Two metals are used for the wire-bonding: aluminium and gold. Both can conduct the electric current however the aluminium is superconducting at cryogenic temperature making it acts as a heat insulator. As such, aluminium wires are commonly used and gold wires are reserved for the creation of a controlled thermal leak as discussed in the chapter 3.

In the case of simple electrodes like the PL38 design or the RED80 detector, several wires link the top (and bottom) electrodes to a conductive pad on the detector copper chassis. The conductive pad is then cabled to the ionization electronics. With more complex design like the FID38 design or the REDN1 detector, wires are used to connect different aluminium deposits, essentially imposing the same electric potential to those. With two wire bridges, it is possible to create interleaved electrodes with a biasing scheme based on the co-planar grid technique for event localisation used in the FID detectors of the EDELWEISS-III experiment. This biasing scheme is later described in this chapter for the FID38 design.

4.1.6 Shockley–Ramo Theorem

The ionization channel is based on the induction of a voltage signal ΔV on the electrodes of capacitance C by collecting drifting charges ΔQ. A naive but false explanation to this signal generation is to consider that the charge ΔQ is entirely deposited instantly when the charges reach the electrode. The correct explanation is to consider the current i induced on the electrode starting from the moment the electrons and holes drift in the crystal. This signal induction is theorized with the Shockley-Ramo theorem [53] [48] which states that the current I_X induced on

a given electrode, labeled X, due to the motion of a charge in an given electric field $\vec{E}$ created by multiples electrodes, is given by:

$$I_X = q\left(\vec{E}_X \cdot \vec{v}\right) \tag{4.10}$$

where q is the charge of the particle, $\vec{v}$ its velocity and $\vec{E}_X$ the "weighting electric field" associated to the electrode X. This weighting field $\vec{E}_X$ is virtual and differs from the actual electric field $\vec{E}$ in the crystal. The weighting electric field $\vec{E}_X$ associated to the electrode X corresponds to the electric fields in the crystal with all free charges removed, the given electrode X raised to unit potential $V_X = 1\,\mathrm{V}$, and all other conductors grounded. This theorem ensues from the Gauss theorem. An interpretation of the Shockley-Ramo theorem is that a charge moving in the vicinity of an electrode induces an instantaneous electric current by affecting the electrostatic field lines ending on the electrode. This theorem can be integrated to access the instantaneous induced charge Q_X on the given electrode X. In the case of a drifting charge q of initial position $\vec{r}_{q,i}$ and final position $\vec{r}_{q,f}$, the total integrated charge induced on the electrode X is:

$$Q_X = q\left(\Phi_X(\vec{r}_{q,f}) - \Phi_X(\vec{r}_{q,i})\right) \tag{4.11}$$

The term $\Phi_X(\vec{r})$ is called the "weighting potential" of the electrode X at the position $\vec{r}$. It is derived from the weighting electric field associated to the electrode X using the usual formula:

$$\vec{E}_X(\vec{r}) = -\left.\overrightarrow{\mathrm{grad}}\left(\Phi_X\right)\right|_{\vec{r}} \tag{4.12}$$

By definition of the weighting electric field $\vec{E}_X$, the weighting potential ϕ_X takes its values from the $[0, 1]$ interval. The weighting potential field associated with a point-like electrode X situated at a position $\vec{r}_X$ in an empty space is Φ_X with the following properties:

$$\begin{cases} \lim_{||\vec{r}-\vec{r}_X||\to\infty} \Phi_X(\vec{r}) = 0 \\ \lim_{||\vec{r}-\vec{r}_X||\to 0} \Phi_X(\vec{r}) = 1 \end{cases} \tag{4.13}$$

This property is generalized to any other shape of electrode at any point on its surface.

The Shockley-Ramo theorem benefits from the superposition theorem such that it is possible to express the signal induced on the electrode X by charges drifting after the creation of a number N_p of electron-hole pairs:

$$\begin{aligned} Q_X &= \sum_{n=1}^{N_p} \left(Q_X^n(e^-) + Q_X^n(h^+)\right) \\ &= \sum_{n=1}^{N_p} -e\left(\Phi_X(\vec{r}^{\,n}_{e^-,f}) - \Phi_X^n(\vec{r}^{\,n}_{e^-,i})\right) + e\left(\Phi_X^n(\vec{r}^{\,n}_{h^+,f}) - \Phi_X(\vec{r}^{\,n}_{h^+,i})\right) \end{aligned} \tag{4.14}$$

where exponent n expresses the association with the carrier of the n-th pair. When considering the drifting of a single electron-hole pair, the initial position is the same for both charges with:

$$\forall n, \quad \Phi_X(\vec{r}^{\,n}_{e^-,i}) = \Phi_X(\vec{r}^{\,n}_{h,i}) \tag{4.15}$$

The charge induced by the drifting of N_p electron-hole pairs is simplified to:

$$Q_X = e\sum_{n=1}^{N_p}\left(\Phi_X(\vec{r}^{\,n}_{e,f}) - \Phi_X(\vec{r}^{\,n}_{h,f})\right) \tag{4.16}$$

An important remark is that the induced signal solely depends on the weighted potential of the

final position of the charges. As mentioned in the previous section, the charge trapping process induces a loss in signal. Indeed, they prevent the drifting charge from reaching an electrode where its contribution to the induced charge is maximal.

The total weighting potential (TWP) field is defined as the sum of the weighting potentials associated with all the N electrodes X_k composing the ionization channel:

$$Q_T(\vec{r}) = \sum_{k}^{N} Q_{X_k}(\vec{r}) \tag{4.17}$$

If the electrodes of the detector form a perfect Faraday cage, all the field lines end on the electrodes and none is leaving the crystal. As a result, when considering a unique charge q in the crystal, the total weighted potential Q_T is equal to the charge at any moment of the drift, $Q_T = q$. When considering N_p electron-holes pairs, the Faraday cage imposes the charge conservation on the total weighting potential such that $Q_T = 0$.

In section 4.2.4, we further the discussion on the weighting potentials using the electrostatic simulation of the PL38 and FID38 detector designs as illustration. Also, the Shockley-Ramo theorem is used to model the signal generation for these detectors.

4.1.7 Luke-Neganov Effect

The Luke-Neganov effect has major impacts on the heat channel and the efficiency of the discrimination provided by the combination of the heat and ionization channels. While this effect depends on the electric field applied by the electrodes, it has no influence on the charge collection or the signal generation on the electrodes of the detectors.

When electric charges drift under the influence of the applied electric field $\vec{E}$ in the germanium crystal, they create phonons. This process is called the Luke-Neganov effect. This phenomenon happening in semiconductors is analogous to the well-known Joule Effect present in conductors. The phonons created draw their energies from the work W of the electric field $\vec{E}$ on the drifting charge q such that:

$$W = q \int_{\vec{r}_{q,i}}^{\vec{r}_{q,f}} \vec{E}\, \mathrm{d}\vec{r}_q = q \int_{\vec{r}_{q,i}}^{\vec{r}_{q,f}} \frac{\partial V}{\partial \vec{r}} d\vec{r} = q\left(V(\vec{r}_{q,f}) - V(\vec{r}_{q,i})\right) \tag{4.18}$$

In the case of a recoil producing N_p electron-hole pairs, the work provided by the electric field going into the phonon bath and eventually the heat channel is defined as the Luke-Neganov energy E_{NL}, also known as the Luke-Neganov boost as it is added to the initial heat energy of the recoil. It is expressed as:

$$E_{NL} = e\sum_{n}^{N_p}\left(V(\vec{r}^{\,n}_{h^+,f}) - V(\vec{r}^{\,n}_{q,i})\right) + (-e)\sum_{n}^{N_p}\left(V(\vec{r}^{\,n}_{e^-,f}) - V(\vec{r}^{\,n}_{e^-,i})\right) \tag{4.19}$$

Similarly to the application of the Shockley-Ramo theorem to a recoil, the electron and the hole of a same pair have the same initial position such that $V(\vec{r}^{\,n}_{q,i}) = V(\vec{r}^{\,n}_{e^-,i})$. As such, the expression of the Luke-Neganov energy simplifies to:

$$E_{NL} = e\sum_{i=0}^{N_p}\left(V(\vec{r}^{\,n}_{h^+,f}) - V(\vec{r}^{\,n}_{e^-,f})\right) \tag{4.20}$$

It appears that E_{NL} depends solely on the electric potential V in the crystal at the final positions of the electron $\vec{r}^{\,n}_{e^-,f}$ and the hole $\vec{r}^{\,n}_{h^+,f}$.

A useful, and mostly accurate, assumption is to consider the complete charge collection: all the charges end their drift by reaching the electrodes polarized at potentials V_+ and V_-. The Luke-Neganov boost is further simplified to:

$$E_{NL} = N_p e(V_+ - V_-) = N_p e\Delta V \tag{4.21}$$

The Luke-Neganov effect is proportional to the number of pairs N_p created in the ionization process and the voltage bias ΔV of the detector. Using the equation 4.6, we can express the boost as a function of the recoil energy E_R and the quenching factor Q:

$$E_{Luke-Neganov} = \frac{E_{Ion.}}{\epsilon_{e^- - h^+}} e\Delta V = Q\frac{E_R}{\epsilon_{e^- - h^+}} e\Delta V \tag{4.22}$$

Although they deposit the same recoil energy E_R, an electronic recoil benefits more than a nuclear recoil from the Luke-Neganov boost according to the hierarchy of their quenching factor $Q_{ER} > Q_{NR}$. A useful simplification is to consider that $e/\epsilon_{e^- - h^+} = 1/2.97\ \mathrm{V}^{-1}$, and to have a final expression of the Luke-Neganov boost as:

$$E_{NL} = QE_R\frac{\Delta V}{2.97} \tag{4.23}$$

It is essential to take into account the Luke-Neganov energy when reconstructing the recoil energy E_R from the measured heat energy E_{heat} given that:

$$E_{heat} = E_R + E_{NL} = E_R\left(1 + Q\frac{\Delta V}{2.97}\right) \tag{4.24}$$

The Luke-Neganov effect is a very interesting strategy to enhance the sensitivity of the heat channel. However, this heat channel boost is applied at the expanse of the discrimination ability of the detectors thanks to the double heat-ionization energy measurement. When operating the detector with voltages higher than $\sim 10\,\mathrm{V}$, the Luke-Neganov boost dominates in the expression of the measured heat energy E_{heat}:

$$\Delta V \gg \frac{2.97}{Q} \quad \Rightarrow \quad E_{heat} \approx E_{NL} \propto E_{Ion.} \tag{4.25}$$

The heat energy becomes equals to the ionization energy ignoring the multiplicative factor. As such, it becomes impossible to distinguish discriminate the electronic recoils from the nuclear recoils as their signature in the same. In fact, this observation can be further at any voltage bias: the existence of the Luke-Neganov effect diminishes the discrimination power of the ER and NR events. As this feature is essential for the correct operation of the detector and to reach their scientific goals, the Luke-Neganov effect should be kept minimal by aiming at low voltage bias in the detector design (*e.g.* $\Delta V \sim 8\,\mathrm{V}$ for FID800 detectors of EDELWEISS-III).

4.1.8 Polarization and Readout Electronics of the Ionization Channel

The electronics associated with the ionization channel has two functions: the signal readout and the polarization of the electrodes. As usual, the electronics are separated in two stages: the cold electronic inside the cryostat, before any signal amplification, and the hot electronics outside of the cryostat transferring the amplified signal. This section focuses on the cold electronics which has major influence on the resolution of the ionization channel and the operation of the ionization channel. The readout and the polarization of all the electrodes of a detector are driven by a single computer. However, we can consider that each electrode is equipped with an independent cold electronic line.

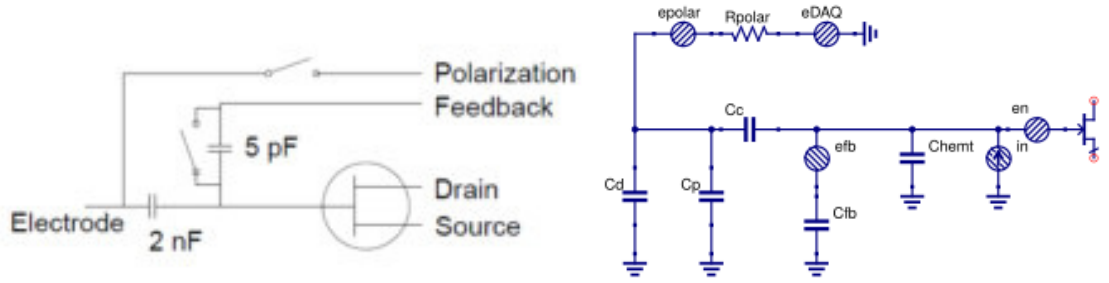

Figure 4.5: Scheme of a cold electronics line for the ionization channel currently used at IP2I (left) and in development with HEMT technology (right). The electronics line assures the polarization of the electrode and the signal readout. One of the main difference is the floating state of the current electronic (heaviside signal) versus the polarization resistance of the HEMT (decaying exponential signal).

Figure 4.5 shows two electric circuits of the electronic line of a single electrode of a detector. The circuit on the left represents the current electronics of the IP2I cryostat used to realize all the ionization measurements presented in this work. It uses Junction Field Effect Transistor (JFET). On the right is a representation of a High Electron Mobility Transistor (HEMT) based electronics in development for building the RICOCHET experiment [35] and enhancing the performance of the EDELWEISS experiment.

The readout of the JFET-based and HEMT-based electronics lines measure the same physical quantity: the electric potential of the electrode. The JFET and HEMT are used to readout and amplify the voltage signal. This method can differ from other experiments equipped for reading the current induced by the drifting charge on a feedback capacitance with a charge amplifier. Compared to a charge amplifier, a voltage amplifier does not involve any resistor in the amplification scheme, resulting a lower electronic noise. However, the use of a voltage amplifier is only possible with low leakage current lower than 0.1 fA. One should note that the amplifying transistor situated at the end of the electronic line is separated from the electrode, represented by the capacitance C_d, by a coupling capacitor of higher value $C_c \sim \mathcal{O}(1\,\text{nF})$. The role of this decoupling capacitance C_d is to isolate the transistor gate from the bias voltage applied on the electrodes of the detector.

The electronics lines are designed to assure their functions while keeping the electronics noise as low as possible. Once the signal is amplified, it is transmitted to the acquisition computer through the hot electronics without adding additional noise.

There are several differences between the current JFET-based and the future HEMT-based electronics. The main change concerns the technology of the voltage amplifier. The JFET are operated at a low temperature of 100 K inside the cryostat. At the time of design for the EDW-III experiment, this technology offered the best performances. Nowadays, recent breakthrough in the electronics field adapts the HEMT technology to the constraints of the EDELWEISS and RICOCHET experiments. With a HEMT operating at the lower cryogenic temperature of 1 K, the thermal noise of the electronic components is reduced leading to an overall reduced noise injection in the amplification scheme.

The other main differences resides in the polarization of the electrodes. The polarization is the process of fixing the electric potential of an electrode. In the current JFET-based electronics, this process is assured by a mechanical relay (represented by the polarization switch on the figure 4.5) linking the electrode to a constant voltage source. By switching on, the electrode, acting as the plate of a capacitor, is accumulating charges and eventually reaches the aimed potential. By switching off, the electrode keeps the accumulating charge and its now at fixed electric potential. Due to the relay opening the circuit, the constant voltage source cannot induce any

electronic noise on the electrode. The downside of this method is the progressive neutralization of the polarization as the electrode collects charges. Moreover, in the case of the RICOCHET experiment with surface operation of the bolometers, the event rate is high leading to a faster discharge. The counter is to periodically switching on and off the relay in order to re-establish the wanted potential on the electrode. This procedure is called "maintenance". In reality, a maintenance lasts one minute and consists in multiples relay switches and relay changeovers. During this one minute of maintenance, the detector is not available for data taking. This is enforced by the "maintenance cut" described in section 6.2.5. The frequency of maintenance is adapted to the condition of operation of the detector: too much maintenance induces unnecessary dead time while too few leads to a lower and uncontrolled voltage bias. For above ground operation at IP2I, the usual maintenance period is of about 30 minutes and should be empirically adjusted to the detector and the event rate. For the HEMT-based electronics, the polarization is continuously assured by a constant voltage source $eDAQ$ in series with a resistor of high impedance $R_{Polar.} = 10^{10}\,\Omega$. While this method induced supplementary electronic noise, there is no more dead time and the maintenance procedure is not needed.

The ionization channel readout is sampled at an initial frequency of 100 kHz. This means the period of the measurement points is 10 µs which is still greater than the estimated time span of an ionization signal of a few µs. As a result, an ionization signal is recorded as an Heaviside function. No information can be obtained on the shape of the signal. The high readout sampling was historically chosen in EDELWEISS for the purpose of synchronizing an external detector vetoing incoming muons with a good timing resolution. The highly sampled ionization signal is then averaged in order to produce a signal of sampling frequency f_s. This sampling frequency is a parameter of the acquisition and can be set in the range $[200, 1000]$ Hz. This lower sampling records the information contained in the Heaviside-shaped ionization signal (its amplitude mainly) while being lightweight in term of disk space, which is essential considering the recording and processing resources at our disposal. The saved ionization signal of sampling frequency f_s is composed of points whose values are averages of $100\,\text{kHz}/f_s$ points. In the end, the saved signal of an event of sampling frequency f_s is therefore Heaviside-like function $H(t)$ with a varying value $H(t = 0)$.

The ionization signal is readout as a digital signal which can take, by definition, a limited number of values. This readout range contains 64000 values which are sorted on the so-called readout dynamic range $[-32000, +32000]$ expressed in Analog-to-Digital Unit (ADU). For the ionization channel, the correspondence between ADU and Volt is 67.4 nV/ADU. As such, the dynamic range can records perturbation with a maximum amplitude of 2.156 V. As a reference, the sensitivity of the ionization channel is about $60\,\text{ADU/keV} \approx 4\,\mu\text{V} \cdot \text{keV}^{-1}$. A high event rate of low energy events or single high energy events can rapidly make the data stream fall out of this dynamic range, effectively saturating the acquisition electronics. As to avoid this phenomenon and correct it, both electronics circuits feature a feedback line. A procedure called "reset" consists in linking the input of the amplifying transistor to a null potential as to recenter the recorded signal on 0 ADU. The linking is assured in the feedback line with mechanical relays. Each reset induces an artifact signal on both the heat and ionization channels. While it can be easily discriminate from real events due to its shape, these artifact signals are discarded by applying the reset cut during the data analysis presented in the section 6.2.5. As such, reset procedures creates dead times during which the detector is not available for data acquisition. Similarly to the maintenance period, the period of the reset is empirically adjusted to reach a balance between dead time and dynamic range saturation. The period of the resets is of a few seconds. In the case of surfaces operation at IP2I, the event rate is high and lot of charges are accumulated which needs for a shorter period before reset than an underground operation.

4.1.9 Objective of the Electrodes Study

Three chapters of this work are dedicated to the study of the ionization channel and the electrodes design: this chapter 4 introducing the theory and the electrostatic simulation of the ionization channel, chapter 5 scanning over the parameters of the electrostatics simulation, and the chapter 6 comparing the electrostatics simulation to experimental results.

The main objective of these studies is to propose an electrode design for 38 g germanium crystals with optimal performances of the ionization channel. The performances of the ionization channel depends on several aspects: the energy resolution, the effective volume and the charge collection. As such, the study aims at drawing relation between the electrodes design and these aspects.

The energy resolution is roughly a signal-to-noise ratio. There is two ways to lower the energy resolution: increase the sensitivity to the signal or reducing the noise affecting the measure. The sensitivity of the ionization channel is described in a simplistic manner with the equation 4.1. The voltage signal is inversely proportional to the capacitance of the electrodes. The modelization of the ionization channel is furthered in the later section 4.2 with a more accurate theorization of the signal generation, yet pointing towards a similar relation between sensitivity and electrode capacitance. As a starting point, we can model a simple and naive ionization channel as a parallel plate capacitor whose dielectric is the cylindrical germanium crystal. The associated capacitance without edge effects is:

$$C = \epsilon_0 \epsilon_r(Ge) \frac{A}{d} = 8.854 \times 10^{-12} \times 16.3 \times \frac{\pi(15 \times 10^{-3})^2}{10 \times 10^{-3}} = 10.20\,\text{pF} \tag{4.26}$$

with ϵ_0 the electric constant and $\epsilon_r(Ge)$ the relative permittivity of the germanium. The area A of the circular electrodes is imposed by the geometry of the germanium crystal of height $d = 10\,\text{mm}$ and radius 15 mm. This capacitance of 10 pF yielded by this naive modelization is set as the objective for the electrode design. Regarding the noise affecting the ionization channel, it is for the moment dominated by the voltage and current noise induced by the JFET-based electronics. The intrinsic noise associated with the polarization process is negligible. As such, efforts are made to model the lower noise of the future HEMT-based electronics and optimizing the design of the ionization channel to reduce it further. With some early calculations, and considering the objective of 10 pF capacitance, an objective of 20 eV is set for the energy resolution of the ionization channel.

The effective volume refers to the volume fraction of the germanium crystal in which the ionization energy of events is well reconstructed. This notion is developed later as the fiducial volume. Having a high fiducial fraction close to 100 % ensures that the whole volume acts as a valid target for the particle interaction. As such the exposure of the detector is maximized and more statistics is collected. That is crucial to estimate the scientific goals and the time scale of the RICOCHET and EDELWEISS experiments.

The good charge collection is a broad concept that aims at having a predictable and reliable signal generation by the drifting charges. Collection problems such as charge trapping can induced abnormal signatures increasing the noise in the energy reconstruction or, worse, emulating an inexistent dark matter or CENNS event.

Lastly, this work is part of the research and development of detectors for two experiments. Event though their scientific goals are similar, the operating conditions are different, resulting in different constraints on the detector design. A major difference affecting the electrode design is the high event rate associated with the above ground operation for the RICOCHET experiment compared to the low radioactive background of the underground EDELWEISS experiment.

4.2 Electrostatic Simulation of the Ionization Channel

In this section, the detector designs PL38 and FID38 are simulated using the Finite Element Method software COMSOL® Multiphysics [32]. The modelization of the ionization channel is illustrated with these electrostatics simulation. In particular, the relation between the electrode designs of PL38 and FID38 and their respective sensitivities and electronic noise is thoroughly theorized.

4.2.1 Finite Element Method Applied to Electrostatics

The software COMSOL® Multiphysics aims at simulating physics system based on the finite element method. The finite element method (FEM) is the most widely used method for solving problems of engineering in fields such as structural analysis, heat transfer, fluid flow, mass transport, and increasingly more. The domain which is of interest for this work is the resolution of electrostatics equations. In particular, the simulations of the PL38 and FID38 necessitate the extension "AC/DC" of COMSOL® Multiphysics offering advanced features for the electromagnetic and electronic systems. A cryogenic germanium detector represents a complex electrostatic system whose associated equations do not present easily accessible analytical solutions. The use of an FEM software is motivated by its ability to accurately represent a physical system with a complex geometry. It can takes into account multiples materials with each their own physical properties. The total solution can be easily represented with access to both global properties of the system and local effects. Additionally, such a software offers a readily operational framework for the geometry building, the mesh optimization and the equation resolution. With a relatively short learning period, this permitted to invest an extended period of time to the analysis of the results yielded by the simulation.

The FEM is a particular numerical method for solving the partial differential equations associated with a system in two or three space dimensions. To solve a problem, the FEM subdivides the large system into smaller, simpler parts which are called finite elements. This space discretization is implemented by constructing a mesh of the object with a finite number of nodes, also called vertices. Multiples neighbors vertices forms a finite element. There are multiples geometries possible for a finite element. In this work, the meshes are combinations of lines, triangles and tetrahedrons. For the simulation of the PL38 and FID38 designs, the mesh parametrization is discussed and illustrated in the next section 4.2.2.

Each finite element of the mesh is associated with a set of element equations. The element equations are simple equations that locally approximate the original complex equations of the larger whole system. In this work, these are the electrostatics equations satisfied by the electric potential field V. They are defined by the relation between electric potential and electric field $\vec{E}$:

$$\vec{E} = -\vec{\nabla} V \tag{4.27}$$

and the Gauss law:

$$\vec{\nabla} \cdot \left(\epsilon_0 \epsilon_r \vec{E} \right) = \rho_f \tag{4.28}$$

where ρ_f is the volume density of free charge. The boundary conditions are first set by the interface condition:

$$\vec{n} \cdot \vec{E} = 0 \tag{4.29}$$

with $\vec{n}$ the normal vector at boundaries between materials. Then comes the electric potential fixed by the ground GND and the electrodes X_n:

$$\begin{cases} \forall \vec{r} \in \Sigma(GND) : & V(\vec{r}) = 0 \\ \forall n, \forall \vec{r} \in \Sigma(X_n) : & V(\vec{r}) = V_{X_n} \end{cases} \tag{4.30}$$

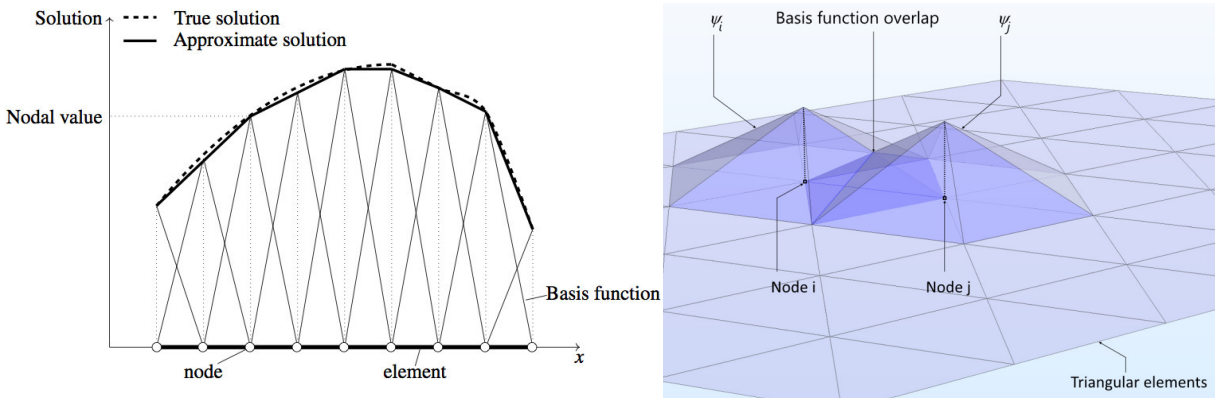

Figure 4.6: Illustration of the Finite Elements methods for a 1-Dimensional problem (on the left) and a 2-Dimensional problem (on the right). The true solution of the global equations of the system is approximated locally by linear functions on the finite elements. Each linear function is derived from basis functions Ψ associated with each node. Left image taken from [50], right image adapted from [32].

where V_{X_n} is the fixed electric potential of the n-th electrode of the detector and Σ designates a surface.

All these equations constitute a steady state problem, independent of the time, in which the original partial differential equations are approximated with a set of polynomial equations. The system is solved by a true solution function, here the electric potential field V which is unknown. As such, this unknown true solution is approximated by the numeric solution V_h. This numeric solution is usually a piecewise function assembling linear approximation over all the finite element. The figure 4.6 illustrates the approximation of a true solution by an approximate numeric solution V_h. On the left, a 1-Dimensional problem is solved. The numeric solution is a linear combinations of basis functions Ψ_i such that

$$V_h(\vec{r}) = \sum_i V_i \cdot \Psi_i(\vec{r}) \tag{4.31}$$

where V_i are the weights. The basis function Ψ_i corresponds to a unitary triangular function centered on the position x_i of the i-th node. The result of the approximation is that all the partial differential terms are easily calculated. This choice of approximation applied to the equation 4.27 on the i-th node of the 1-D problem yields:

$$\vec{E}(x_i) \approx \frac{-1}{2}\left[\nabla\left(V_h\right)|_{x_i^-} + \nabla\left(V_h\right)|_{x_i^+}\right] = \frac{-1}{2}\left[\frac{V_i - V_{i-1}}{x_i - x_{i-1}} + \frac{V_{i+1} - V_i}{x_{i+1} - x_i}\right] \tag{4.32}$$

The right panel of figure 4.6 illustrates the generalization of this approximation at higher dimensions. Here, the problem is 2-Dimensional with finite elements being triangular with adapted basis function Ψ_i.

In the end, the approximate numeric solution $V_h \approx V$ is obtained through numerical linear algebra methods coupled with variational methods minimizing an error function over the whole mesh.

4.2.2 Mesh Parametrization

A cryogenic germanium bolometer equipped with an ionization channel is a 3-Dimensional electrostatics problem. The most straightforward way of building its associated geometry is to reproduce the detector in 3D inside the FEM software. A cylindrical coordinates system centered

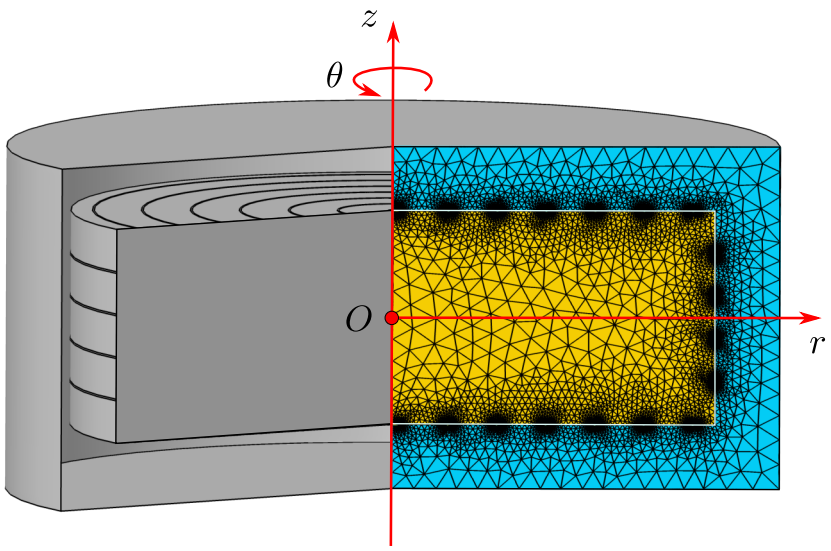

Figure 4.7: Illustration of the 2D-axisymmetric geometry used to simulate the FID38 design. A section of the detector is shown. The equations are solved on a slice of the detector considering the cylindrical symmetry such that $V(r,\theta,z) = V(r,z)$. The coordinates origin $O(r = 0, z = 0)$ corresponds to the center of the cylindrical crystal. The mesh is automatically constructed with the "Physics-based" mesh scale of "Fine".

on an origin O is adapted for this system with the three spatial parameters: r the radius, θ the angle and z the height. The figure 4.7 displays a cut 3D view of the FID38 design with the cylindrical coordinates system drawn in red.

Although this 3D geometry is valid and yields correct numeric solutions, it is not efficient. Indeed, this 3D geometry does not benefit from the intrinsic cylindrical geometry of the electric potential field V in the resolution $V(r,\theta,z) = V(r,z)$. Instead, the 3D geometry generates a mesh in the entire volume of the detector with a high number of nodes and a lengthy numeric resolution of the electrostatics equations.

An alternative approach is to consider a resolution on a radial slice of the detector with built-in cylindrical symmetry. Inside the FEM software, the geometry is built with the 2D-axisymmetry. The figure 4.7 displays this radial section. The equations are now solved over a 2D mesh also yielding the correct numeric solution. A major advantages of the 2D-axisymmetry over the 3D geometry is the much lower number of vertices composing the mesh. This translates into significantly shorter resolution times. The amount of scanning studies presented in the next chapter 5 is a direct results of this gain in time. The main drawback to the use of the 2D-axisymmetry is by definition the need to have a system respecting the cylindrical symmetry. In this work, several characteristics of the detector were ignored in the electrostatics simulation due to not respecting the symmetry: the Teflon clamps holding the crystal, the NTD thermal sensor and the aluminium wire-bridges between the aluminium deposits. Their influence on the whole system is considered negligible. In order to study the local effects of these non-symmetric features, the 3D geometry should be used.

When solving a problem with the finite element method, the choice of the meshing is essential. Due to the FEM approximating the analytical solution with a numerical approach over the vertices of the mesh, the meshing should be well constructed to assure a precise estimation. For a given physic system, the analytical solution can be more precisely approximated as the number of vertices is increased. However, a high number of vertices induces an equal number of local numerical solving. The COMSOL® software offers an automatic optimization of the meshing which adapts the size of meshing to the geometry of the system. Such an optimized mesh

Mesh Scale	Planar38			FID38		
	# Triangles	Capacitance [pF]	Relative Error [%]	# Triangles	Capacitance [pF]	Relative Error [%]
Extremely Fine	37837	14.923	0	106028	19.217	0
Extra Fine	11721	14.923	0	41991	19.223	0.03
Finer	6306	14.923	0	29996	19.222	0.02
Fine	4368	14.923	0	22504	19.232	0.08
Normal	4258	14.923	0	22340	19.232	0.08
Coarse	2472	14.924	0.01	15288	19.263	0.24
Coarser	1303	14.934	0.07	7596	19.475	1.34
Extra Coarse	1260	14.964	0.27	7915	19.693	2.47
Extremely Coarse	1937	15.037	0.76	19714	19.625	2.12

Table 4.1: Scanning the mesh scale of the simulated PL38 and FID38 design. The control values are the number of triangles forming mesh, the first diagonal term of the Maxwell capacitance matrix and the relative error on the capacitance calculation with the "Extremely Fine" scale chosen as reference.

is presented on the figure 4.7. There are a lot of vertices near small geometric features such as in vicinity of the aluminium rings of the electrodes at the surface of the Ge crystal. This assures that a rapidly varying electric field is correctly mapped. At the same time, there are only few vertices at location where the electric field is almost uniform as in the bulk of the crystal.

This optimization of the meshing is possible with the “Physics-based” option of COMSOL® which automatizes the meshing process taking as single parameter the mesh scale. Simulation of the reference designs PL38 and FID38 were ran with different mesh scales and the results are presented in table 4.1. There are nine mesh scales proposed by COMSOL®, starting from the "Extremely Coarse" scale with a low number of simplex, a low accuracy and very quick run time, and continuing with increasingly refined scale to the "Normal" scale, which should result in a trade-off between simulation time and precision, eventually reaching the "Extremely Fine" scale with a very high precision obtained after a long calculation time.

As expected, the more refined the scale is and the more triangles are used for the simulation (except for Extremely Coarse, maybe a non-optimized meshing algorithm is in use). As the FID38 design has more electrodes of small size than the simpler PL38 design, the mesh is generated with more simplex. It is consistent with the fact that the simulation of the PL38 design runs quicker than for the FID38. In order to estimate the accuracy of the simulation scanning over the different scales, a capacitance value corresponding to the first diagonal term of the Maxwell capacitance matrix (see next section 4.2.6) is evaluated as control quantity. Additionally, a percentage of the relative error on the capacitance calculation is given. The capacitance of the "Extremely Fine" scale is chosen to be the reference for this relative error. By definition, the relative error of the "Extremely Fine" is zero. Table 4.1 shows that as the scale is more refined, the capacitance is getting closer to the reference capacitance. In the case of the PL38, the relative error starts at 0.78 % and eventually reaches zero for the "Normal" scale. Concerning the FID38 design, the relative error is greater for all scales compared to the PL38. This may be due to the more complex geometry. Although the error is superior to 1 % for the less refined scales, from the "Normal" scales the error is inferior to 0.1 %. Considering that the "Normal" and "Fine" scale possess a similar number of simplex and resolution time, the simulation presented in this work are run with the "Fine" scale. The capacitance calculation are affected by a relative error of about 0.1 %.

4.2.3 Geometry and Physics of the PL38 and FID38 Simulation

This section is dedicated to building the geometry and defining the electrodes of the PL38 and FID38 design simulations. The description of these detector designs is illustrated with the annotated schemes 4.8 for the PL38 and 4.9 for the FID38. These scheme are used as reference for

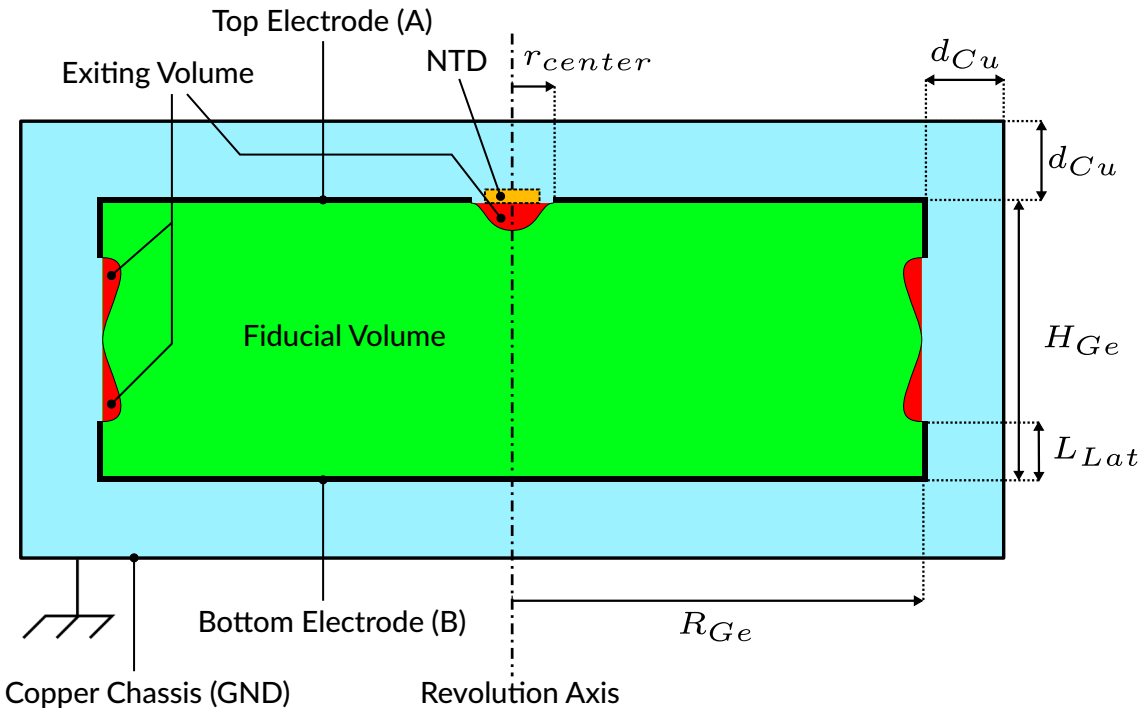

Figure 4.8: Cross-section scheme of the PL38 detector design. The scheme is not to scale and the dimensions and parameters of this design are listed in the table 4.2. The copper chassis is represented by the electrically grounded rectangle. It is separated from the germanium crystal by the vacuum colored light-blue. The two aluminium electrodes are represented in black at the surface of the crystal. The default polarization of PL38 is $(V_A, V_B) = (+1, -1)$ V. The colored volumes inside the crystal are drawn from electric field lines with common start and end points.

building the geometry in the FEM software. The schemes are not entirely at scale and are thus accompanied with the lists of the parameter values 4.2 and 4.3 for the PL38 and FID38 designs respectively.

The two PL38 and FID38 detector designs use cylindrical germanium crystals of height $H_{Ge} = 10$ mm and radius $R_{Ge} = 15$ mm as absorber. The mass of these crystals are about 38 g hence the name of the designs as to differentiate them from more massive 200 g and 800 g EDELWEISS detectors. Each crystal is surrounded by an hollow cylindrical chassis which is electrically grounded to 0 V. This copper chassis is spaced from the crystal by a distance $d_{Cu} = 3$ mm of vacuum. The vacuum is simulated with a relative electric permittivity of $\epsilon_r(\text{Vacuum}) = 1$ and the germanium crystal possesses a much higher value of $\epsilon_r(\text{Ge}) = 16.3$. Although present in real detectors to maintain the crystal, Teflon clamps are not simulated. Indeed, their influences is considered negligible due to their small size and low permittivity $\epsilon_r(\text{Teflon}) = 2.1$. Similarly, the real detectors inspired by the PL38 and FID38 design should possess NTD thermal sensors but these thermistances are not simulated. Their predicted gluing locations are annotated on the scheme. These locations are chosen as to reduce the contact of the NTD with the aluminium electrode. For the PL38 design, the NTD is located in the central hole of the top electrode in contact with the bare germanium surface. For the FID38 design, the NTD should be glued on top of a veto electrode ring. As such, a majority of the NTD surface should be in contact with the bare germanium surface while perturbing the electric field very locally in the top veto volume. The main difference between the two detector designs concern the number and shape of aluminium electrodes. The PL38 design holds its name from the two full planar electrodes while the FID38 design features four fully inter-digitized electrodes. The simpler PL38 design is presented first

Parameter	Symbol	Default Value
Ge crystal Height	H_{Ge}	10 mm
Ge crystal Radius	R_{Ge}	15 mm
Distance between crystal and copper chassis	d_{Cu}	3 mm
Electrode Thickness	h_{Al}	1 µm
Radius of the central NTD hole	r_{center}	1.5 mm
Corner length	L_{lat}	2 mm
Main Voltage Bias	V_{bias}	2 V
Symmetric factor of the voltage bias	S_{bias}	0.5

Table 4.2: List and Value of the default parameters for the PL38 design.

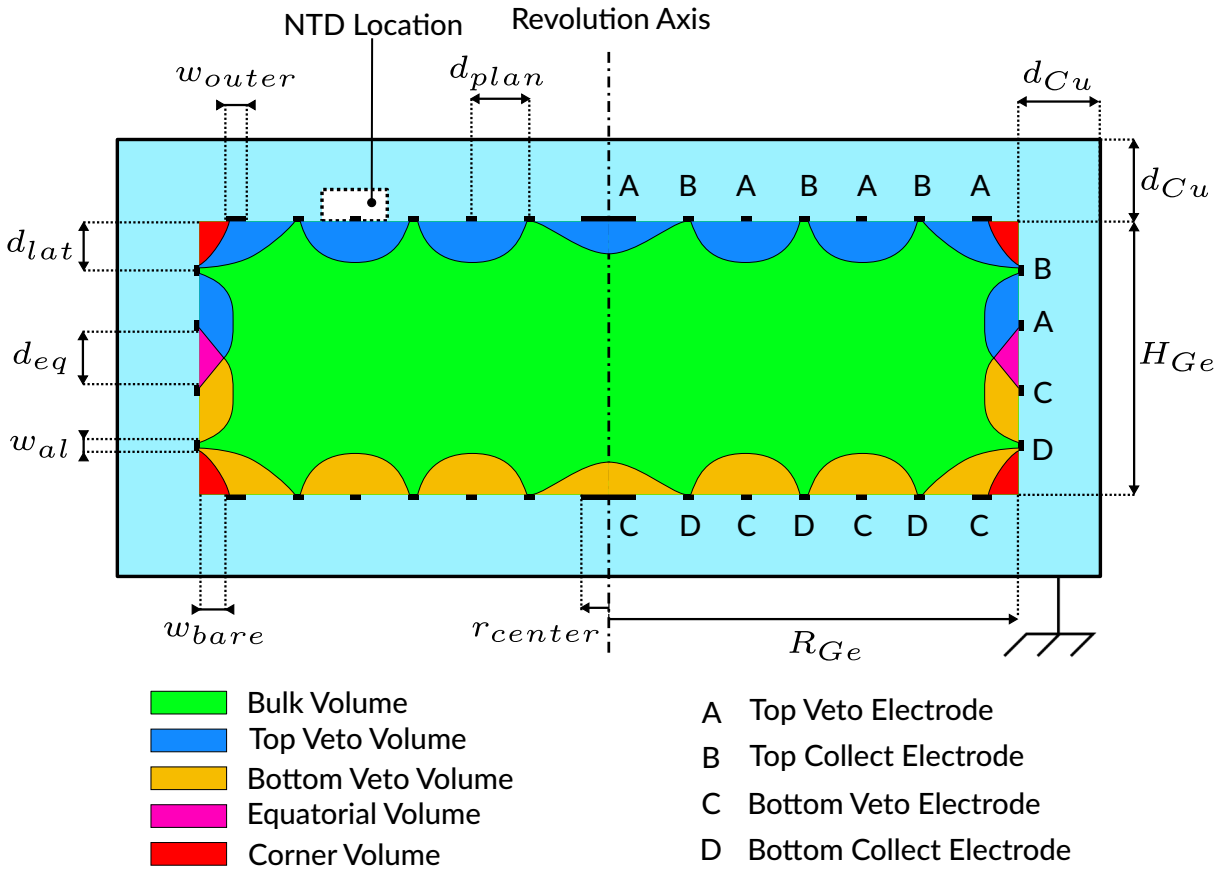

Figure 4.9: Cross-section scheme of the FID38 detector design. The scheme is not to scale and the dimensions and parameters of this design are listed in the table 4.3. The copper chassis is represented by the electrically grounded rectangle. It is separated from the germanium crystal by the vacuum colored light-blue. The aluminium pads and rings are represented in black at the surface of the crystal and labeled according to their electrode of attribution. The default polarization of FID38 is $(V_A, V_B, V_C, V_D) = (-0.25, +1, +0.25, -1)$ V. The colored volumes inside the crystal are drawn from electric field lines with common start and end points.

Parameter	Symbol	Default Value
Ge crystal Height	H_{Ge}	10 mm
Ge crystal Radius	R_{Ge}	15 mm
Distance between crystal and copper chassis	d_{Cu}	3 mm
Electrode Thickness	h_{Al}	1 µm
Electrode Width	w_{Al}	80 µm
Radius of the innermost planar electrode	r_{center}	0.25 mm
Width of bare Ge crystal on corners	w_{bare}	0.3 mm
Width of the outermost veto electrode	w_{outer}	0.08 mm
Number of planar electrodes	n_{plan}	7
Number of lateral electrodes	n_{lat}	2
Interdistance of Planar electrodes	d_{plan}	1.98 mm
Interdistance of Lateral electrodes	d_{lat}	2.40 mm
Equatorial distance	d_{eq}	2 mm
Main Voltage Bias	V_{bias}	2 V
Ratio Veto/Main voltage bias	R_{veto}	−0.25
Symmetric factor of the voltage bias	S_{bias}	0.5

Table 4.3: List and Value of the default parameters for the FID38 design.

followed by the description of the more complex FID38 design.

The ionization channel of the PL38 detector design consists in two collecting electrodes readily visible of the scheme 4.8. Each electrode is denominated by its location on the top or bottom surface but for more clarification we can define the following convention for the electrode denomination and indexes in this work:

$$\{\text{Top}, \text{Bottom}\} \Leftrightarrow \{A, B\} \Leftrightarrow \{1, 2\} \tag{4.33}$$

Each electrode is basically a continuous aluminium deposit on the full surface with some extension on the lateral surface. The extension length on the lateral surface is noted L_{lat} with a default value of 2 mm. While the bottom electrode B covers the full bottom surface of the crystal, the top electrode A features a central hole. This hole is meant to provide the NTD thermal sensor with a bare germanium as to increases the fraction of athermal phonons. The hole is circular of radius r_{center}. Its default value of 1.5 mm is meant to host a NTD of small standard area (2×2) mm.

The design FID38 has a more complex ionization channel composed of four electrodes labeled A through D. The denomination of these electrodes in this work follows the convention:

$$\{\text{Top Veto}, \text{Top Collect}, \text{Bottom Veto}, \text{Bottom Collect}\} \Leftrightarrow \{A, B, C, D\} \Leftrightarrow \{1, 2, 3, 4\} \tag{4.34}$$

As displayed on the scheme 4.9, each electrode is an association of aluminium pads and rings. For real detectors, this association is made by linking the aluminum deposits with aluminium wires bridging over the germanium surface. Inside the electrostatic simulation software, multiple deposits can be assigned to the same electric terminal thus sharing their potential and charges. It is therefore possible to avoid the simulation of the wire-bonding bridges between the different aluminium deposits. These deposits consists in two pads and multiples rings whose shape depends on several parameters. The radius of the circular central pads on the top and bottom surfaces is noted r_{center} and is by default set to 0.25 mm. The width of the concentric aluminium rings is by default set to the minimal value of $w_{Al} = 80$ µm. The outermost planar rings are attributed a specific independent width w_{outer} with the same default value. The number of total separated deposits, pads and rings, is noted n_{plan} for the planar surface and n_{lat} for the lateral surfaces. The default configuration sets these numbers to $n_{plan} = 7$ and $n_{lat} = 2$. The radius

of the outermost ring is limited to the radius of the germanium crystal minus a band of width $r_{edge} = 0.3\,\text{mm}$. This comes from the limits of the aluminium deposition technique employed: it is not possible to have a thin aluminium electrode at less than 0.3 mm from the edge of the planar surface of the germanium crystal. The concentric aluminium rings are spaced evenly on the planar surfaces with a distance $d_{plan} = 2.40\,\text{mm}$ between their center. On the lateral surface, aluminium rings respect the mirror symmetry with the equator of the cylindrical germanium crystal. The two most centered lateral electrodes, deemed equatorial rings, are distant from each other by $d_{eq} = 2\,\text{mm}$. The remaining lateral electrodes are evenly separated by the lateral spacing of default value $d_{lat}^{lateral} = 1.98\,\text{mm}$ between the equatorial rings and the crystals corners. Now that the aluminium deposits are defined, they can be attributed to an electrode. The electrodes respect a top-bottom symmetry with A and B being the top electrode with C and D being their bottom counterpart. The electrodes B and D corresponds to the main collecting electrodes, also called collect electrodes. Their function is to record the signal induced by recoils located in the bulk of the crystal. The electrodes A and C corresponds to auxiliary veto electrodes, also called veto electrodes. Their function is to collect the electric charges produces near the surface of the absorber. This surface tagging ability is the motivation behind the FID-like detector designs. In order to create a usable veto volume on the surface, the equatorial rings, the outermost planar electrodes and the central pads are attributed to the veto electrodes A and C. The remaining rings are attributing in order to obtain a succession of collect and veto electrodes. This attribution process imposed constraints on the number of planar and lateral aluminium deposits. Indeed, the interleaving of collect and veto deposits necessitates n_{plan} to be an odd integer and n_{lat} to be even.

For the PL38 and FID38 designs, the polarization of the electrodes is controlled by several parameters. First is the voltage bias of the detector, noted V_{bias}, corresponding to the voltage between the two main collecting electrodes. For both design, its default value is 2 V. Then comes the bias symmetry factor S_{bias} representing the symmetry of the top and bottom electrodes potential with respect to the 0 V ground voltage. At the default value of 0.5, polarizations are considered symmetric with opposite-side electrodes having opposite electric potential. With this two parameters, the polarization of the PL38 design is expressed as:

$$\begin{cases} V_A = V_{bias} S_{bias} \\ V_B = -V_{bias}(1 - S_{bias}) \end{cases} \Rightarrow \text{with } S_{bias} = 0.5, \begin{cases} V_A = V_{bias}/2 \\ V_B = -V_{bias}/2 \end{cases} \tag{4.35}$$

The default polarization of the PL38 design corresponds to:

$$(V_A, V_B) = (+1, -1)\ \text{V} \tag{4.36}$$

As such, the top electrode A should collect the electrons of negative electric charge while the bottom electrode B collects the positively charged holes.

With two auxiliary veto electrodes, the FID38 necessitates an additional parameters to fix the polarization of its electrodes. The veto ratio factor noted R_{veto} is used to define the voltage difference between the main collecting and the auxiliary veto electrodes. Its default value for the FID 38 design is -0.25. The polarization of the FID38 design is therefore expressed as:

$$\begin{cases} V_A = V_{bias}\left(S_{bias} - \dfrac{(1 + R_{veto})}{2}\right) \\ V_B = V_{bias} S_{bias} \\ V_C = V_{bias}\left(S_{bias} + \dfrac{(-1 + R_{veto})}{2}\right) \\ V_D = -V_{bias}(1 - S_{bias}) \end{cases} \Rightarrow \text{with } S_{bias} = 0.5, \begin{cases} V_A = -R_{veto} \cdot V_{bias}/2 \\ V_B = V_{bias}/2 \\ V_C = R_{veto} \cdot V_{bias}/2 \\ V_D = -V_{bias}/2 \end{cases} \tag{4.37}$$

The default polarization of the FID38 design corresponds to:

$$(V_A, V_B, V_C, V_D) = (-0.25, +1, +0.25, -1)\ \mathrm{V} \tag{4.38}$$

The electric equations are solved only in the insulators domains corresponding to the germanium crystal and the surrounding vacuum inside the copper chassis. The aluminium electrodes are set to a fixed potential and thus their interior is excluded from the simulation.

4.2.4 Weighted Potential Study

The following discussion is the continuation of section 4.1.6 introducing the signal generation on the electrodes by drifting electric charges with the Shockley-Ramo theorem. It concluded with the equation 4.16 modeling the signal generated on the electrodes of the detector. This signal induced on the electrode X depends on its weighting potential Φ_X at final positions of the drifting carriers in the crystal $\vec{r}_{q,f}$. This section presents the study of the weighting potentials associated with the ionization channel of the PL38 and FID38 design (in their default configurations). Electrodes are denominated by the labels $X, Y \in \{A, B\}$ for the PL38 design or $X, Y \in \{A, B, C, D\}$ for the FID38 design.

For each successive electrode X, all the electrodes are grounded except for the electrode X which is fixed at the unitary potential:

$$\begin{cases} V_X = 1\,\mathrm{V} \\ \forall Y \neq X, V_Y = 0\,\mathrm{V} \end{cases} \tag{4.39}$$

The electric potential fields V, solutions to the resulting electrostatics equations, corresponds to the weighting potentials Φ_X. The total weighting potential Φ_T is calculated with the equation 4.17.

The figure 4.10 displays several graphics illustrating the weighting potentials of the PL38 design (in the left column) and the FID38 design (in the right column). In the top row, the graphics are the color maps of Φ_A for the PL38 and Φ_B for the FID38 design. The pattern drawn by the potentials are consistent with the geometry of the electrodes. In the middle row, the color maps of the total weighting potential Φ_T are plotted for both designs. The bottom row shows graphs presenting weighting potentials Φ_X as function of the height z on a single linear trajectory at a radius $r = 12.65\,\mathrm{mm}$ in the germanium crystal.

The graphics of the top and bottom rows show that the weighting potentials Φ_X are equals to one on their associated electrode X and are null on all others electrodes Y. These observations verify the generalization of the properties of the weighting potential of a single particle of equation 4.13 to a polarized electrode X of any shape. We can admit that for any electrode X its weighting potential Φ_X has the following properties:

$$\begin{cases} \Phi_X\left(\vec{r} \in \Sigma(X)\right) = 1 \\ \forall Y \neq X : \Phi_X\left(\vec{r} \in \Sigma(Y)\right) = 0 \end{cases} \tag{4.40}$$

where $\Sigma(X)$ is the surface of the electrode X.

The total weighting potential Φ_T of the PL38 design is almost uniform in the bulk of the crystal with an average value of $\langle \Phi_T \rangle = 0.98$ close to 1. As such, this detector acts as a very good Faraday cage. In the crystal, Φ_T is maximal near the electrodes and minimal with $\Phi_T = 0.94$ at the equator. This comes from the influence of the grounded chassis. Indeed, near the equator, a fraction $(1 - 0.94 = 0.06)$ of the signal is induced on the chassis. The total potential of very high value can be explained by the full planar electrodes of the PL38 design shielding the interior of

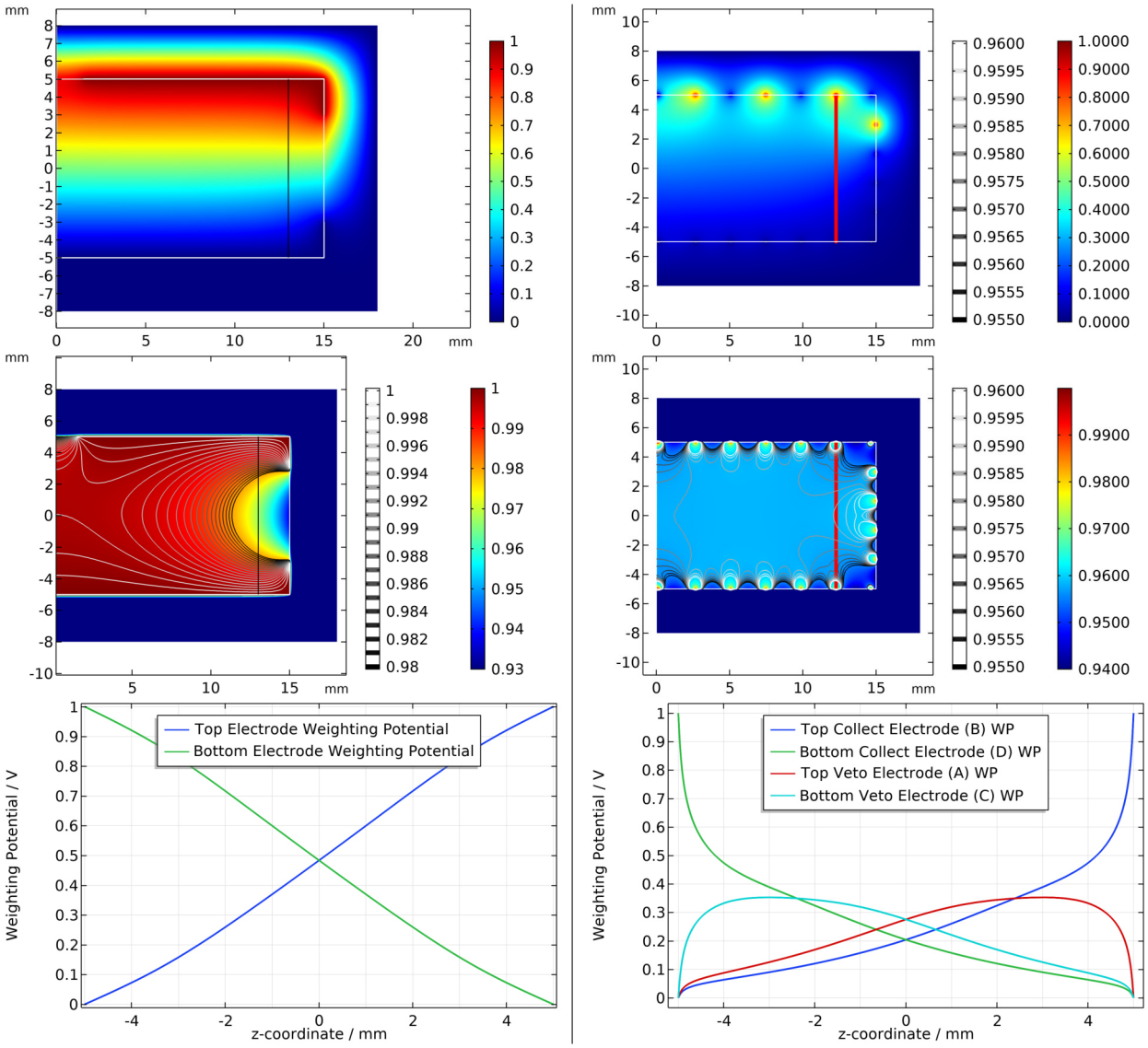

Figure 4.10: Graphics related to the weighting potentials for the default configuration of the PL38 design (in the left column) and the FID38 design (in the right column). The graphics in the top row represents the weighting potential associated with the top electrode A of PL38 design and the top collect electrode B of the FID38 design. The graphics of the middle row are color maps of the total weighting potential of the two designs. Grey contours are plotted to appreciate small variation in the bulk of the crystal. On the bottom row are plotted the weighting potential Φ_X as functions of the z-coordinates on vertical lines between the main collecting electrodes on the radius $r = 12.65\,\text{mm}$. These vertical lines are plotted in the previous color maps in black for the PL38 design and red for the FID38 design.

the crystal from the copper chassis. As as result, in the worst case scenario with charge carriers trapped near the equator, only 6 % of the induced charge are lost.

For the FID38 design, the total weighting potential is globally lower with an average value of $\langle \Phi_T \rangle = 0.95$. Similarly, it tends to 1 near the electrodes and fall in regions with higher influence of the copper chassis. These regions seems to be the bare germanium surfaces between the aluminium rings and in particular the corners of the crystal. The function of Faraday cage of the FID38 is still considered as excellent even if less efficient than the PL38 design.

With the calculation of the weighting potential Φ_X, it is now possible to predict the induced current signal from the final position of the charge carriers thanks to equation 4.16. These finals drift positions of the electrons and holes are estimated in the next section 4.2.5.

For now, we introduce the vector formalism used to model the ionization signal generation. All the induced electric charge Q_X and the electric potential V_X of the electrodes of a detector are gathered in two vectors: the induced charge vector $\vec{Q}$ and the voltage signal vector $\vec{V}$. With two electrodes A and B, these vectors are expressed for the PL38 design as:

$$\vec{Q}^{PL38} = \begin{bmatrix} Q_A \\ Q_B \end{bmatrix} \quad \text{and} \quad \vec{V}^{PL38} = \begin{bmatrix} V_A \\ V_B \end{bmatrix} \tag{4.41}$$

The FID38 possesses two main collecting electrodes B, D and two veto electrodes A, C. The charge and voltage vectors become:

$$\vec{Q}^{FID38} = \begin{bmatrix} Q_A \\ Q_B \\ Q_C \\ Q_D \end{bmatrix} \quad \text{and} \quad \vec{V}^{FID38} = \begin{bmatrix} V_A \\ V_B \\ V_C \\ V_D \end{bmatrix} \tag{4.42}$$

4.2.5 Stationnary Study

The stationary study consists in solving the stationary electrostatic equations for a considered set of parameters. In this chapter, the PL38 and FID38 designs are simulated with the default parameters listed in the table 4.2 and 4.3 respectively. The figure 4.11 plots several quantities derived from these resolutions.

For each design, the simulation yields an electric potential field $V(r, z)$ on the radial slice of the detector. These electric potentials are represented with a color map in the top row of graphics in figure 4.11. By applying a gradient function, the electric field $\vec{E}(r, z)$ is calculated in the detector. Graphics in the middle row are color maps of the magnitude $||\vec{E}(r, z)||$ of the electric field. Superimposed in black are the electric field lines associated (discussed thoroughly later in this section). The graphics of the bottom row of the figure 4.11 corresponds to the density histogram of the electric field norm $||\vec{E}(r, z)||$ over the whole crystal volume. The histograms are completed with the cumulative distribution function. The histograms and cumulatives are computed with the weighting function:

$$W(r, z) = 2\pi r \tag{4.43}$$

This is a consequence of the use of the 2D-axisymmetry: estimating a volume from an area of the radial slice necessitates to revolve it by 2π. Similarly, the later estimation of the fiducial volume is based on this weighting function.

The design PL38 displays equally spaced equipotential lines in the crystal volume with some slight deformation on the lateral surface due to the shape of the electrodes. As a result, the electric field norm is uniform on almost the whole crystal volume. Electric field lines are vertical in the bulk of the crystal with some curvature on the periphery. There are some regions of low magnitude in the corners of the crystal and under the central hole of the top electrode A. The

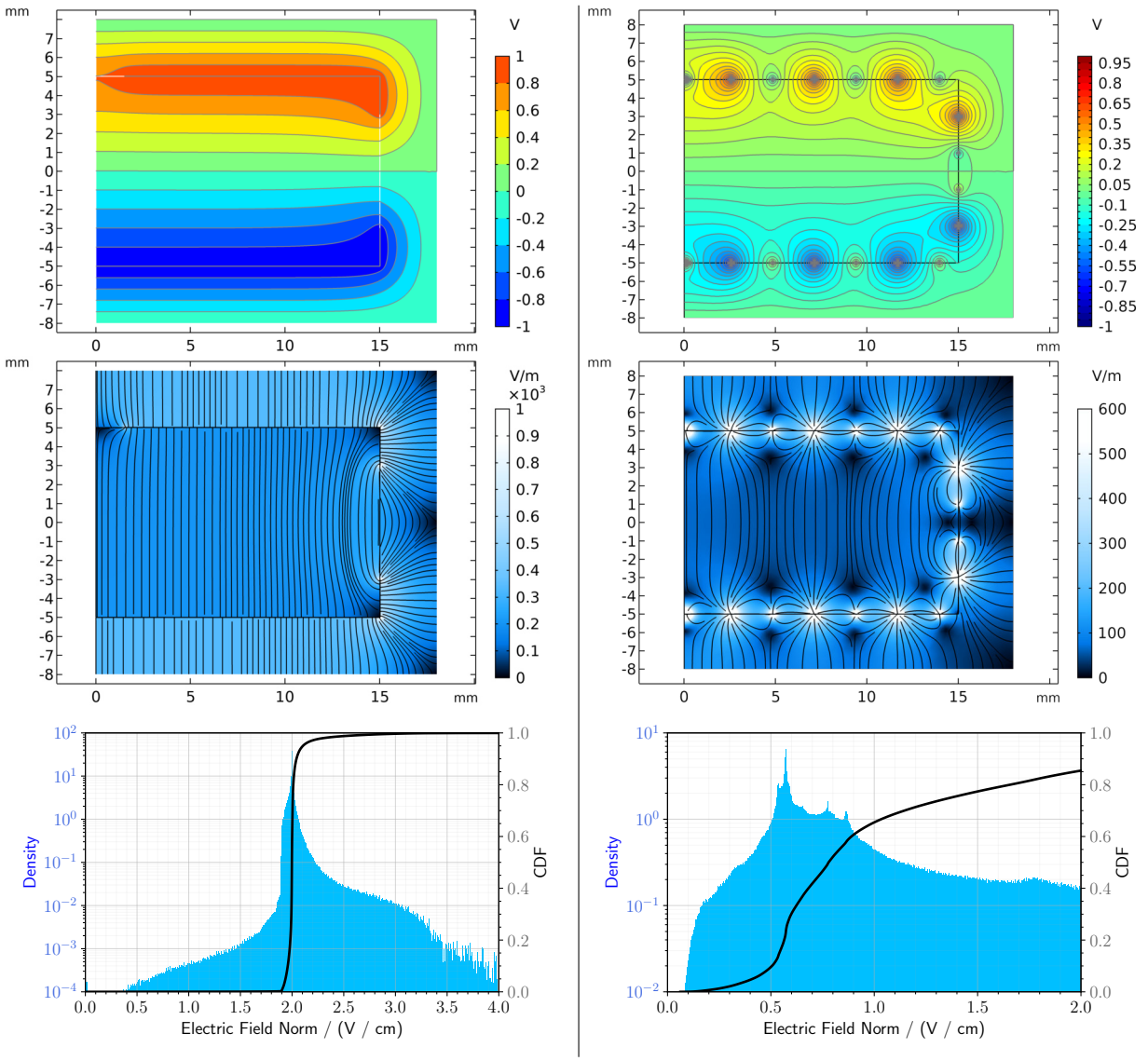

Figure 4.11: Graphics summarizing the resolution of the electrostatic equations for the simulated PL38 (on the left) and FID38 designs (on the right) in their default configuration. The graphics of the top row are colored contours of the electric potential V. The graphics of the middle row are the color maps of the norm of the electric field $||\vec{E}||$ with superimposed black electric field lines. On the bottom row are the density histograms and cumulative distribution functions of $||\vec{E}||$ over the crystal volume.

field lines are diverging from these low magnitude regions to join the electrodes or the grounded chassis. The density histogram of $||\vec{E}||$ is consistent with these observations: the distribution peaks at $2\,\mathrm{V}\cdot\mathrm{cm}^{-1}$ with slight broadening of the distribution at higher or lower values. The value of the peak equals the naive calculation of the electric field E_{naive} between two infinite plate of potential $V_A = 1\,\mathrm{V}$ and $V_B = -1\,\mathrm{V}$ spaced by a distance $H_{Ge} = 10\,\mathrm{mm}$:

$$||\vec{E}^{PL38}_{naive}|| = \left|\frac{V_A - V_B}{H_{Ge}}\right| = 2\,\mathrm{V}\cdot\mathrm{cm}^{-1} \tag{4.44}$$

The higher tail of the distribution with $||\vec{E}|| > 2\,\mathrm{V}\cdot\mathrm{cm}^{-1}$ corresponds to the peripheral volume of the crystal, on the lateral surface. Indeed, the distance between the electrodes is smaller on the lateral side due to the electrode extension of length $L_{lat} = 2\,\mathrm{mm}$ resulting into a higher electric field norm. The lower tail is explained by the presence of the low magnitude central and corner regions.

For the FID38 design, the electric potential field $V(r,z)$ is rapidly changing in the vicinity of the aluminium deposits near the surface. The equipotential lines shows the alternation of the polarization of the electrodes on the surface of the crystal. This FID polarization shapes the electric field near the surface of the crystal. Indeed, surface field lines join same-sided collect and veto electrodes. Due to the electric peak effect created by the aluminium deposit, the magnitude of the electric field is high near the surface. In the bulk of the crystal, the magnitude is of lower value with an uniform electric field demonstrated by the vertical field lines. Interestingly, the electric field is null between 1 to 2 mm deep into the crystal under the aluminium deposits attributed to the veto electrodes A and C. The electric field lines diverges from these low magnitude regions. The volumetric density distribution of the norm of the electric field $||\vec{E}||$ associated to the FID38 design is broader than the distribution of the PL38 design. Indeed, for the FID38, 15 % of the volume have a magnitude superior to $2\,\mathrm{V}\cdot\mathrm{cm}^{-1}$. This higher tail of the distribution is explained by the high intensity of the electric field near the surface due to the electric peak effects. As this tail has no clear features and asymptotically reach a density of zero it is not represented on the graphics. Indeed, the presented density histogram focuses on lower magnitude which features multiples peaks between 0.5 and $1\,\mathrm{V}\cdot\mathrm{cm}^{-1}$. These values corresponds to the bulk volume of the detector without the low magnitude regions. The regions of low electric field norm are associated with the lower tail of the distribution.

As reference for the magnitude of the electric field, we can naively compute the expected $||\vec{E}||$ in the FID38 crystal similarly to the PL38 design in equation 4.44. Far from the surface, the two top (resp. bottom) interleaved electrodes A and B (resp. C and D) would be perceived as a planar electrode of electric potential $V_{top} = (V_B + V_A)/2 = 0.375\,\mathrm{V}$ (resp. $V_{bottom} = (V_D + V_C)/2 = -0.375\,\mathrm{V}$). Assuming the center of the crystal at $z = 0$ being sufficiently far from the surface, the norm of the electric field would be:

$$||\vec{E}^{FID38}_{naive}|| = \left|\frac{V_{top} - V_{bottom}}{H_{Ge}}\right| = 0.75\,\mathrm{V}\cdot\mathrm{cm}^{-1} \tag{4.45}$$

This value corresponds to one of the peaks of the magnitude distribution which can therefore be attributed to the central bulk of the crystal.

The electric field lines in the PL38 and FID38 designs are drawn in black on the graphics of the middle row of figure 4.11. By construction, the field lines are parallel to the direction of the electric field $\vec{E}(r,z)$ and perpendicular to the equipotential of the $V(r,z)$ field. As explained in section 4.1.4, the motion of the holes follows the electric field lines while the electrons propagates in oblique directions with respect to the vertical axis. For the sake of clarity, assuming that the field lines are the trajectories of all the drifting charge carriers is denominated as the "assumption of ideal charge drift". This ideal drift is used to model the ionization signals in a detector. The electric charge Q_X induced on an electrode X of the detector is calculated from its associated

weighting potential field $\phi_X(\vec{r})$ according to the equation 4.16. This application of the Shokley-Ramo theorem discussed in section 4.1.6 is based on the knowledge of the final positions of the electric charges $\vec{r}_{e^-,f}$ and $\vec{r}_{h^+,f}$. The assumption of ideal drift indicates that these final positions corresponds to the start and end points of the electric field line passing by the position of the ionizing recoil $\vec{r}$.

The extremities of the electric fields in the germanium crystal are bound to be either a bare germanium surface or an electrode. While the weighting potential Φ_X associated with an electrode X is variable on the whole bare surface of the germanium, its value is fixed to either 0 or 1 on the surface of the electrodes according to the properties 4.40 of Φ_X. We can therefore classify the electric field lines according to their start and end points and their associated weighting potential Φ_X for each of the electrode X. For each class of field lines, a part of the crystal volume is drawn in the cross-section schemes 4.8 and 4.9. Recoils yielding a fixed ionization energy $E_{Ion.}$ and located in the same volume derived from the electric field lines induces the same ionization signal Q_X under the assumption of ideal drift. These signals are detailed considering a recoil producing a number N_p of electron-hole pairs.

All the drifting electrons represents a total electric charge of $-N_p \cdot e$ while all the drifting holes carry the opposite charge $+N_p \cdot e$.

For the PL38 design, the scheme 4.8 presents two volumes inside the germanium crystal. The green volume deemed "Fiducial volume" is drawn from all the electric field lines starting on the electrode A and ending on B. At default polarization, the top electrode A collects the electrons and the bottom electrode B collects the holes. The induced charge vector associated with a recoil of ionization energy $E_{ion.}$ located in the fiducial volume is:

$$\vec{Q}_{fid.}^{PL38} = \begin{bmatrix} -1 \\ 1 \end{bmatrix} \cdot N_p \cdot e \tag{4.46}$$

The other volume deemed "Exiting volume" and colored red corresponds to electric field lines leaving the germanium crystal volume. These field lines possess at least one of their extremities on the bare surface of the germanium crystal. The exiting points are located on the equatorial surface or on the central hole of the top electrode A. The weighting potential of the bare surface of the crystal is variable between 0 and 1 and is not controlled. As such, the signal created by recoils produced in the exiting volume cannot be characterized and have a detrimental effect on the analysis of the data streams recorded by the detector.

In the case of the FID38 detector, the electric field lines draw five types of collection volume presented in the scheme 4.9. The bigger volume colored green is the "Bulk volume" also designated "Fiducial Volume". It regroups all the electric field lines starting on the top collect electrode B and ending on the bottom collect electrode D. The blue volume is deemed "Top Veto volume". It contains all the field lines starting on the electrode B and ending on the top veto electrode A. The bottom equivalent is the "Bottom Veto volume" colored orange. Its field lines starts on the bottom veto electrode C and end on the bottom collect electrode D. Situated on the equator of the crystal is the "Equatorial volume" colored purple. It is drawn by the field lines starting on C and ending on A.

According to the default polarization 4.38 of the FID38 design, the electrons are collected by the electrodes B and C while the holes are collected by A and D. As such, the induced charge

vector associated with these four collection volumes are expressed:

$$\vec{Q}_{bulk}^{FID38} = \begin{bmatrix} 0 \\ -1 \\ 0 \\ 1 \end{bmatrix} \cdot N_p \cdot e \qquad \vec{Q}_{veto,top}^{FID38} = \begin{bmatrix} 1 \\ -1 \\ 0 \\ 0 \end{bmatrix} \cdot N_p \cdot e$$
$$\vec{Q}_{veto,bottom}^{FID38} = \begin{bmatrix} 0 \\ 0 \\ -1 \\ 1 \end{bmatrix} \cdot N_p \cdot e \qquad \vec{Q}_{equator}^{FID38} = \begin{bmatrix} 1 \\ 0 \\ -1 \\ 0 \end{bmatrix} \cdot N_p \cdot e \tag{4.47}$$

Recoils located in different collection volumes of the FID38 have different signal signatures. Therefore, the FID38 can locate and classify the events according to their ionization signal. This localization ability is especially useful to discard the surface events classified as either veto or equatorial events. Indeed, these surfaces events often present a problematic energy reconstruction which could lead to false nuclear recoils.

The last type of collection volume of of the FID38 design is the "Corner volumes" colored in red. Similarly to the exiting volumes of the PL38 design, this volume is drawn by field lines leaving the germanium crystal. The weighting potential on the bare germanium surface is not controlled. As the top and bottom veto volumes encompass the corner volumes, the signal signature of the corner events should be similar to the veto events with perhaps problematic energy reconstruction.

For both the PL38 and the FID38 designs, the fiducial volume should yields events with good energy reconstruction. These fiducial events are selected during the data analysis and used for the scientific goal of the experiments. This process called the "Bulk cut" is explained in section 6.2.9 and applied in the IP2I neutron background measurement described in the chapter 7. For this reason, the fiducial volume constitutes the actual effective volume of the detector. In this work, this volume efficiency is quantified with the fiducial volume percentage $\%_{fid}$ defined by:

$$\%_{fid} = 100 \times \frac{V(\text{Fiducial})}{V(\text{Ge Crystal})} \tag{4.48}$$

In order to estimate the fiducial volume fraction from the detector electrostatics simulation, a graphical method is used. The goal is to estimate the area of the "fiducial volume" on the radial section and convert it into an actual volume with the 2π rotation weighting function of equation 4.43. This method is illustrated with the figure 4.12 in the case of the FID38 design.

Electric field lines crossing the r-axis at $z = 0$ are calculated with a high density. These field lines corresponds to the fiducial lines in majority but also some exiting lines of the PL38 and equatorial lines of the FID38 design. These unwanted lines are discarded thanks to conditions on their start and end points. Now only a dense pack of fiducial field lines is remaining and the coordinates of their points are saved. An algorithm then processes the coordinates and extract the 2D contour encompassing the fiducial field lines. This fiducial contour is corrected with the 2π rotation weighting function 4.43. With this step, the area of the corrected fiducial contour is now proportional to the fiducial volume. Normalizing this fiducial area with the rectangular area of the crystal yields an estimation of the fiducial volume fraction. With default parameters, the fiducial percentage associated to the PL38 and FID38 designs are evaluated to:

$$\%_{fid}^{PL38} = 98\,\% \tag{4.49}$$
$$\%_{fid}^{FID38} = 69.5\,\% \tag{4.50}$$

Almost the whole crystal volume of the PL38 is fiducial with only some loss due to the

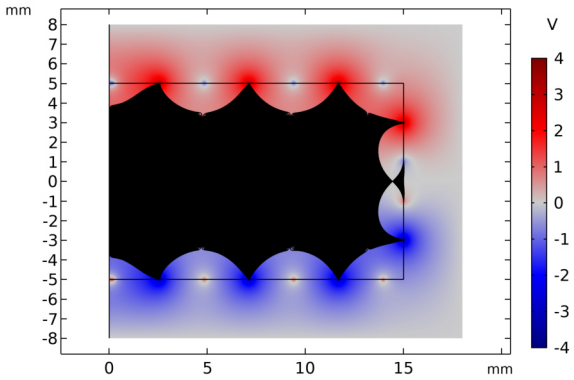

Figure 4.12: Illustration of the fiducial volume (and equatorial volume) of the FID38 design in its default configuration. Electric field lines crossing the equator $z = 0$ are plotted with a very high density. The background corresponds to a color map of the electric potential V in the FID38 simulation.

exiting volumes. This high volume is the major advantage of using a simple two planar electrode design. Concerning the FID38 design, a third of the volume is lost in the veto, equatorial and corner volumes. This fiducial volume loss is one of the price to pay for the ability to tag surface events of the FID electrode design.

4.2.6 Capacitance calculation with the Source Sweep Study

The common form of a capacitance is a parallel-plate capacitor: two conductive plates separated by a dielectric material of relative electric permittivity ϵ_r. For the ideal case of this system, the capacitance C is proportional to the surface area of the electrodes A and inversely proportional to the distance d between them such that:

$$C = \epsilon_0 \epsilon_r \frac{A}{d} \tag{4.51}$$

For this system composed of only two electrodes, the capacitance C governs the amount of electric charges on the plates Q and $-Q$ needed to impose a voltage V between them according to the equation:

$$C = \frac{Q}{V} \tag{4.52}$$

In the case of the electrodes of the germanium detectors, the capacitance is more complex as it takes into accounts the grounded copper chassis, two main collecting electrodes and, depending on the considered design, two auxiliary electrodes (guard or veto). The previous equation does not apply in systems with more than two capacitor plate (one electrode and the grounded chassis) and should be generalized to any electric system with a number N of electrodes. For such a system, the charge and electric potential of all the electrodes are represented by the charge vector $\vec{Q}$ and the potential vector $\vec{V}$ as:

$$\vec{Q} = \begin{pmatrix} Q_1 \\ Q_2 \\ \vdots \\ Q_N \end{pmatrix} \quad \text{and} \quad \vec{V} = \begin{pmatrix} V_1 \\ V_2 \\ \vdots \\ V_N \end{pmatrix} \tag{4.53}$$

In order to generalize the calculation of the capacitance to the electrodes of the bolometer, the concept of Maxwell capacitance matrix $\boldsymbol{C}$ is introduced:

$$\boldsymbol{C} = \begin{pmatrix} C_{11} & C_{12} & \cdots & C_{1N} \\ C_{21} & C_{22} & \cdots & C_{2N} \\ \vdots & \vdots & \ddots & \vdots \\ C_{N1} & C_{N2} & \cdots & C_{NN} \end{pmatrix} \quad \text{with} \quad \boldsymbol{C}_{ij} = \frac{\partial Q_i}{\partial V_j} \tag{4.54}$$

This matrix describes the relation between the charge Q_i and the voltage V_i of all the conductors in the system, and generalizes the equation 4.52 to higher dimensions such that:

$$\vec{Q} = \boldsymbol{C}\vec{V} \quad \Leftrightarrow \quad \vec{V} = \boldsymbol{C}^{-1}\vec{Q} = \boldsymbol{P}\vec{Q} \tag{4.55}$$

with $\boldsymbol{P}$ being the inverse of the Maxwell capacitance matrix named the elastance matrix. Its terms $\boldsymbol{P}_{ij}$ are called the coefficients of potential with:

$$\boldsymbol{P} = \begin{pmatrix} P_{11} & P_{12} & \cdots & P_{1N} \\ P_{21} & P_{22} & \cdots & P_{2N} \\ \vdots & \vdots & \ddots & \vdots \\ P_{N1} & P_{N2} & \cdots & P_{NN} \end{pmatrix} \quad \text{with} \quad \boldsymbol{P}_{ij} = \frac{\partial V_i}{\partial Q_j} \tag{4.56}$$

The coefficients of potential are symmetrical such that $\boldsymbol{P}_{ij} = \boldsymbol{P}_{ji}$ which induces that the Maxwell capacitance matrix is symmetric as well.

A key observation when comparing the two-plates capacitance equation 4.52 to the multiple plates capacitance equation 4.55 is that the electric charge Q_i and potential V_i of a given electrode i are no longer proportional with multiple plates. With the generalized view, adding a charge on a single electrode changes the potential of all the electrodes in the system.

While the Maxwell capacitance matrix is useful to study the generation of signal from charge collected by the electrodes with the equation 4.55, there is no clear interpretation for its term. An alternative to the Maxwell capacitance matrix is the mutual capacitance matrix $\boldsymbol{C}^m$. The terms of this mutual capacitance hold the benefit of being easily illustrated as single capacitances between the electrodes of a system. The figure 4.13 presents a scheme of the four electrodes of the FID38 design enclosed in the grounded copper chassis GND.

Each term $\boldsymbol{C}^m_{ij}$ can be interpreted as a single lumped capacitance between two electrodes i and j and as such, is represented with the common parallel-plate capacitor symbol. One can notice that the diagonal mutual capacitance terms $\boldsymbol{C}^m_{ii}$ are interpreted as the capacitance between the electrode i and the ground (here the copper chassis). It is important to note that this matrix does not represent the relation between the electric charge $\vec{Q}$ and potential $\vec{V}$ of the electrodes of the system and therefore the equation 4.55 cannot be applied with the mutual capacitance matrix. Instead, the mutual capacitance matrix should be used as a modelization and interpretation tool. It is possible to obtain the Maxwell capacitance matrix from the mutual capacitance matrix according to the relations:

$$\begin{cases} \forall i: & C_{ii} = \sum_j C^m_{ij} \\ \forall i \neq j: & C_{ij} = -C^m_{ij} \end{cases} \quad \Leftrightarrow \quad \begin{cases} \forall i: & C^m_{ii} = \sum_j C_{ij} \\ \forall i \neq j: & C^m_{ij} = -C_{ij} \end{cases} \tag{4.57}$$

With the interpretation of the mutual matrix as lumped capacitances, we see that the diagonal terms $\boldsymbol{C}_{ii}$ of the Maxwell capacitance matrix are simply the equivalent capacitance to all the lumped mutual capacitance $\boldsymbol{C}_{ij}$ put in parallel $C_{ii} = \sum_{j=1}^{N} C^m_{ij}$. As the non-diagonal terms of the Maxwell and the mutual capacitance matrix are opposite, the mutual capacitance matrix is also symmetric.

COMSOL® offers a functionality called Stationary Source Sweep to evaluate the elastance and the capacitance matrices. Considering the equation 4.56, an electrode j is excited with an electric charge Q_j while the charges of all the other electrodes $i \neq j$ are maintained to $Q_i = 0$.

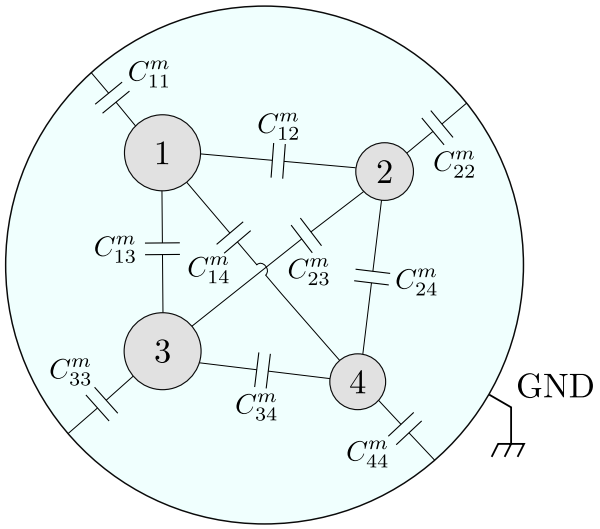

$$\Leftrightarrow \quad \boldsymbol{C}^m = \begin{pmatrix} C^m_{11} & C^m_{12} & C^m_{13} & C^m_{14} \\ C^m_{21} & C^m_{22} & C^m_{23} & C^m_{24} \\ C^m_{31} & C^m_{32} & C^m_{33} & C^m_{34} \\ C^m_{41} & C^m_{42} & C^m_{43} & C^m_{44} \end{pmatrix}$$

Figure 4.13: Scheme representing a electric system composed of 4 electrodes $\{1, 2, 3, 4\}$ surrounded by an electric ground GND. Each capacitance coupling corresponds to a term of the associated Mutual capacitance matrix. The diagonal terms C^m_{ii} of the mutual capacitance matrix are called the self-capacitance and are modeled by a capacitance linking an electrode i to the ground.

The electrostatic system is numerically solved and the coefficient of potential can be deduced from the electric potential of the electrodes V_i as:

$$\boldsymbol{P}_{ij} = \frac{V_i}{Q_j} \tag{4.58}$$

This procedure is repeated for each electrode until the full elastance matrix $\boldsymbol{P}$ is evaluated. The capacitance matrices are then calculated using the equations 4.54 and 4.57. In order to facilitate the discussion, the indexes of the matrices are swapped with the label of the electrodes.

For the PL38 detector design in its default configuration, the elastance and capacitance matrices are evaluated to:

$$\begin{aligned} \boldsymbol{P} &= \begin{pmatrix} P_{AA} & P_{AB} \\ P_{BA} & P_{BB} \end{pmatrix} = \begin{pmatrix} 1.42 & 1.04 \\ 1.04 & 1.42 \end{pmatrix} \cdot 10^{11}\,\mathrm{F}^{-1} \\ \Rightarrow \quad \boldsymbol{C} &= \begin{pmatrix} C_{AA} & C_{AB} \\ C_{BA} & C_{BB} \end{pmatrix} = \begin{pmatrix} 14.92 & -10.86 \\ -10.86 & 14.92 \end{pmatrix} \cdot 10^{-12}\,\mathrm{F} \\ \Rightarrow \quad \boldsymbol{C}^m &= \begin{pmatrix} C^m_{AA} & C^m_{AB} \\ C^m_{BA} & C^m_{BB} \end{pmatrix} = \begin{pmatrix} 4.06 & 10.86 \\ 10.86 & 4.06 \end{pmatrix} \cdot 10^{-12}\,\mathrm{F} \end{aligned} \tag{4.59}$$

As expected from a similarly designed parallel-plate capacitor using the equation 4.1, the Mutual capacitance are closed to the tens of pF. As expected from the interpretation of the Mutual capacitance matrix, all of its terms are positive. Observing the Mutual capacitance matrix, we note that the capacitance between the electrodes $C^m_{AB} = 10.86\,\mathrm{pF}$ is greater than the self-capacitance of the electrodes $C^m_{AA} = C^m_{BB} = 4.06\,\mathrm{pF}$. According to the parallel-plate capacitor equation 4.1, there are multiple arguments pointing towards an opposite observation: the grounded chassis is surrounding the electrodes, presenting very large area and the distance electrode-chassis is smaller than the height of the crystal. However, the self-capacitance is mainly formed in the vacuum between the absorber and the chassis, with a relative electric permittivity $\epsilon_r(\mathsf{Vacuum}) = 1$ whereas the mutual capacitance between the electrodes A and B is forming in the germanium crystal which imposes a relative permittivity of $\epsilon_r(\mathsf{Ge}) = 16.3$. This

significant difference in material permittivity explains the hierarchy of the mutual capacitance for the PL38 design.

For the FID38 design with default parameters, the elastance and capacitance matrices are evaluated to:

$$\begin{aligned}
\boldsymbol{P} &= \begin{pmatrix} P_{AA} & P_{AB} & P_{AC} & P_{AD} \\ P_{BA} & P_{BB} & P_{BC} & P_{BD} \\ P_{CA} & P_{CB} & P_{CC} & P_{CD} \\ P_{DA} & P_{DB} & P_{DC} & P_{DD} \end{pmatrix} = \begin{pmatrix} 2.23 & 1.92 & 1.71 & 1.69 \\ 1.92 & 2.34 & 1.69 & 1.68 \\ 1.71 & 1.69 & 2.23 & 1.92 \\ 1.69 & 1.68 & 1.92 & 2.34 \end{pmatrix} \cdot 10^{11}\,\mathrm{F}^{-1} \\
\Rightarrow \quad \boldsymbol{C} &= \begin{pmatrix} C_{AA} & C_{AB} & C_{AC} & C_{AD} \\ C_{BA} & C_{BB} & C_{BC} & C_{BD} \\ C_{CA} & C_{CB} & C_{CC} & C_{CD} \\ C_{DA} & C_{DB} & C_{DC} & C_{DD} \end{pmatrix} = \begin{pmatrix} 18.25 & -10.19 & -4.02 & -2.58 \\ -10.19 & 15.94 & -2.58 & -1.98 \\ -4.02 & -2.58 & 18.25 & -10.19 \\ -2.58 & -1.98 & -10.19 & 15.94 \end{pmatrix} \cdot 10^{-12}\,\mathrm{F} \\
\Rightarrow \quad \boldsymbol{C}^m &= \begin{pmatrix} C^m_{AA} & C^m_{AB} & C^m_{AC} & C^m_{AD} \\ C^m_{BA} & C^m_{BB} & C^m_{BC} & C^m_{BD} \\ C^m_{CA} & C^m_{CB} & C^m_{CC} & C^m_{CD} \\ C^m_{DA} & C^m_{DB} & C^m_{DC} & C^m_{DD} \end{pmatrix} = \begin{pmatrix} 1.46 & 10.19 & 4.02 & 2.58 \\ 10.19 & 1.18 & 2.58 & 1.98 \\ 4.02 & 2.58 & 1.46 & 10.19 \\ 2.58 & 1.98 & 10.19 & 1.18 \end{pmatrix} \cdot 10^{-12}\,\mathrm{F}
\end{aligned} \tag{4.60}$$

The observations made previously for the PL38 design still holds for the FID38 design: capacitances are close to tens of pF and the self-capacitance terms are the smaller terms. In particular, we note that the Mutual capacitance is dominated by the terms $C^m_{AB} = C^m_{BA} = C^m_{CD} = C^m_{DC} = 10.19\,\mathrm{pF}$. Indeed, as the electrodes A, B and C, D are interleaved, their capacitive coupling is high as it emulates a situation with two close plates. The next higher term is $C^m_{AC} = 4.02\,\mathrm{pF}$ coming from the two veto electrodes which are facing each other and coming very close to one another near the equator leading to an increase in coupling. The hierarchy of the remaining terms can be explained by the fact that there are more veto electrode rings than collect electrode rings, thus emulating a higher electrode area in the equation 4.1.

4.2.7 Sensitivity Calculation

The sensitivity of an electrode X designated the amplitude of its voltage signal V normalized by the ionization energy $E_{Ion.}$ created by a recoil. The unit of the sensitivity is the $\mathrm{V} \cdot \mathrm{keV}^{-1}$. In this paragraph, the sensitivities of each electrodes of the PL38 and FID38 design is calculated. The ionization signal is considered to be generated by an electronic recoil depositing an ionization energy $E_{Ion.} = E_R = 1\,\mathrm{keV}$. With application of the equation 4.6, we deduce the average number of electron-hole pairs created $N_p = 1000/2.97 = 337$. The induced charge vectors $\vec{Q}$ were discussed in section 4.2.5. The voltage signal vector $\vec{V}$ is computed using the relation 4.55. For the sake of simplicity, this voltage signal $\vec{V}$ is expressed in $\mathrm{V} \cdot \mathrm{keV}^{-1}$ after normalizing by 1 keV, so that it equals the sensitivity.

In the case of the PL38 design, we refer to the equation 4.46 for the induced charge vectors. The sensitivity of the electrodes A and B to a recoil in the fiducial volume is:

$$\vec{V}_{fid} = \boldsymbol{P}\vec{Q}_{fid} = \begin{bmatrix} -P_{AA} + P_{AB} \\ -P_{BA} + P_{BB} \end{bmatrix} \cdot N_p \cdot e = \begin{bmatrix} -0.39 \\ \\ 0.39 \end{bmatrix} \cdot N_p \cdot e \cdot 10^{11} = \begin{bmatrix} -2.08 \\ 2.08 \end{bmatrix} \mu\mathrm{V} \cdot \mathrm{keV}^{-1} \tag{4.61}$$

In the case of the FID38, we refer to the equation 4.47 for the four signature charge vectors. There are four corresponding voltage signal vectors:

$$\vec{V}_{bulk} = \boldsymbol{P}\vec{Q}_{bulk} = \begin{bmatrix} -P_{AB} + P_{AD} \\ -P_{BB} + P_{BD} \\ -P_{CB} + P_{CD} \\ -P_{DB} + P_{DD} \end{bmatrix} \cdot N_p \cdot e = \begin{bmatrix} -0.23 \\ -0.66 \\ 0.23 \\ 0.66 \end{bmatrix} \cdot N_p \cdot e \cdot 10^{11} = \begin{bmatrix} -1.23 \\ -3.52 \\ 1.23 \\ 3.52 \end{bmatrix} \mu\text{V} \cdot \text{keV}^{-1} \tag{4.62}$$

$$\vec{V}_{veto,top} = \boldsymbol{P}\vec{Q}_{veto,top} = \begin{bmatrix} +P_{AA} - P_{AB} \\ +P_{BA} - P_{BB} \\ +P_{CA} - P_{CB} \\ +P_{DA} - P_{DB} \end{bmatrix} \cdot N_p \cdot e = \begin{bmatrix} 0.31 \\ -0.42 \\ 0.02 \\ 0.01 \end{bmatrix} \cdot N_p \cdot e \cdot 10^{11} = \begin{bmatrix} 1.65 \\ -2.24 \\ 0.11 \\ 0.05 \end{bmatrix} \mu\text{V} \cdot \text{keV}^{-1} \tag{4.63}$$

$$\vec{V}_{veto,bottom} = \boldsymbol{P}\vec{Q}_{veto,bottom} = \begin{bmatrix} -P_{AC} + P_{AD} \\ -P_{BC} + P_{BD} \\ -P_{CC} + P_{CD} \\ -P_{DC} + P_{DD} \end{bmatrix} \cdot N_p \cdot e = \begin{bmatrix} 0.02 \\ 0.01 \\ -0.31 \\ -0.42 \end{bmatrix} \cdot N_p \cdot e \cdot 10^{11} = \begin{bmatrix} 0.11 \\ 0.05 \\ -1.65 \\ 2.24 \end{bmatrix} \mu\text{V} \cdot \text{keV}^{-1} \tag{4.64}$$

$$\vec{V}_{equator} = \boldsymbol{P}\vec{Q}_{equator} = \begin{bmatrix} -P_{AA} + P_{AC} \\ -P_{BA} + P_{BC} \\ -P_{CA} + P_{CC} \\ -P_{DA} + P_{DC} \end{bmatrix} \cdot N_p \cdot e = \begin{bmatrix} 0.52 \\ 0.23 \\ -0.52 \\ -0.23 \end{bmatrix} \cdot N_p \cdot e \cdot 10^{11} = \begin{bmatrix} 2.77 \\ 1.23 \\ -2.77 \\ -1.23 \end{bmatrix} \mu\text{V} \cdot \text{keV}^{-1} \tag{4.65}$$

The first thing one can note is that even though for each case the electrons and holes were collected by two electrodes, an electric potential perturbation was created on all the electrodes. This phenomenon is referred as "capacitive cross-talk". Then, we note that the amplitude of the signal depends on the electrode and depends of the event type.

The sensitivity vectors associated to the PL38 and FID38 designs possessing multiples electrodes are calculated. We can discuss the "efficiency" of the multiple electrodes design compared to a single equivalent reference capacitor. This reference capacitance $C^{ref}_{X,type}$ corresponds to a two-plate capacitor of same sensitivity as the electrode X for a given event type. By applying the formula 4.1 for this reference capacitor, its capacitance is expressed as:

$$C^{ref}_{X,type} = \frac{N_p \cdot e}{|V_{X,type}|} \tag{4.66}$$

In the case of the PL38 detector, there is only one type of event (fiducial events) for two electrodes with equal sensitivities. The common reference capacitance is:

$$C^{ref}_{top} = C^{ref}_{bottom} = (|-P_{AA} + P_{AB}|)^{-1} = (0.39 \cdot 10^{11})^{-1} = 26 \times 10^{-12}\,\text{F} \tag{4.67}$$

It is greater than any term of the Maxwell or mutual capacitance matrices 4.59 for the PL38 design. This indicates that this design has a worse efficiency than the two-plate capacitor design. The calculation of the sensitivity in equation 4.61 and the reference capacitance in equation 4.67 shows that the sensitivity is proportional to the term $|-P_{AA} + P_{AB}| = |-P_{AB} + P_{BB}|$. This term can be interpreted as the difference between the diagonal terms, P_{AA} and P_{BB}, of the elastance matrix and the non-diagonal term P_{AB} expressing the coupling between the two collecting electrodes.

As a 2×2 matrix, expressing the elastance $\boldsymbol{P}$ with the capacitance terms is relatively straightforward:

$$\boldsymbol{P} = \boldsymbol{C}^{-1} = \frac{1}{C_{11}C_{22} - (C_{12}^m)^2} \begin{pmatrix} C_{22} & -C_{12} \\ -C_{12} & C_{11} \end{pmatrix} \tag{4.68}$$

The expression of the reference capacitance becomes:

$$C_{top}^{ref} = (|-P_{AA} + P_{AB}|)^{-1} = \frac{C_{11}C_{22} - (C_{12}^m)^2}{C_{22} + C_{12}} = C_{11}^m + C_{12}^m \left(1 + \frac{C_{11}^m}{C_{22}^m}\right) \tag{4.69}$$

Considering the self-capacitance of A and B are almost equals, $C_{11}^m \approx C_{22}^m$, these expressions are simplified to:

$$C_{top}^{ref} = C_{22} - C_{12} = C_{22}^m + 2C_{12}^m = 25.78\,\text{pF} \tag{4.70}$$

In the end, in term of sensitivity, the electrodes A and B are equivalent to their self-capacitance C_{22}^m in parallel with two coupling capacitance C_{12}^m. In a sense, this coupling capacitance has two times more effect on the sensitivity than the self-capacitance, which is detrimental here as the C_{12}^m is the highest term of the mutual capacitance $\boldsymbol{C}^m$ of the PL38 design.

In the case of the FID38 detector, there are four types of events and four electrodes, resulting in a total of 16 sensitivities from equation 4.62. Among all these values, some are more relevant for the ionization channel performance than the others. The auxiliary veto electrodes A, C are used to determine if an event is a bulk or veto event (see section 6.2.9). Therefore, the sensitivities of these veto electrodes are relevant in the case of *veto* events of sensitivity $|V_{\text{veto top},A}| = |V_{\text{veto bottom},C}|$, and *equator* events with $|V_{\text{equator},A}| = |V_{\text{equator},C}|$. The main electrodes B, D are used to reconstruct the ionization energy $E_{Ion.}$ of the *bulk* events. Thus, their sensitivities are relevant for *bulk* recoils, $|V_{\text{bulk},B}| = |V_{\text{bulk},D}|$. From these sensitivities, the equivalent reference capacitances are deduced:

$$C_{A,veto}^{ref} = C_{C,veto}^{ref} = (|P_{AA} - P_{AB}|)^{-1} = (|-P_{CC} + P_{CB}|)^{-1} = (0.31 \cdot 10^{11})^{-1} = 32 \times 10^{-12}\,\text{F} \tag{4.71}$$

$$C_{A,equator}^{ref} = C_{C,equator}^{ref} = (|P_{AA} - P_{AC}|)^{-1} = (|-P_{CC} + P_{AC}|)^{-1} = (0.52 \cdot 10^{11})^{-1} = 19 \times 10^{-12}\,\text{F} \tag{4.72}$$

$$C_{B,bulk}^{ref} = C_{D,bulk}^{ref} = (|-P_{BB} + P_{BD}|)^{-1} = (|P_{DD} - P_{BD}|)^{-1} = (0.66 \cdot 10^{11})^{-1} = 15 \times 10^{-12}\,\text{F} \tag{4.73}$$

With a reference capacitance of 32 pF, the same observation as for the FID38 can be made for the veto electrodes A and C in their sensitivity to *veto* events. The reference capacitance is higher than any term of the mutual capacitance $\boldsymbol{C}^m$ or the diagonal term of the Maxwell capacitance $\boldsymbol{C}$. The efficiency of these electrodes is worse than a basic two-plate capacitor.

In the case of the *equator* events however, the reference capacitance $C_{A,equator}^{ref}$ seems to corresponds to the diagonal term of the Maxwell matrix $C_{AA} = 18.25\,\text{pF}$. Similarly, the reference capacitance $C_{B,bulk}^{ref}$ associated with the electrodes B and D for *bulk* events is close to $C_{BB} = 15.94\,\text{pF}$. In other words, for these two examples, an electrodes is as sensitive as the parallel association of all of its associated mutual capacitances in parallel.

Further interpretation of the reference capacitance and sensitivity is hampered due to the higher dimensions 4×4 of the elastance matrix $\boldsymbol{P}$ of the FID38 design. An analytical expression of the reference capacitance like for PL38 in equation 4.70 is not easily accessible and should prove to be much more complex.

There is a specific cross-talk and sensitivity for each type of events. When analyzing the detector data, there should therefore be a specific calibration and cross-talk correction associated

to each of this type of signal. However, to this day, the EDELWEISS experiment as well as the R&D for RICOCHET have used only a single analysis pipeline with a single calibration value for each electrodes and a single cross-talk correction matrix, independently of the type of event. Furthermore, the analysis seemed valid and no significant deviation was observed from the simple, yet wrong, ionization model where events creating the same amounts of electron-hole pairs presents the same electrode sensitivity and capacitive cross-talk. This can be explained by the fact that the capacitances of the detector are dominated by the greater capacitance of the cabling. It is important to recall that this work is focused on the capacitance of the electrodes of a detector, and did not considered the capacitance of the cabling between the electrodes and the amplifying electronics. In the experimental setup, the electrodes are connected to the electronics with coaxial cables. While a coaxial cable shield the signal from exterior interferences, it also creates a significant capacitive coupling between the ground and the core (in this case, the electrode). Let's consider a 50 pF capacitance between the ground and each electrodes, the associated cabling capacitance matrix is:

$$\boldsymbol{C}_{cabling} = \boldsymbol{C}^{m}_{cabling} = \mathbb{1}50 \times 10^{12}\,\mathrm{F} \tag{4.74}$$

As the Maxwell matrix $\boldsymbol{C}_{cabling}$ is diagonal, it is equal to the mutual matrix $\boldsymbol{C}^{m}_{cabling}$. The total Maxwell and mutual capacitance matrices of the detector and cabling are given by:

$$\begin{cases} \boldsymbol{C}_{tot} &= \boldsymbol{C}_{detector} + \boldsymbol{C}_{cabling} \\ \boldsymbol{C}^{m}_{tot} &= \boldsymbol{C}^{m}_{detector} + \boldsymbol{C}^{m}_{cabling} \end{cases} \tag{4.75}$$

where $\boldsymbol{C}_{detector}$ and $\boldsymbol{C}^{m}_{detector}$ are the Maxwell and mutual capacitance matrices of the detector designs PL38 and FID38 evaluated in the equations 4.59 and 4.60 respectively. The elastance matrices of the detectors and the cabling is now evaluated to:

$$\boldsymbol{P}^{PL38}_{tot} = \begin{bmatrix} 0.158 & 0.027 \\ 0.027 & 0.158 \end{bmatrix} \cdot 10^{11}\,\mathrm{F}^{-1} \qquad \boldsymbol{P}^{FID38}_{tot} = \begin{bmatrix} 0.151 & 0.024 & 0.011 & 0.008 \\ 0.024 & 0.156 & 0.008 & 0.007 \\ 0.011 & 0.008 & 0.151 & 0.024 \\ 0.008 & 0.007 & 0.024 & 0.156 \end{bmatrix} \cdot 10^{11}\,\mathrm{F}^{-1} \tag{4.76}$$

For the PL38 design with the capacitive cabling, the sensitivity and associated reference capacitance are now:

$$\vec{V}_{event} = \begin{bmatrix} 0.131 \\ -0.131 \end{bmatrix} \cdot 10^{11} = \begin{bmatrix} 0.71 \\ -0.71 \end{bmatrix} \mu\mathrm{V} \cdot \mathrm{keV}^{-1} \tag{4.77}$$

$$C^{ref}_{top,bottom} = 0.131 \cdot 10^{11} = 76 \times 10^{-12}\,\mathrm{F} \tag{4.78}$$

In the case of the FID38 with the capacitive cabling, the sensitivity and associated reference capacitance are:

$$\vec{V}_{bulk} = \begin{bmatrix} -0.016 \\ -0.149 \\ 0.016 \\ 0.149 \end{bmatrix} \cdot 10^{11} = \begin{bmatrix} -0.05 \\ -0.80 \\ 0.05 \\ 0.80 \end{bmatrix} \mu V \cdot keV^{-1} \tag{4.79}$$

$$\vec{V}_{veto,top} = \begin{bmatrix} 0.127 \\ -0.132 \\ 0.003 \\ 0.001 \end{bmatrix} \cdot 10^{11} = \begin{bmatrix} 0.69 \\ -0.75 \\ 0 \\ 0 \end{bmatrix} \mu V \cdot keV^{-1} \tag{4.80}$$

$$\vec{V}_{veto,bottom} = \begin{bmatrix} -0.003 \\ -0.001 \\ -0.127 \\ 0.132 \end{bmatrix} \cdot 10^{11} = \begin{bmatrix} 0 \\ 0 \\ -0.69 \\ 0.75 \end{bmatrix} \mu V \cdot keV^{-1} \tag{4.81}$$

$$\vec{V}_{equator} = \begin{bmatrix} 0.140 \\ 0.016 \\ -0.140 \\ -0.016 \end{bmatrix} \cdot 10^{11} = \begin{bmatrix} 0.75 \\ 0.05 \\ -0.75 \\ -0.05 \end{bmatrix} \mu V \cdot keV^{-1} \tag{4.82}$$

$$C^{ref}_{A,veto} = C^{ref}_{C,veto} = 0.127 \cdot 10^{11} = 78.7 \times 10^{-12}\,F \tag{4.83}$$

$$C^{ref}_{A,equator} = C^{ref}_{C,equator} = 0.140 \cdot 10^{11} = 71.4 \times 10^{-12}\,F \tag{4.84}$$

$$C^{ref}_{B,bulk} = C^{ref}_{D,bulk} = 0.149 \cdot 10^{11} = 67.1 \times 10^{-12}\,F \tag{4.85}$$

We see that by adding the capacitance of the cabling, the cross-talk phenomenon is significantly lessened: the self-capacitance term $\boldsymbol{C}^{m}_{tot}$ dominates the mutual matrix and heavily influences the calculation of the elastance matrix $\boldsymbol{P}_{tot}$. The electrode sensitivities all tends to a unique value of $\approx 75\,pF$ in absolute value for all the types of events. This unified sensitivity is characteristic of the results yielded by the ionization channel of the EDELWEISS-III experiment and IP2I R&D. The high cabling capacitance muffles the cross-talk phenomenon and the differences in sensitivity. Indeed as the capacitive coupling with the ground through the coaxial cabling is increased, the cross-talk and difference in sensitivity vanish.

In order to fully appreciate the impact of the cabling capacity, the figure 4.14 presents the corner plot of the sensitivity vectors in a FID38 detector with (black points) and without (colored points) 150 pF cabling capacitance.

The first major observation is that the cabling capacitance drastically reduces the sensitivities of the electrodes. Then, the sensitivities of the FID38 with cabling forms a square-like pattern in the $V_B(V_D), V_C(V_D), V_B(V_A), V_C(V_A)$ subplots illustrating that all electrodes have almost the same sensitivity. The square pattern emerges from the low cross-talks of about $0.05/0.80 = 6\,\%$ and $0.05/0.75 = 7\,\%$. This pattern is redundant in the data analysis of the EDELWEISS-III and IP2I R&D data streams (see chapter 6 discussing the data analysis). In the case of EDELWEISS-III with a cabling of capacitance $> 150\,pF$, the simple ionization signal generation model as presented in this chapter introduction 4.1 is sufficient to explain the experimental observations. The eventual low cross-talks phenomena were absorbed in the ionization resolution or attributed to unknown parasite capacitance in the electronics.

The new HEMT-based electronics in development is situated very close to the detector load in the cryostat. This implies a reduced coaxial cable length and a lowered cabling capacitance. The major advantage is a significant gain in sensitivity, which was expected and now demonstrated in this study. The novelty brought with this theorization of the ionization channel is

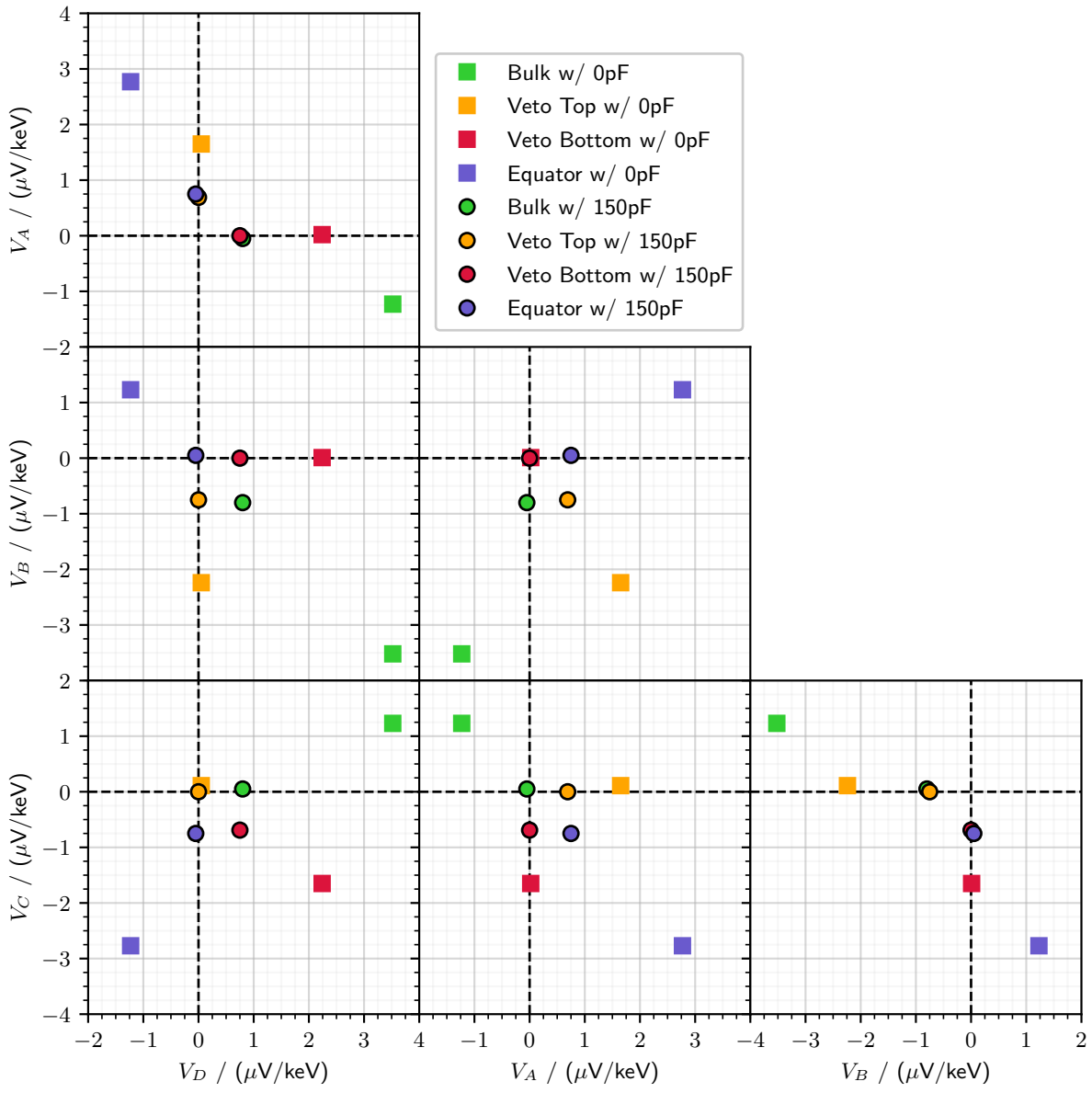

Figure 4.14: Illustration of the expected sensitivities with a FID38 detector with ("w/ 150 pF" black circles) and without ("w/ 0 pF" color squares) capacitive cabling. The rectangular-like shape formed by the sensitivities of the FID38 with cabling is characteristic of the current IP2I R&D results.

that with low cabling capacitance, the signal on the electrodes will differ. The 4 events populations do not form a square pattern anymore and presents the high cross-talk phenomenon $1.23/3.52 = 35\,\%$ and $1.23/2.77 = 44\,\%$.

4.2.8 Noise and Resolution Calculation

The previous section presented how, with low cabling capacitance, the capacitive coupling between each electrodes affects the sensitivity of the ionization channel. This section discusses the impact of this capacitive coupling on the noise affecting the measurement and eventually the resolution of the ionization channel. As discussed in section 4.1.8, the dominating noise source affecting the ionization energy measurement is the electronics noise. By combining the electric circuit of the HEMT-based electronics line and the lumped capacitance model from equation 4.13 of the PL38 and FID38 designs, we can predict the noise affecting the ionization channel. The method of noise propagation is the same as used in the chapter 3 with the modelization of the heat channel.

In order to motivate this study, the noise calculation is first done on a very simple model: the PL38 design with a heavily simplified HEMT line featuring only the polarization resistor $R_{polar.}$ and its associated Johnson noise e_J. The LPSD associated with the Johnson noise is expressed as:

$$e_J = \sqrt{4 \cdot k_B \cdot T \cdot R_{polar.}} \tag{4.86}$$

with the temperature of the polarization resistor set to $T = 10\,\text{mK}$. The scheme of this simplified model is presented in the figure 4.16. Thanks to the superposition theorem and successive Thevenin-Norton transformations of the electric circuit, it is possible to propagate the two Johnson noise sources $e_{J,A}$ and $e_{J,B}$ to the measurement point S_B.

The voltage noise affecting the measurement at the node S_B is characterized by the LPSD $e_{tot}^{S_B}$ in $\text{V}/\sqrt{\text{Hz}}$. It is expressed as:

$$\left(e_{tot}^{S_B}\right)^2 = e^{S_B}\left(e_J^A\right)^2 + e^{S_B}\left(e_J^B\right)^2 \tag{4.87}$$

with the components $e^{S_B}(\text{source})$ being the propagation of the different noise sources onto the node S_B.

The propagation of the noise is done with multiple Thevenin-Norton transformations of the electric circuit. We use the parallel operator $\parallel$ to express the parallel association of two impedance Z_1 and Z_2 such that:

$$Z_1 \parallel Z_2 = \left(\frac{1}{Z_1} + \frac{1}{Z_2}\right)^{-1} = \frac{Z_1 \cdot Z_2}{Z_1 + Z_2} \tag{4.88}$$

In the case of the simplified electric circuit representing the PL38 design, the propagation of the Johnson voltage noises e_J onto the node S_B is expressed:

$$e^{S_B}\left(e_J^B\right) = e_J^B \cdot \frac{1}{R_{polar.}} \cdot \left(R_{polar.} \parallel (j\omega C_{22}^m)^{-1} \parallel Z_{eq}\right) \tag{4.89}$$

$$e^{S_B}\left(e_J^A\right) = e_J^A \cdot \frac{R_{polar.} \parallel (j\omega C_{11}^m)^{-1}}{R_{polar.} \cdot Z_{eq}} \cdot \left(R_{polar.} \parallel (j\omega C_{22}^m)^{-1} \parallel Z_{eq}\right) \tag{4.90}$$

and with the equivalent impedance Z_{eq} expressed as:

$$Z_{eq} = \left(R_{polar.} \parallel (j\omega C_{11}^m)^{-1}\right) + (j\omega C_{12}^m)^{-1} = \frac{1 + j\omega R_{polar.}(C_{11}^m + C_{12}^m)}{(1 + j\omega R_{polar.} C_{11}^m) \cdot j\omega C_{12}^m} \tag{4.91}$$

As a result, the ratio of the components is:

$$\begin{aligned}\left|\frac{e^{S_B}\left(e_J^A\right)}{e^{S_B}\left(e_J^B\right)}\right| &= \left|\frac{R_{polar.} \parallel (j\omega C_{11}^m)^{-1}}{R_{polar.} \cdot Z_{eq}}\right| \\ &= \left|\frac{R_{polar.}}{1+j\omega R_{polar.} C_{11}^m} \cdot \frac{(1+j\omega R_{polar.} C_{11}^m) \cdot j\omega C_{12}^m}{1+j\omega R_{polar.}(C_{11}^m + C_{12}^m)}\right| \\ &= \left|\frac{j\omega R_{polar} C_{12}^m}{1+j\omega R_{polar}\left(C_{12}^m + C_{11}^m\right)}\right|\end{aligned} \tag{4.92}$$

This ratio is consistent with a high-pass filtering assured by the coupling capacitance C_{12}. The asymptotic value of the ratio is:

$$\lim_{\omega\to\infty}\left|\frac{e^{S_B}\left(e_J^A\right)}{e^{S_B}\left(e_J^B\right)}\right| = \frac{C_{12}^m}{C_{12}^m + C_{11}^m} = \frac{-C_{12}}{C_{11}} = \frac{10.86\,\text{pF}}{14.92\,\text{pF}} = 0.7279 \tag{4.93}$$

The cutoff frequency f_c associated with this ratio function is calculated as:

$$\begin{aligned}&\left|\frac{e^{S_B}\left(e_J^A\right)}{e^{S_B}\left(e_J^B\right)}\right|(\omega=\omega_c) = \frac{1}{\sqrt{2}}\lim_{\omega\to\infty}\left|\frac{e^{S_B}\left(e_J^A\right)}{e^{S_B}\left(e_J^B\right)}\right| \\ \Leftrightarrow\quad &\frac{j\omega_c R_{polar}\left(C_{12}^m + C_{11}^m\right)}{1+j\omega R_{polar}\left(C_{12}^m + C_{11}^m\right)} = \frac{1}{\sqrt{2}} \\ \Leftrightarrow\quad &\omega_c = \frac{1}{R_{polar}\left(C_{12}^m + C_{11}^m\right)} = 6.702\,\text{rad}\cdot\text{s}^{-1} \\ \Leftrightarrow\quad &f_c = \frac{\omega_c}{2\pi} = 1.067\,\text{Hz}\end{aligned} \tag{4.94}$$

The total noise and its components measured at S_B are plotted as functions of the frequency in the top plot of figure 4.15. Events though the original Johnson voltage noise source are modeled as white noise whose levels are independent from the frequency, since the total voltage noise affecting the measurement at node S_B presents a low-pass filter profile. This is consistent with the studied electric system as the node S_B is linked to the electric ground through the two capacitors C_{22} and C_{11}: at high frequency, they act as closed circuit and the electric potential of the node S_B tends to 0 V. The dominant component of the noise is the Johnson noise $e_{J,B}$ of the HEMT line of the electrode B where the measurement is made. It is less dampened than the other Johnson noise source $e_{J,A}$ which is filtered by the capacitance C_{12} coupling the two electrodes A and B. The bottom plot of figure 4.15 shows the ratio of the two Johnson noise components $e_{J,A}/e_{J,B}$ as a function of the frequency.

Above the cutoff frequency $f_c = 1.067\,\text{Hz}$, the ratio tends to 0.73. As the time windows is 1 s, the lowest frequency explored is 1 Hz which is very close to f_c. As such, the ratio corresponds to its asymptotic behavior on almost the whole frequency space. According to the previous equation 4.93, the ratio depends on the ratio of the non-diagonal over the diagonal terms of the Maxwell capacitance matrix of the PL38 detector (from equation 4.59). This ratio of Maxwell capacitances is comprised between 0 and 1, and reaches its maximum if the capacitive coupling C_{12}^m between the two electrodes A and B is much greater than the self-capacitance C_{11}^m of the electrode A.

As the two Johnson noises are not correlated, their squared noise level is added to form the total noise level which is tends to be $\sqrt{1^2 + (0.73)^2} = 1.24$ times the original Johnson noise level

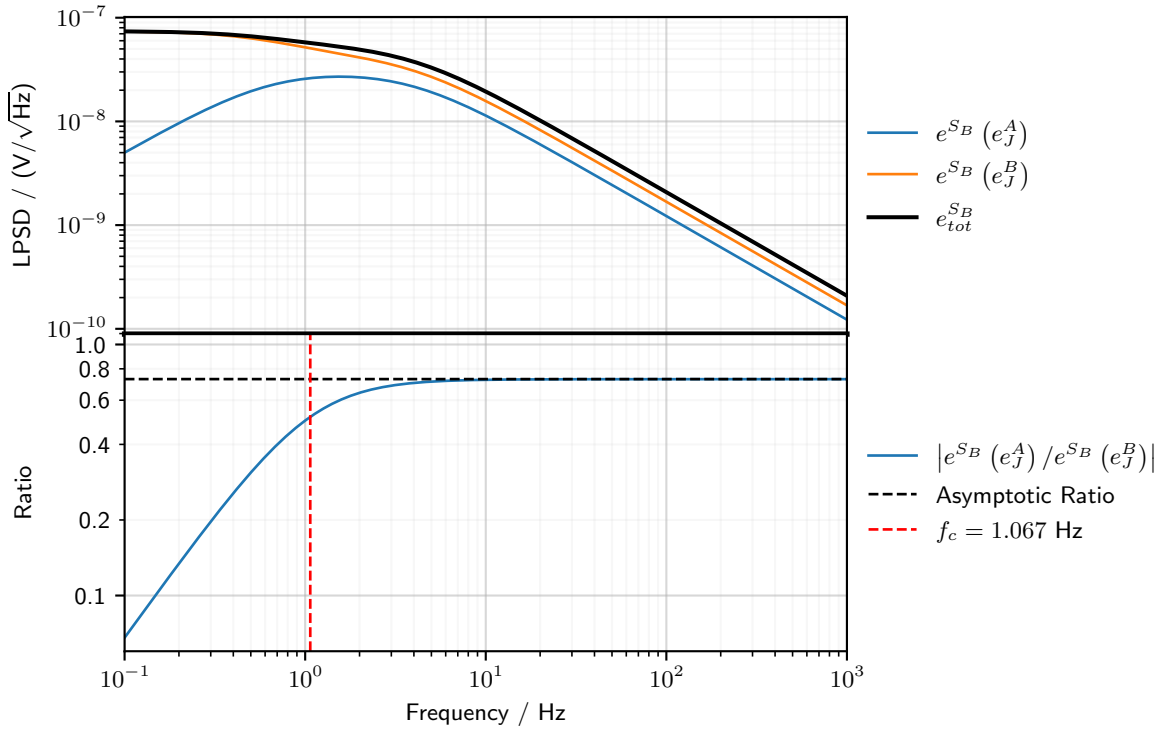

Figure 4.15: The top plot presents the total voltage noise LPSD measured at the node S_B along with its to propagated Johnson noise components as functions of the frequency. The bottom plot compares these two components by plotting their ratio as a function of the frequency.

caused by $e_{J,B}$ alone. For the given PL38 design with the simplified HEMT line, the noise level is increased by 24 % on the majority of the frequency space. This demonstrates that the effect of the coupling between the electrodes is far from negligible and should be properly studied for the two reference designs FID38 and PL38 with a full model with a complete HEMT line on each of the electrodes.

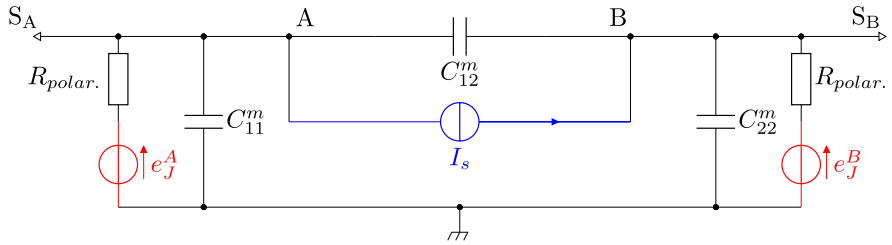

Figure 4.16: Electric scheme of the PL38 design with its two electrodes A and B solely equipped with the polarization line. The lumped capacitance model is used to model the PL38 design as an association of capacitors. Their capacitance corresponds to the term of the mutual capacitance matrix C^m of the PL38 design. The transient signal sources are colored blue while the noise source are in red.

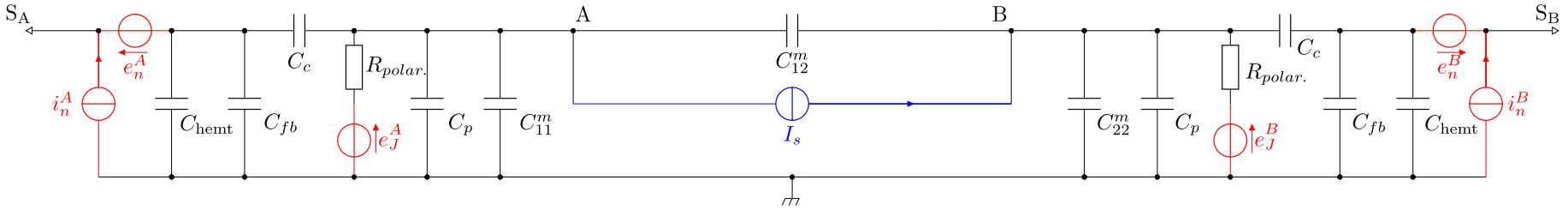

Figure 4.17: Electric scheme of the PL38 design with its two electrodes A and B equipped with an HEMT line readout. The lumped capacitance model is used to model the PL38 design as an association of capacitors. Their capacitance corresponds to the term of the mutual capacitance matrix C^m of the PL38 design. The transient signal sources are colored blue while the noise source are in red.

Circuit Component	Symbol	Value
Parasite Capacitance	C_p	$5 \times 10^{-12}\,\mathrm{F}$
Polarization Resistance	R_{polar}	$1 \times 10^{10}\,\Omega$
Coupling Capacitance	C_c	$2 \times 10^{-9}\,\mathrm{F}$
HEMT Capacitance	C_{hemt}	$5 \times 10^{-12}\,\mathrm{F}$
Feedback Resistance	R_{fb}	$1 \times 10^{10}\,\Omega$
Feedback Capacitance	C_{fb}	$3 \times 10^{-12}\,\mathrm{F}$

Table 4.4: List and Values of the electrical components of the circuits 4.16, 4.17, 4.19 and 4.20.

The PL38 detector cabled with the full HEMT line is illustrated in the scheme 4.17. The detector is composed of the three mutual capacitance C_{ij}^m linked to the nodes A, B. There is a measurement node for each electrode S_A and S_B, acting as an ideal voltmeter with the electric ground as reference. There is a total of 6 noise sources coming from the HEMT lines. The signal induced by an event is modeled as a transient current source $I_{event} = N_p \cdot e \cdot \delta(t)$ between A and B. The intrinsic current i_n and voltage e_n source of the amplifying electronic have their LSPD modeled as:

$$\begin{cases} i_n(f) & = \sqrt{i_0^2 + (i_a \cdot \sqrt{f})^2} \\ i_0 & = 4.0 \times 10^{-23}\,\mathrm{A} \\ i_a & = 2.6 \times 10^{-18}\,\mathrm{A}/\sqrt{\mathrm{Hz}} \\ e_n(f) & = \sqrt{e_0^2 + (\frac{e_a}{\sqrt{f}})^2 + (\frac{e_a}{f})^2} \\ e_0 & = 2.56 \times 10^{-10}\,\mathrm{V} \\ e_a & = 2.965 \times 10^{-8}\,\mathrm{V} \cdot \sqrt{\mathrm{Hz}} \\ e_b & = 5.343 \times 10^{-9}\,\mathrm{V} \cdot \mathrm{Hz} \end{cases} \tag{4.95}$$

with f the frequency, based on experimental measurements. The multiple noise source and the event signal are propagated to the measurement node S_B using the analytical circuit resolution algorithm from the Python module "Lcapy" [31].

The figure 4.18 presents the total noise and its components measured at S_B as a function of the frequency for the FID38 design. The predominant noises are the Johnson noise e_J^B of the HEMT line of the electrode B at low frequency and the intrinsic current noise i_n^B at high frequency. The Johnson noise e_J^A from the other HEMT line of the electrode A is slightly present below 2 Hz, but is surpassed by the intrinsic voltage source e_n^B. In the end, we observe that the noise sources from the auxiliary HEMT line on A are heavily filtered and do not propagate significantly to the measurement node S_B. When comparing to the previous simplified electric circuit where the propagation was significant, one of the main difference is now the presence of the feedback capacitance, the HEMT intrinsic capacitance and the cabling capacitance (representing in this case 5+3+5 = 13 pF. These capacitances are added to the diagonal term of the Maxwell capacitance matrix and reduce the propagation of the noise source through the coupling capacitance C_{12}^m.

The figure 4.18 also compares the total noise power spectral density to the power spectrum of the signal induced by the transient I_{bulk}. The noise follows a $1/\sqrt{f}$ trend while the signal has $1/f$ profile. As such, the majority of the information of the signal is contained in the low frequency of the data stream. When integrating between 1 Hz and infinity, the ionization energy resolution is evaluated to $\sigma_B = 30.8\,\mathrm{eV}$. There is a factor 1.5 between this predicted resolution and the objective of 20 eV resolution discussed in the section 4.1.9. By combining the signal of the two electrodes, a lower resolution $\sigma_{A+B} = \sigma_B/\sqrt{2} = 21.8\,\mathrm{eV}$ is reached.

The FID38 detector cabled with the full HEMT line is illustrated in the scheme 4.19. The

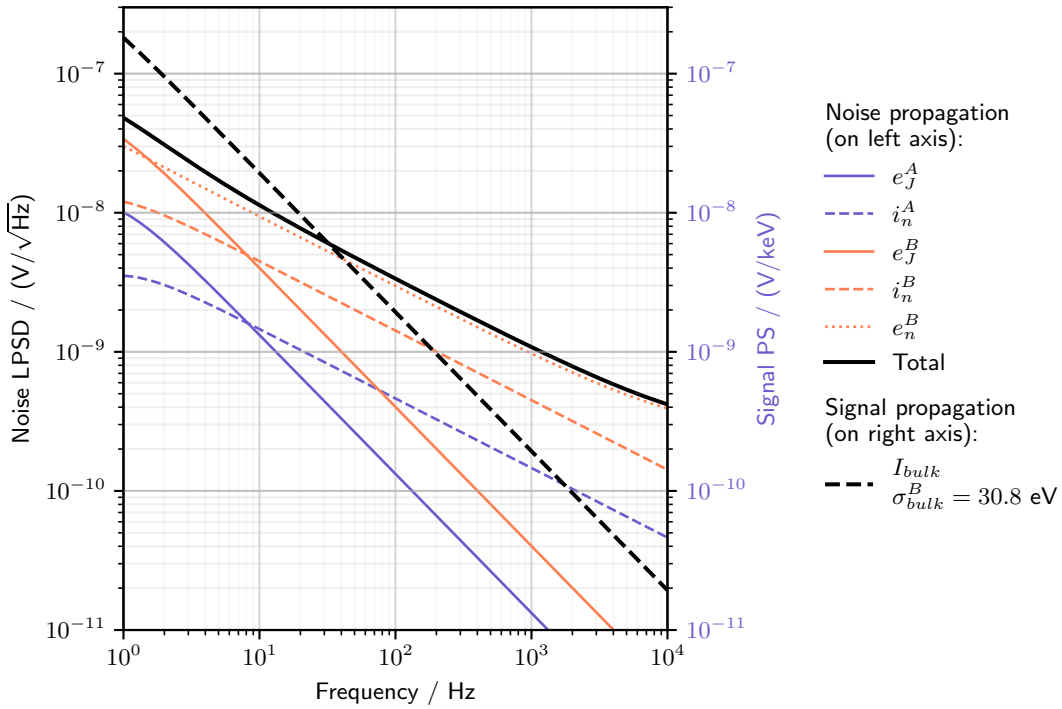

Figure 4.18: Representation of the total voltage noise LPSD the node S_B along with its components as functions of the frequency. The value of the signal power spectrum (PS) is read on the right axis. The calculation and integration from 1 Hz of the noise equivalent power yields the ionization energy resolution $\sigma_B = 30.8\,\text{eV}$.

detector is composed of the ten mutual capacitance C_{ij}^m linked to the nodes A, B, C, D. There is a measurement node for each electrode S_A, S_B, S_c, S_D, acting as an ideal voltmeter with the electric ground as reference. There is a total of $4 \times 3 = 12$ noise sources coming from the four HEMT lines. Signals induced by the *bulk*, *veto* and *equator* events are modeled as transient current sources $I = N_p \cdot e \cdot \delta(t)$ between two electrode nodes. Once again, the multiple noise source and the event signals are propagated to the measurement node S_B.

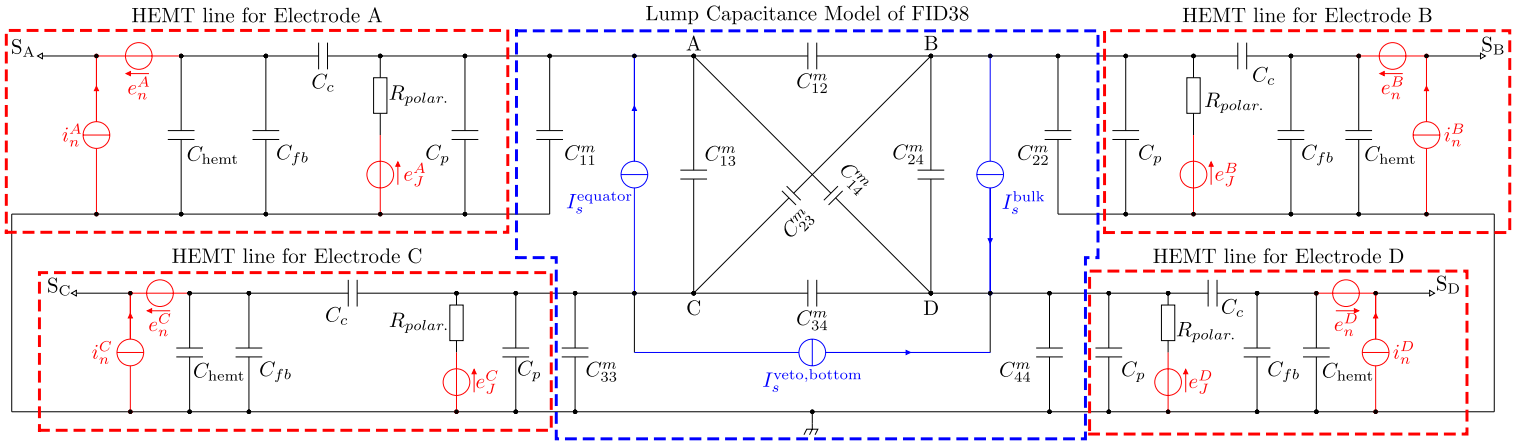

Figure 4.19: Electric scheme of the FID38 design with its four electrodes A, B, C and D each equipped with an HEMT line readout. The lumped capacitance model is used to model the FID38 design as an association of capacitors. Their capacitance corresponds to the term of the mutual capacitance matrix C^m of the FID38 design. The transient signal sources are colored blue while the noise source are in red.

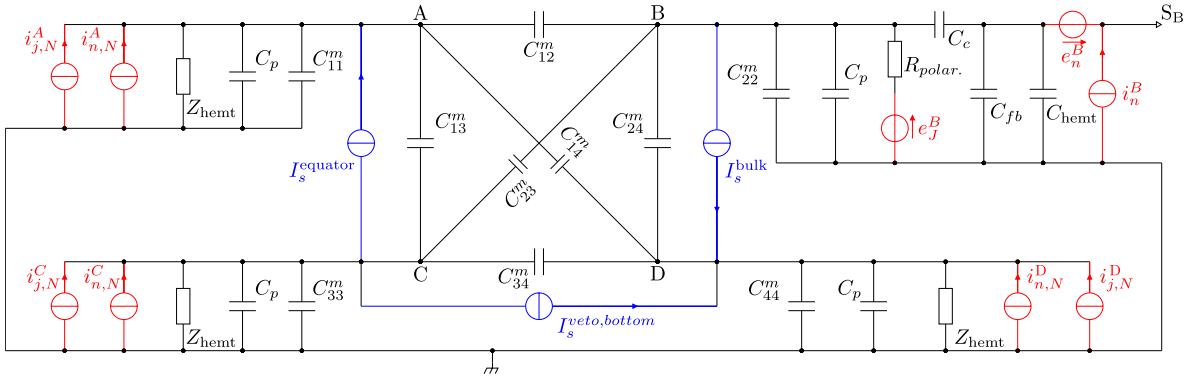

Figure 4.20: Simplification of the previous electric scheme 4.19 for the calculation of the sensitivity and the propagation of the noise on the readout of the electrode B.

The figure 4.21 presents the total noise and its components measured at S_B as a function of the frequency. The predominant noise are the Johnson noise $e_{J,B}$ of the HEMT line of the electrode B at low frequency and the intrinsic current noise i_n^B at high frequency. The Johnson noise e_J^A from the other HEMT line of the electrode A is slightly present below 2 Hz, but is quickly dominated by the intrinsic voltage source e_n^B. All in all, the results are quite similar to what was observed with the PL38 design: the Johnson noise from the most coupled electrode is significant at very low frequency and is quickly dominated by the intrinsic voltage noise source of the HEMT line B. Again, this can be explained by a boosted diagonal term in the Maxwell capacitance matrix which heavily filters the noise sources from spreading to other HEMT line efficiently. In the case of the FID38, there are three possible signal power spectra associated with the *bulk*, *veto* and *equator* events. All this power spectra have the same $1/f$ profile and only differ by a multiplicative factor. Once again, due to the $1/\sqrt{f}$ shape of the total noise, most of the information is held in the low frequency of the data stream. The ionization energy resolutions are calculated from the three event types. For the bulk and veto events, the resolutions are pretty similar around 30 eV. The resolution associated with the equator events is a very high 151 eV as only a small fraction of the charges is actually induced on the collect electrode B. This indicates that the performance of the FID38 ionization channel drops for equatorial events. This might be problematic in tagging surface events near the equator. The lowest resolution concerns the bulk events with $\sigma_{bulk}^B = 24.1$ eV. By combining the two collecting signal of the collecting electrodes B and D, it is possible to lower the ionization energy resolution to $\sigma_{bulk}^{B+D} = 17.1$ eV. As such, it possible to reach the objective ionization resolution of 20 eV.

The performance of a detector is partly quantified by the resolution of its ionization channel. Thus, the resolutions calculated previously for the PL38 and FID38 are figure of merit. However, these calculation are long as they necessitate to simulate a detector design in the FEM software to compute the Mutual capacitance matrix and then simulate the detector cabled with the HEMT lines with a separate Python script using the Lcapy module.

The resolution of the electrodes of a detector design depends on the whole Maxwell capacitance matrix (3 independent terms for the PL38, and 10 independents terms for the FID38). It might be possible to access some basic trends of the resolution by scanning over basic parameters.

The left part of figure 4.22 is a graph of the calculated resolution as a function of the cabling capacitance C_p of the HEMT lines while keeping fixed all the other component values of Table 4.4. This parameter scan can be interpreted as studying the resolution as a function of the diagonal terms of the Maxwell capacitance terms. We observe that a high cabling capacitance increases the resolution of the ionization channel. As the cabling capacitance decreases, the resolutions seem to cap. This indicates that C_p is not the limiting component in the detector under ≈ 5 pF.

The right part of figure 4.22 is a graph of the resolution as a function of a global multiplicative factor of the Maxwell capacitance matrix for the PL38 design. The Maxwell capacitance $\boldsymbol{C}_{new}$ used for the resolution calculation is:

$$\boldsymbol{C}_{new} = \boldsymbol{C} \times \alpha \tag{4.96}$$

with α the multiplicative factor. A multiplier factor of 1 corresponds to a resolution calculation with the capacitance matrices presented in equation 4.59. It is possible to artificially change all the capacitance terms of the capacitance matrix with this global multiplicative factor. Compared to the previous scan on the diagonal terms of the Maxwell matrix, this scan impact the whole matrix. In order to realistically apply this transformation, we could think of a up- or down-scaling of the detector size or changing the electric permittivity with another absorber material. We observe that the resolution is proportional to the global multiplicative factor.

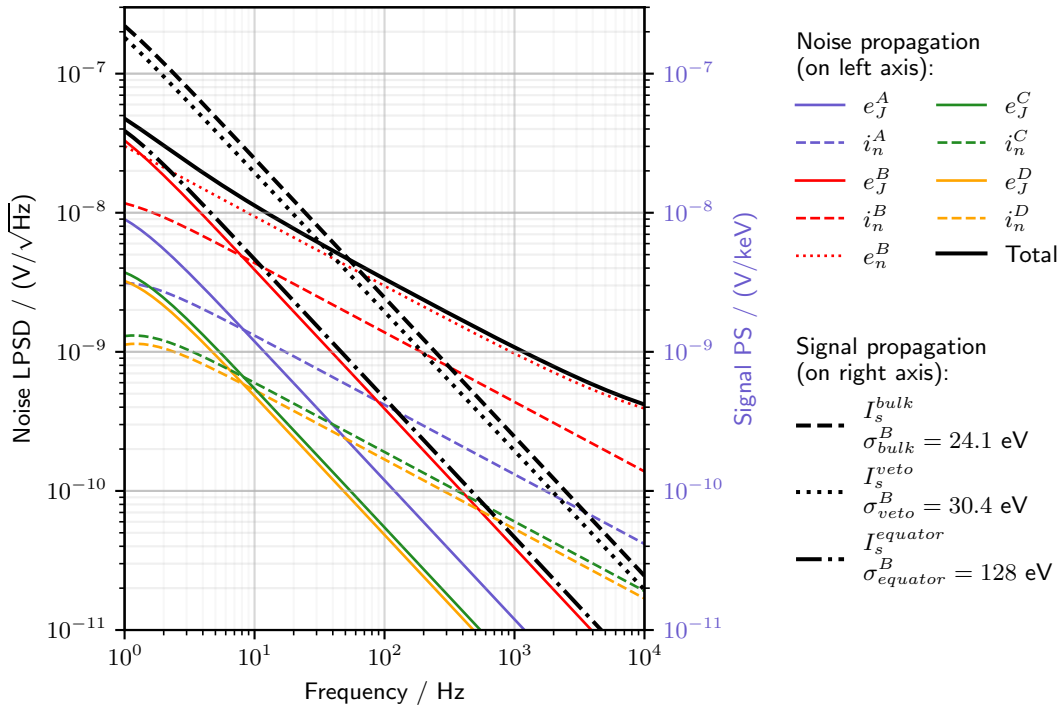

Figure 4.21: Representation of the total voltage noise LPSD the node S_B along with its components as functions of the frequency. The values of the signal PS associated with the *bulk*, *veto* and *equator* events are read on the right axis. The calculation and integration from 1 Hz of the noise equivalent power yields the ionization energy resolutions.

These two observations are consistent with what could be expected from the very basic understanding of the ionization channel presented in section 4.1.1: the resolution decreases as the capacitances of the detector decrease. In order to optimize the ionization channel, the research should be focused on lowering the capacitance of the cabling, and lowering the capacitances of the electrodes. The cabling links the electrodes evaporated on the germanium crystal and the HEMT electronics. Its capacitance depends on the type of cabling (shielded, material) and is proportional to its length. As a result, lowering the cabling capacitance is ultimately a geometric challenge on the cryostat configuration and the suspended tower. Currently, the cabling capacitance is guaranteed to be lower than 20 pF. As discussed, this would still limit the ionization resolution. With further research on the placement of the HEMT-based electronics in the cryostat a lower resolution could be reached. If the cabling capacitance goes to 5 pF, it would not be the limiting factor for the resolution anymore, while the capacitance of the electrodes becomes limiting. This capacitance depends on the design of the detector and is heavily discussed in the chapter 5.

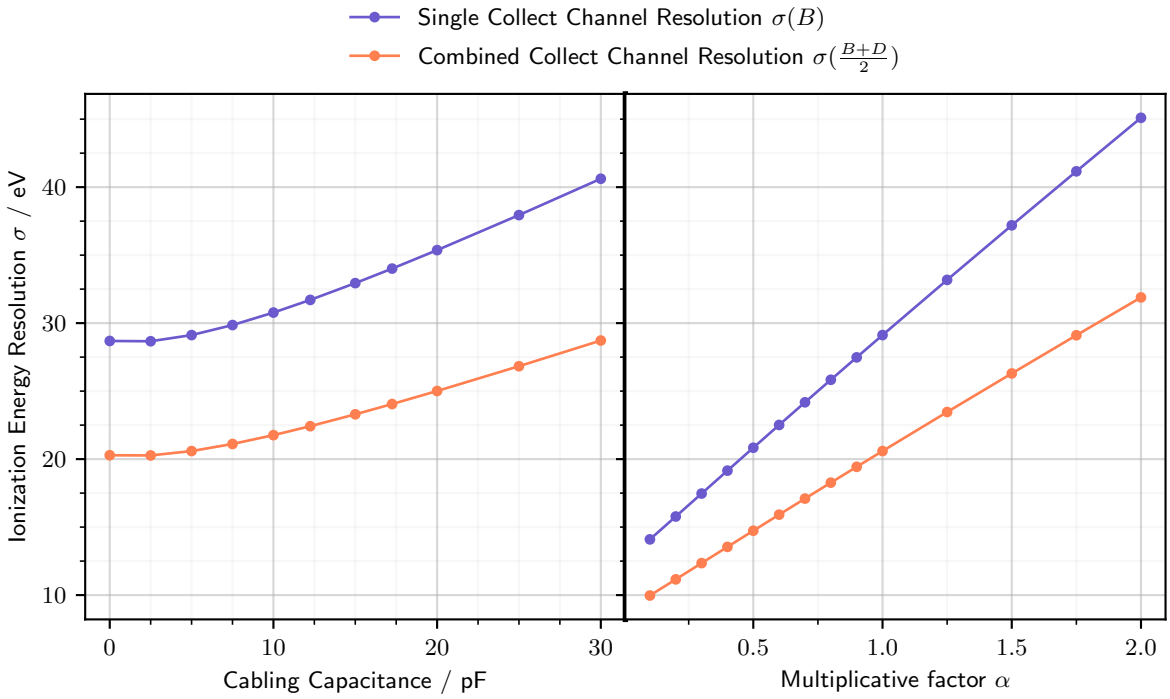

Figure 4.22: Ionization energy resolutions of the PL38 design as functions of the cabling capacitance C_p of the HEMT line and the global multiplicative factor α of the detector Maxwell matrix. The blue curve corresponds to the resolution of the single collect electrode B. The orange curves corresponds to the combination of the signal from B and D inducing a gain of factor $1/\sqrt{2}$ on the initial resolution.

Chapter 5

Electrode Design Optimization

This chapter presents the results of scanning over the parameters of the PL38 and the FID38 design electrostatic simulation. These scans aim at understanding the influence of each parameter on the ionization channel operation. All the design parameters were introduced in the previous chapter 4. For a prompt description of the parameters of the PL38 design, the reader should refer to the table 4.2 and the scheme 4.8. For parameters relative to the FID38 design, the reader should refer to the table 4.3 and the scheme 4.9. This chapter first introduces the methodology used for the parametric scan. It follows with a study of the impact of design parameters shared by both the PL38 and the FID38 designs. Then are presented the studies on the influence of parameters specific to each of these designs.

5.1 Parametric Scanning Methodology

As discussed in the previous chapter 4, the performance of the ionization channel mainly hold in a good charge collection and a low baseline resolution. In order to obtain a low baseline resolution, the ionization channel should present a low noise level combined with a high signal sensitivity. In section 4.2.8, the resolution is derived from the computation of the signal sensitivity and the noise level of the two detectors designs. These computations are based on the Maxwell matrix capacitance obtained from the electrostatic simulation of PL38 and FID38 designs. Scanning the multi-dimensional parameter space of the two detector designs does not allow for this resource-intensive computation chain. However, it was shown in 4.2.8, that the baseline resolution of the ionization channel roughly follows a linear law with the terms of the Maxwell capacitance matrix. Tempering this observation with further insights presented in the previous chapter 4, the Maxwell and mutual capacitance terms can be used as a valid metric when discussing the influence of the design parameters on the detector resolution. The charge collection is a broad expression covering the 1) fiducial volume, 2) the trapping rate and 3) the signal generation from the drifting electric charges. While the real fiducial volume can only be accessed through experimentation, it can be inferred from the knowledge on the electric charge drifting in germanium (see section 4.1.4) and the theoretical fiducial volume obtained with electrostatic simulation (see section 4.2.5). A precise value for the electric charge trapping rate is difficult to forecast in the bulk. However, it is known that region of the crystal with low magnitude of electric field exhibit a higher propensity to charge trapping. It will be demonstrated in chapter 6 using the analysis of the RED80 data, that below a critical threshold of $|\vec{E}| \sim 0.1\,\mathrm{V}\cdot\mathrm{cm}^{-1}$, the trapping rate can be significant. On further notice concerning the signal generation, the electric charge conservation given in equation 6.13 depends on the quality of the Faraday cage formed by the aluminium electrodes which is quantified by the total weighing potential (TWP), as described in section 4.2.4. A low TWP coupled with a high trapping rate could result in substantial fraction of the events to be discarded or worse, ill-reconstructed, in the analysis.

On those grounds, a metric is established for the study of the design parameters influence. For each scanned configuration, the variations over the terms of the Maxwell $\boldsymbol{C}$ and mutual

$\boldsymbol{C}^m$ capacitance matrices, the fiducial volume fraction $\%_{fid}$, the electric field norm $|\vec{E}|$ as well as the weighting potentials Φ_X are documented. In some cases, the variation over the considered capacitance terms C_{XX} is more appropriately illustrated with a ratio:

$$\frac{C_{XX}\,(p = x)}{C_{XX}\,(p = p_0)} \tag{5.1}$$

where p is the scanned parameter, p_0 a reference value (usually the default value) and x the scanned value.

For each detector designs, the configuration of the electrostatic simulation is set by several parameters. Thus, this study calls for a multi-dimensional scan over the design parameters and could even result in a semi-automated optimization of the design like what is achieved for the heat channel in chapter 3. Nevertheless, the performance of the ionization channel cannot be gauged with a single quantity and invalidate such a ionization channel design optimization. As such, the study presented in this chapter focuses on understanding the influence of each parameter by carrying multiples one-dimensional scans. Only one parameter is scanned over at each time with all the other parameters sets to default values. Hence, the control quantities resulting from a scan can be compared to the default design value which was discussed in the previous chapter 4. Although simpler, this method explicitly omits a massive portion of the parametric space. This introduces the risk of scanning far from an optimal configuration and collecting only marginal insights on the ionization channel design. However, this risk is heavily mitigated by the fact that the default configuration of the PL38 and the FID38 detectors designs presented in the chapter 4 are the product of a manual optimization inspired by the whole thesis work on ionization channel.

5.2 Common Parameters

In this section, each subsection presents the scan over a parameter common to the PL38 and the FID38 detector designs. These common parameters are namely the thickness of the aluminium deposit h_{Al}, the distance between the grounded chassis and the germanium crystal d_{Cu}, the bias voltage V_{bias} and the polarization symmetry S_{bias}.

5.2.1 Aluminium Deposit Thickness, h_{Al}

The thickness of the aluminium electrodes used in the COMSOL simulation is noted h_{Al}. It is not in itself a design parameter as the actual thickness depends on the fabrication process and is usually of about 50 nm. This value is much lower than any geometric feature in the COMSOL simulation which, if implemented as is, would induce a complex meshing and a long simulation time. As to keep the simulation resource cost reasonable, the electrostatics simulation are ran with a greater thickness than in reality at the price of small supplementary errors. For the FID38 geometry, the electrostatic simulation is ran multiple times scanning over the electrode thickness h_{Al}. The table 5.1 presents for each value of h_{Al} the number of triangles in the mesh, the diagonal Maxwell capacitance of top collect (B) electrode C_{BB} and the relative error on this capacitance. The reference for the error calculation is considered to be the capacitance computed for the lowest value $h_{Al} = 0.1\,\mu\text{m} = 100\,\text{nm}$ which is very close to the actual 50 nm thickness of the aluminium deposits.

As expected from simulating thin electrodes, the number of triangles composing the mesh is drastically increased. Also, as the electrodes presents a lower area, their capacitance is slightly lowered, eventually capping for the lowest thickness values. In other words, the computation of the capacitance term is getting more precise with decreasing electrode thickness. A trade-off

h_{Al} / µm	# Triangles	C_{BB} / pF	Relative Error / %
100	7413	20.419	7.3
30	13959	19.560	2.8
10	22504	19.232	1.1
3	34745	19.102	0.4
1	58815	19.053	0.1
0.3	76637	19.034	0.02
0.1	106057	19.029	0

Table 5.1: Scanning over the electrode thickness h_{Al} of the FID38 design. The control values are the number of triangles in the mesh, the first diagonal term of the Maxwell capacitance matrix and the relative error on the capacitance calculation with the lowest thickness $h_{Al} = 0.1\,\mu m$ chosen as reference.

is selected at $h_{Al} = 1\,\mu m$ with a relative error of 0.1 %. Indeed, this quantity is reminiscent of the relative error of 0.08 % induced by the chosen mesh scale "Fine" presented in section 4.2.2.

5.2.2 Chassis Distance, d_{Cu}

The chassis distance d_{Cu} is the distance between the grounded copper chassis and the planar and lateral faces of the germanium crystal. Its default value is set to 3 mm for both the PL38 and the FID38 design. The scan is performed on a logarithmic scale from 0.1 mm to 10 mm. The results are presented in the figure 5.1 for the PL38 design and in the figure 5.2 for the FID38 design. Both figures display the terms of the Maxwell $\boldsymbol{C}$ and mutual capacitance matrix $\boldsymbol{C}^m$ along with the fiducial volume fraction $\%_{fid}$ as functions of the chassis distance d_{Cu} for their respective detector design. Additionally, percentiles f_x of the electric field norm $\|\mathbf{E}\|$ distribution are plotted for the FID38 design.

We can first discuss the trends common to both design. The percentage of fiducial volume $\%_{fid}$ increases with the chassis distance d_{Cu} and reaches a plateau. This effect is slight in the case of the PL38, with a gain of about 2.75 % between the extremes values of d_{Cu}. This is explained by a contraction of the exiting streamlines regions on the lateral surfaces and under the central NTD hole. In the case of the FID38, the effect is more significant with a growth of about 6.5 % from 10^{-1} mm to 10^{1} mm. The reason is the reduction of the depth of the veto regions inducing a raise in fiducial volume.

For both detector designs, the non-diagonal term of the mutual matrices C^m_{XY} increases with the chassis distance to reach a plateau. The asymptotic values of these plateaus corresponds to the grounded chassis being infinitely far from the electrodes. In the case of the PL38 design, the asymptotic mutual capacitance $C^m_{AB}(d_{Cu} \to \infty) \approx 11.5\,pF$ is close to the naive parallel two-plate capacitor $C_{\parallel} = 10.2\,pF$, the capacitance of PL28 being superior due to the corner aluminium deposits on the lateral surface. With the increasing distance between the grounded chassis and the electrodes, the diagonal terms of the Maxwell capacitance matrix C_{XX} diminishes following two emerging regimes. In the first regime for low chassis distance ($d_{Cu} \leq 1\,mm$ for PL38 and $d_{Cu} \lesssim 0.6\,mm$ for FID38), the self-capacitance term dominates the calculation of the diagonal Maxwell terms. Indeed, with a very close chassis, the capacitive coupling between the ground and the electrodes overshadows the other couplings. As the chassis moves away, the calculation of the diagonal Maxwell terms is dominated by the inter-electrodes coupling terms C^m_{XY}.

The heightened influence of the copper chassis is also observed for the total weighting potential (TWP). On the surfaces of the detectors bare of aluminium electrodes, the TWP is as low

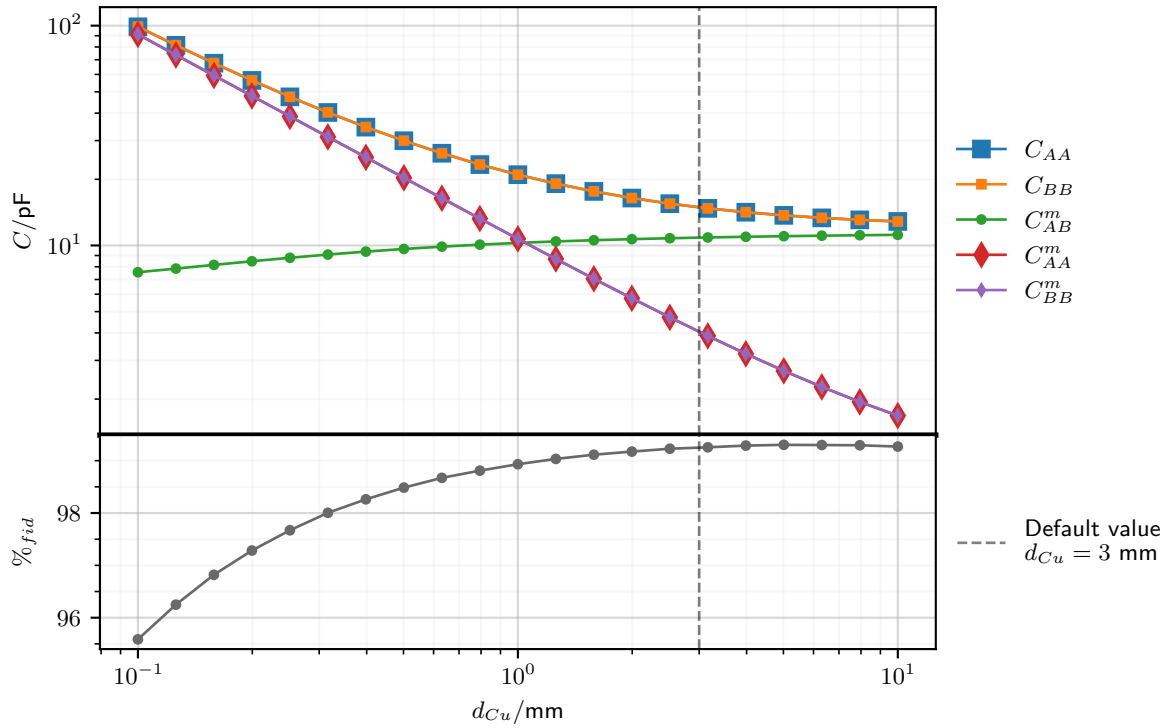

Figure 5.1: Scan over the chassis distance d_{Cu} for the PL38 design. The Maxwell and mutual capacitance terms and the percentage of fiducial volume $\%_{fid}$ are plotted separately. The default value $d_{Cu} = 3\,\text{mm}$ is represented by the dashed vertical line. Error bars are smaller than the marker size.

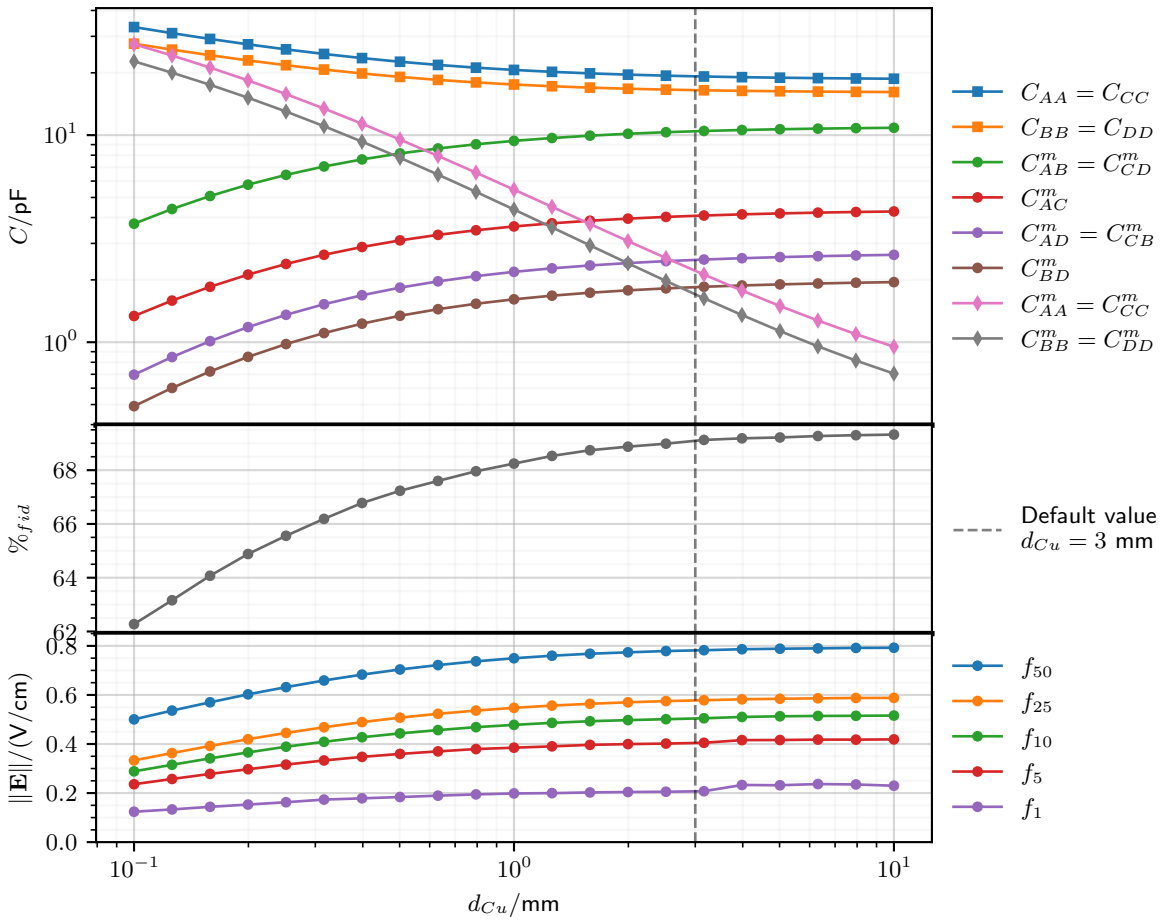

Figure 5.2: Scan over the chassis distance d_{Cu} for the FID38 design. The Maxwell and mutual capacitance terms, the percentage of fiducial volume $\%_{fid}$ and some percentiles f_x of the electric field norm $\|\mathbf{E}\|$ are plotted separately. The default value $d_{Cu} = 3\,\text{mm}$ is represented by the dashed vertical line. Error bars are smaller than the marker size.

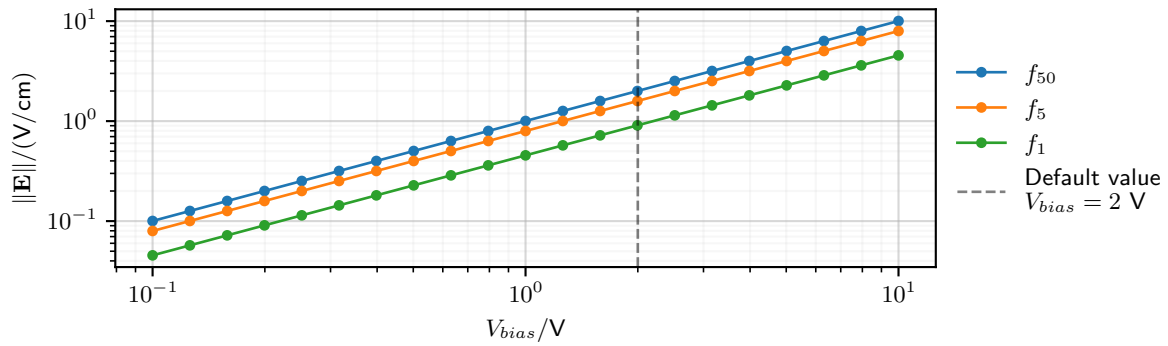

Figure 5.3: Scan over the bias voltage V_{bias} of the PL38 design. Some percentiles f_x of the electric field norm $\|\mathbf{E}\|$ are plotted. The default value $V_{bias} = 2\,\mathrm{V}$ is represented by the dashed vertical line. Error bars are smaller than the marker size.

as 0.3 for minimal d_{Cu} as the drifting electric charges induce a lot of signal on the close electric ground. For the maximal value of d_{Cu}, the TWP reaches 0.975 on the surface as the copper chassis is too far away from the drifting charges to collect a significant fraction of the signal.

The behavior of the magnitude of the electric field $\|\mathbf{E}\|$ differs between the PL38 and FID38 designs. For the former, the magnitude is almost constant in the crystal except for slight variation on the bare lateral surface and the under the central NTD hole. For the latter design, the last subplot of the figure 5.2 shows a global increase of the electric field norm with the chassis distance as all the percentiles of the distribution are concerned by the growth.

The results points towards better detector performances with a high chassis distance. Indeed, for both designs, the fiducial fraction increases, the capacitance terms globally decreases, the total weighting potential tends to 1 and the electric field norm even grows for the FID38. The constraint on the chassis distance is imposed by the maximal dimensions of the detector load in the cryostat. As all the control quantities asymptotically reach a plateau with high chassis distance starting from $d_{Cu} \gtrsim 1\,\mathrm{mm}$, the value $d_{Cu} = 3\,\mathrm{mm}$ is chosen for the detector designs. At this value, the contribution to the Maxwell capacitance C_{XX} from the chassis through the self-capacitance C^m_{XX} represents approximately 30 % for the PL38 and 10 % for the FID38 design.

5.2.3 Bias Voltage, V_{bias}

The bias voltage V_{bias} corresponds to the voltage between the two main electrodes of the detectors. By default, it set to 2 V in order to apply the standard electric field magnitude of $2\,\mathrm{V}\cdot\mathrm{cm}^{-1}$ used for the operation of the EDELWEISS germanium detectors. The scan is performed on a logarithmic scale from 10^{-1} V to 10^{1} V. The results are presented in the figure 5.3 for the PL38 design and in the figure 5.4 for the FID38 design. Both figures display some percentiles f_x of the electric field norm $\|\mathbf{E}\|$ distribution.

As the bias voltage solely affects the polarization of the electrodes, the capacitance terms and the total weighting potential are unaffected for this scan. Moreover, according to the equations 4.35 and 4.37 , the electric potential of all the electrodes are proportional to the parameter V_{bias}. As such, the electric field lines as well as the theoretical fiducial volume are unchanged for this scan. For both designs, the electric field in the crystal scales proportionally with the voltage bias V_{bias}. At lower voltage, the magnitude could be lower than the critical threshold.

A high magnitude is preferred for a good charge collection. However, according to the discussion in section 2.3.2, a low voltage bias yields a better discrimination between electronic and nuclear recoils thanks to the lowered Luke-Neganov effect. Balancing this two aspects, we choose the lowest bias voltage possible while keeping a reasonable fraction of the volume above

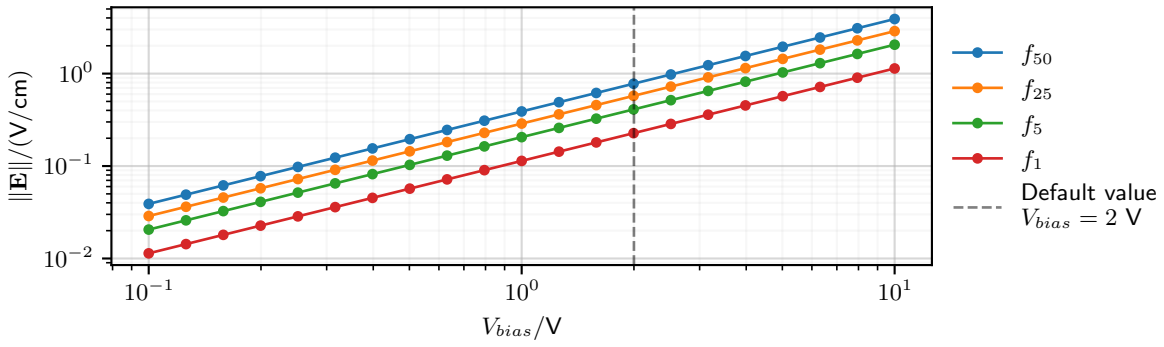

Figure 5.4: Scan over the bias voltage V_{bias} of the FID38 design. Some percentiles f_x of the electric field norm $\|\mathbf{E}\|$ are plotted. The default value $V_{bias} = 2\,\mathrm{V}$ is represented by the dashed vertical line. Error bars are smaller than the marker size.

the critical magnitude threshold. For now, the bias voltage $V_{bias} = 2\,\mathrm{V}$ is selected for both the PL38 and FID38 designs.

5.2.4 Polarization Symmetry, S_{bias}

The polarization symmetry S_{bias} is a parameter used to set the global symmetry of the polarization for the PL38 according to equation 4.35 and FID38 according to equation 4.37. The scan is performed on a linear scale from 0 to 1, with $S_{bias} = 0.5$ fixing a symmetric polarization and being the default value for this parameter. As the polarization symmetry parameter S_{bias} solely affects the electric potential of the electrodes, the capacitance terms and the total weighting potential are unaffected in both designs for this scan. As such, the impact of the polarization symmetry S_{bias} on the electrode design is quantified with the distribution of the electric field magnitude $\|\vec{E}\|$ over the germanium crystal volume. For the PL38 design, the fiducial volume percentage $\%_{fid}$ and some percentiles f_x of the electric field norm $\|\vec{E}\|$ distribution are plotted in the figure 5.5.

The symmetry parameter S_{bias} has more influence for the PL38 design. As shown in the figure 5.5, asymmetrical polarization feature a slightly lowered fiducial volume percentage compared to the optimum for the symmetrical polarization. As the electric potential of the top or bottom electrode goes to 0 V, same as the grounded copper chassis, more field lines near the surface are exiting the crystal. Additionally, the electrode with nullified potential sees its low electric field magnitude corner gain in volume. As a result, the magnitude distribution over the crystal volume is broaden towards lower value as shown by the significant decrease of the percentiles f_1 and f_5 for asymmetrical polarization value. The influence of the parameter S_{bias} is mitigated by the lateral corners of the electrodes and their length L_{lat}. The observed trends are expected to be exacerbated for PL38 designs with lower or non-existent lateral corners.

It seems that the effects of the parameter S_{bias} are minors. While there exists an optimum in performances for a symmetric polarization at $S_{bias} = 0.5$, operating the PL38 and FID38 with asymmetrical electrode potential is viable and could potentially alleviate some future issues with the influence of the NTD thermal sensor on the electric field or unexpected leakage currents.

In the case of the FID 38 design, the fiducial volume and the electric field norm distribution are unchanged. With varying S_{bias}, variations in the electric potential are plenty in the vacuum surrounding the crystal and only negligible changes in the shape of the electric field lines are observed inside the germanium crystal near the equator.

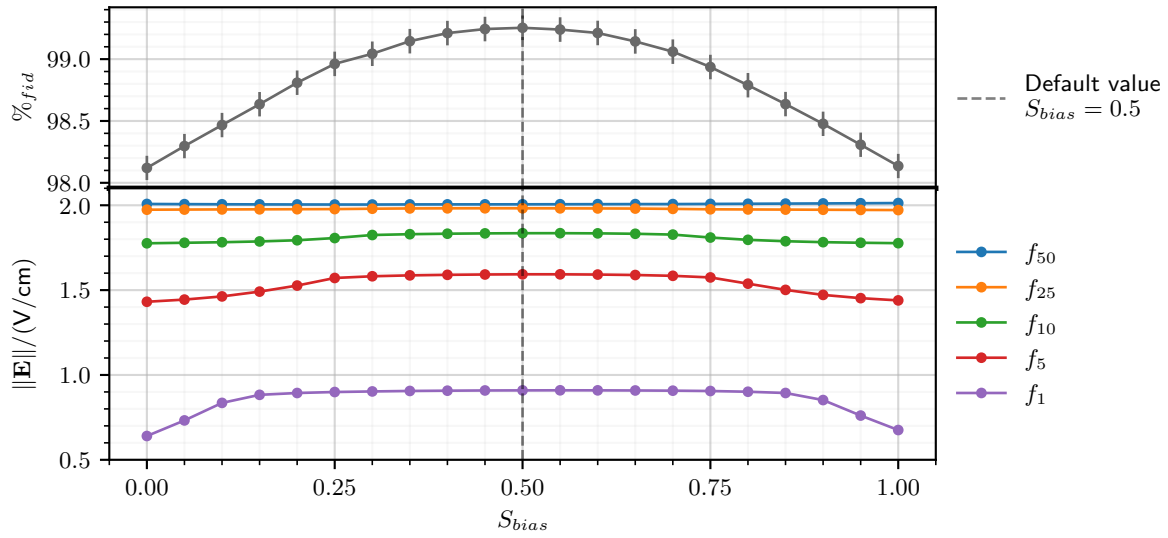

Figure 5.5: Scan over the polarization symmetry S_{bias} of the PL38 design. The percentage of fiducial volume and some percentiles f_x of the electric field norm $\|\mathbf{E}\|$ are plotted. The default value $S_{bias} = 0.5$, corresponding to the symmetric polarization, is represented by the dashed vertical line. Error bars are smaller than the marker size.

5.3 Specific to PL38

This section is attributed to the PL38 design. Each subsection presents the scan over a parameter. They are namely the radius of the central NTD hole r_{center} and the length of the lateral corners of the electrodes L_{lat}.

5.3.1 Radius of the central hole for the NTD, r_{center}

In order to glue the NTD thermal sensor on bare germanium, a central hole of radius r_{center} is made on the top electrode of the PL38 design. By default, the radius is set to $r_{center} = 1.5\,\mathrm{mm}$ to fit a standard $(2 \times 2)\,\mathrm{mm}$ NTD thermal sensor. Another significant radius is $r_{center} = 3\,\mathrm{mm}$ which can fit a larger $(4 \times 4)\,\mathrm{mm}$ NTD thermal sensor. The scan is performed on a linear scale from 0 mm to 5 mm. The results of the scan are presented in figure 5.6 with the fiducial volume percentage and capacitance term ratio.

The figure shows that all the capacitance terms decreases with r_{center} except for the self-capacitance of the bottom electrode C^m_{BB}. Indeed, as the hole in the top electrode A grows, the bottom electrode B faces an increasing area of grounded chassis through the hole. On the contrary, as the hole grows in size, the top electrode A lose in area thus reducing its coupling with the ground and the bottom electrode B. The inter-electrode coupling term C^m_{AB} is dominant in the calculation of the diagonal Maxwell terms C_{XX} and imposes its decreasing trend with r_{center}. One should note that the variations on the capacitance terms are inferior to 3 % and thus almost negligible. The growing central hole in the electrode induces a greater low electric field magnitude region under it. Electric field lines are diverging from this low magnitude region resulting in a lower theoretical fiducial volume. However, according to the figure 5.6, this reduction is almost negligible with just about 0.3 % between the extrema. This negligible impact is also showed by the percentiles of the electric field norm f_x which seem rather constant with a perceptible decreasing trends for high value values of r_{center}. Indeed, as the change induced by the central radius r_{center} is located on the central axis of the crystal, it affects only a marginal fraction of the total volume. In line with this remark, the distribution of the electric field magnitude

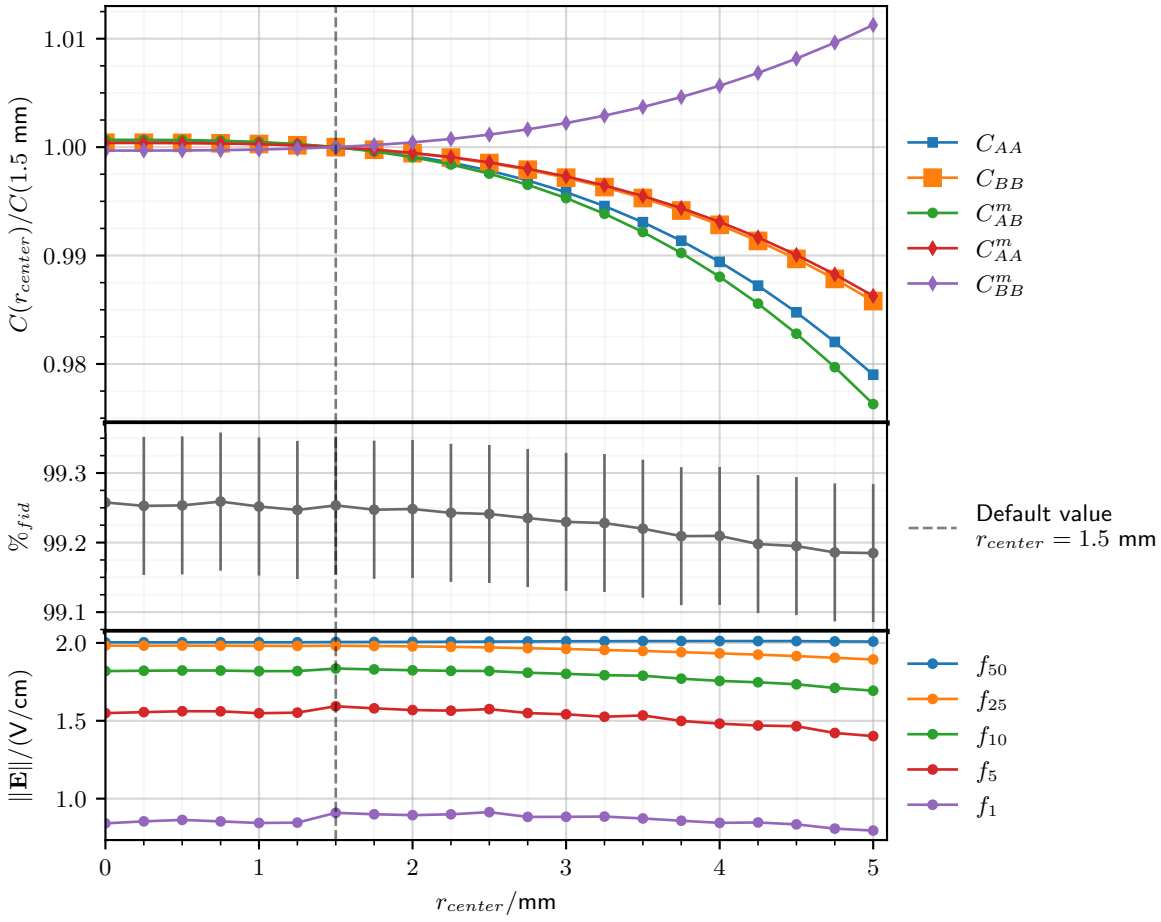

Figure 5.6: Scan over the radius of the central NTD hole r_{center} of the PL38 design. The Maxwell and mutual capacitance terms ratio, the percentage $\%_{fid}$ of fiducial volume and some percentiles f_x of the electric field norm $\|\mathbf{E}\|$ are plotted. The capacitance term ratio is calculated with the default capacitance value, from equation 4.59, as denominator. The default value $r_{center} = 1.5\,\mathrm{mm}$ is represented by the dashed vertical line.

on the volume is negligibly affected by the scan over r_{center}. Even though the impacted volume is very low, the central hole creates a surface bare aluminium electrode with a very low electric field. As a result, recoils in this region should be prone to surface trapping.

As for the total weighting potential, there is a slight decrease on the surface in the central hole from 1, with a non-existent hole, to 0.94, with the largest value $r_{center} = 5\,\text{mm}$.

Although the performances of the ionization channel would be optimal with no central NTD hole, with $r_{center} = 0\,\text{mm}$, the variation on the control values are almost negligible. The trade-off presented by the parameter r_{center} holds in a balance between a higher heat sensitivity with a NTD thermal sensor glued on bare germanium and a possible problematic charge collection under the central NTD hole. As a result, the lowest radius possible is favored for the designs. In the case of the standard (2×2) mm NTD thermal sensors, it corresponds to $r_{center} = 1.5\,\text{mm}$.

5.3.2 Corner length, L_{lat}

The planar electrodes of the PL38 design extends on the lateral surfaces on a length L_{lat} deemed corner length. The default value is $L_{lat} = 2\,\text{mm}$. The scan is performed on a linear scale from 0 mm to 4.8 mm (at a value of 5 mm, the top and bottom electrode would be in contact). The results of the scan are presented in the figure 5.7 with the terms of the Maxwell and mutual capacitance matrices, the percentage of fiducial volume and some percentiles of the electric field magnitude distribution.

As the corner length increases, the area of the top and bottom electrode grows. The self-capacitance terms C^m_{XX} increases as the coupling with the ground rises but eventually seem to reach a plateau. The inter-electrode coupling term C^m_{AB} increases with L_{lat} especially at the highest values. Indeed, at high value of L_{lat}, the electrodes A and B are larger and also closer near the equator. As the corner length tends to 5 mm, with virtually touching top and bottom electrodes, the diagonal Maxwell terms diverge. On the same line, the electric field at the equator also diverge with ever closer top and bottom electrode, broadening the magnitude distribution toward higher values. On the contrary, the electric field norm is lessened in the corners as the corner length increases and these low magnitude corner regions grow in size. As a result, the magnitude distribution expands toward lower values. This is illustrated with the decreasing percentiles f_1 to f_{25} on the figure 5.7. As a side note, the median magnitude of the electric field f_{50} is constant for this scan. In the case of very short corner electrodes $L_{lat} \leq 0.5\,\text{mm}$, the electric field norm is almost homogeneously equal to $2\,\text{V} \cdot \text{cm}^{-1}$ in the crystal. In fact, the electric field is almost uniform with the surface electric field lines bending towards the outside and eventually exiting the crystal, resulting in a loss of fiducial volume at low L_{lat} values. With larger corner length, the fiducial volume fraction increases and caps at 99.4 %. This limit is set by the streamlines which are exiting the crystal at the surface of the central NTD hole. The total weighting potential on the bare lateral surface of the crystal increases slightly with the corner, starting from 0.94 for a non existent corner $L_{lat} = 0\,\text{mm}$ and reaching 0.99 for a maximum corner length of 4.8 mm.

This scan over the corner length L_{lat} features a performance balance: at low corner length, the capacitance terms are lowered and a high electric field norm is achieved, while for a high corner length, the fiducial volume is greater. As the variation on the fiducial volume is small, the control values points towards a performance optimization for the lowest value of the corner length $L_{lat} = 0\,\text{mm}$. However, with this minimal value, the whole lateral surface of the germanium crystal is bare and prone to surface trapping due to the transversal trajectory of the electron in the crystal, as discussed in paragraph 4.1.4. A conservative trade-off value is the default value $L_{lat} = 2\,\text{mm}$.

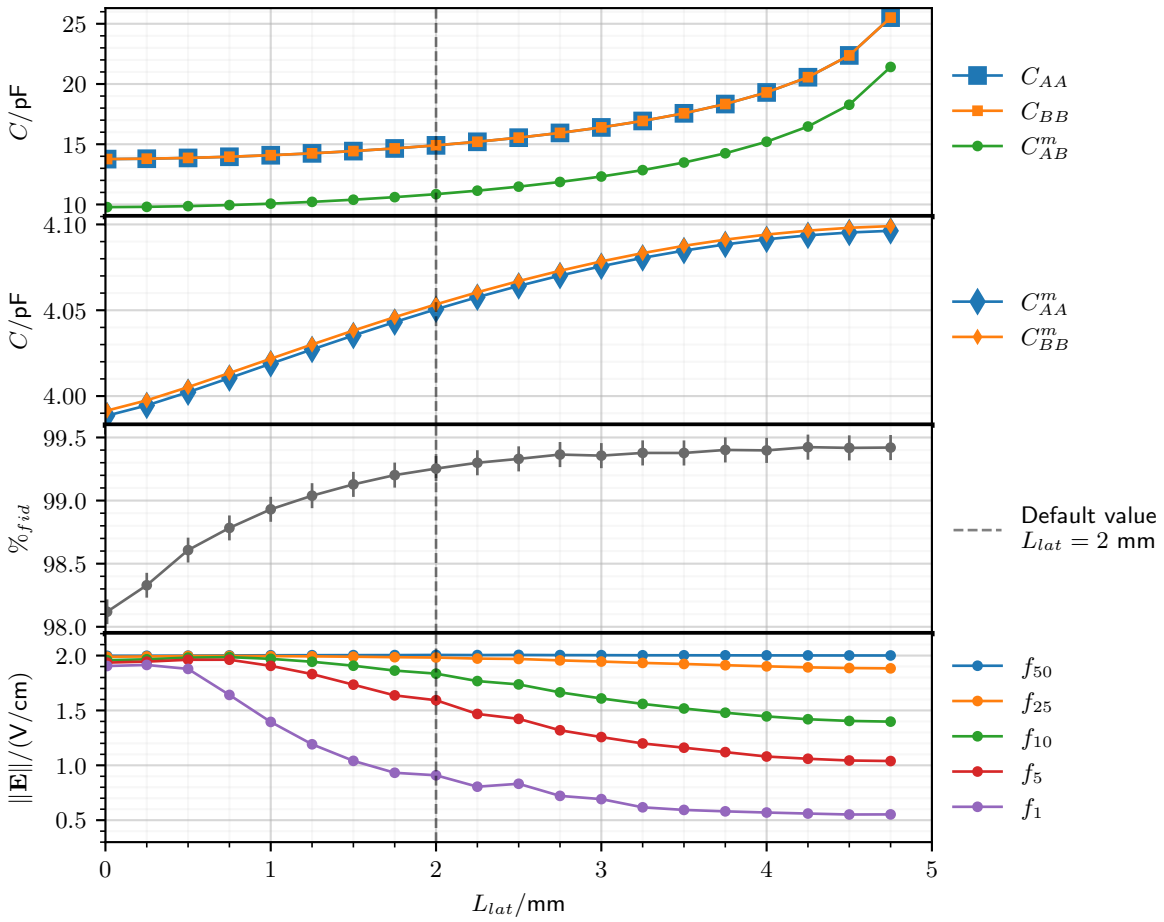

Figure 5.7: Scan over the corner length L_{lat} for the PL38 design. The Maxwell and mutual capacitance terms, the percentage of fiducial volume and some percentiles of the electric field magnitude distribution are plotted. The default value $L_{lat} = 2$ mm is represented by the dashed vertical line. Error bars for the capacitance terms are smaller than the marker size.

5.4 Specific to FID38

This section is attributed to the FID design. Each subsection presents the scan over a given parameter. They are namely the width of the electrode rings w_{Al}, the radius of the central veto pad r_{center}, the distance between the edge of the crystal and the outermost planar electrode w_{bare}, the width of the outermost planar electrode w_{outer}, the equatorial distance d_{eq}, the polarization ratio R_{veto} and the number of planar and lateral electrodes, n_{plan} and n_{lat} respectively. As the effects of the four latter parameters are heavily correlated, one part of this section is dedicated to the global scaling of the electrode density, scanning over selected configurations of this four parameters.

5.4.1 Width of the Electrode Rings, w_{Al}

The width w_{Al} of the rings composing the electrodes is set by default to 0.08 mm. The scan is performed on a linear scale from 0.05 mm to 1.55 mm. The results of the scan are presented in figure 5.8. They consist in graphs of the terms of the Maxwell and mutual capacitance matrices, the percentage of fiducial volume $\%_{fid}$ and some percentiles f_x of the electric field magnitude distribution.

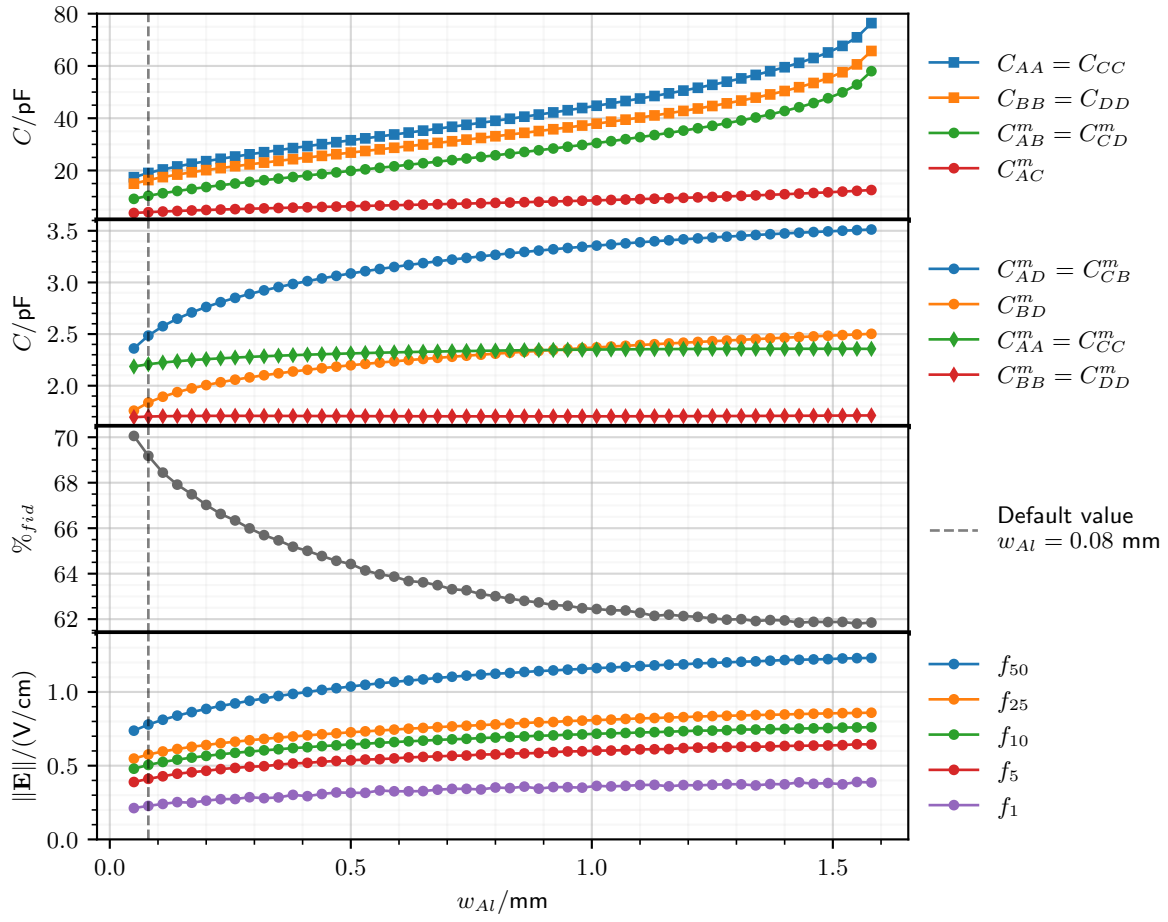

Figure 5.8: Scan over the width of the electrode rings w_{Al} for the FID38 design. The Maxwell and mutual capacitance terms, the percentage of fiducial volume and some percentiles of the electric field magnitude distribution over the crystal are plotted. The default value $w_{Al} = 0.08$ mm is represented by the dashed vertical line. Error bars are smaller than the marker size.

With a rising ring width w_{Al}, all electrodes gets closer to each other and their effective facing area increases. This explains the global rise of the capacitance with the ring width. The effect is most pronounced for the capacitive coupling term between same-sided veto and collect electrode C^m_{AB} and C^m_{CD} which diverges as the electrode spacing tends to zero. The coupling between the two veto electrodes C^m_{AC} moderately grows from the equatorial rings getting slightly closer. The remaining mutual term do not benefit from the decreasing spacing, and thus the increase induced by w_{Al} is light. As sums of the mutual terms, the diagonal Maxwell capacitance term follows the increasing trend with diverging for high ring width. There is a significant decrease of the fiducial volume with increasing ring width until approximately 1 mm where a lower cap seems to be reached. As the electrode ring gets larger, the veto regions gain in depth, reducing the fiducial volume. This is consistent with the position of the low electric field magnitude regions under the veto rings getting deeper into the crystal. As the veto and collect electrodes are getting closer, the electric field in the veto regions greatly increases and grows more gently in the bulk of the crystal. Overall, the electric field norm globally rises with the ring width w_{Al} and approaches a plateau at high value. With higher w_{Al}, the total weighting potential on bare germanium surface slightly rises from 0.94 for the thinnest ring, to 0.98 for the largest ring possible before contact. Indeed, the grounded chassis is overshadowed by the large electrode and receives a reduced induced signal from the drifting electric charge.

The results of the scan show that a high width for the electrode rings is very detrimental to the capacitance terms and the fiducial volume. The only upside to large electrodes would be a guaranteed charge collection in the vicinity of the electrodes in response to a surplus of surface trapping. This issue has yet to be seen experimentally on any detector with thin electrodes. Moreover, as the electric field is amplified near the electrode though point effect, drifting electric charge in their vicinity is even less prone to transversal trajectory and surface trapping. As such, the FID38 design can have its best performance with the lowest ring width feasible, $w_{Al} = 0.05$ mm. At the moment, this parameter is subject to technical constraints as it is not possible to reliably deposit continuous aluminum ring of width inferior to 50 µm.

5.4.2 Central Pad Radius, r_{center}

In place of a hollow ring, the centers of the planar surfaces are occupied by a central disk pad of radius r_{center}. This central pad is attributed to the veto electrodes A and C. Its default value is of 0.25 mm. While for the default FID38 design, the NTD thermal sensor is meant to be glued on a veto electrode ring, an alternative would be to use a large central pad for the NTD gluing. The scan is performed on a linear scale from 0.08 mm to 5 mm. The results of the scan are presented in the figure 5.9. They consist in graphs of the Maxwell C_{XY} and mutual C^m_{XY} capacitance matrices terms, the percentage of fiducial volume $\%_{fid}$ and some percentiles f_x of the electric field magnitude distribution.

As r_{center} increases, the free planar space remaining for the other planar electrode rings decreases. This results in an increase in the planar ring density and a decrease in the planar ring spacing d_{plan}. The variation of the capacitance terms are modest for this scan. Therefore, the first plot of the figure 5.9 is the ratio of the capacitance terms over their value at default value 0.25 mm. The two decreasing capacitance terms are the self-capacitance of the main collect electrode B and D, as well as their coupling term C^m_{BD}. As the central veto pad grows, the innermost collect electrode rings are pushed away from the center. Apparently it emulates a loss of facing electrode area between the top collect electrode B , the bottom collect electrode D and the ground. The coupling term between the two veto electrodes C^m_{AC} is increased, which can be attributed to the growth of the central veto pad facing each other. The highest augmentation in capacitance is held by the coupling terms between same-sided veto and collect electrode $C^m_{AB} = C^m_{CD}$. It is explained by the lowered spacing between the planar electrode rings. As usual, the diagonal Maxwell capacitance terms C_{XX} follows a similar trends to the dominating terms

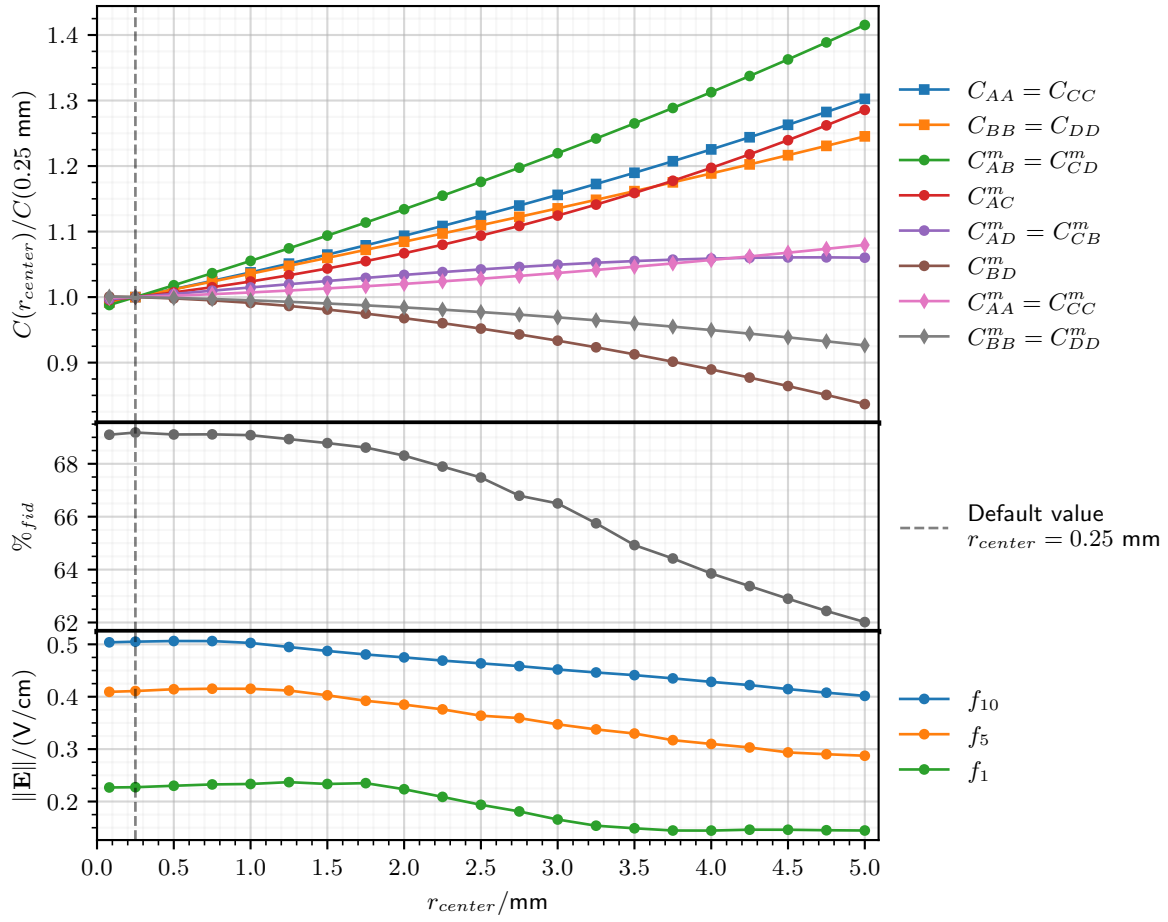

Figure 5.9: Scan over the radius r_{center} of the central planar aluminium pad for the FID38 design. The ratio of Maxwell and mutual capacitance terms, the percentage of fiducial volume and some percentiles of the electric field magnitude distribution are plotted. The default value $r_{center} = 0.25$ mm is represented by the dashed vertical line. Error bars for the capacitance ratio are smaller than the marker size.

$C^m_{AB} = C^m_{CD}$. Concerning the fiducial volume, its percentage decreases with increasing central pad radius r_{center}. In fact, this loss is attributed to the growth of the veto region under the central pad. As this loss is centered on the rotational axis of the crystal, the loss is very light for low value of r_{center}. The remarkable value $r_{center} = 1.5\,\text{mm}$, allowing for the gluing of a $(2 \times 2)\,\text{mm}$ NTD, shows a negligible decrease. However, the diminution in fiducial volume gets significant with higher radius. Only the electric field norm in the center of the crystal is lowered by rising scanned parameter r_{center}. While the median f_{50} of the magnitude distribution (not represented on figure 5.9) is constant, the distribution is expanded towards lower values. This is illustrated by the decreasing values of the percentiles f_1 to f_{10}. The explanation is the growth of the top and bottom low magnitude regions under the central veto pads which eventually merge for 3 mm. At this point, the electric field is nullified at the center of the crystal. With greater r_{center}, the electric field changes in direction with field lines connecting the top and bottom central veto pads.

The result shows that all aspects of the performance of the ionization channel would profit from a small central pad radius r_{center}. The minimal value corresponds to the width of the electrode rings $r_{center} = 0.08\,\text{mm}$. This study also demonstrates that at the cost of a small increase in capacitance, it would be viable to use a radius of 1.5 mm to fit a small NTD thermal sensor if needed.

5.4.3 Edge Veto Electrodes

The outermost rings of the veto electrodes near the planar edge of the crystal are called the edge veto electrodes. Due to their important role in shaping the electric field in the corners of the crystal and the constraints on the aluminum deposition at this location, the geometry of these corner veto electrodes calls for particular attention. The constraints on the aluminum deposition depends on the techniques used. When using a deposition with mask, aluminum cannot be closer than 0.3 mm from the edge of the crystal. This results in the creation of a bare edge of width $w_{edge,bare} \geq 0.3\,\text{mm}$. In the case of a deposition on the whole planar faces followed by photo-lithography, aluminum cannot be removed closer than 1 mm from the edge of the crystal. This technique thus results in large corner veto electrodes of width $w_{outer} \geq 1\,\text{mm}$. This section is separated in two studies, each investigating the two geometries for these edge veto electrodes.

Thin Outer Ring Spaced from the Crystal Edge, Scan over w_{bare}

In this paragraph, we consider an aluminium deposition with a mask. The outermost planar ring is thin with a width of $w_{outer} = 0.08\,\text{mm}$. This outermost ring is spaced by a bare germanium surface of width w_{bare} from the edge of the crystal. The scan is performed over the this bare germanium width w_{bare} with a linear scale from 0 mm to 2 mm. The reference configuration corresponds to the default FID38 design presented in the previous chapter 4. The edge veto electrodes are set to be as close as possible to the edge of the crystal with $w_{bare} = 0.3mm$. The results of the scan are presented in the figure 5.10. They consist in graphs of the ratio of the terms of the Maxwell and mutual capacitance matrices, the percentage of fiducial volume $\%_{fid}$ and some percentiles f_x of the electric field magnitude distribution. The constraint on the minimal feasible bare width $w_{bare} \geq 0.3\,\text{mm}$ is represented by the shaded region.

As the width of the bare edge increases, the free space available for the deposition of the other planar electrode ring diminishes. As a result, with the parameter w_{bare} rising, the planar ring spacing d_{plan} decreases. The variation of the capacitance terms is very low, in the range of 5 %, for this scan. Thus, the first plot of the figure 5.9 is the ratio of the capacitance terms over their value at default value 0.3 mm. A large width w_{bare} induces an increase in capacitance, due to the lowered planar spacing. The coupling term of same-sided veto collect $C^m_{AB} = C^m_{CD}$ decreases for low or high value of w_{bare} with a maximum near 0.6 mm. For low w_{bare} value, the

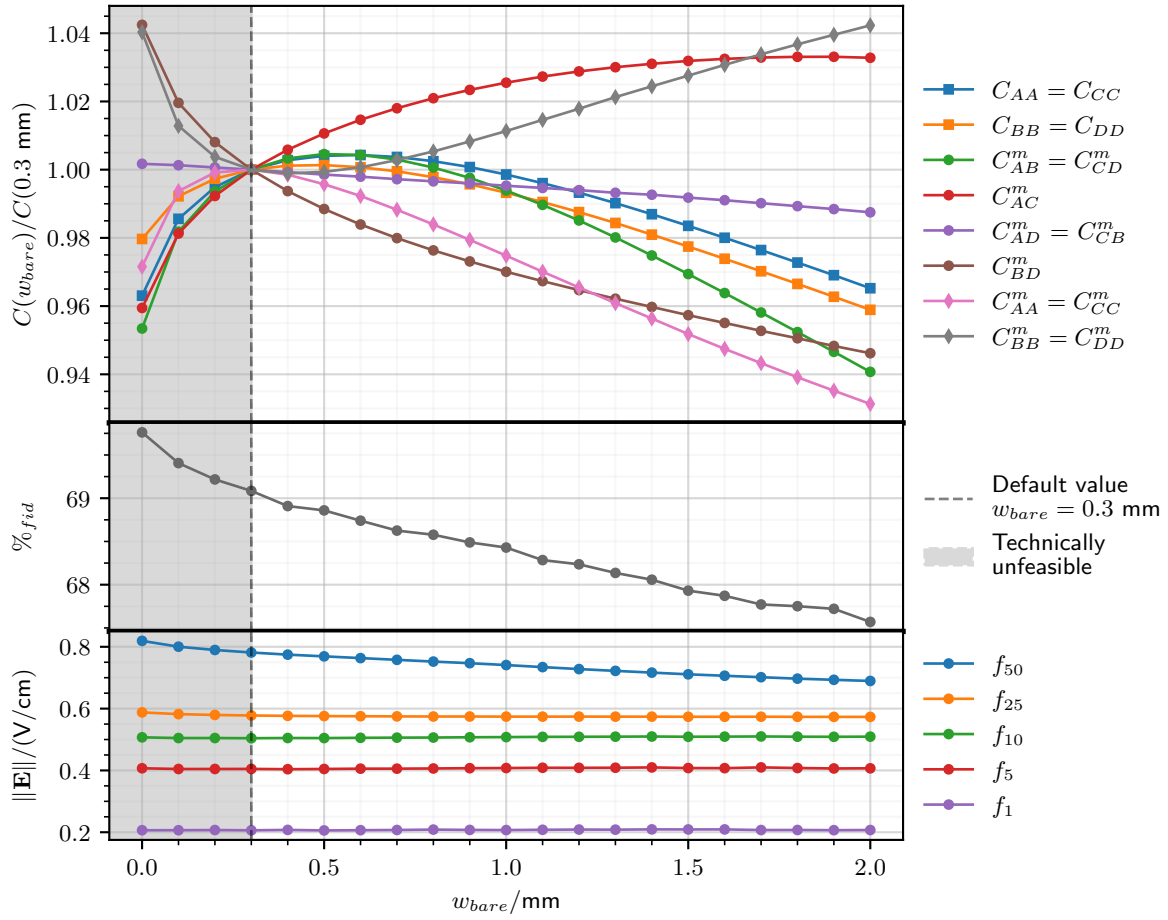

Figure 5.10: Scan over the width of bare germanium w_{bare} between the outermost planar electrode ring and the crystal edge for the FID38 design. The ratio of the Maxwell and mutual capacitance terms, the percentage of fiducial volume and some percentiles of the electric field magnitude distribution over the crystal volume are plotted. The capacitance term ratio is calculated with the default capacitance value as denominator. The default value $w_{bare} = 0.3\,\mathrm{mm}$ is represented by the dashed vertical line. A width strictly inferior to 0.3 mm is technically unfeasible which is represented by the shaded area. Error bars are smaller than the marker size.

planar spacing d_{plan} is high which explains the lowered capacitance between same-sided veto and collect electrode $C^m_{AB} = C^m_{CD}$. For high w_{bare}, the planar spacing d_{plan} diminishes, explaining the maximum, but is eventually dominated by the loss of coupling due to the larger distance between the planar rings and the lateral rings. The coupling term of the veto electrodes C^m_{AC} increases and cap with w_{bare}: the veto edge electrode rings are no longer overshadowed by the lateral collect electrodes. The coupling term of the collect electrodes C^m_{BD} decreases with w_{bare} as their effective facing area is lowered by their contracting rings. The self-capacitance of the veto electrodes $C^m_{AA} = C^m_{CC}$ shows a maximum around 0.3 mm. The self-capacitance of the collect electrodes $C^m_{BB} = C^m_{DD}$ features a minimum around 0.4 mm. In the end, the diagonal terms of the Maxwell capacitance matrix C_{XX} follows the trend of the dominant term C^m_{AB} with smooth maximum between 0.3 mm and 0.8 mm. The bare germanium width slightly changes the shape of the electric field lines in the crystal corners. The veto regions are growing near the corners As a result, the fiducial volume is slightly decreasing with rising w_{bare}. We also note that with $w_{bare} > 0$ mm, there is appearance of the corner regions with uncertain charge collection, as discussed in the previous chapter 4. In the vicinity of the corners, the total weighting potential on the surface is lightly affected. It decreases from 0.94 at default configuration to 0.86 with $w_{bare} = 2$ mm. With a high w_{bare} corner regions feature a lower value than default electric field norm. As a result, the median of the magnitude distribution in the crystal volume decreases moderately. However, the lower percentiles $f_{x\leq 25}$ remains stable.

For the best value considering the bare width, the results points towards the minimal $w_{bare} = 0$ mm which is not currently feasible. A high w_{bare} would reduce marginally the capacitance values at the cost of creating large corner regions with uncontrolled charge collection. All in all, the minimum technically feasible value $w_{bare} = 0.3$ mm seems to be the best configuration for a thin outer veto electrode ring.

Large Outer Ring on the Crystal Edge, Scan over w_{outer}

We now consider an aluminium deposition on the full planar surface followed by photo-lithography. The outermost planar ring is in contact with the crystal edge for $w_{bare} = 0$ mm. This outermost ring is large with a width of w_{outer} which is scanned over in this paragraph. The scan is performed over a linear scale from 0 mm to 2 mm. The results of the scan are presented in figure 5.11. They consist in graphs of the ratio of the terms of the Maxwell and mutual capacitance matrices, the percentage of fiducial volume $\%_{fid}$ and some percentiles f_x of the electric field magnitude distribution. The constraint on the minimal feasible outer ring width $w_{bare} \geq 1$ mm is represented by the shaded region. For the capacitance ratio, the reference configuration corresponds to the minimal width of 1 mm.

As the width of the outer ring w_{outer} increases, the free space available for the deposition of the other planar electrode ring diminishes. As a result, with the parameter w_{outer} rising, the planar ring spacing d_{plan} decreases. The influence of w_{outer} on the capacitance terms is subtle. The results on capacitance are presented in the first plot of the figure 5.9 as ratio of the capacitance terms over their reference value for 1 mm. The dominant term $C^m_{AB} = C^m_{CD}$ increases and reach a cap near 1.5 mm. The collect coupling term C^m_{BD} decreases significantly. Indeed, the collect electrodes lose in effective area in regard of the growing outer veto electrode which overshadows the influence of the opposite collecting electrode. The self-capacitance of the collect electrode $C^m_{BB} = C^m_{DD}$ decreases as the collect electrode rings shrink, emulating a loss of effective area for capacitive coupling with the ground. Following the trend of C^m_{AC}, the diagonal veto term $C_{AA} = C_{CC}$ of the Maxwell matrix increases and caps. The diagonal collect term $C_{BB} = C_{DD}$ of the Maxwell matrix remains pretty constant with a maximum at the default value 1 mm. The increasing trends of the veto collect coupling term C^m_{AB} are mitigated by the trends of the other capacitance relative to the collect electrodes. The fiducial volume decreases with w_{outer} because the veto region on the corners are getting bigger. As this growth in veto volume is located on the

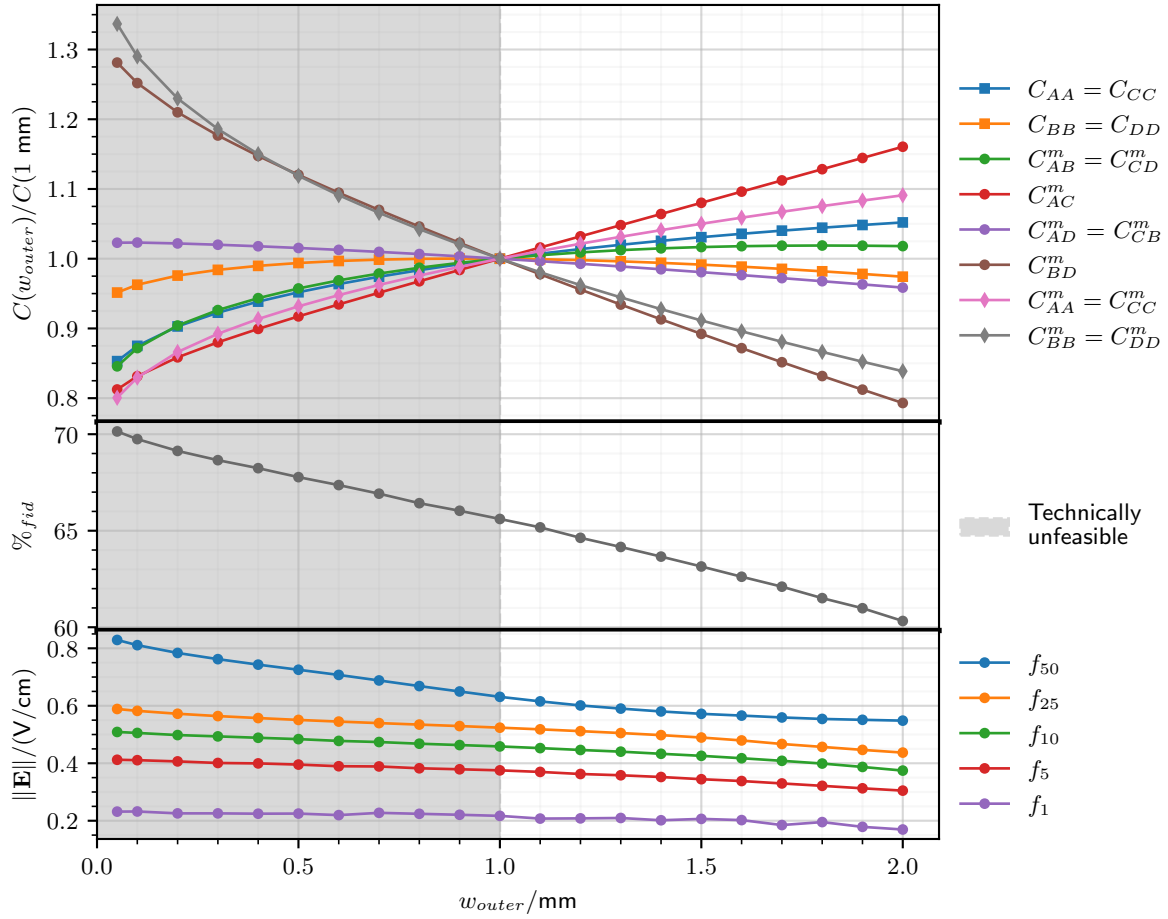

Figure 5.11: Scan over the width of the outermost veto electrode ring w_{outer} for the FID38 design. The ratio of the Maxwell and mutual capacitance terms, the percentage of fiducial volume and some percentiles of the electric field magnitude distribution over the crystal volume are plotted. The capacitance term ratio is calculated with the capacitance value at $w_{outer} = 1\,\mathrm{mm}$ as reference. A width strictly inferior to 1 mm is technically unfeasible which is represented by the shaded area. Error bars are smaller than the marker size.

periphery of the crystal, it represents a significant decrease in volume. This is also in agreement with the observation on the electric field. The low electric field norm regions situated below the outer veto electrode rings gets deeper and closer to the center with increasing outer width w_{outer}. Consequently, the bulk and surface regions see their electric field magnitude globally decrease. This is illustrated by all the diminishing percentiles of the magnitude distribution.

The influence on the capacitance term is noticeable but not that significant. On the contrary, the fiducial volume is significantly impacted by the parameter w_{outer}. The best design solution would be to have a minimal width of $w_{outer} = 0\,\text{mm}$ which is not technically feasible. Thus, for now, the best configuration would be to consider the lowest possible width of 1 mm.

Comparing the Two Geometries

With the insights gathered from the scan over w_{bare} and w_{outer}, we discuss and compare the two geometries from the edge veto electrodes. Both studies points towards the same ideal best solution: having a thin $w_{Al} = 0.08\,\text{mm}$ outer veto electrode ring in contact $w_{bare} = 0\,\text{mm}$ with the edge of the crystal for low capacitance values and higher fiducial volume. This configuration is not possible technically for now. As discussed in the previous paragraph, the best compromise offered by the two next best geometries are:

- Thin Outer Ring Spaced from the Crystal Edge, $\{w_{outer} = 0.08\,\text{mm}, w_{bare} = 0.3\,\text{mm}\}$
- Large Outer Ring on the Crystal Edge, $\{w_{outer} = 1\,\text{mm}, w_{bare} = 0\,\text{mm}\}$

The lowest capacitance value and highest fiducial volume are obtained with the thin outer electrode. With these geometries, it is expected for the ionization resolution to lower and to have the best ionization channel performances. The main drawback associated is the uncontrolled corner volumes. This could result in surface trapped charges inducing events with problematic event reconstruction. Although these corner volumes are encompassed in the top and bottom veto volumes, which could lead to a good surface event tagging (see section 3.1.2), there are still uncertainties. For the time being, the thin outer geometry is favored and should be tested on its charge collection in the corner volumes. The large outer ring geometry constitutes a backup design which should solve eventual charge collection problems at the cost of a moderate increase in capacitance and some loss of fiducial volume.

5.4.4 Equatorial Distance, d_{eq}

The equatorial distance $d_{equator}$ corresponds to the distance between the two veto electrodes on the middle of the lateral surface of the crystal. By default, it is set to 2 mm. The scan is performed over a linear scale from 0.2 mm to 6 mm. The results of the scan are presented in figure 5.12 illustrating the terms of the Maxwell C_{XX} and mutual C^m_{XY} capacitance matrices, the percentage of fiducial volume $\%_{fid}$ and some percentiles f_x of the electric field magnitude distribution.

As the equatorial distance d_{eq} increases, the free lateral space available for the other lateral electrode rings diminishes. Thus, the lateral electrode density increases and the lateral spacing d_{lat} shrinks. This explains the augmentation of the capacitance term coupling same-sided veto and collect electrode $C^m_{AB} = C^m_{CD}$ at d_{eq}, which also fixes the trend of the diagonal Maxwell collect term $C_{BB} = C_{DD}$. On the contrary, the coupling term of the two veto electrodes C^m_{AC} diverges as their separating distance d_{eq} tends to zero. This remark is also valid at a lesser extent for the coupling term C^m_{BD} and $C^m_{AD} = C^m_{BC}$, as their associated separating distance on the lateral surface decreases with low value of d_{eq}. In the end, the diagonal Maxwell term of the veto electrodes $C_{AA} = C_{CC}$ has the same divergence as the term C^m_{AC} at low d_{eq} and becomes almost constant with a very smooth minimum from 2 mm to 5 mm. Scanning over the equatorial distance strongly affects the shape of the electric field lines near the equator. At low values, the

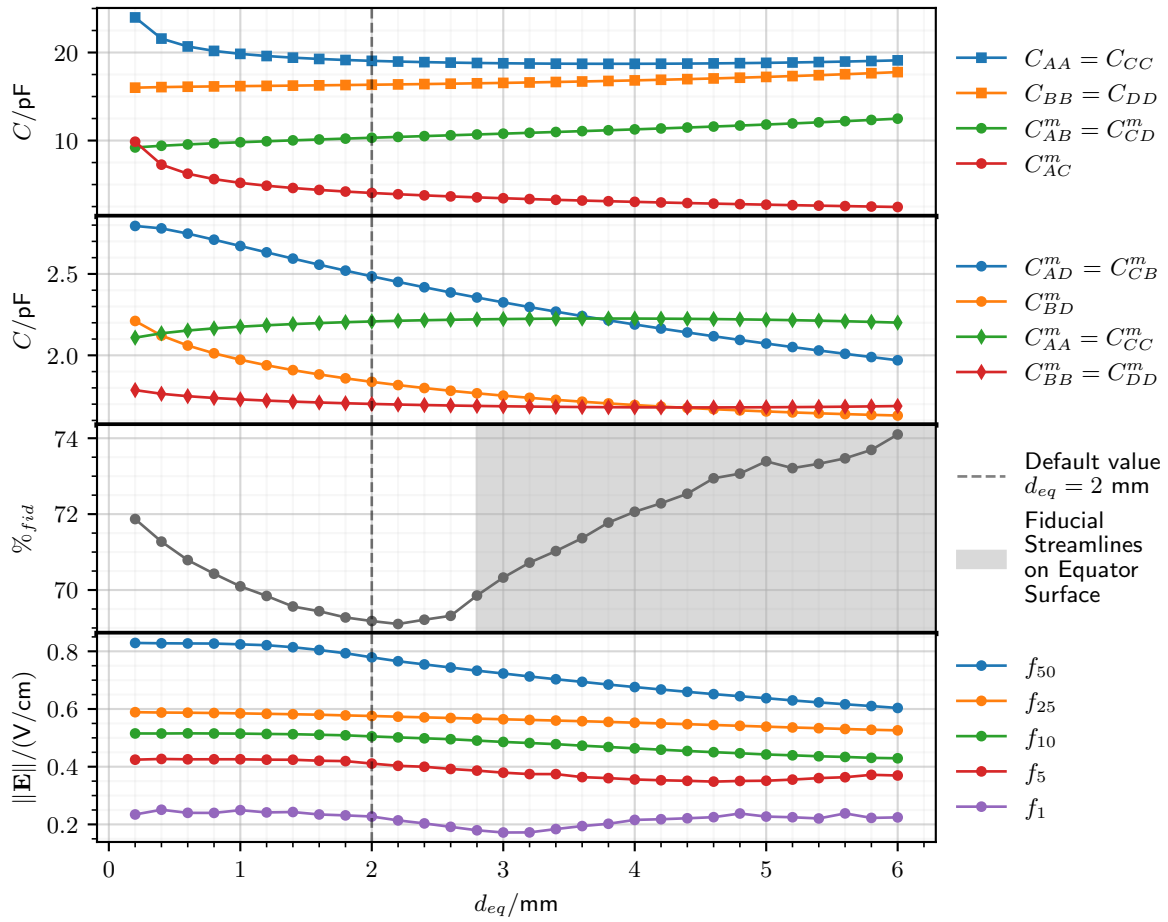

Figure 5.12: Scan over the equatorial distance d_{eq} of the FID38 design. The Maxwell and mutual capacitance terms, the percentage of fiducial volume ans some percentiles of the electric field magnitude distribution over the crystal volume are plotted. The default value $d_{eq} = 2\,\mathrm{mm}$ is represented by the dashed vertical line. Starting from 2.8 mm, fiducial streamlines are in contact with and exiting the crystal on the equatorial surface, this is represented by the shaded area. Error bars for the capacitance ratio are smaller than the marker size.

equatorial region defined on scheme 4.9 is clearly defined. With increasing equatorial distance, the lateral veto regions grow deeper and fiducial volume as well as the equatorial region shrink. According to the fiducial graph, the fiducial fraction gets a minimum for 2.2 mm. Starting from 2.8 mm, there are no more equatorial field lines and the ever growing fraction of fiducial field lines comes into contact with the equatorial surface of the crystal. This transition is illustrated by the shaded on the figure 5.12 featuring a rise in the fiducial volume. This configuration of the field lines nullify the use of the FID design aiming at discarding any surface event. Any surface event happening in the vicinity of the equator would not be tagged by the veto electrodes and would be heavily prone to surface trapping on the equator surface. In this regime of high d_{eq} values, the low electric field magnitude regions associated with the veto equatorial electrodes are large and covers a majority of the peripheral volume of the crystal. As a result, the median f_{50} of the magnitude distribution shifts towards lower values. However, the lower percentiles $f_{x\leq 25}$ are less affected. Concerning the generation of the signal for electric charge possibly trapped on the equatorial surface, the total weighting potential is negatively affected by the rising d_{eq} with a value of 0.99 of the equator value at $d_{eq} = 0.2$ mm dropping to 0.90 with the maximal equatorial distance of 6 mm.

In the end, by considering the shape of the electric field, the FID38 design can only operate with an equatorial distance d_{eq} from 0.2 mm to 2.6 mm. At the lowest distance, a very low 2 % increase in fiducial volume is obtained at the cost of a significantly increased capacitance. A good balance is found for an equatorial distance d_{eq} in the range from 1.2 mm to 2.6 mm. Keeping the default value of $d_{eq} = 2$ mm seems reasonable as to benefit from low capacitance terms and a good charge collection with the controlled electric field norm distribution at the marginal detriment of a slightly lowered fiducial volume at $\%_{fid} = 68.5\,\%$.

The influence of the equatorial distance d_{eq} on the capacitance terms and the electric field strongly depends on the values of the parameters $\{R_{veto}, n_{plan}, n_{lat}\}$. In particular, the behavior of the electric field lines near the equator for $d_{eq} \geq 2.8$ mm can be mitigated by judiciously chosen polarization ratio value different from the default one $R_{veto} = 0.25$. The study of the interaction between these four parameters is presented in section 5.4.8.

5.4.5 Polarization Ratio, R_{veto}

The polarization ratio R_{veto} fixes the electric potential of the veto electrodes in regard to the polarization of the collect electrodes. This parameter is introduced in the equation 4.37 in the previous chapter 4 where its default value for the FID38 design is set to 0.25. The scan is performed over a linear scale from -1 to 1. The results of the scan are presented in the figure 5.13. They consist in graphs of the percentage of fiducial volume $\%_{fid}$ and some percentiles f_x of the electric field magnitude distribution.

As the polarization ratio R_{veto} only sets the electric potential of the electrodes and leaves intact the geometry of the electrodes, the capacitance matrices as well as the weighting potentials remain unaffected for this study. The fiducial volume fraction decreases with R_{veto} and reaches a maximum of about 95 % for $R_{veto} = -1$. This configuration corresponds to an electric field very similar to a planar detector (like the PL38 design) where same-sided electrodes are equally collecting drifting charges. This mode of operation (discussed previously in chapter 4) is not compatible with the tagging of the surface events. The fiducial volume fraction reaches a minimum for $R_{veto} = 1$ when $V_A = V_D = -V_B = -V_C$. In this configuration, the electric field in the bulk of the crystal is nullified, if not slightly reverses due to the higher total number of veto electrode rings. For R_{veto} in the $[-1, -0.3]$ range, the FID38 detector is in a planar-like polarization. There is no veto region. All the electrodes behaves as collecting electrodes. For $R_{veto} \in [-0.3, 0]$, shallow veto regions appears. Small regions of low electric field norm are present under the veto electrodes rings. However, the electric field in the equatorial region has the same direction

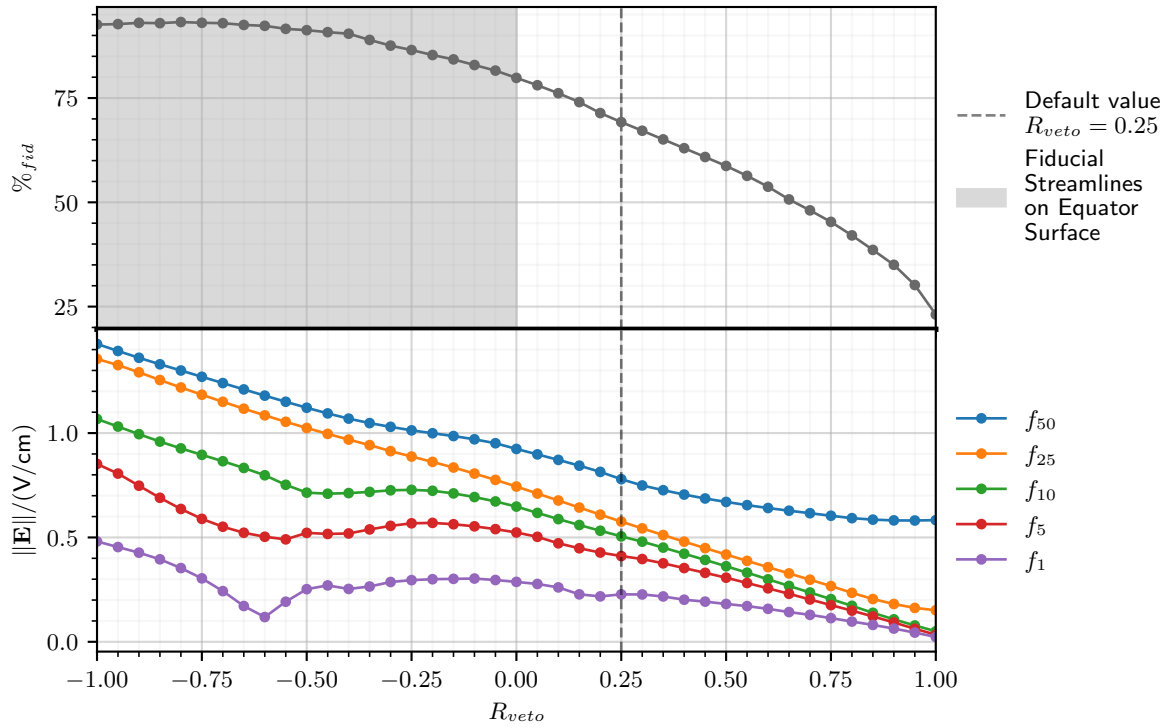

Figure 5.13: Scan over the polarization ratio R_{veto} of the FID38 design. The percentage of fiducial volume and some percentiles of the electric field magnitude distribution over the crystal volume are plotted. The default value $R_{veto} = 0.25\,\mathrm{mm}$ is represented by the dashed vertical line. For values lower than 0.2, electric field lines are incompatible with a correct operation of the FID detector. This is represented by the shaded area. Error bars for the capacitance ratio are smaller than the marker size.

as the electric field in the bulk region. In this condition, it is expected that a lot of bulk events would deposit some signal on the equatorial rings and be discarded in the analysis.

In the range $[0, 0.2]$, veto regions along with the low $\|\vec{E}\|$ associated regions are getting deeper. The equatorial volume has vanished as the fiducial streamlines are now touching the crystal equatorial surface.

In the remaining range, for $R_{veto} \in [0.2, 1]$, the equatorial volume comes back to existence. Now, its electric field has an opposite direction to the one in the bulk region. The electric field structure is standard for a FID operation as presented in the scheme 4.9. As the polarization ratio R_{veto} increases, the veto regions and the equatorial region grow in size, reducing the fiducial volume. Eventually, the regions of low electric field magnitude under the veto electrodes are big and deep enough to merge and hold the bulk of the crystal. The magnitude of the electric field in the bulk of the crystal decreases with the rising R_{veto}. This trend is visible in the naive calculation of the electric field in the center of FID38 in equation 4.45.

R_{veto} should be high enough to be in a polarization mode compatible with the tagging of surface events, while being low enough to keep a good fiducial volume fraction. The lower threshold on a valid R_{veto} is imposed by the existence of an equatorial region of sufficient size with an electric field of opposite direction to the bulk electric field. As described before, these conditions can be met for a polarization ratio R_{veto} in the $[0.2, 1]$ range. The fiducial streamlines should not be in contact with the equatorial surface. The default value 0.25 is chosen as the equatorial volume reaches 1 mm deep into the crystal. This minimal depth is useful has to form a buffer between the bulk volume and the bare germanium surface and avoid surface trapping due to the transversal trajectories of the electrons in the semi-conducting germanium crystal.

The influence of the polarization ratio R_{veto} on the electric field strongly depends on the values of the parameters $\{R_{veto}, n_{plan}, n_{lat}\}$. In particular, the behavior of the electric field lines near the equator for $R_{veto} \leq 0$ can be compensated by adapting the value of the equatorial distance d_{eq} instead of fixing it to its default value of 2 mm. The study of the interaction between these four parameters is presented in section 5.4.8.

5.4.6 Number of Planar Electrode Rings, n_{plan}

The collect and veto electrodes of the FID38 design consists in concentric aluminium rings deposited on the planar and lateral surfaces of the germanium crystal. The number of concentric planar rings, including the central veto pad, on single planar surface corresponds to the parameter n_{plan}. As the FID38 design is based on having the collect electrodes B, D interleaved with the veto electrodes A, C, it is necessary to assign the central aluminium pad and the outermost ring to the veto electrodes. Therefore, n_{plan} is an odd integer. As the electrode rings are evenly spread on the free planar surface of the crystal of fixed radius $R_{Ge} = 15\,\text{mm}$, their number n_{plan} sets the planar ring spacing d_{plan} and their density on the surface. By default, n_{plan} is set to 7 which corresponds to the spacing between the planar rings to $d_{plan} = 2.40\,\text{mm}$. The scan is performed for the values 3, 5, 7, 9 and 11. The results of the scan are presented in the figure 5.14.

By construction, the planar spacing d_{plan} is proportional to the inverse of the number of planar rings n_{plan}. A higher number of aluminium rings emulates a higher area available for capacitive coupling and also decreases the distance between the electrodes. As a result, all coupling terms increase with the number of planar rings. Small variations are observed for the terms C^m_{AC} and C^m_{XX} as the distance to the chassis and the equatorial distance between the veto electrodes A and C remains the same. As usual, the diagonal Maxwell terms are dominated by the trend of $C^m_{AB} = C^m_{CD}$. Apart from the first point, the fiducial volume grows with an increasing number of planar rings. This is explained by a loss of depth and volume of the surface veto regions. The minimal number of planar electrodes $n_{plan} = 3$ shows a particular behavior. For this configuration, the fiducial volume is maximal. However, a lot of fiducial streamlines are almost parallel to the planar surface, which could be problematic with the transversal trajectory of the electrons.

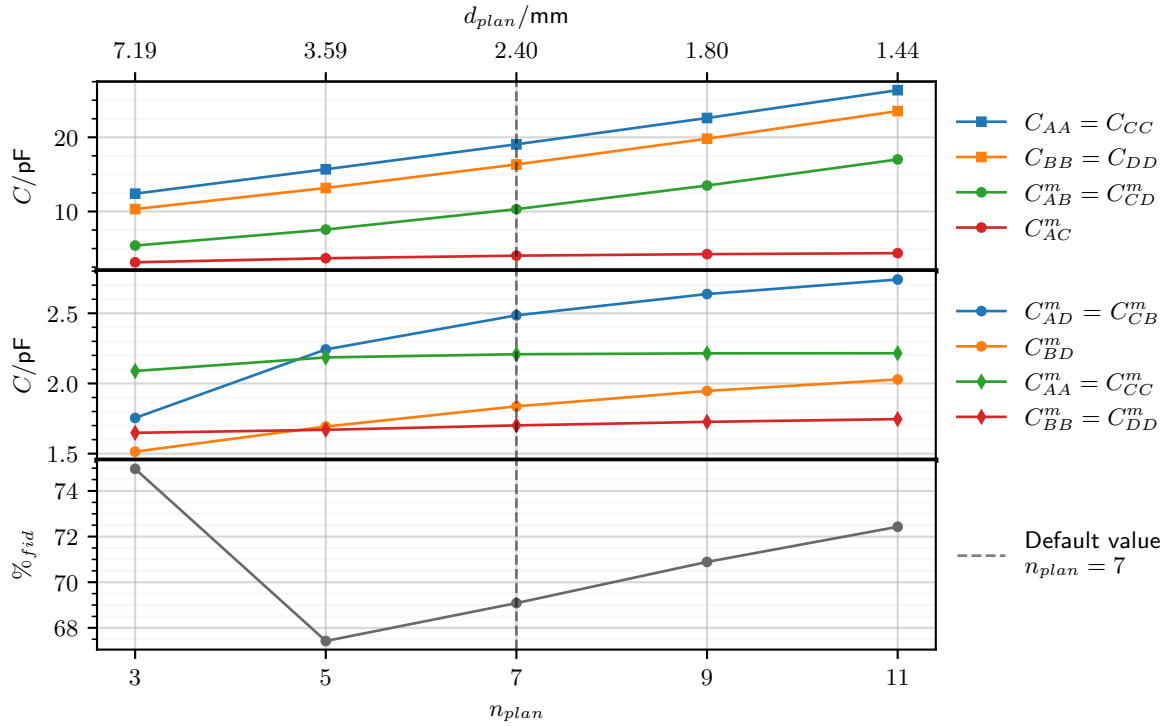

Figure 5.14: Scan over the number of planar electrode rings n_{plan}. The Maxwell and mutual capacitance terms and percentage of fiducial volume are plotted. The default value $n_{plan} = 7$ is represented by the dashed vertical line. The parameter n_{plan} is restricted to odd integers in order to assign the central pads and the outermost rings to the veto electrodes A and C. The corresponding values of spacing between planar rings d_{plan} are mentioned at the top of the graph. Error bars are smaller than the marker size.

Moreover, the regions of low electric field magnitude associated to the veto electrodes are in contact with the planar surface, surely resulting in high fraction of trapped events on the planar surface.

The number of planar electrode rings n_{plan} can be used to have a better control on the shape of the electric field with a higher fiducial volume at the price of a significant increase in capacitance. Alone, this parameter mainly affects the behavior near the center of the detector as the number of lateral electrode rings n_{lat} is fixed. Its effect on the fiducial volume is strongly correlated with the influence of the polarization ratio r_{veto}. In section 5.4.8, the number of planar rings n_{plan} is scanned over with adapted number of lateral electrode n_{lat} and the polarization ratio R_{veto}. The effect of the number of planar rings n_{plan} on the capacitance and electric field strongly depends on the values of the parameters $\{n_{lat}, R_{veto}, d_{eq}\}$. In particular, it is more efficient to have a similar ring density on the planar and lateral surfaces in order to lower the capacitive cost of shaping the electric field in the crystal. The study of the interaction between these four parameters is in section 5.4.8.

5.4.7 Number of Lateral Electrode Rings, n_{lat}

The collect and veto electrodes of the FID38 design consists in concentric aluminium rings deposited on the planar and lateral surfaces of the germanium crystal. The lateral surface is divided in two parts, top and bottom, separated by the equator line of the crystal. In the top part of the lateral surface is located the aluminium attributed to the electrodes A and B. In the bottom part of the lateral surface is located the aluminium attributed to the electrodes C and D. The parameter n_{lat} corresponds to the number of lateral rings in either the top or the bottom part of the lateral surface. The total number of aluminium rings on the whole lateral surface is therefore $2n_{lat}$. As the FID38 design is based on having the collect electrodes B, D interleaved with the veto electrodes A, C, it is necessary to assign the ring closest to the equator to the veto electrodes A and C and the ring closest to the edge of the crystal to the collect electrodes B and D. As such, n_{lat} is an even integer. As the electrode rings are evenly spread on the free lateral surface of the crystal of fixed height $H_{Ge} = 10\,\text{mm}$, the parameter n_{lat} sets the lateral ring spacing d_{lat} and their density on the surface. By default, n_{lat} is set to 2 which corresponds to a spacing between the lateral rings of $d_{lat} = 1.98\,\text{mm}$. The scan is performed for the values 2, 4, 6 and 8. The results of the scan are presented in the figure 5.15.

The observations resulting from the scan over n_{lat} are very similar to the ones from the scan over the number of planar rings n_{plan} presented in previous section 5.4.6, with a few differences. With an increasing number of lateral rings, almost all the capacitance terms increase and the fiducial volume grows. For this scan, the increasing fiducial volume is associated to the shrinking of the surface veto regions, the parameter n_{lat} does not affect much the center ($r \lesssim 10\,\text{mm}$) of the crystal. However, this growth is also associated to the disappearance of the equatorial volume. Indeed, for $n_{lat} \geq 4$, fiducial streamlines comes into contact with the equatorial surface and leave the crystal. These configurations are therefore not compatible with the correct FID operation.

The number of planar electrode rings n_{plan} can be used to have a better control on the shape of the electric field with a higher fiducial volume at the price of a significant increase in capacitance. Alone, this parameter mainly affects the behavior on the periphery of the detector as the number of planar electrode rings n_{plan} is fixed. The effect of the number of lateral rings n_{lat} on the capacitance and electric field strongly depends on the values of the parameters $\{n_{plan}, R_{veto}, d_{eq}\}$. In particular, the behavior of the electric field lines for $n_{lat} \geq 4$ can be suppressed with an adaptation of the equatorial distance d_{eq} and the polarization ratio R_{veto}. The study of the interaction between these four parameters is presented in section 5.4.8.

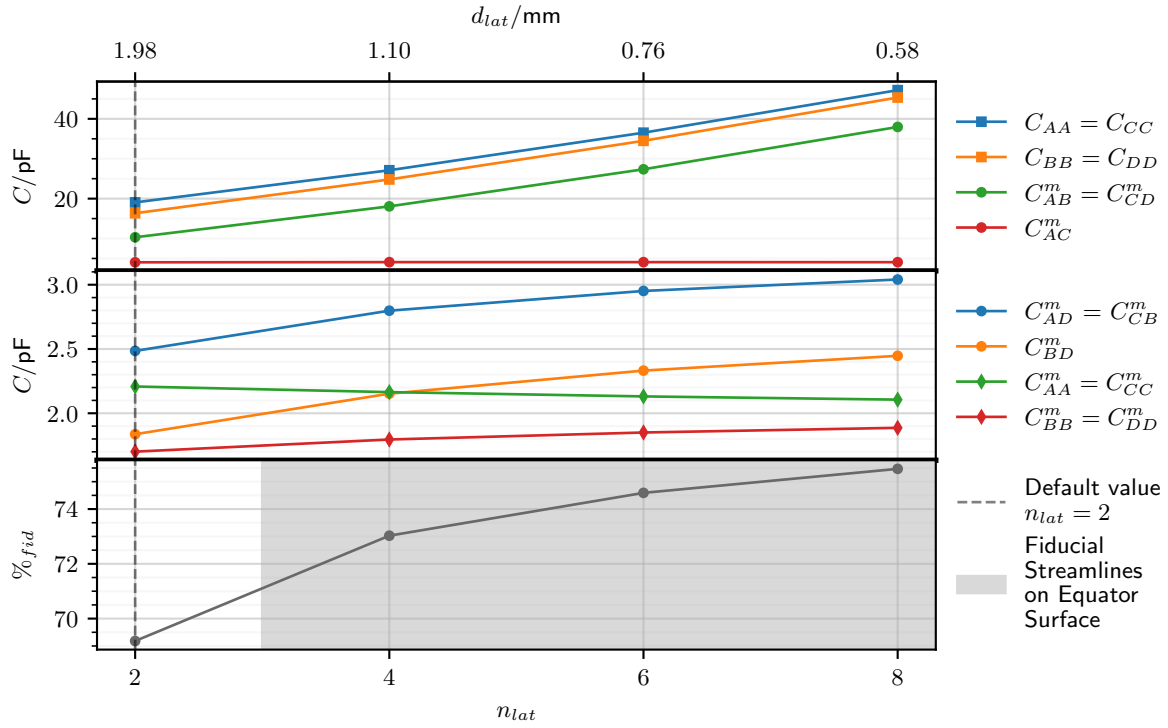

Figure 5.15: Scan over the number of planar electrode rings n_{lat}. The Maxwell and mutual capacitance terms and percentage of fiducial volume are plotted. The default value $n_{lat} = 2$ is represented by the dashed vertical line. The parameter n_{lat} is restricted to even integers in order to equatorial ring to the veto electrodes and the ring closest to the crystal edge to the collect electrodes. The corresponding values of spacing between lateral rings d_{lat} are mentioned at the top of the graph. Error bars are smaller than the marker size.

5.4.8 Global Density of the Electrode Rings, $\{n_{plan}, n_{lat}, R_{veto}, d_{eq}\}$

Sections 5.4.4 to 5.4.7 were dedicated to uni-dimensional scan over the parameters n_{plan}, n_{lat}, R_{veto} and d_{eq}. In this section, these four parameters are scanned over simultaneously in order to emulate an increasing and uniform global density of the electrode rings with adapted polarization. The parameters $\{n_{plan}, n_{lat}\}$ participate in shaping the electric field at the cost of heightened capacitance term, in the center and in the periphery of the crystal respectively. Performance of the ionization channel are uniform in the whole volume of the crystal if the electric field demonstrates homogeneous properties in the crystal. Namely, the density of the electrode rings should be equivalent on the planar surfaces and the lateral surfaces. Thus, the parameters $\{n_{plan}, n_{lat}\}$ are chosen such that the planar d_{plan} and lateral d_{lat} spacings are as close as possible. It happens that the same values of n_{plan} or n_{lat} can be used in multiple configurations. Nevertheless, the results are presented with a monotonically increasing number of total electrodes rings on the detector. The results related to the three parameters $\{n_{lat}, R_{veto}, d_{eq}\}$ shows that a significant part of the parametric space is not compatible with a correct operation of the FID38 design with working surface event tagging. With judicious choice in the values of these parameters, it is possible to explore a viable part of the parametric space. As the parameter n_{lat} is imposed by the choice of n_{plan}, the remaining parameters R_{veto} and d_{eq} should be considered as functions of the parameter n_{lat}. Considering the insights of section 5.4.4 with the scan over the equatorial distance d_{eq}, the default value of 2 mm is in the viable range and happen to be almost equal to default lateral spacing $d_{lat} = 1.98\,\text{mm}$. A simplistic relation between n_{lat} and the equatorial distance d_{eq} is to have the later equal to the lateral spacing d_{lat}. As to avoid the needlessly complex solution of a second-order polynomial equation, the equatorial distance is set to:

$$d_{eq}\left(n_{lat}\right) = \frac{H_{Ge}}{1+2n_{lat}} \approx d_{lat} \tag{5.2}$$

The last unfixed parameter is the polarization ratio R_{veto}. As discussed previously in sections 5.4.4, 5.4.5 and 5.4.7, an existing equatorial region is necessary to the viable operation of an FID detector. The condition for the equatorial region to appear is that the electric field at the equator is nullified:

$$\boldsymbol{E}\left(z = 0\,\text{mm}, r = 15\,\text{mm}\right) \cdot \hat{\boldsymbol{z}} \geq 0 \tag{5.3}$$

The numerical resolution of this equation is surely possible with the electrostatic simulation. However, for the sake of simplicity in this explanatory scan, the polarization ratio is set to the following empirical function:

$$R_{veto} = \left(1 + 4\frac{d_{lat}}{d_{eq}}\right)^{-1} \approx 0.2 \tag{5.4}$$

With this choice on the three parameters $\{n_{lat}, R_{veto}, d_{eq}\}$, the equatorial regions exists and possesses enough volume to guarantee a good rejection of the surface events.

The simulation is ran with the considered set of values and the results are presented in the figure 5.16. They consist in graphs of the terms of the Maxwell C_{XX} and mutual C^m_{XY} capacitance matrices, the percentage of fiducial volume $\%_{fid}$ and some percentiles f_x of the electric field magnitude distribution over the crystal volume. One should note that the set value is close to the default value of the FID38 design, $R_{veto} = 0.25$. As a result, the reference configurations on the graph $\left(n_{plan}, n_{lat}\right) = (7, 2)$ demonstrates a slightly higher fiducial volume and global electric field than the default FID38 configuration presented in the previous chapter 4.

Almost all the capacitance terms increase with the higher number of electrode rings. The coupling term related to same-sided veto and collect electrodes $C^m_{AB} = C^m_{CD}$ is greatly increased as the planar and lateral spacings shrink. As this term is dominant in their calculation, the

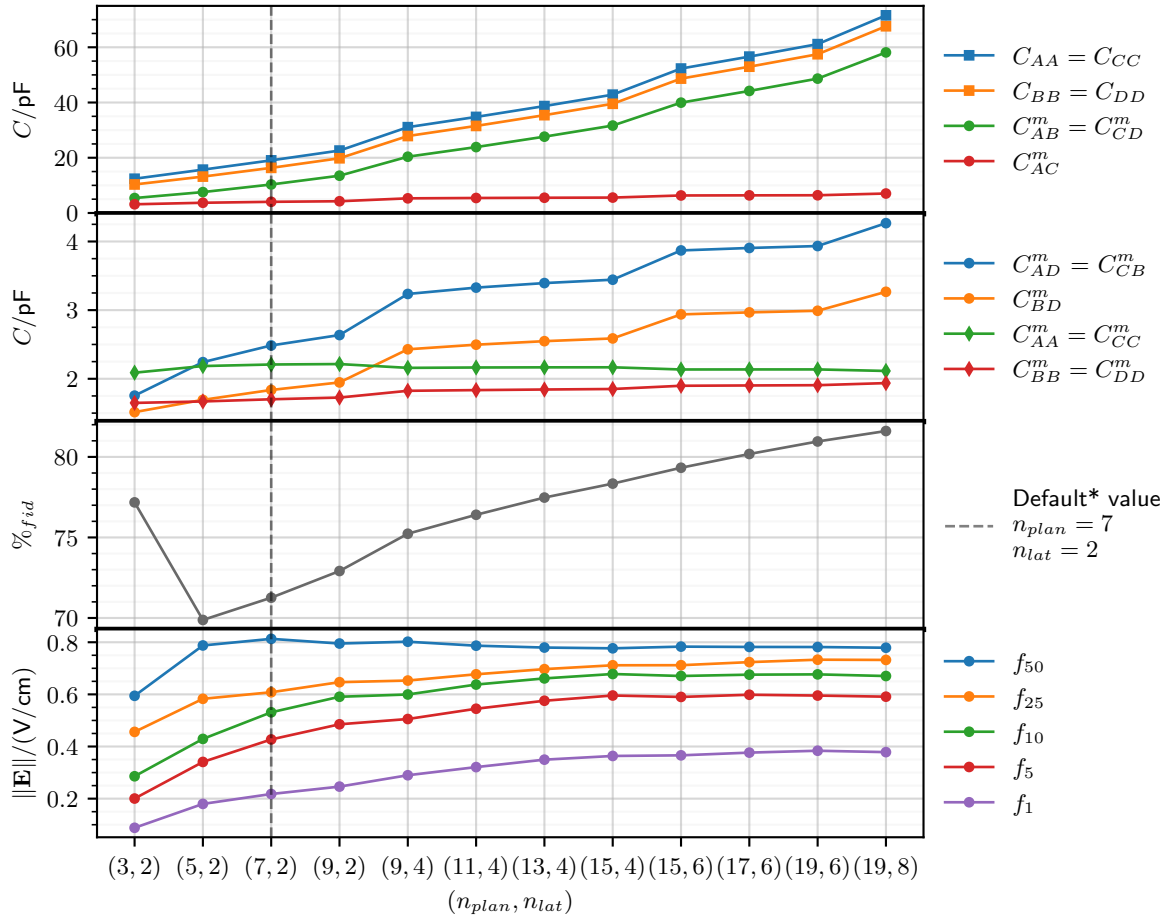

Figure 5.16: Scan over selected sets of values for the parameters $\{n_{plan}, n_{lat}, R_{veto}, d_{eq}\}$ emulating an increasing homogeneous ring density for the FID38 design. The Maxwell and mutual capacitance terms, the percentage of fiducial volume and some percentiles of the electric field magnitude distribution over the crystal volume are plotted. The default configuration $(n_{plan}, n_{lat}) = (7, 2)$ is represented by the dashed vertical line, the polarization ratio $R_{veto} = 0.2$ is different from the default configuration (with $R_{veto} = 0.25$). Error bars are smaller than the marker size.

diagonal terms of the Maxwell matrix capacitance C_{XX} follow the same trend. With a higher number of electrode rings, the effective area available for capacitive coupling is higher for all electrodes, which explains the growth of the terms C^m_{BD} and $C^m_{AD} = C^m_{CB}$ related to the coupling of electrodes on opposite sides. The self-capacitance terms are only slightly affected, and even decrease in the case of $C^m_{AA} = C^m_{CC}$. This can be associated with the overshadowing of the ground by the increasing number of rings which prevent further capacitive coupling with the electrodes. The fiducial volume demonstrates a behavior similar to the uni-dimensional scan over n_{plan} and n_{lat}. Its percentage grows significantly with the number of electrodes, with a gain of 12.5 % between the extrema. Indeed, with closer collect and veto electrodes, the veto regions lose depth and volume. However, the veto regions also gains in electric field norm with smaller low electric field magnitude regions. As a result, the electric field is more uniform in the crystal as illustrated by the stable median f_{50} of the magnitude distribution and increasing lower percentiles. The first point with $n_{plan} = 3$ remains an exception in the trend of the fiducial volume. Fiducial field lines occupy a larger portion of the volume at the cost of a low electric field magnitude in the planar veto regions. Indeed, all the percentiles of the magnitude distribution drop. Moreover, the discussion of section 5.4.6 is still valid: with field lines parallel to the planar surface and low electric field, electrons are more prone to surface trapping because of their transversal trajectory in the germanium. For this particular configuration $(3, 2)$, the total weighting potential on the surface of the crystal is about 0.84. This value rises rapidly to reach the default value of 0.95 and caps at 0.98 for the maximal number of rings for the configuration $(19, 8)$.

With the exception of the first point $(3, 2)$ demonstrating a potentially bad charge collection, an increasing density of the electrode rings yields a better control of the electric field with the growth of the fiducial volume at the price of the global rise in the capacitance terms. The configurations $(5, 2)$, $(7, 2)$ and $(9, 2)$ seems all viable and offer some flexibility on the FID38 design. With the lowest amount of electrodes $(5, 2)$, the fiducial volume is relatively low, with a percentage of 70 %, but features better resolution for the ionization channel thanks to lowered capacitance terms. The configuration $(9, 2)$ loses in resolution, with a rough estimation of the loss of 15 % by referring to the capacitance values, with a somewhat marginal gain in the percentage of theoretical fiducial volume of 3 %.

Chapter 6

Simulation and Experimental Studies of the detectors RED80 and REDN1

In this chapter, the electrostatics simulations are compared to the experimental data collected from the operation of the detectors RED80 and REDN1. Their designs differ from the already presented PL38 and FID38 designs. Consequently, the first section is dedicated to the presentation of the detectors RED80 and REDN1, their numerical simulation and their predicted performance for the ionization channel. The section exposes the processing and analysis pipelines used to treat the experimental data and extract observable quantities which can be compared to the simulations. The actual confrontation of the results is presented in the last and third section.

6.1 Electrostatic Simulation of the detectors RED80 and REDN1

The detectors RED80 and REDN1 were both based on cylindrical germanium crystals of height $H_{Ge} = 10\,\text{mm}$ and radius $R_{Ge} = 15\,\text{mm}$. Due to technological constraints, these germanium cylinders feature a round filet on their corners with an estimated radius between 200 µm and 300 µm. The figure 6.1 displays the photos of the detectors. In both cliches, the covers of the copper chassis are removed as to allow the completion of the cabling of the thermal sensor and the electrodes. The incomplete chassis visible on the photos are spaced by a distance $d_{Cu} = 3\,\text{mm}$ from the surface of the crystals. The germanium absorber is maintained by six Teflon clamps. These detectors possesses the two energy measurement channels, heat and ionization, described in section 2.3.2. The NTD thermal sensors, used for the heat channel, are glued at the center of the top surface of the crystals. These thermistances are linked with several gold wires to conductive tracks above the crystal. These gold wires assured the electric cabling of the NTD as well as the thermalization of the germanium crystal. The ionization channel consists in electrodes made out of aluminium pads and rings deposited on the germanium surface as explained in section 4.1.5. In the case of REDN1, the aluminium rings are linked together using wire bridges. The electrodes are wired to conductive tracks on the chassis with aluminium wires as to prevent thermal leak through them.

Each detector has its own particularities which are assessed in the following sections 6.1.1 and 6.1.2 dedicated to the design and the electrostatics simulation of RED80 and REDN1 respectively.

6.1.1 RED80 detector

The description of RED80 is accompanied with the figure 6.2 displaying a cross-section scheme of the detector. This scheme is used as reference for the electrostatics simulation. The scheme is not to scale and all the dimensions used in the simulation are listed in the table 6.1. The copper chassis is modeled by an exterior electrically grounded rectangle. The germanium crystal is held separated from the germanium crystal by vacuum represented by the light blue surrounding

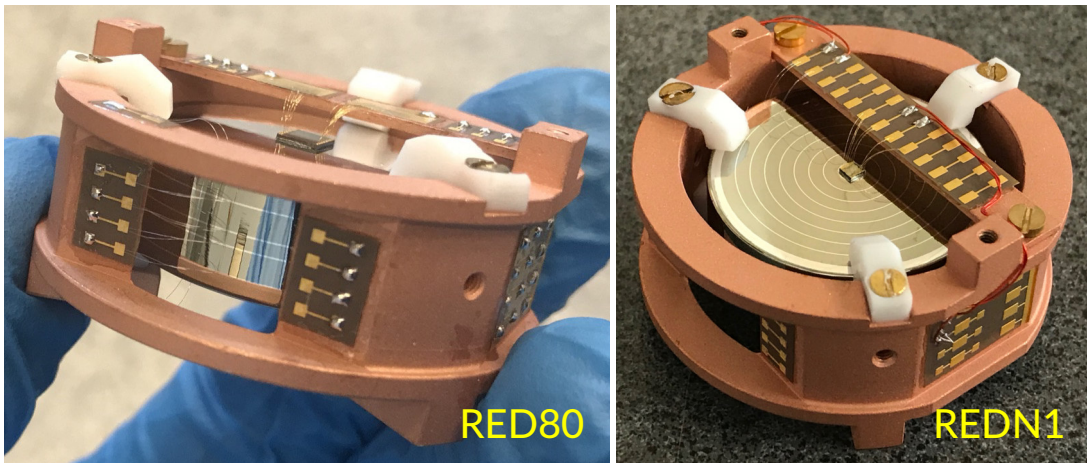

Figure 6.1: Photos of the detectors RED80 and REDN1 taken during their montage. The covers of the copper chassis are removed to finish the cabling.

volume. The Teflon clamps are not represented in the scheme and are not a part of the simulation. The heat channel of RED80 consists of a GeNTD thermistance labeled K58. Its dimensions are the larger EDELWEISS standard of $(4 \times 4 \times 0.45)$ mm. It is glued on aluminium at the center of the top surface as represented by the white rectangle. Although represented, the NTD is not simulated. The ionization channel consists in four electrodes labeled A through D separated in pairs of main collect electrodes and auxiliary guard electrodes. Each aluminium deposit is labeled on the scheme 6.2 according to the electrode it is attributed to. The main electrodes are B and D. They consists of two planar full aluminium electrodes of radius $r_{center} = 13.5\,\text{mm}$ centered on the top and bottom surfaces of the germanium crystal. The role of these electrodes is to collect the majority of the drifting charges produced in the crystal. As such, they are deemed "collect electrodes". The auxiliary electrodes are A and C. They are formed by two pairs of circular rings of width $w_{Al} = 100\,\mu\text{m}$ deposited on the lateral surface of the germanium crystal. In each pair, the rings are separated by the lateral spacing $d_{lat} = 2.4\,\text{mm}$, from their center. The two pairs are spaced by the equatorial distance $d_{eq} = 1\,\text{mm}$, from the center of the centermost rings. The function of these electrodes is to collect any charges in the periphery of the crystal as to tag any surface recoil similarly to the veto electrodes of the FID38 design. These electrodes are deemed "guard electrodes". The difference with the veto one holds in their polarization and in the direction of the electric field being the same between the collect and the guard electrodes. One should note that the guard electrodes are not centered on the equator of the crystal, represented by the finely-dashed horizontal line passing through the origin $(0,0)$ in the scheme 6.2. Instead, the axis of mirror symmetry for the guard electrodes is the sparsely-dashed horizontal line passing through the coordinates $(0, z_{eq}) = (0, -0.5)\text{mm}$. This is the result of an offset in height of the mask used during the deposition of the aluminium rings. While this feature is unintentional as it induces an slight asymmetry in the design of RED80, it shall provide interesting insights considering the intrinsic asymmetry of the electron and hole drift in the semi-conducting germanium as discussed in section 4.1.4.

The electrostatic simulation of the presented geometry yields the capacitance matrices of the detector RED80. The convention regarding indexes introduced in the chapter 4 is still in use. Each electrode is attributed to an index such that:

$$\{A, B, C, D\} \Leftrightarrow \{1, 2, 3, 4\} \tag{6.1}$$

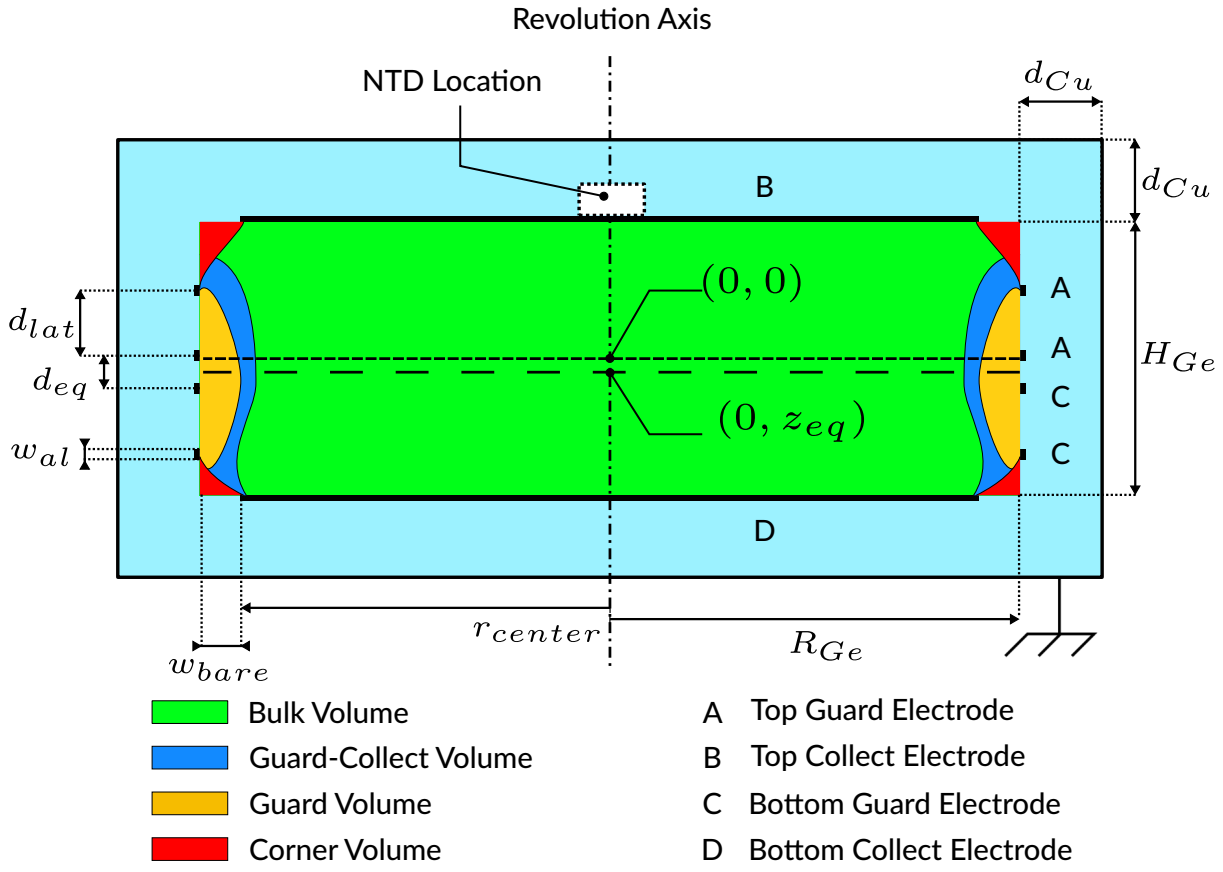

Figure 6.2: Cross-section scheme of the RED80 detector. This scheme is not to scale and the main dimensions are listed in the table 6.1. The dashed horizontal lines are axis of symmetry: finely-dashed through $(0,0)$ is for the crystal, sparsely-dashed through $(0,z_{eq}) = (0,-0.5)$mm is for the guard rings A, C. The electrically grounded rectangle is the cooper chassis separated from the germanium crystal by vacuum in light blue. The aluminium pads and rings are represented in black at the surface of the crystal and labeled according to their electrode of attribution. The default potential of the electrodes are $(V_A, V_B, V_C, V_D) = (+1,+1,-1,-1)$V. The colored volumes inside the crystal are drawn from electric field lines with common start and end points.

Parameter	Symbol	Default Value
Ge crystal Height	H_{Ge}	10 mm
Ge crystal Radius	R_{Ge}	15 mm
Distance between crystal and copper chassis	d_{Cu}	3 mm
Aluminium Deposit Thickness	h_{Al}	1 µm
Width of the Lateral Rings	w_{Al}	80 µm
Radius of the Planar Electrode Pad	r_{center}	13.5 mm
Width of bare Ge crystal on edge	w_{bare}	1.5 mm
Spacing between Lateral Rings	d_{lat}	2.4 mm
Equatorial distance	d_{eq}	1.2 mm
Offset on Equator Height	z_{eq}	−0.5 mm
Main Voltage Bias	V_{bias}	2 V
Symmetric factor of the voltage bias	S_{bias}	0.5

Table 6.1: Parameter values for the design and default polarization of RED80.

In this light, the Maxwell capacitance matrix associated with the electrodes of RED80 is evaluated to:

$$\boldsymbol{C} = \begin{pmatrix} 13.93 & -6.32 & -3.89 & -2.57 \\ -6.32 & 17.17 & -1.91 & -6.06 \\ -3.89 & -1.91 & 14.25 & -7.28 \\ -2.57 & -6.06 & -7.28 & 18.61 \end{pmatrix} \times 10^{-12}\,\mathrm{F} \tag{6.2}$$

Using the equations 4.57, the mutual capacitance matrix of RED80 is evaluated to:

$$\boldsymbol{C}^m = \begin{pmatrix} 1.15 & 6.32 & 3.89 & 2.57 \\ 6.32 & 2.88 & 1.91 & 6.06 \\ 3.89 & 1.91 & 1.17 & 7.28 \\ 2.57 & 6.06 & 7.28 & 2.70 \end{pmatrix} \times 10^{-12}\,\mathrm{F} \tag{6.3}$$

One remarkable property of these RED80 capacitance matrices, compared to the other capacitance matrices of PL38, FID38 and REDN1 discussed in this work, is the absence of symmetry between top and bottom. This is a direct consequence of the asymmetrical geometry of RED80 with its offset guard electrodes. According to the diagonal terms of the Maxwell matrix C_{XX}, the main collect electrodes B and D display globally more capacitive coupling than the auxiliary guard electrodes A and C. This can be readily explained by the difference in area between the collect and guard electrodes. This interpretation is supported by the relatively high mutual capacitance term C^m_{BD} associated to the opposite-sided collect electrodes B and D. The coupling terms between same-sided collect and veto electrodes C^m_{AB} and C^m_{CD} are the highest terms of the mutual matrix $\boldsymbol{C}^m$. This is due to the proximity of same-sided electrode. This is confirmed by the observation that $C^m_{CD} > C^m_{AB}$: the height offset z_{eq} of the guard electrodes leads to a shorter distance between C and D than between A and B. As what was observed in chapter 5 for the designs PL38 and FID38, the self-capacitance terms C^m_{XX} are among the smallest terms in the capacitance matrix $\boldsymbol{C}^m$. This is attributed to the high difference in relative dielectric permittivity between the germanium and the vacuum.

Without fixing the polarization of RED80 yet, the electrostatics can yield the map of the total weighting potential presented in the figure 6.3. As discussed in 4.1.6, the Shockley-Ramo theorem indicates that this total weighting potential indicates the quality of the Faraday cage formed by the RED80 electrodes, which is of paramount importance for trapped charges which do not reach the electrodes. The corners display a lessened total weighting potential due to the absence of aluminium deposit in these regions.

For standard operation, same-sided guard and collect electrodes have the same electric potential. The polarization of the detector can therefore be fixed with two parameters such that:

$$V_A = V_B = V_{bias} \cdot S_{bias} \tag{6.4}$$

$$V_C = V_D = -\,V_{bias} \cdot (1 - S_{bias}) \tag{6.5}$$

with V_{bias} being the bias voltage and S_{bias} the polarization symmetry parameter. The default polarization is set at $(V_{bias}, S_{bias}) = (2\,\mathrm{V}, 0.5)$. In this state, the electric potential of the electrodes are:

$$(V_A, V_B, V_C, V_D) = (+1, +1, -1, -1)\ \mathrm{V} \tag{6.6}$$

With this polarization, the electrostatic equations are numerically solved. The figure 6.3 presents a map of the electric potential with isopotential contours. The figure 6.4 displays two graphs relative to the electric field. On the left is the map of the magnitude of the electric field $\|\vec{E}\|$ with a white overlay representing the electric field lines. On the right are the histogram and the cumulative distribution function of the field magnitude distribution over the crystal volume. Apart from the periphery of the crystal, the volume of RED80 hosts neatly equally spaced isopotential contours. As a result, the electric field norm is indeed uniform in the crystal and the field

lines are all parallel and vertical linking the collect electrodes B and D. Indeed, the magnitude distribution features a neatly defined peak at $\|\vec{E}\| = 2\,\mathrm{V}\cdot\mathrm{cm}^{-1}$. Near the lateral surface, the field lines now link the guard electrodes and collect electrodes. The equatorial region has high electric field norm due to the close equatorial guard rings. This participates in broadening the magnitude distribution towards value greater than the median $2\,\mathrm{V}\cdot\mathrm{cm}^{-1}$. On the contrary, the corners show very low magnitude values which coincide with divergence points for the electric field lines. It seems like in the corners of the crystal, the field lines leave the crystal to end on the copper chassis. This observation leads us to expect surface trapping in the corners. It also explains the electric field magnitude extension at the lowest values.

An advanced study of the field lines can separate the crystal volume in several regions with different collecting behavior depending on the start and the end point of the field lines. For RED80, there are four different regions which are drawn on the scheme 6.2. The main region is the "bulk volume" also called "fiducial volume", colored in green on the scheme, and corresponding to field lines linking the two main collect electrodes B and D. Its volume is the important theoretical fiducial volume. At default polarization, its percentage is estimated at $\%_{fid} = 80.75\,\%$. This value is obtained with the method discussed in paragraph 4.2.5. The percentage of the volume attributed to other regions is less precise due to the limitation of the estimation technique. On the lateral surface of the crystal, the electric field lines linking the two guard electrodes A and C form the so-called "guard volume" illustrated as the orange region on the scheme. Its volume percentage is estimated to $\%_{guard} \approx 7\,\%$. As a consequence of the height offset z_{eq} of the guard electrodes, a significant portion of the electric field lines start on the top guard electrode A and end on the bottom collect electrode D. These lines draw the blue region deemed "guard-collect volume". Its volume percentage is approximated to $\%_{guard-collect} \approx 6\,\%$. The last volume corresponds to the corner regions with the field lines leaving the crystal to end on the copper chassis. This so-called "corner volume" is colored red and has a volume percentage of about $\%_{corners} \approx 5\,\%$.

Each region has a specific electric charge signal vector $\vec{Q}$ induced by a number N_p of electron-hole pairs created in the crystal such that $Q = N_p e$. Assuming an ideal charge collection following the electric field lines and without transversal component, the Shockley-Ramo is used to express the first three charge vectors:

$$\vec{Q}_{bulk} = \begin{bmatrix} 0 \\ -1 \\ 0 \\ 1 \end{bmatrix} \cdot N_p \cdot e \quad ; \quad \vec{Q}_{guard} = \begin{bmatrix} -1 \\ 0 \\ 1 \\ 0 \end{bmatrix} \cdot N_p \cdot e \quad ; \quad \vec{Q}_{guard-collect} = \begin{bmatrix} -1 \\ 0 \\ 0 \\ 1 \end{bmatrix} \cdot N_p \cdot e \tag{6.7}$$

The charge vector corresponding to the corner volume Q_{corner} is not readily available as all the drifting charge should theoretically be subject to surface trapping.

In section 6.3.2, the RED80 simulation presented here is compared to the experimental data taken during the operation of RED80. In particular, a scan over the voltage bias V_{bias} is performed. As discussed in the section 5 with the scans of the designs PL38 and FID38, a change of the voltage bias solely scales the magnitude of the electric field in the crystal. Any other quantities deduced from the simulation of RED80, like the fiducial volume and the capacitance matrices, are unaffected.

6.1.2 REDN1 detector

The description of REDN1 is illustrated with the figure 6.5 displaying a cross-section scheme of the detector. This scheme is used as reference for the electrostatics simulation. The scheme is not to scale and all the dimensions used in the simulation are listed in the table 6.2. The copper chassis is modeled by an exterior electrically grounded rectangle. The germanium crystal is

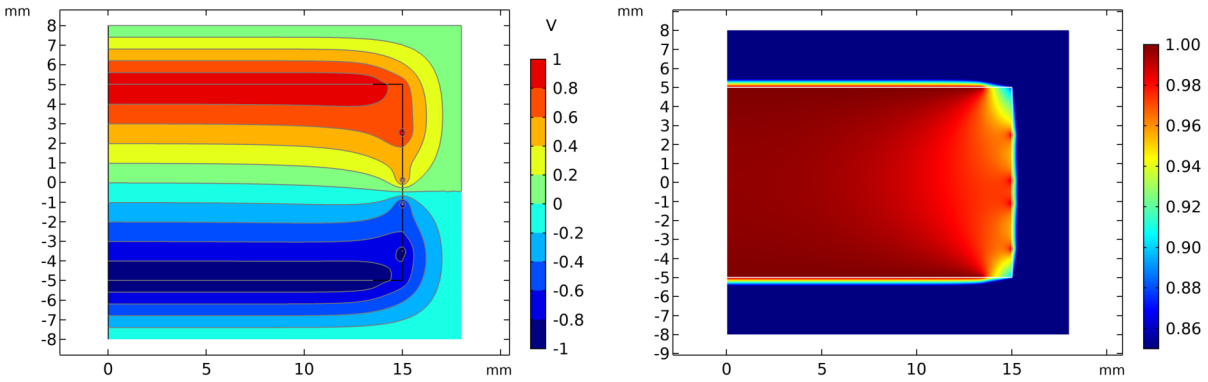

Figure 6.3: Color maps of the electric potential (on the left) and the total weighting potential (on the right) from the simulation of RED80. For the left graph, the default polarization is used.

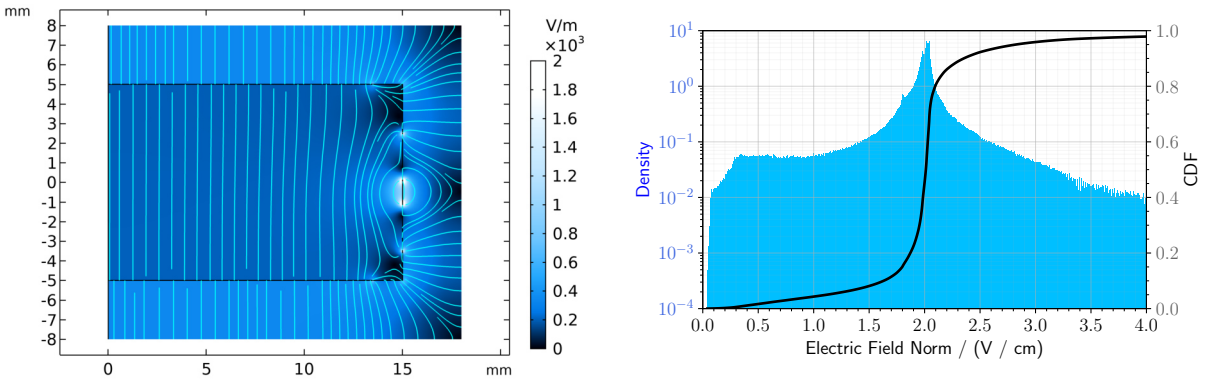

Figure 6.4: (On the left) Color map of the magnitude of the electric field with white representation of the electric field lines from the simulation of RED80. The default polarization is used. The colored volumes in the scheme 6.2 are drawn from the electric field lines with common start and end points. (On the right) Histogram and Cumulative Distribution Function of the distribution of the magnitude of the electric field over the crystal volume from the simulation of RED80.

Parameter	Symbol	Default Value
Ge crystal Height	H_{Ge}	10 mm
Ge crystal Radius	R_{Ge}	15 mm
Distance between crystal and copper chassis	d_{Cu}	3 mm
Electrode Thickness	h_{Al}	1 µm
Electrode Width	w_{Al}	100 µm
Radius of the innermost planar electrode	r_{center}	1.5 mm
Width of bare Ge crystal on corners	w_{bare}	0 mm
Width of the outermost veto electrode	w_{outer}	1 mm
Number of planar electrodes	n_{plan}	9
Interdistance of Planar electrodes	d_{plan}	1.563 mm
Main Voltage Bias	V_{bias}	2 V
Ratio Veto/Main voltage bias	R_{veto}	0.4
Symmetric factor of the voltage bias	S_{bias}	0.5

Table 6.2: Parameter values for the design and default polarization of REDN1.

separated from the copper chassis by vacuum represented by the light blue surrounding volume. The Teflon clamps are not represented in the scheme and are not a part of the simulation. The heat channel of REDN1 consists in a NTD of small standard dimensions $(2 \times 2 \times 0.45)$ mm. It is glued on aluminium at the center of the top surface as represented by the white rectangle. Although represented, the NTD is not simulated. The ionization channel of REDN1 has an electrode geometry called Inter Digitized (ID) differing from the FID geometry by not having any aluminium deposit on the lateral surface. Each electrodes is composed of multiple aluminium rings or pads linked with aluminium-wire bridge. There is a central pad of radius $r_{center} = 1.5$ mm on the top and bottom planar surfaces of the crystal. The top central pad hosts the NTD thermal sensor. Surrounding the central pads are 7 thin concentric rings of width $w_{Al} = 80$ µm. The crystal edges features large outer rings of width $w_{outer} = 1$ mm. As a result, each planar surface possesses a number $n_{plan} = 9$ of distinct aluminium deposits. Each deposit, ring and pad, are centered and distanced from their neighbor by the planar spacing $d_{plan} = 1.563$ mm. The ionization channel of REDN1 consists in four electrodes labeled A through D. The aluminium deposits of the top (resp. bottom) surface are attributed to the electrodes A, B (resp. C, D) according to the labels on the scheme 6.5. The main electrodes are B and D. Their function is to collect the drifting charges produced in the bulk of the crystal. As such, they are deemed "collect electrodes". The auxiliary electrodes are A and C. Their role is to collect any charges produced near the surface of the crystal. As for the FID detectors, these electrodes allow for the tagging of any surface recoil. The denomination "veto electrodes" is kept for these electrodes. Same-sided collect and veto electrodes have their aluminium rings interleaved as to correctly shape the electric field. In order to tag recoil happening on the lateral surface and under the NTD, the central pads and the outermost large rings are attributed to the veto electrodes A and C.

With the now fixed electrode geometry, the electrostatics simulation is run and can output the capacitance matrices relative to REDN1. The usual equivalence between electrodes and indexes displayed in equation 6.1 is used. As such, the Maxwell capacitance matrix associated with the electrodes of REDN1 is evaluated to:

$$\boldsymbol{C} = \begin{pmatrix} 19.46 & -11.84 & -3.00 & -1.89 \\ -11.84 & 16.17 & -1.89 & -1.26 \\ -3.00 & -1.89 & 19.46 & -11.84 \\ -1.89 & -1.26 & -11.84 & 16.17 \end{pmatrix} \times 10^{-12}\,\mathrm{F} \tag{6.8}$$

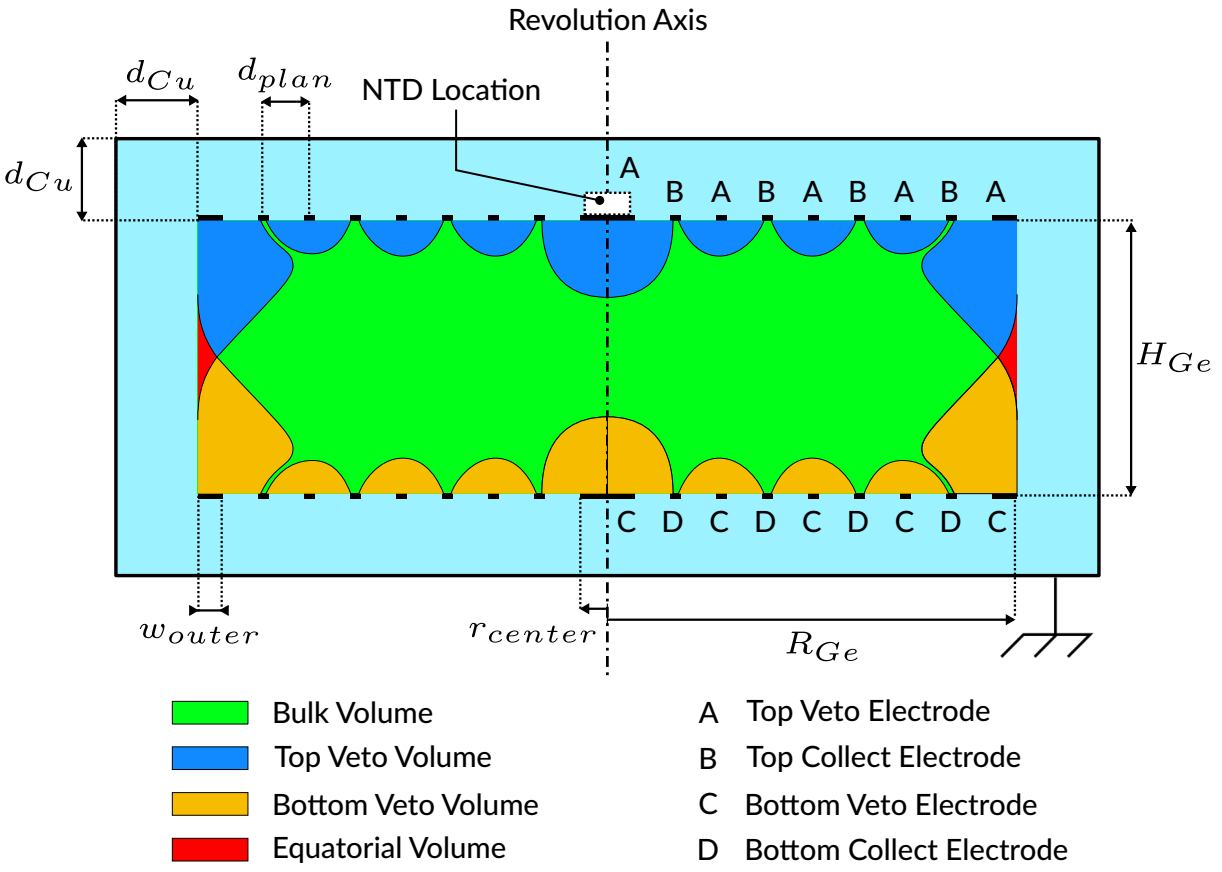

Figure 6.5: Cross-section scheme of the REDN1 detector. This scheme is not to scale and the main dimensions are listed in the table 6.2. The electrically grounded rectangle is the cooper chassis separated from the germanium crystal by vacuum in light blue. The aluminium pads and rings are represented in black at the surface of the crystal and labeled according to their electrode of attribution. The default potential of the electrodes are $(V_A, V_B, V_C, V_D) = (-0.4, +1, +0.4, -1)$V. The colored volumes inside the crystal are drawn from electric field lines with common start and end points.

Using the equations 4.57, the mutual capacitance matrix of REDN1 is evaluated to:

$$\boldsymbol{C}^m = \begin{pmatrix} 2.73 & 11.84 & 3.00 & 1.89 \\ 11.84 & 1.18 & 1.89 & 1.26 \\ 3.00 & 1.89 & 2.73 & 11.84 \\ 1.89 & 1.26 & 11.84 & 1.18 \end{pmatrix} \times 10^{-12}\,\mathrm{F} \tag{6.9}$$

The hierarchy of the capacitance terms of REDN1 is very similar to the one discussed for the FID38 design in section 4.2.6. The dominant capacitance terms are the one associated to same-sided collect and veto electrodes $C^m_{AB} = C^m_{CD}$. This is explained by same-sided electrodes having interleaved rings thus emulating a high area and low distance in regards to their capacitive coupling. As usual, the self-capacitance C^m_{XX} are small due to the high dielectric constant of the germanium compared to vacuum. The only significant difference between REDN1 and FID38 is the relatively low capacitance term between the veto electrodes C^m_{AC} in the case of REDN1. Indeed, as this detector has no aluminium deposit on its lateral surface, it does not have the equatorial veto rings notorious for their low equatorial distance d_{eq} leading to heightened capacitance.

Another result independent from the polarization of REDN1 is the map of the total weighting potential presented in the figure 6.6. In this graph, red colored regions corresponds to a total weighting potential tending to unity, thus mitigating the adverse effect of charge trapping on the signal generation. These regions are mostly present near the electrodes and near the center of the crystal. Blue-colored regions indicates a lower total weighting potential and are present on the periphery of the crystal. This is due to the absence of aluminium deposit on the lateral surface of REDN1. As such, a significant portion of the signal is induced on the grounded chassis.

The polarization of REDN1 is the same as for the design FID38 which is displayed in equation 4.37. The potential of the electrodes are fixed by the same three parameters: the bias voltage V_{bias}, the polarization symmetry S_{bias} and the polarization ratio R_{veto}. The default polarization is set at $(V_{bias}, S_{bias}, R_{veto}) = (2\,\mathrm{V}, 0.5, 0.4)$. In this state, the electric potential of the electrodes are:

$$(V_A, V_B, V_C, V_D) = (-0.4, +1, +0.4, -1)\ \mathrm{V} \tag{6.10}$$

The electrostatic equations are numerically solved using this default polarization. The figure 6.6 presents a map of the electric potential with isopotential contours. The figure 6.7 displays two graphs relative to the electric field. On the left is the map of the magnitude of the electric field $\|\vec{E}\|$ with a white overlay representing the electric field lines. On the right are the histogram and the cumulative distribution function of the magnitude distribution over the crystal volume. Apart from the periphery of the crystal, the electric potential and magnitude are very similar to the ones obtained with the simulation of the FID38 design. In the bulk of the crystal, the electric field is almost uniform and participates to the magnitude peak at $\|\vec{E}\| = 0.4\,\mathrm{V}\cdot\mathrm{cm}^{-1}$. On the top and bottom surface, the alternating potential volume shapes the electric field line to form veto volumes. As the electric field is nullified under the veto rings, we observe associated small low magnitude regions. The electric field on the lateral surface of the crystal is dominated by the influence of the large outermost veto rings and the grounded chassis. The electric field is nullified close to the equator at the divergence point for the field lines. The CDF of the magnitude distribution conforms that a significant fraction of the volume has a low magnitude value.

A close study of the field lines separate the crystal volume in several regions with different collecting behaviors depending on the start and the end points of the field lines. For REDN1, there are four different regions which are drawn on the scheme 6.5. The main region is the "bulk volume" also called "fiducial volume", colored in green on the scheme, which corresponds to field lines linking the two main collect electrodes B and D. Its volume is the important theoretical fiducial volume. At default polarization, its percentage is estimated at $\%_{fid} = 51.75\,\%$.

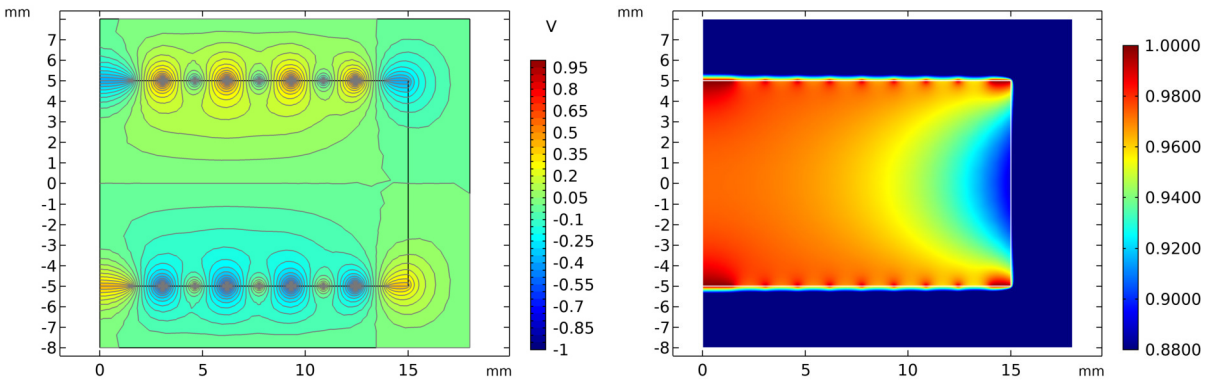

Figure 6.6: Color maps of the electric potential (on the left) and the total weighting potential (on the right) from the simulation of REDN1. For the left graph, the default polarization is used.

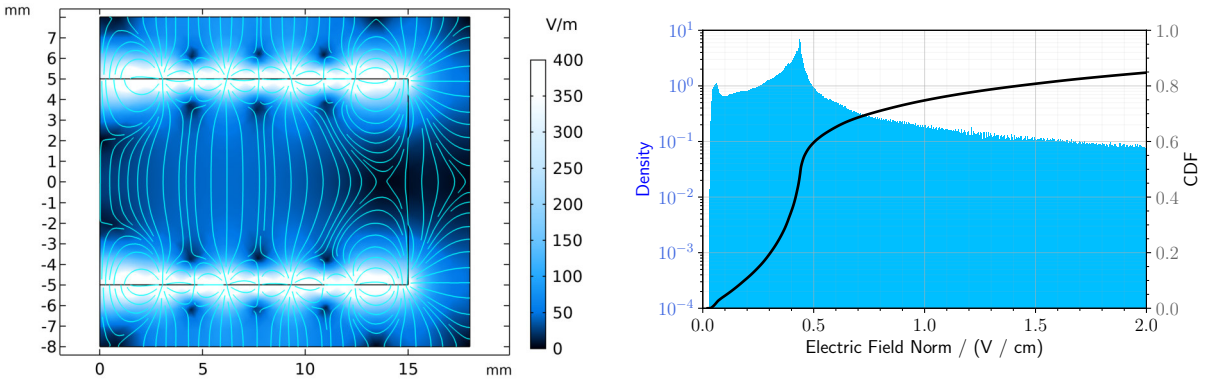

Figure 6.7: (On the left) Color map of the magnitude of the electric field with white representation of the electric field lines from the simulation of REDN1. The default polarization is used. The colored volumes in the scheme 6.5 are drawn from the electric field lines with common start and end points. (On the right) Histogram and Cumulative Distribution Function of the distribution of the magnitude of the electric field over the crystal volume from the simulation of REDN1.

Near the top (resp. bottom) surface of the crystal, the electric field lines link the same-sided veto and collect electrodes A and B (resp. C and D). Just as for the FID38 design, this regions is called the top (resp. bottom) veto volume and is colored in blue (resp. orange) on the scheme. The estimated theoretical volume percentages of the top or bottom veto volumes are $\%_{top,veto} = \%_{bottom,veto} \approx 22\,\%$. The last volume is drawn by the field lines connecting the top and bottom veto electrodes A and C, even though a majority of these field lines leave the crystal. The denomination "equatorial volume" is in use and it is illustrated by the red region near the equator. Its volume percentage is of about $\%_{equator} \approx 2\,\%$.

Each region has a specific electric charge signal vector $\vec{Q}$ induced by a number N_p of electron-hole pairs created in the crystal such that $Q = N_p e$. We consider an ideal charge collection where electron and hole trajectories correspond to the field lines. The charge vectors are the same as for the design FID38 displayed in equation 4.47. Assuming the electric charges exactly follows the electric field lines, the overwhelming majority of the charges produced in the equatorial volume should be trapped on the lateral surface of the crystal. As such, the charge vector $\vec{Q}_{equator}$ would depends on the weighting potential of each electrodes on the lateral surface.

In section 6.3.3, the REDN1 simulation is compared to the experimental data taken during the operation of REDN1. Specifically, two distinct scans were conducted over the voltage bias V_{bias} and the polarization ratio R_{veto}. As discussed in the previous chapter 5, V_{bias} leaves all

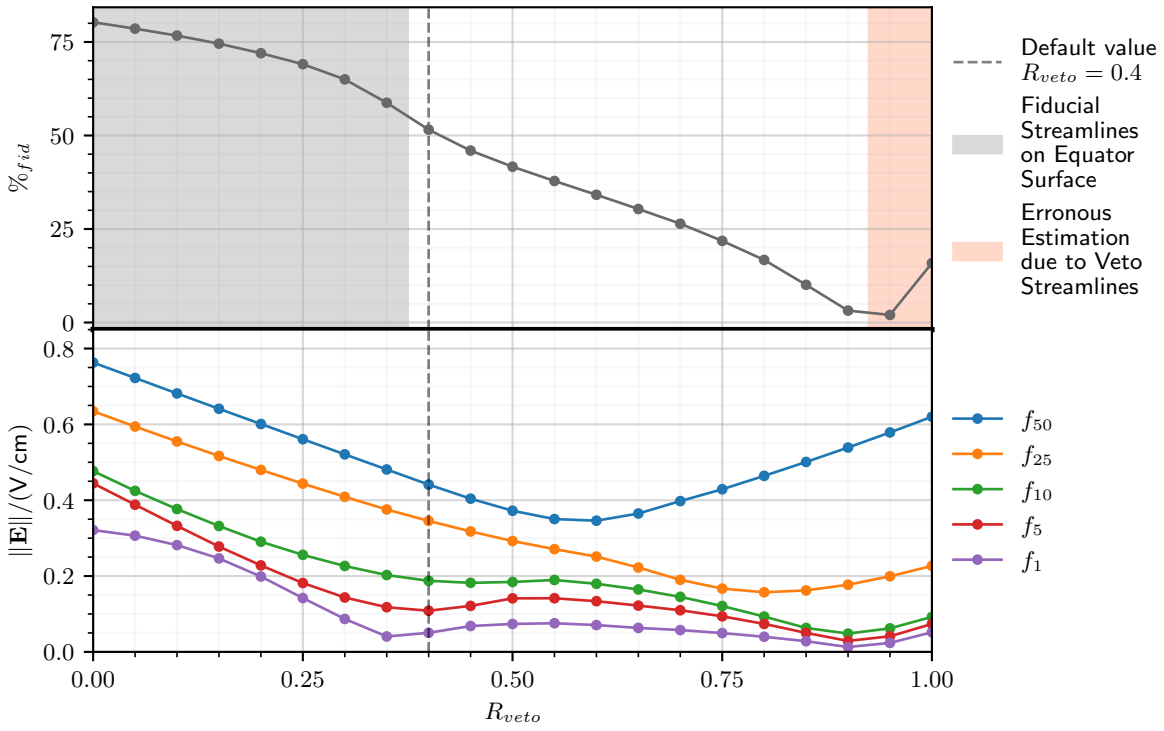

Figure 6.8: Scan over the polarization ratio parameter R_{veto} from the simulation of REDN1. The plotted quantities are the fiducial volume percentage $\%_{fid}$ and some percentiles f_x of the electric field norm. The red-shaded area indicates an overestimation of the fiducial volume through the erroneous integration of veto volume in the used algorithm. Fiducial percentage are this area should not be considered.

the quantities evaluated from the simulation of REDN1 unaffected except for a scaling of the magnitude of the electric field. However, scanning over R_{veto} induces changes on the fiducial volume and the electric field. Therefore, this scan was conducted with the REDN1 simulation as to compare with experimental data later. The scan is performed over a linear scale from 0 to 1 with the default configuration being $R_{veto} = 0.4$. The results are presented as graphs in the figure 6.8. The top graph corresponds to the fiducial volume percentage $\%_{fid}$ while the bottom graph displays some percentiles f_x of the electric field magnitude distribution. The grey-shaded range from 0 to 0.375 indicates that fiducial field lines are in contact with the lateral surface of the crystal. Such a configuration is expected to have adversarial effects on the surface tagging ability of the detector. The red-shaded range for $R_{veto} > 0.925$ indicates that the fiducial values were overestimated due to the unexpected integration of some veto volume. As such, the percentages should not be considered. The global trend of the fiducial percentage is a significant decrease with rising R_{veto}. Indeed, as this parameter increases, the veto volumes grows deeper into the bulk of the crystal. This observation is on par with the decrease in the electric field norm in the crystal. This is due to the potential of the veto electrodes increasing in absolute value with R_{veto} up to 0.6. From this point onward, the median magnitude greatly recovers while other percentiles $f_{x\leq 0.25}$ see their value lowers and stabilizes. Indeed, with the ever decreasing fiducial volume, the veto and equatorial volume grow significantly in size and field strength. On the contrary, the bulk volume shrinks and has a lowered field strength.

Stream	V_{bias} / V	Polarization / V	
		A, B	C, D
tg10l002	-4	-2	+2
tg10l001	-2	-1	+1
tg10l003	-1	-0.5	+0.5
tg11l001	-0.5	-0.2	+0.2
tg11l003	-0.2	-0.1	+0.1
tg12l000	-0.1	-0.05	+0.05
tg12l001 tg12l002	0.1	0.05	-0.05
tg11l002	0.2	+0.1	-0.1
tg11l000	0.5	+0.2	-0.2
tg10l004	1	+0.5	-0.5
tg09l000	2	+1	-1
tg09l002	4	+2	-2

Table 6.3: List of the streams with their polarization for the experimental study of RED80 in the Run 57.

6.2 Detector Operation and Analysis Pipeline

This section presents rapidly the operation of the RED80 and REDN1 detectors in the cryostat and then heavily focuses on the analysis of the data streams. A majority of the analysis pipeline is common to the study of the detectors for comparison with the electrostatics simulation and the study of the IP2I neutron background assessed in the next chapter 7. As such, the different steps may be illustrated with data streams from the neutron measurement.

6.2.1 Experimental Setup

The detectors RED80 and REDN1 were studied in two separate cryostat runs: the Run 57 and 61 respectively. In each of the runs, detectors were placed in the suspended tower described in section 2.2. The germanium crystals of the detectors were activated with the AmBe neutron source as described in section 2.3.4. As such, RED80 and REDN1 are operated with an intrinsic calibration peak of 10.37 keV electronic recoils with uniform distribution over the detector volume. The data collection consists in multiple streams with different ionization channel configurations. Each streams is at least 2 hours long as to explore enough configuration points while gathering enough statistics for the analysis. Some occasional streams are longer as taken during nights and weekends. Some ionization configurations were repeated and can be used to estimate the reproducibility of the measurements. The streams along with their corresponding polarization configuration are listed in the tables 6.3 for RED80 and 6.4 for REDN1.

The detector RED80 was operated in the Run 57 along with the detector RED70. Although it was very similar to the FID38 design, RED70 showed very high leakage currents between the electrodes, even at very low voltage bias $V_{bias} \approx 0.1\,\text{V}$. Such currents leads to a huge increase in temperature and a quick saturation of the ionization electronics. As such, RED70 is virtually unusable with polarized electrodes, and is not studied in this work.

The detector RED80 was operated with two different heat channel configurations. Before and up to the stream tg17l000, RED80 was regulated at the temperature $T_{cryo} = 18\,\text{mK}$ with a bias current $I_{bias} = 2\,\text{nA}$ through its NTD of resistance $R_{NTD} = 1.6\,\text{M}\Omega$. From and after the stream tg17l001, the regulation temperature was decreased to $T_{cryo} = 16\,\text{mK}$ with a bias current $I_{bias} = 1\,\text{nA}$ with the NTD resistance measured at $R_{NTD} = 3.8\,\text{M}\Omega$. As addressed in section 4.1.4,

Stream	V_{bias} / V	R_{veto}	Polarization / V			
			A	B	C	D
tk18l001	-2	0.4	+0.4	-1	-0.4	+1
tk19l001	0.25	0.4	-0.05	+0.125	+0.05	-0.125
tk19l000	0.5	0.4	-0.1	+0.25	+0.1	-0.25
tk18l000	1	0.4	-0.2	+0.5	+0.2	-0.5
tk15l005 tk16l000	2	0.4	-0.4	+1	+0.4	-1
tk20l000 tk25l000	4	0.4	-0.8	+2	+0.8	-2
tk25l001	8	0.4	-1.6	+4	+1.6	-4
tk27l001	4	0.2	-0.4	+2	+0.4	-2
tk26l001	4	0.3	-0.6	+2	+0.6	-2
tk26l000	4	0.5	-1	+2	+1	-2
tk20l003	2	0.6	-0.6	+1	+0.6	-1
tk27l002	4	0.7	-1.4	+2	+1.4	-2

Table 6.4: List of the streams with their polarization for the experimental study of REDN1 in the Run 61.

the ionization channel performance are independent from the configuration of the heat channel. So, in the case of RED80, the comparison of stream with different current bias I_{bias} of the NTD is valid.

The detector REDN1 was operated along with the detector RED90 in the Run 61. RED90 is used for NTD characterization like detectors RED1 and RED10 studied in chapter 3. It consists in a germanium crystal with a bare surface and a single NTD thermal sensor and does not possess an ionization channel. The temperature of the detector REDN1 is regulated at the temperature $T_{cryo} = 14\,\text{mK}$ for the whole run with a single configuration of its heat channel: the bias current was set to $I_{bias} = 0.54\,\text{nA}$ through the NTD of resistance $R_{NTD} = 6.6\,\text{M}\Omega$.

6.2.2 Raw Data format and Decorrelation

The signals of the ionization and heat channel of the germanium detectors are continuously recorded during operation as a data stream. The signal of the ionization channel is the four electric potential of the electrodes. The signal of the heat channel is the voltage of the NTD thermal sensor. A data stream consists in time series of these ionization and heat signals. For both the detectors RED80 and REDN1, possessing one NTD and four electrodes, a data stream saves five electric potentials every time step dt. In this work, the sampling frequency is $f_s = 400\,\text{Hz}$ with $dt = 2.5\,\text{ms}$. These voltage values are extracted by an analog-to-digital conversion system and thus expressed in Analog-to-Digital Unit (ADU) as introduced in section 4.1.8. The data stream is later processed into events with the software NEPAL as described in the section 6.2.3. An event is a time window from a data stream of length $T_{win.}$. In this work, this time length is $T_{win.} = 0.5\,\text{s}$. Considering the sampling frequency, an event is a time series of 200 points t_i with five voltage $V_{CH}(t_i)$ with $CH \in \{heat, A, B, C, D\}$. As an example, four triggering events are displayed in the figure 6.9.

The raw voltage measured $V_{CH}(t)$ as a function of the time t, is the superposition of a signal function $S_{CH}(t)$ and a noise function $N_{CH}(t)$ such that:

$$\forall CH \in \{heat, A, B, C, D\} : \quad V_{CH}(t) = S_{CH}(t) + N_{CH}(t) \tag{6.11}$$

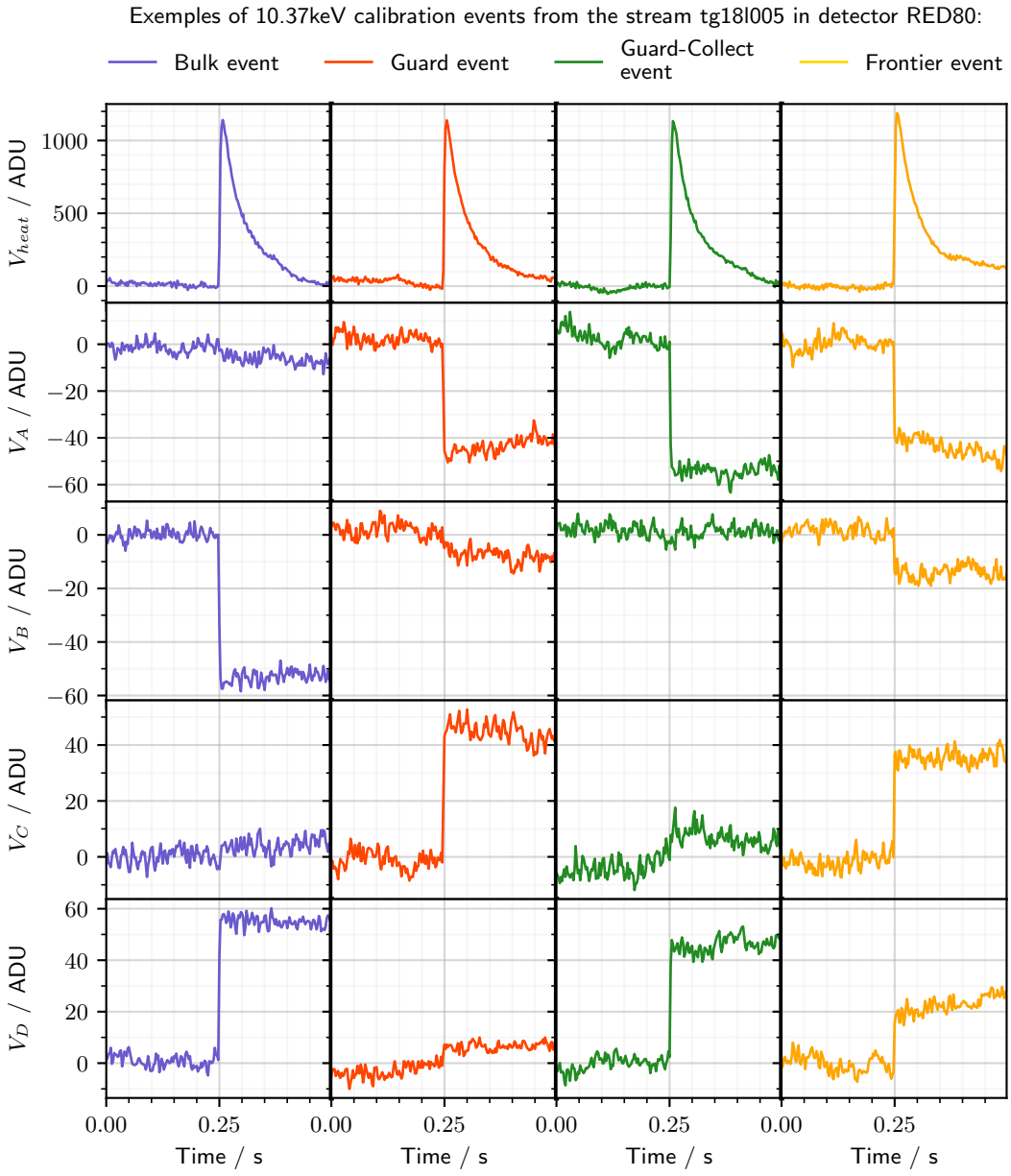

Figure 6.9: Examples of decorrelated triggering events for the detector RED80. An event is a 0.5 s time window of the data stream corresponding to five time series $V_{CH}(t)$ with $CH \in \{heat, A, B, C, D\}$. The ionization signals of the bulk, guard and guard-collect events are consistent with the expected signatures in RED80 given in equation 6.7. The frontier event corresponds to a linear combination of all these signatures.

The noise functions $N_{CH}(t)$ are characterized by their PSD in $\mathrm{ADU}^2/\mathrm{Hz}$. The modelization of these functions for the heat and ionization channels are discussed in the corresponding chapters 3 and 4. In the case of the ionization channel, the noise function can be separated into two components:

$$N_{CH}(t) = n_{CH}^{uncorr.}(t) + n^{corr.}(t) \tag{6.12}$$

The first component $n_{CH}^{uncorr.}(t)$ is the uncorrelated noise which is specific to each electrode. The second component $n^{corr.}(t)$ refers to the correlated common noise to the four electrodes A, B, C, D. This correlated noise can be subtracted from the measurement by a "decorrelation" processing step based on combining the ionization signals. The charge conservation in the detector is expressed as:

$$Q_A + Q_B + Q_C + Q_D = 0 \quad \Leftrightarrow \quad \begin{pmatrix} 1 & 1 & 1 & 1 \end{pmatrix} \cdot \vec{Q} = 0 \tag{6.13}$$

with Q_X the charge induced on the electrode X composing the induced charge vector $\vec{Q}$. By combining this conservation equation with the expression of the charge vector (eq. 4.55), we obtain the charge conservation expressed with the electric potential of the electrodes:

$$\begin{aligned} & \begin{pmatrix} 1 & 1 & 1 & 1 \end{pmatrix} \cdot \boldsymbol{C}^{tot} \cdot \vec{V} = 0 \\ \Leftrightarrow \quad & \begin{pmatrix} \sum_i C_{i1}^{tot} & \sum_i C_{i2}^{tot} & \sum_i C_{i3}^{tot} & \sum_i C_{i4}^{tot} \end{pmatrix} \cdot \vec{V} = 0 \\ \Leftrightarrow \quad & C_{AA}^{tot,m} V_A + C_{BB}^{tot,m} V_B + C_{CC}^{tot,m} V_C + C_{DD}^{tot,m} V_D = 0 \end{aligned} \tag{6.14}$$

where $\boldsymbol{C}^{tot}$ and $\boldsymbol{C}^{tot,m}$ are the Maxwell and mutual capacitance matrices of the considered detector with the capacitive cabling according to the equation 4.75. In section 6.2.6, the cabling capacitance affecting all the electrodes is estimated to about 125 pF which is much greater than the self-capacitance term C_{XX}^{m} of the detector RED80 and REDN1 evaluated in equations 6.3 and 6.9. As a result, we can consider:

$$C_{AA}^{tot,m} \approx C_{BB}^{tot,m} \approx C_{CC}^{tot,m} \approx C_{DD}^{tot,m} \tag{6.15}$$

The expression of the charge conservation with the electric potential now simplifies to:

$$V_A + V_B + V_C + V_D = 0 \tag{6.16}$$

One should note that this simplification is only valid in this work because of the high cabling capacitance $C^{cabling}$ imposed by the current JFET-based electronics. In the future, the use of the HEMT-based electronics aiming at the low cabling capacitance of 5 pF will discard this simplification. The simplified charge equation 6.16 indicates that the measurement of one of the potential is redundant as it can be calculated from the others. As illustration, the electric potential of the electrode A is given by:

$$V_A(t) = -V_B(t) - V_C(t) - V_D(t) \tag{6.17}$$

This redundancy allows a clever change of variables to improve the channel resolution and subtract the correlate noise. We define the decorrelated electric potentials $V_A^{decor.}(t)$ as:

$$\begin{cases} V_A^{decor.}(t) = \alpha \cdot V_A(t) + (1-\alpha) \cdot (-V_B(t) - V_C(t) - V_D(t)) \\ \text{idem for electrodes } B, C, D \end{cases} \tag{6.18}$$

with α a constant. Assuming the same baseline energy resolution σ_0 for each of the raw electric potential measurement $V_X(t)$, its optimal value is $\alpha = \frac{3}{4}$. By replacing the expressions

6.11 and 6.12 in the expression of decorrelated measurements 6.18, one can check that correlated noise is indeed suppressed. Moreover, the resolution on the decorrelated measurement is lower $\sigma_0^{decor.} = \frac{\sqrt{3}}{2}\sigma_0$. Although this combination of the electrode signals is advantageous, it requires the charge conservation to be satisfied which is enforced by the "charge conservation cut" discussed in section 6.2.8. For the rest of this work, the terms "ionization signal" will refer to these decorrelated signals $V_X^{decor.}(t)$. The ionization signals events presented in the figure 6.9 are decorrelated.

For each channel CH, the signal function $S_{CH}(t)$ is modeled as the scaling of a signal template $s_{CH}(t)$ as:

$$S_{CH}(t) = A_{CH} \cdot s_{CH}(t) \tag{6.19}$$

with the amplitude A_{CH} expressed in ADU. The theorization of the heat and ionization signals are discussed in the chapter 3 and chapter 4 respectively. The signal function of the heat channel is model by a linear combination of decaying exponential. The template of the heat signal of unitary amplitude is expressed:

$$\begin{aligned} s_{heat}(t) = (1-\epsilon-v) \times (&\exp(-t/\tau_1) - \exp(-t/\tau_{th}) \\ &+ \epsilon\,(\exp(-t/\tau_2) - \exp(-t/\tau_{th})) \\ &+ v\,(\exp(-t/\tau_3) - \exp(-t/\tau_{th})) \end{aligned} \tag{6.20}$$

with the parameters $\epsilon, v, \tau_{th}, \tau_1, \tau_2, \tau_3$ fixed by the thermal properties of the detector. The heat amplitude A_{heat} is proportional to the heat energy E_{heat}. In the "calibration" step of the analysis pipeline, the conversion rate between amplitude and energy is determined experimentally. For the ionization channel, the template signals $s_X(t)$ for $X \in \{A, B, C, D\}$ simply corresponds to the Heaviside function:

$$\forall CH \in \{A, B, C, D\} : \quad s_{CH}(t) = \Theta(t) \tag{6.21}$$

Under the assumption of ideal drift of the charge carriers in the germanium crystal, the ionization amplitudes A_{CH} are proportional to the terms of the voltage vector $\vec{V}$ calculated in equations 6.7 and 4.47. The corresponding proportionality factor estimates the ionization energy $E_{Ion.}$ of the event. The figure 6.9 displays four events attributed to different collection volumes of the detector RED80. The signatures of the bulk, guard and guard-collect events are consistent with their modelization given in equation 6.7. The frontier event is attributed to a recoil located at the frontier between the collection volumes in the scheme 6.2. The charge carriers are separated between the different volumes and induce a signal on all the electrodes.

6.2.3 Optimal Filtering, Trigger and Event Processing

The data are recorded continuously under the form of data stream sampled at $f_s = 400\,\text{Hz}$. The pulse signals induced by particles interacting with the germanium crystal are identified into events by processing the stream. These data streams are processed by the script NEPAL developed by the MANOIR research group. There are several processing steps applied by this script: the decorrelation (already discussed in section 6.2.2), the filtering, the trigger and the event processing.

Each channel $V_{CH}(t)$ of a data stream is filtered with a high-pass filter and then an Optimal Filter (OF). This first high-pass filter consists in a second-order Butterworth numerical filter with a cut-off frequency of 4 Hz. Its role is to suppress any noise structures at frequencies below the analysis range, from $1/T_{win.} = 2\,\text{Hz}$ to $f_s/2 = 200\,\text{Hz}$.

The optimal filter is a filter matched on the frequency dependence of the observed signal and noise. The figure 6.10 illustrates the optimal filtering applied to the heat channel of the detector RED20 from the paper [10]. A noticeable difference lies in the length of the time windows. In this work, for the analysis of the RED80 and REDN1 data streams, an event lasts $T_{win.} = 0.5\,\text{s}$. In

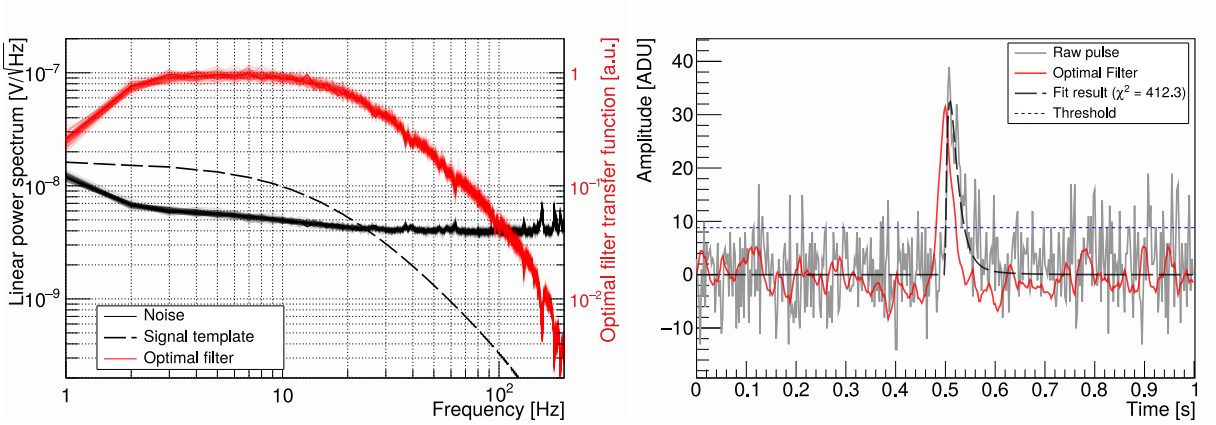

Figure 6.10: Illustrations of the Optimal Filtering applied to the heat channel of the detector RED20 taken from [10]. On the left are displayed the hourly-averaged noise Power Spectral Densities (PSD) (black curves), detector signal bandwidth (black dashed line), and resulting optimal filter transfer functions (red curves) as a function of frequency, for the six days of data acquisition. The 137 separate PSDs and transfer functions are overlayed. On the right is an unfiltered raw trace (grey solid line) and output of the optimal filter (red solid line). The trigger level at 3σ is shown as the blue dotted line. The result of the pulse fitting procedure, with a $\chi^2/\mathrm{ndf} = 1.03$, is shown as the black long-dashed line.

the illustration using the analysis of the detector REd20, events are longer with a time length of 1 s.

The noise PSDs $J_{CH}(f)$ of the heat and ionization channels are determined experimentally each hour with samples of 0.5 s time traces without pulses. These so-called "noise events" are uniformly selected as randoms throughout the entire data stream on that hour. The signal functions $s_{CH}(t)$ correspond to the signal templates 6.20 for the heat channel and 6.21 for the ionization channels. The hourly heat noise LPSDs and signal power spectrum associated with RED20, corrected for the 2 Hz filter gain, are overlaid on the left subplot of figure 6.10.

For each channel CH and for each hour, an optimal filter function $H_{CH}(f)$ is derived from the noise PSD $J_{CH}(f)$ and the conjugate of the signal Fourier transform $\hat{s}^*_{CH}(f)$ such that:

$$H_{CH}(f_i) = h \cdot \frac{\hat{s}^*_{CH}(f_i)}{J_{CH}(f_i)} \cdot e^{-i2\pi f_i t^M} \quad \text{with} \quad h = \left(\sum_i \frac{|\hat{s}_{CH}(f_i)|^2}{J_{CH}(f_i)} \right)^{-1} \tag{6.22}$$

with the frequencies $f_i \in [-f_s/2 \,..\, f_s/2]$ and t^M as the time position of the pulse template maximum. The term h is a normalization constant that preserves the amplitude of the pulse signal. The moduli $|H_{heat}(f_i)|$ associated with RED20 are shown as the red solid lines in the left panel of figure 6.10. This plot confirms that the optimal filter gives more weight to frequencies with high signal-to-noise ratio. The optimal filters are applied to the five heat and ionization channels of the data stream.

The trigger step of the processing consists in identifying candidate pulses in the filtered data stream as an event. An event is a time window of length $T_{win.} = 0.5\,\mathrm{s}$ from a data stream. A triggering event is defined when a filtered channel exceeds a given threshold level $A^{trig.}_{CH}$. The event is centered on the local maximum of the OF filtered data stream passing this amplitude threshold. The instances when multiples such local maxima are identified within the same 0.5 s time windows are called "pile-up" events. In this cases, only one event is defined centered on the pulse with the highest amplitude, imposing an exclusion interval of $\pm 0.25\,\mathrm{s}$ where the lowest pulses cannot trigger. This energy ordering of the pulse finding algorithm affects the energy

dependence of the triggering efficiency. For instance, the dead-time associated to the search for low-energy events is effectively greater than that associated to large pulses which are favored in the triggering process. A dedicated data-driven procedure, the pulse simulation presented in section 7.4.1, is applied to take into account these effects in the determination of the efficiency as a function of energy.

The right subplot of the figure 6.10 displays a triggering event. It compares the raw heat pulse and its OF version. The amplitude threshold $A_{CH}^{trig.}$ is represented by the horizontal line. The threshold level is defined as a fixed number n of the baseline energy resolution σ_{CH}^{OF}. This resolution corresponds to the standard deviation of the amplitudes of the noise events. The value of n was chosen such that the rate of noise induced triggers is significantly smaller than the rate of physical events. In this analysis, the trigger threshold is set to $A_{CH}^{trig.} = 3 \cdot \sigma_{CH}^{OF}$. For the default polarization of the detector RED80, the trigger thresholds are in average:

$$\begin{cases} A_{heat}^{trig.} \approx 3 \times 9\,\text{ADU} = 27\,\text{ADU} = 240\,\text{eV} \\ \forall X \in \{A, B, C, D\}, A_{X}^{trig.} \approx 3 \times 1.3\,\text{ADU} = 3.9\,\text{ADU} = 735\,\text{eV} \end{cases} \tag{6.23}$$

A pulse can trigger with either its heat or ionization signals. However, due to the low heat resolutions, most events trigger with the heat channel especially at the lowest recoil energies.

Each triggering event is further processed to estimate its amplitude. Each channel CH is adjusted by the corresponding signal models, in equation 6.20 for the heat channel and equation 6.21 for the ionization channels. The model adjustment is done by minimizing a χ^2 function defined in the frequency domain:

$$\chi^2_{CH}(a, t^0) = \sum_i \frac{|\hat{V}_{CH}(f_i) - a \cdot \hat{s}_{CH}(f_i) \cdot e^{-i2\pi f_i t^0}|^2}{J_{CH}(f_i)} \tag{6.24}$$

where a corresponds to the scaling factor of the unitary signal template and t^0 is the starting time of the pulse. Considering the number of points composing an event, each χ^2 functions should tend to 200. The minimization yields several quantities. First, the minimal χ^2 value of the event which is the minimizing amplitude which quantifies the quality of the fit. This value is used to enforce the χ^2 cut described in the next section 6.2.5. Then, the minimizing parameters a and t. The amplitude a is an estimation of the amplitude A_{CH} of the signal. The five amplitudes of the heat and ionization channel are used to reconstruct the heat E_{heat} and ionization $E_{Ion.}$ energies. Eventually this leads to the estimation of the recoil energy E_R deposited in the germanium crystal by an interacting particle. The time t^0, called the timestamp of the event, corresponds to the location of the event within the data stream. It is used to monitor the performances of the detector over time and define the live time, as described in section 6.2.4. Moreover, the timestamp of an event is compared to the maintenance period and the reset times of a detector as part of the quality cuts in section 6.2.5.

Another quantity can be extracted from the raw signals: the offset, which corresponds to the baseline of an event inside the ADU dynamic range. In the case of the heat channel, the heat offset is a linear function of the resistivity of the NTD thermal sensor. By monitoring the heat offset, we can access the temperature of the detector $T_{abs} \approx T_{NTD}$. If represented as a function of the timestamp t_0, it is possible to check on the stability of the detector thermalization which is used to define the live time cut in section 6.2.4. For the ionization channel, the offsets of all the electrodes are periodically set to 0 ADU by the reset procedure described in section 4.1.8 as not to leave the dynamic range of the acquisition electronics. The ionization offset is further discussed in section 6.2.5 as to define the "offset cut".

6.2.4 Live Time Cut

The live time T_{live} corresponds to the period of time where the detector is considered available for data taking. While we would like the live time to equal the whole running time of the detector, it is often not the case. There can be some periods where the temperature regulation of the cryostat can be defective (temperature spikes, power cuts) which degrade the heat sensitivity of the detector. These periods are pruned as to keep only the data with optimal operation of the detectors. Some periods are also affected from various malfunctions not clearly understood relative to the acquisition electronics. These portions of the streams were corrupted with no data saved all together. During this time, the detector is not considered to be alive. The live time are manually defined by monitoring all the control values defined in section 6.2.2 as functions of the timestamp.

Although a high live time is linked with a high events statistics, the estimation of T_{live} is used in the calculation of the exposure of the detector. This exposure is discussed later in section 7.8 when presenting the results of the IP2I neutron background measurement. Indeed, this exposure is used to normalize the counts as to derive the event rate. The live times associated to the RED80 streams for the neutron study are listed in the table 7.2 in the next chapter 7.

In this section, the results are not normalized by the exposure, and the live times are of minimal importance. As such for the RED80 and REDN1 data streams used for the comparison to electrostatics simulation, the live time is considered to be the length of the data stream of an average of 2 hours. As such, for all the streams listed in tables 6.3 and 6.4, all the events pass the live time cut.

6.2.5 Quality Cuts

The objective of the "Quality cuts" is to discard any event with problematic characteristics which would result in an incorrect energy reconstruction. The term "Quality cuts" refers to an ensemble of analysis cuts: the live time cut (described in the previous paragraph), the maintenance cut, the reset cut, the offset cut and the χ^2 cut. Events passing all these quality cuts are designated as "quality events". In addition to the description of each of the quality cuts, this paragraph presents the parametrization specific to the data streams listed in the tables 6.3 for RED80 and 6.4 for REDN1. The parametrization of the quality cuts for the IP2I neutron measurement is presented in the next chapter 7.

The maintenance and reset procedures are introduced in section 4.1.8. The objective of the maintenance is to recharge the electrodes in order to enforce a constant voltage bias on the whole stream. The reset procedures prevents the digital readout of the ionization channels from saturating. Both procedures periodically induce parasite signals in the data streams. Although these electronics artifacts could be easily discarded due to their shape differing from the expected heat and ionization signals, this is no more the case for signals of low energies. Such events could be considered as a valid signal and bias the science results. Therefore, these signals are reliably rejected using the knowledge of the frequency and duration of the maintenance and reset procedures within a data stream.

The "Maintenance cut" enforces that all the events with a timestamp t_0 within a maintenance period is discarded. In this work, a maintenance lasts $1\,\text{min} = 60\,\text{s}$ and occurs every $864\,\text{s} \approx 14.2\,\text{min}$. In the end, the maintenance procedures induces a down time rate of $60/(60+864) = 6.6\,\%$. An event passes the maintenance cut if it does not occur during a maintenance.

Contrary to the maintenance, a reset is almost instantaneous, generating a single artifact pulse. Consequently, the "Reset cut" rejects events occurring shortly after each reset procedure. As the detectors are operated in above ground conditions, the event rate is high which calls for the very low period of reset $T_{reset} = 2\,\text{s}$. An event of timestamp t^0 passes the reset cut is the time

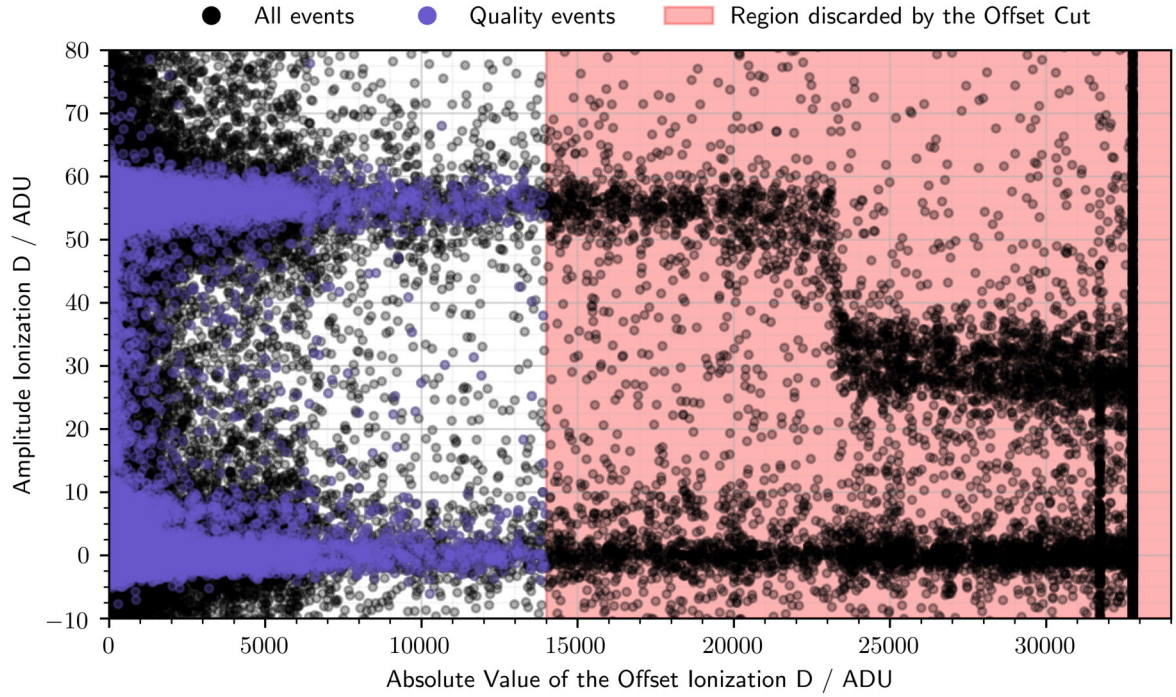

Figure 6.11: Graph of the amplitude A_D of the triggering events of the data stream tg18l005 for detector RED80 versus their offset value. The dense population of amplitude $A_D \approx 55$ ADU corresponds to the 10.37 keV calibration events. From 23 000 ADU in offset, their amplitude drops to about 30 ADU, demonstrating the 1/2 gain loss of the electronics. The red overlay span illustrates the offset cut for the electrode D.

elapsed since the last reset procedure at $t(\text{last reset})$ are greater than a tolerance:

$$t(\text{last reset}) - t^0 > \Delta t_{tol} = 5\,\text{ms} \tag{6.25}$$

Even if the artifact pulses generated by the resets are discarded in the analysis, they can still overlap with neighboring valid pulses thus creating pile-ups. These pile-ups events are generally rejected in the χ^2 cut.

The need for an "offset cut" originates from a non-linearity of ionization readout electronics. The gain applied to the measured signal V_X depends on the ionization offset value. This behavior is consider as faulty as we expect the electrodes to have a constant sensitivity. This phenomenon is illustrated in the figure 6.11 which plots the ionization amplitude A_D of triggering events as a function of their offset values. For low offsets, the 10.37 keV calibration events form a band of events of amplitude $A_D \approx 55$ ADU. However, at the offset value 23 000 ADU, these calibration events are processed with a suddenly lower amplitude of about 30 ADU. This observation is common to all the electrodes $X \in \{A, B, C, D\}$. We can conclude that the gain of the electronics is constant before 23 000 ADU and almost halved after. As such, only a part of the readout dynamic range ensures an optimal operation of the detector. Applying a significant safety buffer, the valid dynamic range is $[-14000, +14000]$ ADU. Events occurring with half gain are discarded by the offset cut, which is illustrated on the figure 6.11 by the red region.

As introduced in section 6.2.3 describing the event processing, the χ^2_{CH} values of an event quantify the quality of the adjustment by the signal template and consequently, the quality of the estimation of the amplitude A_{CH}. All the events with any estimated χ^2, on the heat channel or one of the ionization channels, above a defined threshold function are discarded from the

Detector	Channel	χ^2_0	A_0	b
RED80	Heat	400	3×10^3	2
	Ionization A, B, C, D		2×10^3	2.2
REDN1	Heat	2000	3×10^3	2
	Ionization A, B, C, D	700	2×10^3	2.2

Table 6.5: Parametrization of the χ^2 cut for the data streams listed in tables 6.3 and 6.4 for the detectors RED80 and REDN1 respectively.

analysis. The cut parametrization is a function of the signal amplitude A_X of a channel X in ADU. Indeed, due to the non-linearity of the thermal response, the shape of the signal does depend on the recoil energy as the first order perturbation theory becomes less and less valid. Thus, we see that the χ^2 values of good events are increasing from $\mathcal{O}(10keV)$. Good events at low energy should have a χ^2 value of about:

$$\mathbb{E}\left(\chi^2\right) = \chi^2_0 = T_{\text{window}} \cdot f_s = 200 \tag{6.26}$$

The expression of the parametrization function is:

$$\chi^2_{cut}(A_X) = \chi^2_0 \cdot \left(1 + \left(\frac{A_X}{A_0}\right)^b\right) \tag{6.27}$$

depending on the three parameters: the baseline threshold χ^2_0, the takeoff amplitude A_0 and the quadratic factor b. The parameters are estimated visually for each streams and presented in table 6.5.

In the end, the χ^2 cut is applied on each channels (as seen in figure 6.12) independently. Only the events passing the cut for all the channels is kept and eligible as a quality event.

6.2.6 Cross-talk correction and Cabling capacitance estimation

Section 4.2.7 discusses the expression of the signal induced on the ionization channel by a recoil. It is demonstrated that a recoil, creating a number N_p of electron-hole pairs, generates a charge perturbation on the electrodes A through D. This perturbation is expressed as the charge perturbation vector $\vec{Q}$. In the case of the REDN1 and RED80, there are different charge perturbation vectors depending on the recoil location in the crystal. Their expressions are displayed in equation 6.7 for RED80 and 4.47 for REDN1, considering an ideal drift of the charges and a complete collection on the electrodes. The voltage signal $\vec{V}$ generated on the electrodes is calculated from the charge vectors and the Maxwell capacitance matrix C of the detector according to the equation 4.55. It is calculated in the equations 4.61 for the PL38 design and the equations 4.62 for the FID38 design. Contrary to the charge vector $\vec{Q}$ which has 2 null components, a voltage signal is generated on all the electrodes of the detector. This phenomenon is called cross-talk. The cross-talk correction is an analysis step consisting in calculating an effective charge vector $\vec{Q}_{eff}$ from the amplitude A_{CH} of the measured ionization voltage signals, corresponding to the measured voltage vector $\vec{V}_{meas.}$. With cross-talk corrected measurement, it is possible to proceed with the calibration of the detector and the rest of the analysis. The calculation is done with the

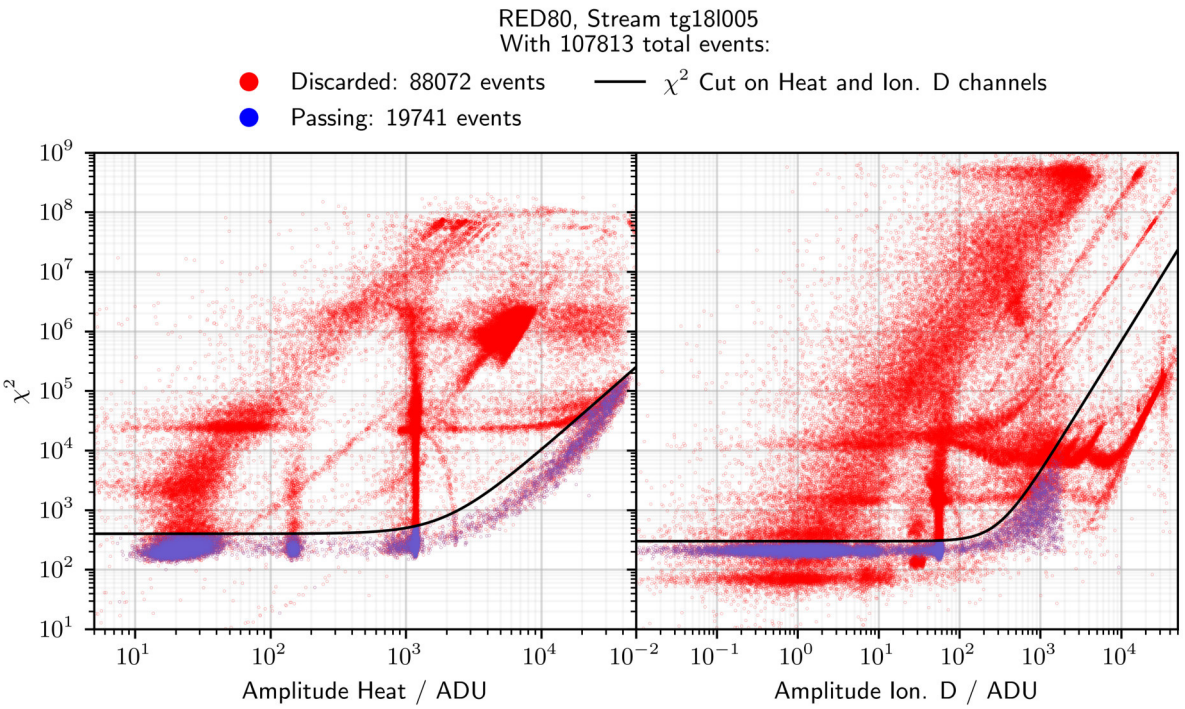

Figure 6.12: χ^2 value for each event as a function of its reconstructed amplitude for the five measuring channels. The cut threshold is represented by the black line. All events are in red, passing events are in blue.

cross-talk correction matrix $\boldsymbol{C}_{tot}$ such that:

$$\vec{Q}_{eff} = \boldsymbol{C}_{tot} \cdot \vec{V}_{meas.} = \boldsymbol{C}_{tot} \cdot \begin{pmatrix} A_A^{corr.} \\ A_B^{corr.} \\ A_C^{corr.} \\ A_D^{corr.} \end{pmatrix} \tag{6.28}$$

with the terms $A_X^{corr.}$ being the cross-talk corrected amplitudes in ADU. This equation is the experimental equivalent of the equation 4.55 dedicated to theoretical perturbation vector $\vec{Q}$ and $\vec{V}$ on electrodes of known total Maxwell capacitance matrix $\boldsymbol{C}_{tot}$. As a result, the cross-talk correction matrix is equal to the Maxwell capacitance matrix of the detector and the cabling such that:

$$\boldsymbol{C}_{tot} = \boldsymbol{C}_{detector} + \boldsymbol{C}_{cabling} \tag{6.29}$$

The Maxwell capacitance matrix of the detector $\boldsymbol{C}_{detector}$ is considered known as it is yielded from the detector simulation in the equations 6.2 and 6.8 for RED80 and REDN1 respectively. Section 4.2.7 explains that the cabling possesses a diagonal Maxwell capacitance matrix. Under the assumption that the properties of the cabling, like its length or its shielding, are the same for all the electrodes, all its diagonal components are equals. Their value is a single cabling capacitance $C_{cabling}$ which is unknown. Therefore, all the non-diagonal terms of the cross-talk correction C_{tot} matrix are known and its diagonal terms are to be defined through the estimation of the cabling capacitance $C_{cabling}$.

This estimation is based on the ionization signatures of the events expected from the fully collected bulk, guard or veto events induced by the 10.37 keV calibration electronic recoils. This

estimation process is therefore iterative as cross-talk correction and energy calibration are interdependent. For this analysis, the cross-talk correction is first approximated with a graphical method. The calculated effective charge signal $\vec{Q}_{eff}$ are then used in the calibration step and in the selection of the calibration events both described in section 6.2.7. The precise cross-talk correction is done with the 10.37 keV calibration events only.

The cross-talk correction matrix $\boldsymbol{C}_{tot}$ and more specifically the cabling capacitance $C_{cabling}$, are approximated with a graphical method. The principle is to have the effective charge perturbation vector $\vec{Q}_{eff}$ corresponding to the theoretical charge perturbation vectors Q for the different collection volume: bulk, guard, veto as expressed in equations 6.7 and 4.47. As the detector is not calibrated yet, the component of the theoretical charge vector are known up to a calibration factor a_X depending on the electrode X. Considering the bulk events of RED80 as reference, the equation that is solved graphically with $C_{cabling}$ as unknown is the following:

$$\begin{bmatrix} a_A & 0 & 0 & 0 \\ 0 & a_B & 0 & 0 \\ 0 & 0 & a_C & 0 \\ 0 & 0 & 0 & a_D \end{bmatrix} \cdot \vec{Q}_{bulk} = \begin{bmatrix} 0 \\ -a_B \\ 0 \\ a_D \end{bmatrix} = \left(\boldsymbol{C}_{detector} + C_{cabling} \cdot \mathbb{1}\right) \cdot \vec{V}_{meas.}(\text{Bulk events}) \tag{6.30}$$

As the calibration coefficient a_X are unknown, it is handy to consider a normalized cross-talk corrected signal vector $\vec{Y}$ expressed as:

$$\begin{aligned} \vec{Y}^{bulk} &= \frac{1}{C_{detector,11} + C_{cabling}} \left(\boldsymbol{C}_{detector} + C_{cabling} \cdot \mathbb{1}\right) \cdot \vec{V}_{meas.}(\text{Bulk events}) \\ &= C^N_{tot} \cdot \vec{V}_{meas.}(\text{Bulk events}) \end{aligned} \tag{6.31}$$

with $(C_{detector,11} + C_{cabling})$, the normalization factor and $\boldsymbol{C}^N_{tot}$ the normalized cross-talk correction matrix.

With a correctly estimated $C_{cabling}$ satisfying the equation 6.30, the cross-talk corrected signal vector $\vec{Y}^{bulk}$ of the bulk event has two null components $Y^{bulk}_A = Y^{bulk}_C = 0$ and two non-null components Y^{bulk}_B and Y^{bulk}_D. In order to visualize the four components of the cross-talk corrected vector $\vec{Y}$, corner plots are used . The figure 6.13 present such a corner plot for the detector RED80 for the stream tg09l000 in the Run 57. Only events passing the quality cuts are plotted. The dashed guide lines indicates the null signal at 0 ADU and the full collection of the 10.37 keV calibration electronic recoils at $\approx \pm 55$ ADU (drawn a fortiori after the calibration step). Each color corresponds to a different cabling capacitance value $C_{cabling}$ with the vector $\vec{Y}(125\,\text{pF})$ colored in orange, $\vec{Y}(0\,\text{pF})$ colored in green and $\vec{Y}(+\infty)$ colored in blue. We note that as $C_{cabling} \to +\infty$, $\boldsymbol{C}^N_{tot} \to \mathbb{1}$. The non-diagonal terms of the normalized cross-talk correction matrix $\boldsymbol{C}^N_{tot}$ are inversely proportional to the cabling capacitance $C_{cabling}$. As a result, we observe a diminishing return in the change of shape of the vector $\vec{Y}$ with increasing $C_{cabling}$.

The correct cabling capacitance $C_{cabling}$ satisfying the equation 6.30 is chosen when the distribution of the components of $\vec{Y}$ in the corner plots mostly correspond to the guide lines. In the case of RED80 and REDN1, the cabling capacitance was first estimated to $C_{cabling} = 120\,\text{pF}$. We can check that the normalized cross-talk correction matrix $\boldsymbol{C}^N_{tot}$ corresponds to the identity matrix at the first order. The correction terms are in the range of few percents, going up to 5.2% in the case of the case of the electrode B inducing signal on the electrode A.

The precise estimation of the cabling capacitance $C_{cabling}$ and the cross-talk correction matrix $\boldsymbol{C}_{tot}$ happens after the calibration step and the selection of the full collected bulk events created by the 10.37 keV calibration electronic recoils. A fiducial recoil leads to the induced charge

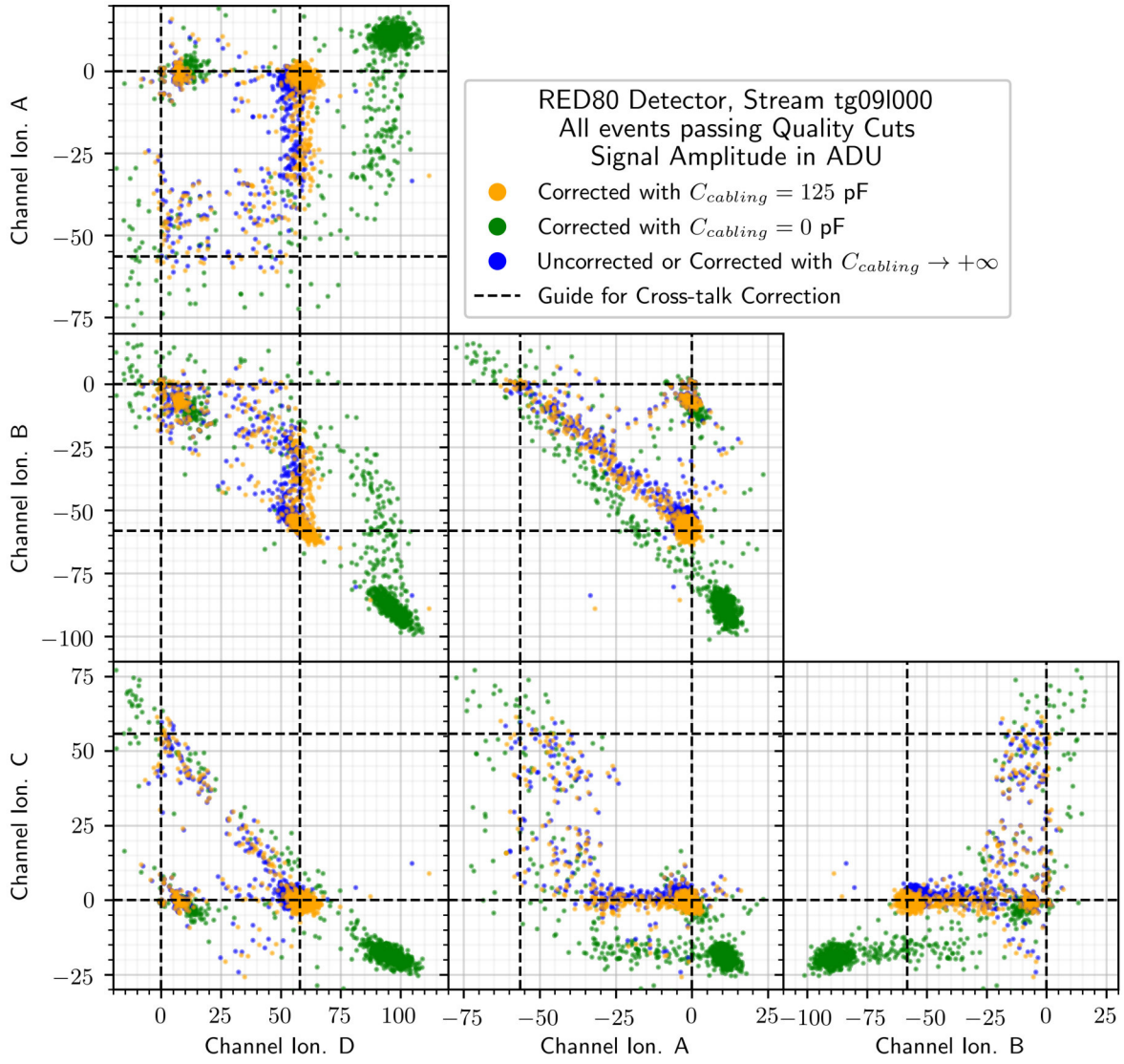

Figure 6.13: Corner plot of the cross-talk corrected amplitude vector $\vec{Y}$ in ADU. The plotted events corresponds to the stream tg09l000 of the run 57 operating the detector RED80. Only events passing the quality cuts are displayed. Each color corresponds to a different cabling capacitance $C_{cabling}$ used to calculate the cross-talk correction matrix $\boldsymbol{C}_{tot}$. The guide lines indicate no collection at 0 ADU and full collection at $\approx \pm 55$ ADU of the 10.37 keV calibration electronic recoils.

vector:

$$\vec{Q}_{fid}^{RED80} = \begin{bmatrix} 0 \\ -1 \\ 0 \\ 1 \end{bmatrix} \cdot Q(10.37\,\text{keV}) \tag{6.32}$$

with the electric charge multiplicative factor being:

$$Q(10.37\,\text{keV}) = N_p(10.37\,\text{keV}) \cdot e = \frac{E_R}{\epsilon} e = \frac{10.37 \times 10^3\,\text{eV}}{2.97\,\text{eV}} e \tag{6.33}$$

According to equation 4.55, the voltage signal induced on the electrodes is expressed by the vector $\vec{V}_{fid}^{RED80}$ obtained with the Maxwell capacitance matrix of the detector and cabling $\boldsymbol{C}_{total} = \boldsymbol{C}_{detector} + \boldsymbol{C}_{cabling}$ such that:

$$\vec{V}_{fid}^{REDN1} = \begin{bmatrix} V_A \\ V_B \\ V_C \\ V_D \end{bmatrix} = \boldsymbol{C}_{total} \cdot \vec{Q}_{fid}^{REDN1} \tag{6.34}$$

In section 4.2.7, the Maxwell capacitance matrix associated with the cabling $C_{cabling}$ is considered to be diagonal with $\forall i \neq j, \boldsymbol{C}_{cabling,ij} = 0$. The previous equation 6.34 can be translated for the terms V_i and Q_i of the vectors $\vec{V}_{fid}^{RED80} = \vec{V}$ and $\vec{Q}_{fid}^{RED80} = \vec{Q}$ respectively:

$$\begin{aligned} V_i &= \sum_{j=1}^{4} C_{total,ij} Q_j \\ &= \sum_{j=1}^{4} C_{detector,ij} Q_j + \sum_{j=1}^{4} C_{cabling,ij} Q_j \\ &= \left(C_{detector,i4} - C_{detector,i2}\right) Q(10.37\,\text{keV}) + C_{cabling,ii} Q_i \end{aligned} \tag{6.35}$$

We assume that the Maxwell capacitance matrix relative to the detector $\boldsymbol{C}_{detector}$ is known as it calculated from the electrostatics simulation of RED80. The diagonal terms $\boldsymbol{C}_{cabling,ii}$ of the cabling capacitance matrix can therefore be evaluated from the voltage signal induced by the 10.37 keV fiducial events $\boldsymbol{V}_i$:

$$C_{cabling,ii} = \frac{1}{Q_i} \left[\boldsymbol{V}_i - \left(C_{detector,i4} - C_{detector,i2}\right) Q(10.37\,\text{keV})\right] \tag{6.36}$$

One should note that as $Q_1 = Q_3 = 0$, the equation 6.36 is only valid for $i \in \{2, 4\}$. This means that the fiducial events collected by the electrodes B and D can only be used to determine the cabling capacitance associated with these electrodes $C_{cabling,22}$ and $C_{cabling,44}$ respectively. A precise estimation of the cabling capacitances affecting the electrodes A and C would necessitate to adjust the veto or guard events which lack statistics.

The figures 6.14 and 6.15 display the histograms derived from the values $C_{cabling,22}$ and $C_{cabling,44}$ computed with the equation 6.36 for each of the 10.37 keV calibration events passing the Bulk cut for the detectors RED80 and REDN1 respectively. The estimation of the cabling capacitances and their associated error bars are extracted from the quantiles 0.16, 0.50 and 0.84 of the distributions:

$$C_{cabling,22}^{RED80} = 129^{+9}_{-8}\ \text{pF} \qquad C_{cabling,44}^{RED80} = 125^{+9}_{-8}\ \text{pF} \tag{6.37}$$

$$C_{cabling,22}^{REDN1} = 124^{+11}_{-7}\ \text{pF} \qquad C_{cabling,44}^{REDN1} = 125^{+10}_{-7}\ \text{pF} \tag{6.38}$$

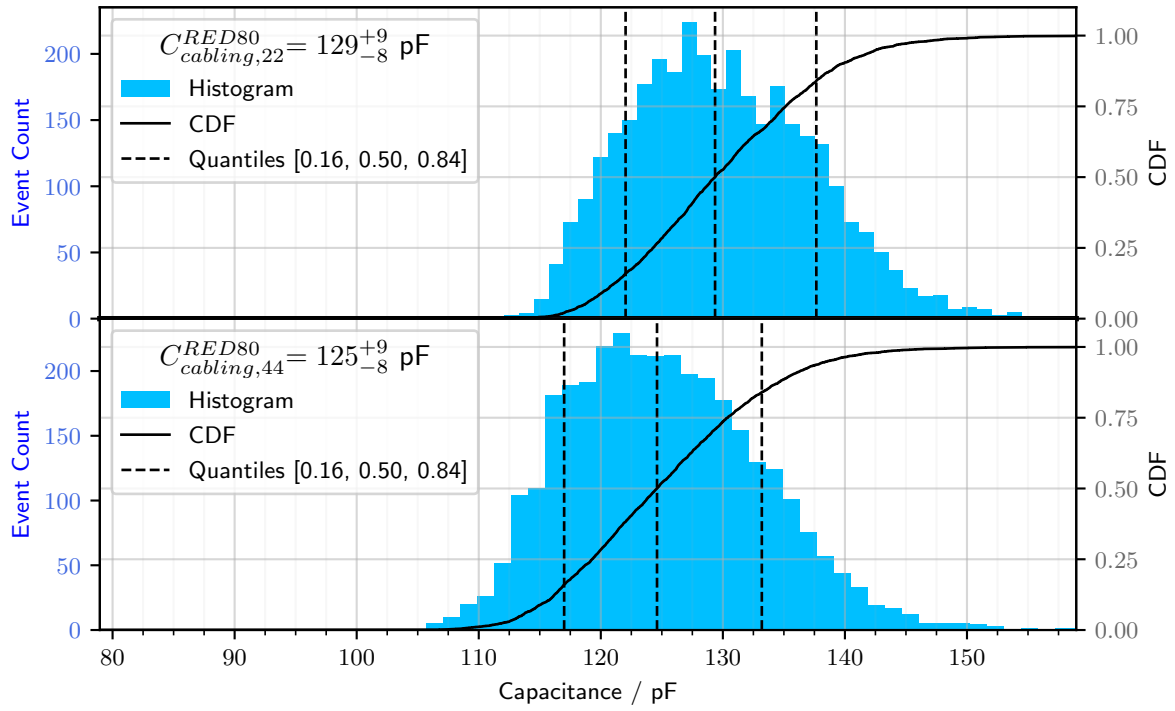

Figure 6.14: Histogram and CDF derived from the experimental estimation of the cabling capacitance $C_{cabling,22}$ and $C_{cabling,44}$ for each Bulk events in the RED80 detector.

All the values are very similar and compatible within their 1σ-error bars. The small differences in cabling capacitance could be explained by small variation in length of the cabling between the conductive tracks on the copper chassis in the suspended tower and the electronics on the fixed mixing chamber of the cryostat.

In the end, we consider the collect electrodes B and D of both detectors RED80 and REDN1 to be affected by a common cabling capacitance $C_{cabling} = 125\,\text{pF}$. We extrapolate this estimation to the auxiliary electrodes A and C. The decorrelated amplitudes A_X are processed into the cross-talk corrected amplitude $A_X^{corr.}$ according to the equation 6.30 using the determined $C_{cabling} = 125\,\text{pF}$.

In future studies and with enough statistics, we can imagine a more complex and precise cross-talk correction by considering one cabling capacitance term specific to each electrode.

6.2.7 Calibration and Selection of the 10.37 keV Calibration Events

The five measurements channels are saving the voltage of their associated sensors in ADU unit specific to each considered channel. In order to proceed with the estimation of the heat E_{heat}, ionization $E_{Ion.}$ and recoil E_R energies, it is now necessary to determine the conversion rates between ADU units and eV for each channel CH. This calibration coefficient α_{CH} are determined experimentally thanks to the intrinsic germanium 10.37 keV calibration line inducing electronic recoils of known heat energy $E_{heat} = 10.37\,\text{keV}_{\text{ee}}$ and ionization energy $E_{Ion.} = 10.37\,\text{keV}$. This subsection first describes the calibration of the ionization channel. Then, it discusses the selection of the 10.37 keV calibration events for the calibration of the heat channel.

The most straightforward calibration method is to determine the position of this calibration peak on the amplitude spectra of the electrodes A, B, C, D. Indeed, according to the charge signatures (eq. 6.7) of the events in the detector RED80, the charge are induced on the two collecting electrodes with equal amplitude. However, due to the oblique propagation of the electrons, a

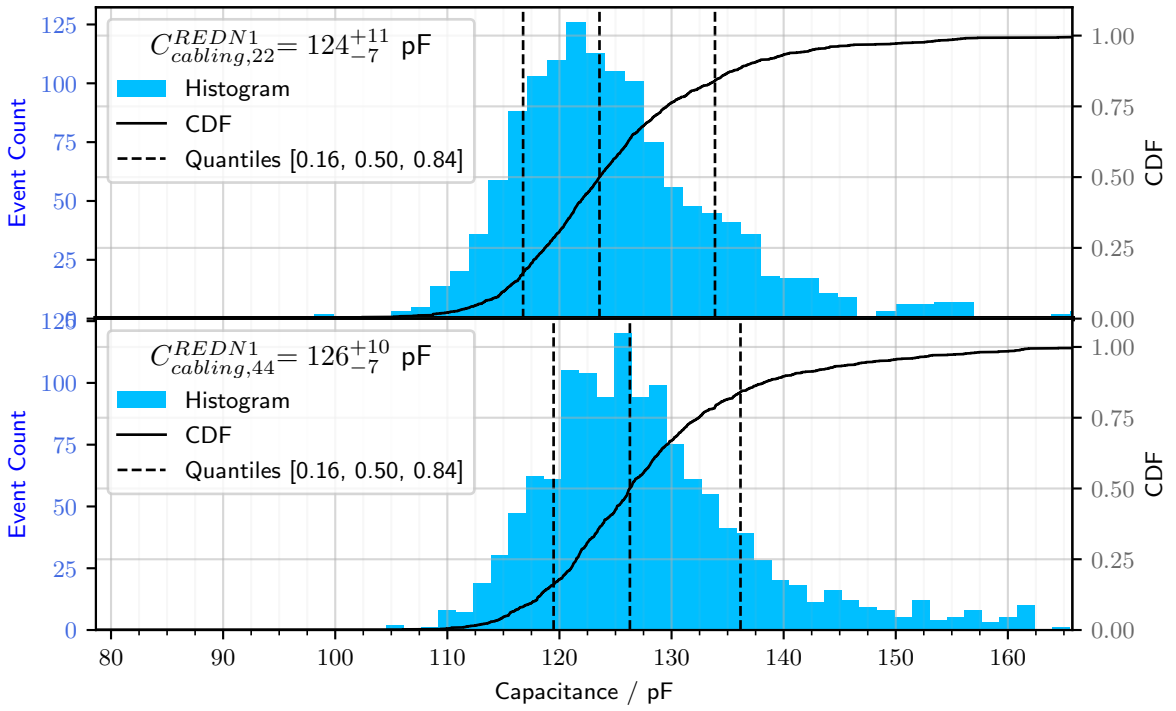

Figure 6.15: Histogram and CDF derived from the experimental estimation of the cabling capacitance $C_{cabling,22}$ and $C_{cabling,44}$ for each Bulk events in the REDN1 detector.

significant fraction of the 10.37 keV events does not possess these archetypal ionization signature but rather a linear combination. Although this phenomenon affects only slightly the calibration of the collect electrodes B and D due to the high fraction of bulk events with complete charge collection, the low amount of well reconstructed guard events render the precise calibration of the guard electrodes A and C impossible.

The alternative calibration method, used in this work, permits the precise calibration of all the electrodes by benefiting from the non-ideal ionization signatures being linear combination of the bulk, guard and guard-collect events. The figure 6.16 illustrates this ionization calibration method for the RED80 data streams relative to the neutron background measurement. The graphics shows the cross-talk corrected amplitudes $A^{corr.}_X$ of all the quality events as red points. The left graphic shows that all events produce negative amplitudes on the electrodes A and B which is consistent with the fact that at the default polarization 6.6, A and B collect electrons. Similarly, the electrodes C and D collect holes inducing signals with positive amplitude.

The blue points are quality events which are selected with the following conditions:

$$\begin{cases} A_{heat} > 500\,\text{ADU} \\ 100\,\text{ADU} > |A^{corr.}_{tot}| > 150\,\text{ADU} \\ \text{with } A^{corr.}_{tot} = \frac{1}{2}\left(-A^{corr.}_A - A^{corr.}_B + A^{corr.}_C + A^{corr.}_D\right) \end{cases} \tag{6.39}$$

with $A^{corr.}_{tot}$ the total ionization amplitude. This selection crudely corresponds to the 10.37 keV calibration events with a complete charge collection $E_{Ion.} \approx 10.37\,\text{keV}$. As the electrons (resp. holes) are collected by both the A and B (resp. C and D) electrodes, the ionization energy $E_{Ion.}$ is split between the two electrodes. The calibration of the electrodes of REDN1 is done using the same method with the difference that the electrons are collected by the electrodes B, C and the holes by A, D with the default polarization 6.10 of the detector REDN1.

The black lines are linear laws adjusted to the blue population using orthogonal distance

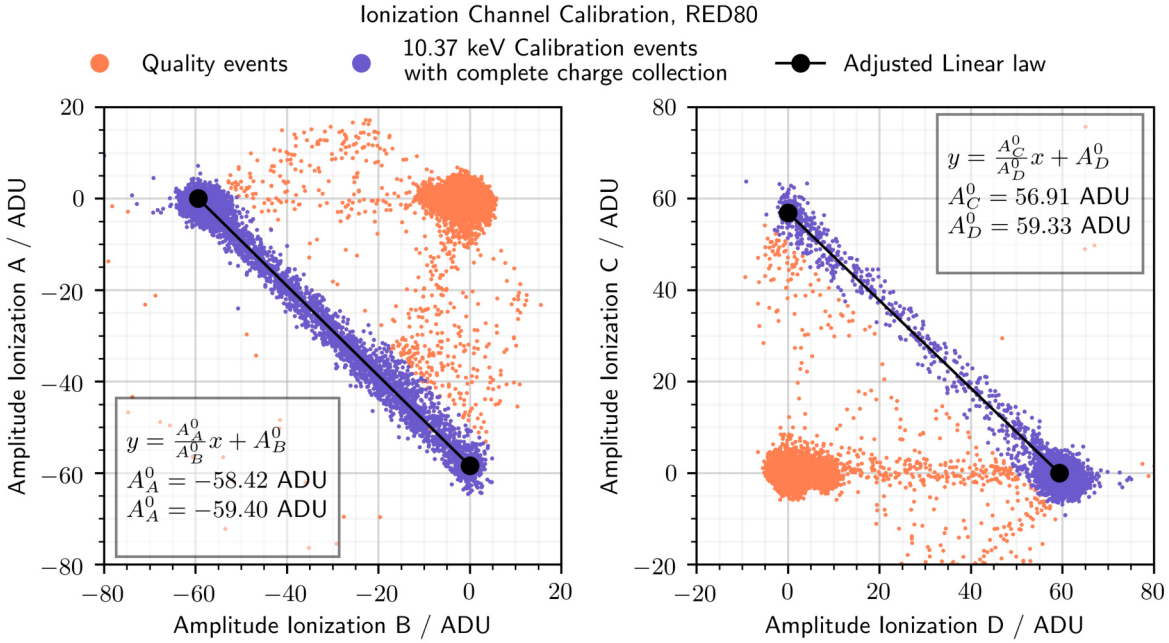

Figure 6.16: Calibration of the electrodes A, B, C, D of the detector RED80 on the data stream tg18l005. The left graphic displays the cross-talk corrected amplitudes $A_A^{corr.}$ versus $A_B^{corr.}$. Similarly, the right graphic plots $A_C^{corr.}$ versus $A_D^{corr.}$. All the quality events are represented in red. The blue events correspond to 10.37 keV calibration quality events with complete charge collection. Their amplitudes is adjusted with a linear law yielding the amplitudes A_X^0 of the fully collected 10.37 keV peak.

regression. The parameters of the linear laws, A_X^0, are the positions of the calibration peaks when fully collected by either one of the electrodes.

The calibration coefficient α_X are defined for each electrodes X as:

$$\alpha_X = \frac{10.37\,\text{keV}}{|A_X^0|} \tag{6.40}$$

The calibrated amplitudes in keV are called the electrode specific ionization energies E_X and defined as:

$$\forall X \in \{A, B, C, D\}, \quad E_X = \alpha_X \cdot A_X^{corr.} \tag{6.41}$$

The ionization energy E_X is proportional to the charge Q_X induced on the electrode X and estimates the fraction of the ionization energy $E_{Ion.}$ measured by this electrode. One should note that within this convention negative ionization energies are possible. The estimation of the ionization energy $E_{Ion.}$ created by the recoil is the quantity $E_{Ion.}^{tot}$ called the total ionization energy. In its default polarization, the total ionization energy for the detector RED80 is expressed as:

$$E_{Ion.}^{tot} = \frac{-E_A - E_B + E_C + E_D}{2} \tag{6.42}$$

In the case of REDN1 with default polarization, the total ionization energy becomes:

$$E_{Ion.}^{tot} = \frac{E_A - E_B - E_C + E_D}{2} \tag{6.43}$$

The calibration of the heat channel is also based on the 10.37 keV calibration events. This

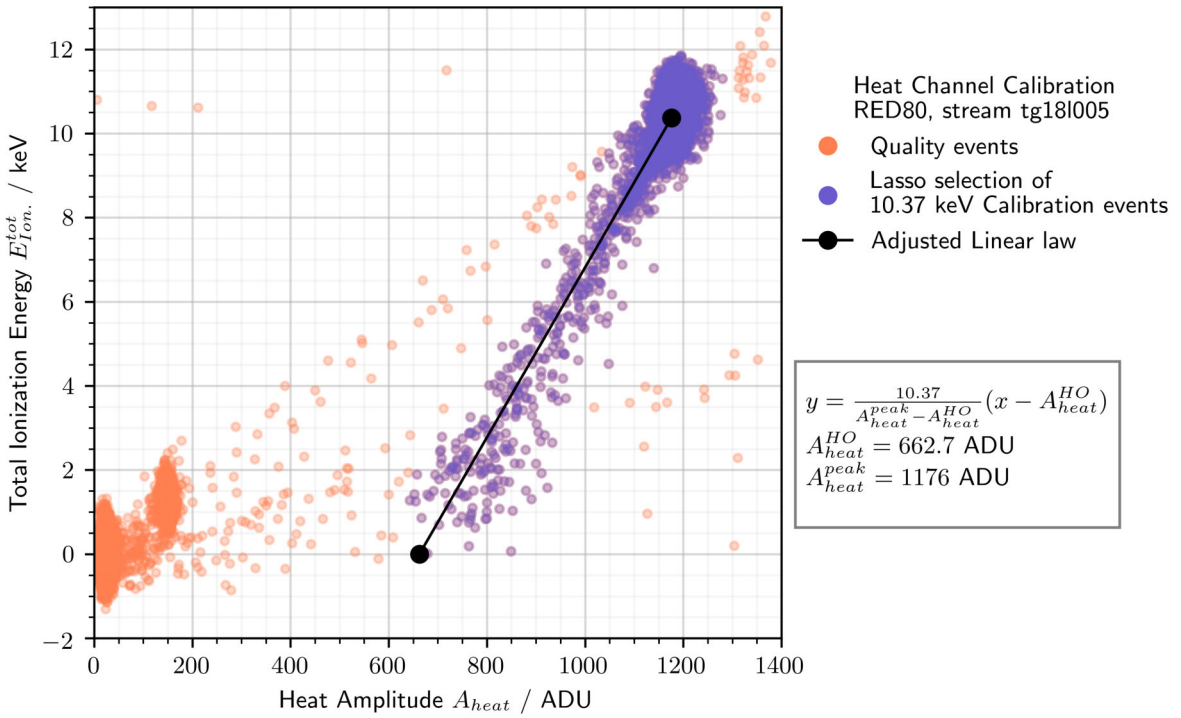

Figure 6.17: Reconstructed Ionization Energy as a function of the Reconstructed Heat Energy, for the quality events of the Calibration configuration. The plot is zoomed up to 12 keV for an easier view of the calibration peaks.

calibration process is illustrated for the detector RED80 on the stream tg18l005. The figure 6.17 presents the total ionization energy $E^{tot}_{Ion.}$ of all the quality events versus their heat amplitude A_{heat}.

Thanks to high rate of calibration events, we easily recognize the band of the 10.37 keV calibration events. This band follows a linear law stretched between two remarkable points. The first corresponds to the 10.37 keV calibration peak, formed by events with a complete charge collection yielding a complete Luke-Neganov boost, located at $A_{heat} \approx 1200$ ADU and $E^{tot}_{Ion.} = 10.37$ keV. The second point is situated at $A_{heat} \approx 700$ ADU and $E^{tot}_{Ion.} = 0$ keV. It corresponds to 10.37 keV calibration events with no charge collection: the electron-hole pairs recombine immediately after the recoil and there is no Luke-Neganov boost on the heat channel. All the calibration events between these points have an incomplete charge collection with only partial Luke-Neganov boost.

The blue events on the figure correspond to the manual selection of the calibration events. This selection is made manually with a graphical lasso selection. All the events of these selection are designated in the analysis as "calibration events" and they are used to determine precisely the heat amplitudes of the two extreme points of the calibration bands. The amplitude of the completely collected calibration peak is A^{peak}_{heat}. The heat amplitude of the calibration events with no charge collection is A^{HO}_{heat}. The exponent HO refers to "Heat-Only", as these events do not induce any ionization signal. The selection of calibration events is adjusted with the linear law:

$$E^{tot}_{Ion.} = \frac{10.37}{A^{peak}_{heat} - A^{HO}_{heat}}(A_{heat} - A^{HO}_{heat}) \tag{6.44}$$

using an orthogonal distance regression algorithm. The calibration coefficient α_{heat} associated with the heat channel is calculated as:

$$\alpha_{heat} = \frac{10.37\,\text{keV}_{\text{ee}}}{A_{heat}^{peak}} \tag{6.45}$$

The calibrated heat amplitude called the heat energy of an event is defined as:

$$E_{heat} = \alpha_{heat} \cdot A_{heat} \tag{6.46}$$

This heat energy is expressed in the unit keV_{ee} where the index *ee* refers to "electronic equivalent". This unit expresses the heat energy E_{heat} generated by an electronic recoil of quenching factor $Q_{ER} = 1$ and recoil energy E_R according to the equation 4.24:

$$E_{heat} = E_R \cdot \left(1 + \frac{V_{bias}}{2.97}\right) \tag{6.47}$$

As such, the heat calibration assumes that every event is induced by an electronic recoil, which is false in the case of neutron recoils with a lower quenching Q_{NR}. This means that apart from the electronic recoils, this experimental heat energy E_{heat} has no physical meaning. However, it is used to access the recoil energy E_R of an event expressed in keV. This recoil energy E_R takes into account the experimental quenching factor of an event Q and the Luke-Neganov Boost E_{NL} associated .

Combining the equations 4.2 and 4.23, the Luke-Neganov energy of an event is derived from the ionization energy as:

$$E_{NL} = E_{Ion.}^{tot} \frac{V_{bias}}{2.97} \tag{6.48}$$

The recoil energy E_R of an event is calculated as:

$$E_R = E_C \cdot \left(1 + \frac{V_{bias}}{2.97}\right) - E_{NL} = E_C \cdot \left(1 + \frac{V_{bias}}{2.97}\right) - E_{Ion.}^{tot} \frac{V_{bias}}{2.97} \tag{6.49}$$

and the associated quenching factor is derived using the usual formula 4.2 with experimental estimation:

$$Q = \frac{E_{Ion.}^{tot}}{E_R} \tag{6.50}$$

6.2.8 Charge Conservation Cut

The charge conservation cut aims at discarding events which does not respect the charge conservation. Indeed, some events might demonstrate charge collection issue. Drifting charges can be trapped in the germanium and may not end up being collected. In section6.2.7, the ionization energies E_X are obtained from amplitudes $A_X^{corr.}$ of the decorrelated voltage signal $V_X^{decor.}$. For the definition the charge conservation cut only, the term E_X refers to the ionization energies calculated from the raw voltage signal V_X without decorellation. As such, E_X is proportional to the charges collected on the electrode X of the detector. We define the energy of charge conservation E_{CC} as:

$$E_{CC} = \frac{1}{2}\left(E_A + E_B + E_C + E_D\right) \tag{6.51}$$

By construction, this quantity is proportional to the excess or lack of total induced charges on the electrodes of the detector. Contrary to the total ionization energy $E_{Ion.}^{tot}$, this quantity is common to RED80 and REDN1 as it is independent from the polarization of the electrodes.

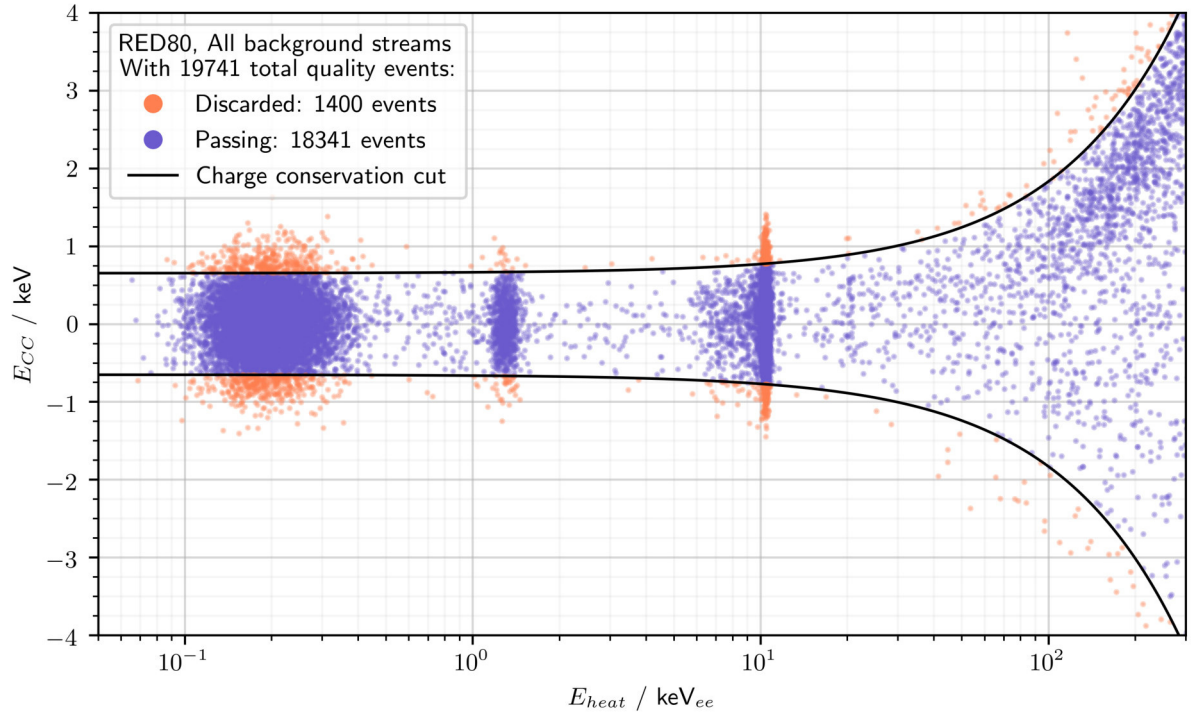

Figure 6.18: Energy of charge conservation E_{CC} as a function of the heat energy E_{heat} for the quality events of the detector RED80 for Background data streams. Passing events are in blue while discarded events are in red.

As a recoil produces electron-hole pairs, the total electric charge carried by the drifting particles in the crystal should be zero as well as the total collected charges. This is characterized by a normal distribution of the E_{CC} around zero with a standard deviation $\sigma(E_{CC})$ depending on the recoil energy. In order to apply the charge conservation cut, the resolution $\sigma(E_{CC})$ is modeled as a linear function of the heat energy E_{heat} expressed in keV$_{ee}$ such that:

$$\sigma(E_{CC})(E_{heat}) = \sigma(E_{CC})(0\,\text{keV}_{ee}) + [\sigma(E_{CC})(10.37\,\text{keV}_{ee}) - \sigma(E_{CC})(0\,\text{keV}_{ee})] \cdot \frac{E_{heat}}{10.37\,\text{keV}_{ee}} \quad (6.52)$$

with $\sigma(E_{CC})(0\,\text{keV}_{ee})$ evaluated from the noise blob and $\sigma(E_{CC})(10.37\,\text{keV}_{ee})$ evaluated on a $0.5\,\text{keV}_{ee}$ bin centered on $10.37\,\text{keV}_{ee}$. Events not respecting the charge conservation would stand out of the gaussian profile and be discarded. An event passes the charge conservation cut if E_{CC} is within a 2σ-margin of the null charge:

$$|E_{CC}| < 2 \cdot \sigma(E_{CC})(E_{heat}) \quad (6.53)$$

The charge conservation cut is illustrated in the figure 6.18 with the Background data streams of the detector RED80 for the measurement of the IP2I neutron background. The graphic plots the quantity E_{CC} versus the heat energy E_{heat} of all the quality events. The 2σ margin is delimited by the black curves. The event passing the charge conservation cut are colored blue while the rejected events are red.

We do not discern any particular population of event which does not conserve the electric charge. The charge conservation cut can therefore be considered as a safety cut eventually pruning rare outlying events.

6.2.9 Fiducial Cut

The fiducial cut, also known as bulk cut, aims at selecting the events generated by recoils located in the fiducial volume of the detector. In other words, the fiducial cut discards any event originating from the other collection volume of the detectors RED80 and REDN1. These other collection volumes, in contact with the crystal surface, generate problematic events which may hurt the measurement of nuclear recoils. One major problem comes from the surface trapping phenomenon, inducing an incomplete charge collection. This eventually leads to some electronic recoils being reconstructed with an artificially low quenching and counted as nuclear recoils. Another issue arises from recoils induced by the natural radioactive background. These recoils, mainly electronic from β radiation, are located in the first µm of the crystal surface. By discarding the surface events, we effectively lower the electronic background affecting the measurements.

The signature of the bulk recoil is known for RED80 in equation 6.7 and REDN1 in equation 4.47. For both detectors, these bulk recoils generate a signal on the main collecting electrodes B and D only. As such, the fiducial cut identifies events of the bulk region as events which did not deposited any signal on the auxiliary electrodes A or C. The tolerance on the signals of A and C is a multiple of their resolution $\sigma(E_A)$ and $\sigma(E_C)$. These resolutions scales with the energy of the recoil and are thus modeled with a linear law adjusted to the baseline resolutions and the resolution on the the resolution $\sigma(E_{CC})$ is modeled as a linear function of the heat energy E_{heat}:

$$\forall X \in \{A, C\}, \quad \sigma(E_X)(E_{heat}) = \sigma(E_X)(0\,\mathrm{keV_{ee}}) + [\sigma(E_X)(10.37\,\mathrm{keV_{ee}}) - \sigma(E_X)(0\,\mathrm{keV_{ee}})] \cdot \frac{E_{heat}}{10.37\,\mathrm{keV_{ee}}} \tag{6.54}$$

Events passing the fiducial cut are designated as fiducial events or bulk events. In this chapter for the electrostatic study of the detector RED80 and REDN1, the bulk events satisfy the system:

$$\begin{cases} |E_A| < 5 \cdot \sigma(E_A)(E_{heat}) \\ |E_C| < 5 \cdot \sigma(E_C)(E_{heat}) \end{cases} \tag{6.55}$$

with a 5σ tolerance.

The fiducial cut is illustrated in figure 6.19 for the data streams of RED80 used in the neutron background measurement. The two subplots presents the ionization energies of the guard electrodes E_A and E_C of all quality events satisfying charge conservation versus the heat energy of the event. As explained in the next chapter, the tolerances of the analysis cut are globally lower. For the fiducial cut, a 2σ margin is chosen and delimited with the black curves. We can notice, especially near the 1.3 keV and 10.37 keV calibration peaks, that a significant fraction of the events, colored red, are discarded. These events correspond to the recoils located in the guard, guard-collect and corners volumes of the detector RED80.

6.3 Experimental Estimation of the Fiducial Volume and Comparison to the Detector Simulation

6.3.1 Control values definition

The electrostatic simulation of the detectors allowed for a theoretical estimation of the fiducial volume percentage according to equation 4.48. This equation compares the fiducial volume drawn by the electric field lines to the total crystal volume. The main assumption made for this calculation is the ideal drift stating that electrons and holes propagates in the germanium following the electric lines. As discussed in section 4.1.4, this assumption differs from the reality. The

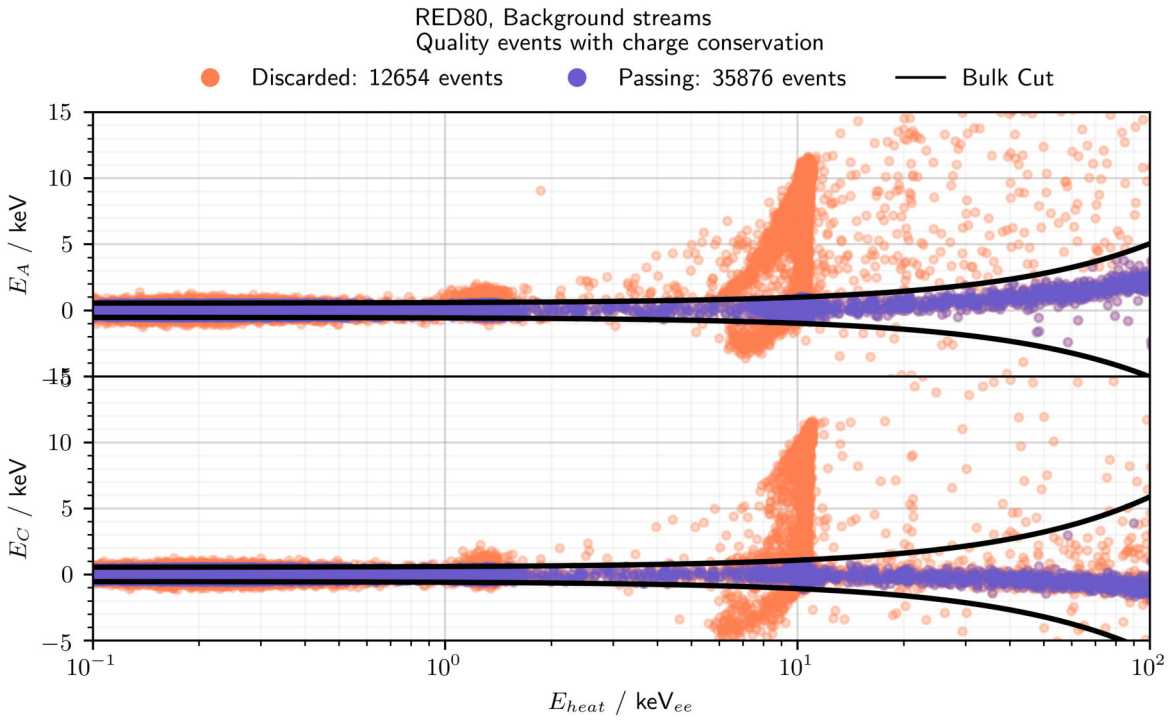

Figure 6.19: Ionization energies E_A and E_C as a function of the heat energy E_{heat} of all the quality events passing the charge conservation cut from the Background data streams of detector RED80. The black curves delimit the 2σ margin centered on 0 keV used to enforce the bulk cut.

main cause is the oblique propagation of the electrons being a consequence of the band structure of the germanium. Another minor cause is the repulsing force between close drifting carriers of the same charge which might also participate in the spread for the trajectories. This paragraph aims at comparing the expected fiducial volume from the RED80 and REDN1 simulations to the experimental results.

The detectors RED80 and REDN1 were operated in the run 57 with multiple different polarizations listed in the table 6.4. Each polarization has an associated data stream eventually yielding one experimental estimation of the fiducial volume percentage $\%_{fid}$ with analysis. This estimation is based on the 10.37 keV electronic recoils of the calibration peak. Indeed, as these events are induced by the neutron activated germanium atoms of the crystal, they have a uniform distribution in the crystal. As such, the count of these calibration events is proportional to the volume of the Ge crystal. In order to assure a good energy reconstruction, only events passing the quality cuts with charge conservation are considered. The figure 6.20 displays the total ionization energy $E^{tot}_{Ion.}$ versus the heat energy E_{heat} of all these events in the case of the stream tg09l000 for the detector RED80. The 10.37 keV calibration events are tagged according to their heat-ionization signature as explained in section 6.2.7.

We define the quantity n_{tot} as the total number of such quality 10.37 keV calibration events in a single data stream. We assume that the number n_{tot} is given by a Poisson distribution Pois(λ) of parameter $\lambda = n_{tot}$ and standard deviation $\sigma(n_{tot}) = \sqrt{n_{tot}}$. This quantity is proportional to the total volume of the Ge crystal.

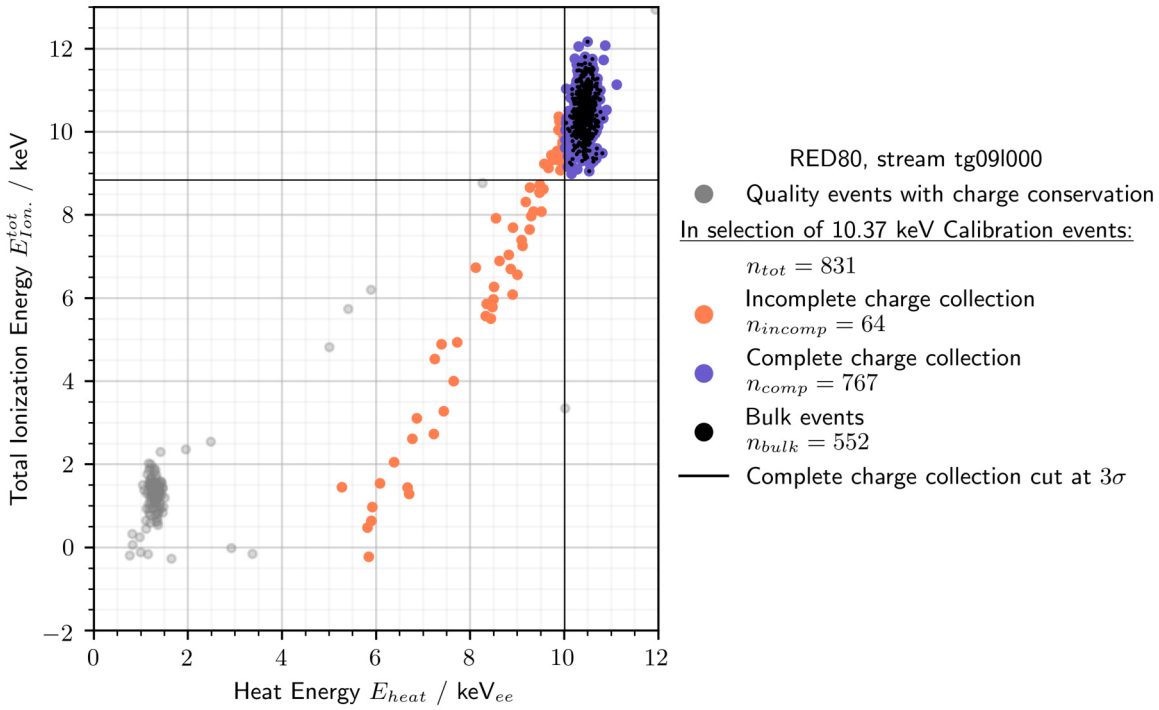

Figure 6.20: Total ionization energy $E^{tot}_{Ion.}$ versus the heat energy E_{heat} of all the quality cuts passing the charge conservation cut of the stream tg09l000 for the detector RED80. All non-grey events are part of the 10.37 keV calibration event selection counting n_{tot} events. The red events, numbered n_{incomp} have an incomplete charge collection with a partial Luke-Neganov boost. The blue events show a complete charge collection, forming the 10.37 keV calibration peak counting n_{comp} events. Among these blue events, there are n_{bulk} bulk events represented in black.

All this n_{tot} events have varying ionization and heat energies linked to the quality of their charge collection. We define the condition of complete charge collection as:

$$\begin{cases} E_{heat} > 10.37\,\text{keV}_{\text{ee}} - 3 \cdot \sigma(E_{heat})(10.37\,\text{keV}_{\text{ee}}) \\ E^{tot}_{Ion.} > 10.37\,\text{keV}_{\text{ee}} - 3 \cdot \sigma(E^{tot}_{Ion.})(10.37\,\text{keV}_{\text{ee}}) \end{cases} \tag{6.56}$$

This condition is delimited with the black lines on the figure. Events with incomplete charge collection are colored red while the events with complete charge collection are blue.

The number $n_{incomplete}$ is the count of quality 10.37 eV calibration events with incomplete collection. As a subset of the quality 10.37 eV calibration events, the number $n_{incomplete}$ is considered to result from a binomial distribution $B(n,p)$ with the parameters $(n,p) = (n_{tot}, \frac{n_{incomplete}}{n_{tot}})$. The number of quality calibration events with complete collection is simply $n_{complete} = n_{tot} - n_{incomplete}$.

The number of quality 10.37 keV calibration events passing the bulk cut is n_{bulk}. This bulk cut is described in section 6.2.9. By definition, the bulk events have a complete collection. As such these events form a subset of the quality calibration, n_{bulk} being associated with a binomial distribution of parameters $(n,p) = (n_{tot}, \frac{n_{bulk}}{n_{tot}})$.

By definition, the incomplete, complete and bulk counts are random variables with a binomial distribution whose parameters (n,p) are functions of the random variable n_{tot}. This induces an overly complex error propagation. For the sake of simplicity, the standard deviation σ associated with the incomplete, complete and bulk events is the same as for the Poisson distribution: $\forall event \in \{incomplete, complete, bulk\}, \sigma(event) = \sqrt{n_{event}}$.

The incomplete percentage quantifies the charge collection of the detector and is expressed:

$$\%_{incomplete} = \frac{n_{incomplete}}{n_{tot}} \cdot 100 \tag{6.57}$$

The fiducial percentage estimates the fiducial volume of the detector and is expressed:

$$\%_{fid} = \frac{n_{bulk}}{n_{complete}} \cdot 100 \tag{6.58}$$

In this percentage, n_{bulk} is considered to be proportional to the fiducial volume such that $n_{bulk} = \alpha \cdot V(\text{Fiducial})$. Similarly, it is considered that the count of events with complete collection is proportional to the full Ge crystal volume with the same multiplicative factor such that $n_{complete} = \alpha \cdot V(\text{Crystal})$.

We define the efficiency percentage as:

$$\%_{eff} = \frac{n_{bulk}}{n_{tot}} \cdot 100 \tag{6.59}$$

This percentage quantifies efficiency of the detector in terms of exposure by combining the effects of both the charge collection and the fiducial volume.

By neglecting the covariance, the error propagation yields an overestimated standard deviation:

$$\begin{aligned} &\forall event \in \{incomplete, eff\}, \\ &\sigma(\%_{event}) = 100 \cdot \sqrt{\left(\frac{1}{n_{tot}}\right)^2 \sigma(n_{event})^2 + \left(\frac{-n_{event}}{n^2_{tot}}\right)^2 \sigma(n_{tot})^2} \\ &= 100 \cdot \frac{1}{n_{tot}} \sqrt{n_{event}\left(1 + \frac{n_{event}}{n_{tot}}\right)} \end{aligned} \tag{6.60}$$

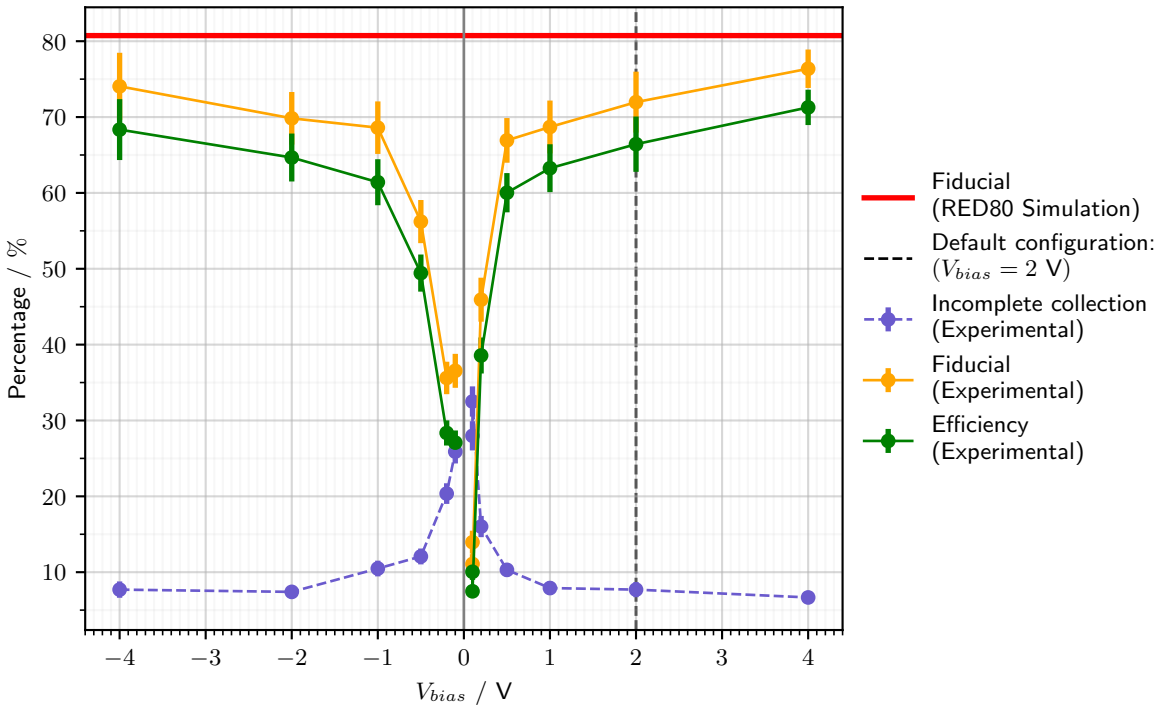

Figure 6.21: Experimental percentages of incomplete collection $\%_{incomplete}$ (in blue), of fiducial events $\%_{fid}$ (in orange) and of the efficiency $\%_{eff}$ (in green) as functions of the voltage bias V_{bias} for the detector RED80. The theoretical fiducial volume percentage $\%_{fid} = 80.75\,\%$ estimated with the RED80 simulation is indicated by the horizontal red line.

In the case of the fiducial percentage, we have:

$$\sigma(\%_{fid}) = 100 \cdot \frac{1}{n_{complete}} \sqrt{n_{bulk}\left(1 + \frac{n_{bulk}}{n_{complete}}\right)} \tag{6.61}$$

6.3.2 Experimental Results of the RED80 Detector

The figure 6.21 presents the incomplete percentage $\%_{incomplete}$, the fiducial percentage $\%_{fid}$ and the efficiency percentage $\%_{eff}$ as functions of the voltage bias V_{bias} of the detector RED80. The uncertainties are represented with 1σ-error bars using the expressions of the standard deviations calculated in the previous paragraph. The fiducial volume percentage $\%_{fid}^{simu.} = 80.75\,\%$ extracted from the RED80 electrostatic simulation is plotted as the red horizontal line. The default polarization of the RED80 detector corresponds to the vertical line at $V_{bias} = 2\,\text{V}$.

The fiducial and efficiency percentages drop at very low voltage bias while they cap at high values. The opposite observation is made for the incomplete percentage which diverges as V_{bias} tends to zero. Moreover, the percentages are almost symmetric between negative and positive V_{bias} values. Due to the shape of the curves, this kind of plot is referred to as "seagull plot". This graphic illustrates the loss of efficiency of the germanium detectors at low voltage bias. Indeed, at $V_{bias} = 0\,\text{V}$, there is no electric field inside of the germanium crystal and electron-hole pairs recombine at the location of the recoil.

The experimental fiducial volume seems to tend to the theoretical fiducial volume for the highest absolute value of V_{bias}. However, the experimental fiducial volume $\%_{fid}$ is at least lower by 10 % from the theoretical volume $\%_{fid}^{simu.}$. This difference can be explained by the oblique

propagation of the electrons which might drift out of the fiducial volume where they were created. This hypothesis is supported by the dependence with the voltage bias V_{bias}. Indeed, with increasing electric field magnitude, the electrons are expected to scatter with higher probability into other inter-valleys, thus following more closely the electric field lines. Another explanation would be recoils located in the vicinity of the frontier between the collection volumes in the RED80 crystal. For such a "frontier event" located at the frontier between the fiducial volume and the guard volume, the carriers are split into these volumes and induce signal on collect and guard electrodes. This phenomenon would be responsible for a constant difference between simulation and experimental fiducial percentages. Consequently, this effect can be measured on the asymptotic fiducial percentage for $V_{bias} > 4\,\mathrm{V}$. In the case of RED80, this effect of the frontier events is responsible for a percentage loss of less than 5 %. Experimentation with voltage bias are necessary to investigate further this phenomenon.

The incomplete charge collection has a low cap attained for $|V_{bias}| \geq 2\,\mathrm{V}$ at a percentage of about 8 %. For lower absolute value of the voltage bias, the incomplete percentage diverges. We estimate that the detector RED80 show good charge collection for an absolute voltage bias greater than 0.5 V, just before the divergence, at a percentage of incomplete charge events of about 13 %.

By definition, the efficiency percentage $\%_{eff}$ combines the trends of the fiducial percentage and the incomplete charge collection percentage. The efficiency drops for $|V_{bias}| < 0.5\,\mathrm{V}$ due to the charge collection. Above this threshold, the efficiency follows the fiducial volume trend by increasing almost linearly with the voltage bias. The detector is considered to have a good efficiency from 1 V with an efficiency percentage comprised between 62 % and 72 %.

6.3.3 Experimental Results of the REDN1 Detector

The figure 6.22 displays the percentage of incomplete events $\%_{incomplete}$, fiducial events $\%_{fid}$ and the efficiency $\%_{eff}$ of the REDN1 detector as a function of its voltage bias V_{bias}, on the left graphic, and its polarization ratio R_{veto} on the right graphic. The fiducial percentage expected from the electrostatic simulation of REDN1 is represented as the red curves. The simulated estimation of the fiducial volume is independent from V_{bias} with a constant value of $\%_{fid}^{simu.} = 50.75\,\%$. However, it does show a somewhat linear decreasing trend with R_{veto}. The default polarization of REDN1 is indicated by vertical lines at $V_{bias} = 2\,\mathrm{V}$ and $R_{veto} = 0.4$.

The left subplot with varying voltage bias V_{bias} is the seagull plot. Contrary to the RED80 study, the negative voltage bias range is map with a single value at $-2\,\mathrm{V}$ which corresponds within the error bars to the percentages of the opposite polarization 2 V. Similarly to the seagull plot of RED80, the fiducial and efficiency percentages drops at very low V_{bias} while the incomplete charge collection diverges. The causes are the same as for RE80: mainly being the transversal trajectories of the electrons which can leave the fiducial volume of REDN1 and perhaps, with minor effect, the frontier events and trapping. For $V_{bias} = 4\,\mathrm{V}$, the experimental fiducial volume is greater than predicted by the simulation, although still in the error bars. The values at $V_{bias} = 8\,\mathrm{V}$ are within a 2σ margin of the values at 4 V and could be produced by a statistical fluctuation. However, the trend of increasing incomplete charge collection is present from 1 V from a minimum at 20.5 % to the value at high bias of 37 %. In the end, the efficiency attains a cap of about 35 % from the voltage bias $V_{bias} = 2\,\mathrm{V}$.

On the right plot, the experimental fiducial percentage is in excellent agreement with the simulation percentage on the R_{veto} range $[0.2, 0.5]$. This agreement stops from $R_{veto} = 0.6$ with a sudden drop of the fiducial percentage. This behavior can be attributed to the observation made on the electric field shape of REDN1 in section 6.1.2. Indeed, for this polarization ratio 0.6, the equatorial volume greatly gains in volume and have and shows an increased electric field. This equatorial value is big enough to overlaps any cone of transversal electron drift in the semiconducting germanium. Concerning the events with incomplete charge collection, their

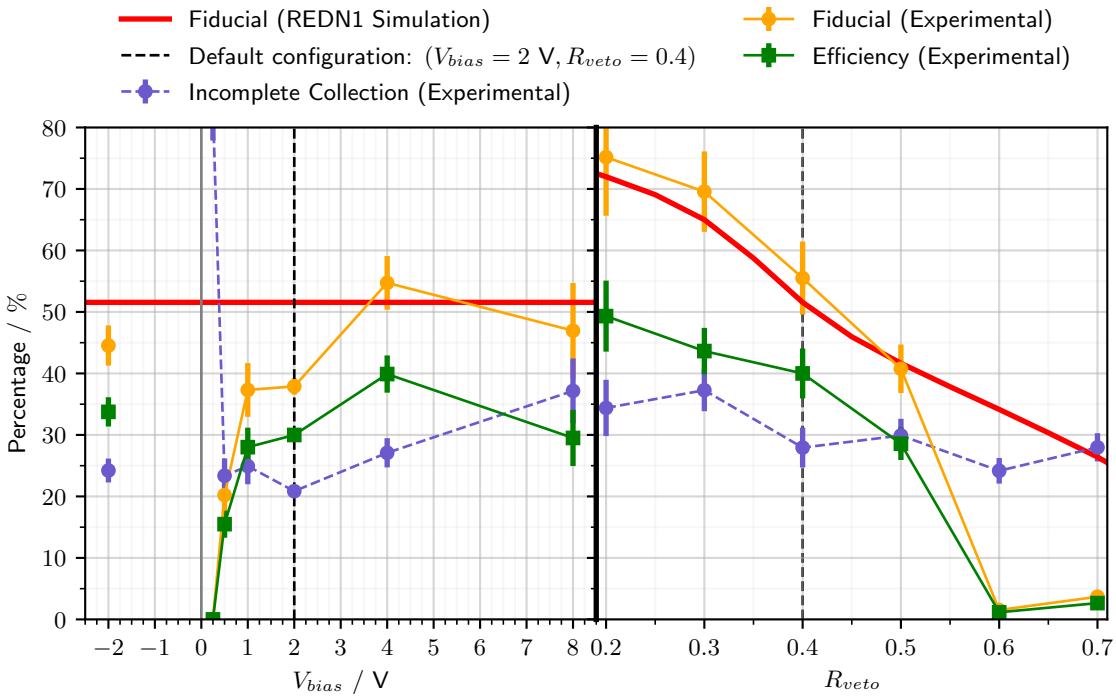

Figure 6.22: Experimental percentages of incomplete collection $\%_{incomplete}$ (in blue), of fiducial events $\%_{fid}$ (in orange) and of the efficiency $\%_{eff}$ (in green) as functions of the voltage bias V_{bias} (on the left) or of the polarization ratio R_{veto} (on the right) for the detector REDN1. The theoretical fiducial volume percentage estimated with the REDN1 simulation is indicated by the red lines.

percentage is quite stable around 30 % with slight decreasing trend. This can be explained by the decrease in average electric field in the REDN1 crystal as R_{veto} increases. This can be illustrated by the naive calculation with the FID38 design in the equation 4.45. In the end, the efficiency follows the fiducial percentage trend by decreasing from 50 % at the lowest polarization ratio 0.2 to 29 % at $R_{veto} = 0.5$.

All in all, the viable polarization range of REDN1 is to have a voltage bias V_{bias} greater than 1 V and a polarization ratio inferior to 0.5. On these ranges, the efficiency of REDN1 is worse than for RED80. This observation is consistent with the simulations and characteristic of the comparison of detectors using full planar electrodes and FID-like electrodes. Moreover, RED80 seems operational at lower absolute voltage bias $|V_{bias}|$ than REDN1. Indeed, the average electric field inside REDN1 is lower than for RED80 at fixed V_{bias}. As a result, REDN1 is more sensible to changes in voltage bias, which is one of the prices to pay for its ability to reject surface events.

6.3.4 Prospectives

For future studies, we can think of several improvements to the presented work. The precision would be enhanced with more statistics obtained with longer data streams. For this study of RED80 and REDN1, the data streams are in average 2 hours long and can easily be prolonged to 8 hours during a working day or during the night. The current limiting constraint is the data acquisition planning of the run. In the near future (few months), the HEMT-based electronics will be replace the current JFET-based electronics. This will results in an important gain in ionization energy resolution. This will directly improve the quality of the analysis cuts, in particular, the incomplete event selection and the bulk cut. We can imagine that with this lowered resolution, the analysis of the ionization corner plots such as in the figure 6.13 could yield, in addition to the fiducial volume, an estimation of the veto, guard or equatorial volumes. A study of the frontier event can also be imagined with this low resolution. It is possible to consider an ionization signal as the linear combination of the main types of signatures, in equations 6.7 and 4.47 for RED80 and REDN1 respectively. With this modelization, we could have access to the number of electric charges carriers attributed to each collection volume. This would eventually lead to further insights on the charge drift in the germanium crystal.

The next step would be to apply the same characterization and analysis methodology as presented here to the PL38 and FID38 detectors designs that I have proposed and optimized in previous Chapter 5, which are the candidates designs for the CryoCube.

Chapter 7

Neutron Measurements at IP2I cryogenic facility

7.1 Motivation

The RICOCHET experiment is based on the operation of cryogenic bolometers with an intense neutrino flux. This flux is produced by the ILL research nuclear reactor. The RICOCHET experimental setup will be located at a few meters of the reactor. As such, there is a risk that the bolometers will be blinded by the radioactive background of the ILL site, produces electronic recoils and nuclear recoils. The electronic recoils are mainly produced by gamma rays and charged particles such as electrons and muons. These recoils are easily discarded from the neutrino-nucleon elastic recoils thanks to the discrimination provided by the double energy measurement (ionization and heat) of the detectors. The nuclear recoils are induced by neutrons. This neutron background generates the same signal as the CENNS and as such cannot be readily discriminated by the detector. It is an unavoidable background for RICOCHET which will limit the CENNS process measurement. Nevertheless, it is possible to achieve a likelihood analysis with an estimation of the nuclear recoil rate produced by the neutron background. This background-induced component can be deducted from the total nuclear recoil spectrum to evaluate the spectrum generated by neutrino-nucleon scattering. Therefore, it is vital to evaluate the neutron background on-site and understand its dependency in the energy. In addition to estimating the limitations on the measurement, the study of the neutron background on-site will also be used in the design of the shielding.

With the current experimental setup, it is not possible to measure the ILL neutron background in the energy range of the detectors. For now, the neutron background is extrapolated from its measurement at higher energy range. The neutron energy spectrum is measured at the ILL site with gaseous Helium-3 Tube Detector based on the neutron capture by ^{3}He:

$$ {}^1_0\mathrm{n} + {}^3_2\mathrm{He} \longrightarrow {}^3_1\mathrm{H} + {}^1_1\mathrm{p} \tag{7.1} $$

This spectroscopy approach is sensitive to fast neutrons of energy $\mathcal{O}(1\,\mathrm{MeV})$. As these fast neutrons produce keV-scale nuclear recoils in germanium detectors via elastic scattering suggesting that a ^{3}He fast neutron measurement will allow us to anticipate the fast neutron background for RICOCHET. This chapter is focused on the measurement of fast neutrons at IP2I achieved with the cryogenic germanium detectors and its corresponding data analysis.

7.2 Experimental Setup

The reference neutron background is measured at the IP2I cryostat facility. The figure 7.1 presents on the right a scheme of the cryostat facility with the position of the detectors. RED80 is operated inside the cryostat. The ^{3}He tube detector is operated inside the disassembled cryostat

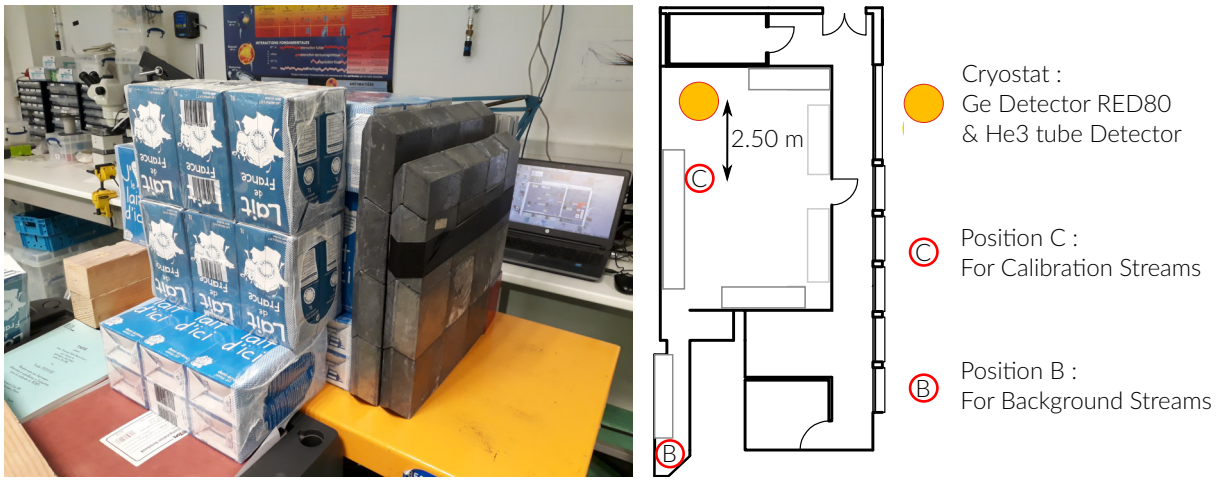

Figure 7.1: On the left, photo of the neutron source used for the Calibration streams in position *C*. It consists in the AmBe neutron source surrounded by milk bricks and a lead brick wall on the cryostat-facing side. On the right, overhead view scheme of the IP2I cryostat facility for the neutron background measurements. The ^{3}He tube detector and RED80 are located on the cryostat. The neutron source can be in position "C" near the detectors for neutron Calibration streams and in position "B" away for the Background streams.

while keeping the same distance to the neutron source. The measurements are separated in two phases: the neutron Calibration and the Background measurement.

During the neutron Calibration phase, the detectors measure a lot of nuclear recoils as to calibrate the analysis yielding the energy spectrum. A neutron source is used to generate these nuclear recoils in the detectors. The figure 7.1 displays on the left a photo of the neutron source setup used for the measurement. It consists in the AmBe neutron source, already use for the neutron activation of the germanium described in paragraph 2.3.4, surrounded by milk bricks and a lead brick wall. The milk bricks create an efficient low-cost water shielding as to thermalize the neutrons. The lead brick wall is positioned between the neutron source and the detectors. Its role is to stop the gamma rays produced by the neutron source and assure a stable radioactive electronic background for the detectors. In this phase, the neutron source is placed at the position *C*, approximately 2.5 m from the center of the cryostat. This position was found empirically to be close enough to provide an intense neutron flux without saturating the detectors.

During the Background measurement phase, the detectors are isolated from the neutron source as to measure nuclear recoils produced solely by the neutron background of the IP2I facility. The source is placed in its storage in position *B* more than 10 m away from the cryostat.

In section 7.9, we compare the ^{3}He capture rate with the nuclear recoil detection rate in cryogenic germanium detectors.

The low energy measurements with RED80 were carried out during the run 57. This run started on 03/07/2019 and ended on 01/08/2019. The detector RED80 was operated in the suspended tower of the cryostat along with the detector RED70 (not studied in this work). The detector RED80 is fully described in the previous chapter 6 using several streams of the run 57.

Before being installed into the cryostat, the germanium crystal of RED80 was activated with an AmBe neutron source as described in section 2.3.4. As such, the detector possesses two intrinsic and uniformly distributed calibration peaks of electronic recoils at 1.3 keV and 10.37 keV. The neutron activation started on 28/06/2019 at 17h08 and ended on 02/07/2019 at 10h08 yielding 89 h of activation.

Several data streams are attributed to the IP2I neutron background measurement. The table 7.1 lists the data streams and their starting date. Depending on the position of the neutron

Configuration	Stream	Starting Date	Stream Duration / h	Cumulative Duration / h
Background	tg18l005	18/07/2019	14.95	52.88
	tg27l000	27/07/2019	16.43	
	tg28l000	28/07/2019	21.50	
Calibration	tg17l007	17/07/2019	11.83	75.99
	tg19l010	19/07/2019	20.86	
	tg20l000	20/07/2019	26.37	
	tg21l000	21/07/2019	16.93	

Table 7.1: Starting data and duration of the data streams attributed to the IP2I neutron background measurement. For the Calibration configuration, the neutron source is facing the cryostat in position *C*. For the Background configuration, the detector is isolated from the neutron source stored in position *B*. The cumulative duration of each configuration is calculated.

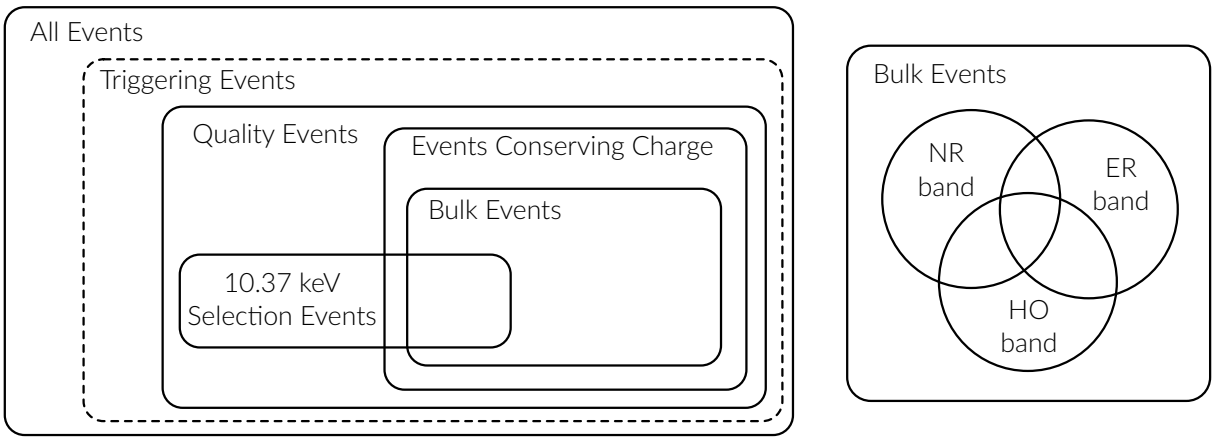

Figure 7.2: Venn diagrams of the events in the presented analysis for the measurement of the neutron background. The dashed class "Triggering Events" is only used for the events generated by the pulse simulation.

source, the streams are attributed to the Background phase or the Calibration phase. Each stream was taken during nights or week-ends to benefit from long time of stable operation. The configurations were mixed in term of dates. This is of importance when measuring the rate of the calibration peak electronic recoils which is decreasing with time as discussed in section 2.3.4.

In all the streams, RED80 was operated at 16 mK with an optimal NTD polarization current of 1 nA. The electrodes were polarized in their default configuration (eq. 6.6) with a voltage bias $V_{bias} = 2\,\mathrm{V}$.

7.3 Analysis of the Data Streams

The data streams are pre-processed with the NEPAL software as discussed in section 6.2. The majority of the analysis steps are already described in the chapter 6. In this section, analysis steps specific to the neutron measurements and differences in the cut parametrization are presented. The figure 7.2 summarizes the event types depending on their passing cuts. Compared to the characterization study of RED80 and REDN1 presented in the previous chapter 6, the stream used for the IP2I neutron background measurement are long and yield plenty of statistics. As such, the analysis cuts are globally more conservative with smaller tolerances compared to previous studies.

Configuration	Stream	Selected Intervals / h	T_{live}
Background	tg18l005	$[0, 7.4] \cup [7.6, 14.95]$	35.93 h = 1.497 d
	tg27l000	$[0, 7] \cup [11.3, 13.8] \cup [14.1, 16.43]$	
	tg28l000	$[0, 7.4] \cup [8.05, 10]$	
Calibration	tg17l007	$[0, 11.83]$	75.60 h = 3.150 d
	tg19l010	$[0, 8.30] \cup [8.70, 11.83]$	
	tg20l000	$[0, 26.73]$	
	tg21l000	$[0, 16.93]$	

Table 7.2: Selected time intervals for live time cut of each stream. The cumulative live time T_{live} is evaluated for the Background and Calibration configurations.

Configuration	Channel	Stream	χ^2_0	A_0	b
Background & Calibration	Heat	tg17l007 tg18l005 tg19l010 tg20l000 tg21l000	400	3×10^2	2
		tg27l000 tg28l000	700		
	Ionization A, B, C, D	All	300	2×10^3	2.2

Table 7.3: Parameters for the quality cuts used in the Neutron Analysis.

7.3.1 Parametrization of the Quality Cuts

The quality cuts are described in the dedicated section 6.2.5. For this analysis, the maintenance cut, the reset cut and the ionization offset cut are applied with the same parametrization. The live time cut and the χ^2 cut are applied with specific parameters.

The table 7.2 lists the selected time intervals for each stream in regards to the live time cut. Even though the data streams were recorded for long and apparently stable operation, some portion of the streams were corrupted. As the exact causes are unknown at this time, the intervals were chosen with some precautionary buffer as to only record data during stable electronics operation. The live time cut is used to evaluate the cumulative live time T_{live} for each configuration. These are used later in section 7.8 in the calculation of the detector exposure.

The table 7.3 lists the parameters used for the χ^2 cuts for each stream of the analysis. The three parameters χ^2_0, A_0 and b corresponds to the χ^2 threshold function defined in equation 6.27.

7.3.2 Cross-talk Correction and Calibration

The analysis steps following the application of the quality cuts are the cross-talk correction, the selection of the 10.37 keV calibration peak events and the calibration of the heat and ionization channels. These steps are described in the section 6.2.

The cross-talk correction relies on the estimation of the capacitance of the cabling. For RED80 in the run 57, this capacitance was already evaluated to $C_{cabling} = 125\,\text{pF}$. Repeating this estimation with the streams yield values within the error bars. As such, this cabling capacitance is conserved for this analysis.

For the measurement of the IP2I neutron background, the selection of the 10.37 keV calibration peak events is solely used for the calibration of the heat and ionization channels. In the case of Background streams, the selection and calibration are the same as for the previous study of

RED80. In the case of Calibration streams, this selection is hampered by the highly populated nuclear band. The selection of the 10.37 keV calibration events described in section 6.2.7 is contaminated with events from the continuous nuclear recoil band. A s such, the calibration of the heat channel is realized with the events above the nuclear recoil band only. There is almost no loss of precision on the estimation of the calibration peak and on the calibration coefficient α_{heat} of equation 6.46.

7.3.3 Charge conservation cut and Parametrization of the Bulk Cut

The electric charge conservation was already discussed for the characterization study of RED80 and REDN1 in the section 6.2.8. There was no clear evidence that a population of events not conserving the electric charge does exist. The charge conservation cut is applied with the same parametrization: events passing this cut have a charge conservation energy E_{CC} inferior to 2 times the associated resolution $\sigma(E_{CC})$ (see equation 6.53).

The bulk cut was introduced in section 6.2.9 also for the characterization of the RED80 and REDN1 detectors. For this analysis dedicated to the measurement of the neutron background, the tolerance on the ionization energies of the guard electrodes E_A and E_C are lower, now corresponding to $2 \cdot \sigma_{E_X}$. Thus, for this analysis, bulk events satisfy the following inequalities:

$$\begin{cases} E_A < 2 \cdot \sigma_{E_A}\,(0\,\text{keV}) \\ E_C < 2 \cdot \sigma_{E_C}\,(0\,\text{keV}) \end{cases} \tag{7.2}$$

For bulk events, it is more advantageous to use the bulk ionization energy $E_{Ion.}^{bulk}$ rather than the total ionization energy $E_{Ion.}^{total}$. Indeed, the bulk ionization energy is only calculated from the signal on the two main collecting electrodes B and D such that:

$$E_{Ion.}^{bulk} = \frac{E_B + E_D}{2} \tag{7.3}$$

As a result, the standard deviation associated is lower than for the $E_{Ion.}^{total}$:

$$\sigma_{E_{Ion.}^{bulk}} = \sqrt{\sigma_{E_B}^2 + \sigma_{E_D}^2} \simeq \frac{\sigma_{E_B}}{\sqrt{2}} \approx \frac{260\,\text{eV}}{\sqrt{2}} = 183\,\text{eV} \tag{7.4}$$

For the rest of the analysis, the ionization energy of the bulk events are therefore estimated with the quantity $E_{Ion.}^{bulk}$. In particular, this propagates to the calculation of the recoil energy E_R and the quenching factor Q.

7.3.4 Comparison of the Calibration and Background Data

Up until now, the analysis was focused on pruning events with possibly bad energy reconstruction energy and calibrating the heat and ionization channel. All the previous analysis steps, summarized on the left of scheme 7.2, yields the bulk events. These events, being from Calibration or Background streams, passed the quality cuts, the charge conservation cut and the bulk cut. Each bulk event is now characterized by two quantities: its heat energy E_{heat} expressed in keV_{ee} and its bulk ionization energy $E_{Ion.}^{bulk}$ in keV. These two quantities can be converted into the recoil energy E_R in keV and the quenching factor Q according to the following equations:

$$E_R = E_{heat} \cdot \left(1 + \frac{V_{bias}}{\epsilon_{e^- - h^+}}\right) - E_{Ion.}^{bulk} \frac{V_{bias}}{\epsilon_{e^- - h^+}} \tag{7.5}$$

$$Q = \frac{E_{Ion.}^{bulk}}{E_R} \tag{7.6}$$

with $V_{bias} = 2\,\text{V}$ the voltage bias of RED80 of use for the Luke-Neganov effect calculation (see equation 6.48) and $\epsilon_{e^- - h^+} = 2.97\,\text{eV}$ the average energy of an electron-hole pairs. The quenching factor Q is useful to illustrate the discrimination between the electronic and the nuclear recoils in the germanium. As for the recoil energy E_R, it corresponds to the total energy that is transferred to the crystal through the particle interaction with the crystal.

The top graphic of the figure 7.3 is a scatter plot of the bulk ionization energy $E_{Ion.}^{bulk}$ versus the heat energy E_{heat} for all the bulk events used in this analysis. The bottom plot represents the quenching Q versus the recoil energy E_R of the bulk events. In both plots, the events originating from the Calibration and Background streams are colored blue and black respectively. The numbers 1 to 6 annotates different event types.

The noise blob, labeled 1, corresponds to triggering noise windows and with events of very low energy. It is a feature common to all the streams. The position of the noise blob is the origin:

$$\begin{cases} E_{Ion.}^{bulk} = 0\,\text{keV} \\ E_{heat} = 0\,\text{keV}_{ee} \end{cases} \tag{7.7}$$

As a result, it is next-to impossible to evaluate the quenching of the events. This explains the shape of the noise blob in the Q vs E_R bottom plot. It covers the entire range of the quenching value with the merging of the electronic, nuclear and heat-only bands.

The population labeled 2 corresponds to the 1.3 keV calibration peak. This population is present in both the Calibration and Background streams. These events are induced by electronic recoils, thus belongs to the electronic recoil band, and are characterized by the following quantities:

$$1.3\,\text{keV line:} \begin{cases} E_{Ion.}^{bulk} = 1.3\,\text{keV} \\ E_{heat} = 1.3\,\text{keV}_{ee} \\ Q = 1 \\ E_R = 1.3\,\text{keV} \end{cases} \tag{7.8}$$

The energies of these events are close to the energy resolution. Consequently, the estimation of the quenching factor Q is imprecise which explains the banana shaped of the population on the Q versus E_R plot.

The 10.37 keV calibration peak is labeled 3. These events are present in all the streams. The population is centered on the quantities:

$$10.37\,\text{keV line:} \begin{cases} E_{Ion.}^{bulk} = 10.37\,\text{keV} \\ E_{heat} = 10.37\,\text{keV}_{ee} \\ Q = 1 \\ E_R = 10.37\,\text{keV} \end{cases} \tag{7.9}$$

Their heat and ionization energies is high enough for a precise estimation of the quenching factor. However, the calculation of the recoil energy E_R leads to a warped blob in the Q versus E_R plot. One can note a remnant of the 10.37 keV calibration events with incomplete charge collection as studied in section 6.2.7. They consists in in the inter-band events between the ER and NR bands with incomplete charge collection.

The electronic recoil band, or ER band, is indicated by the number 4. The majority of the events originating from the Background streams are in this band, indicating that the radioactive background of the IP2I cryostat facility mainly induces electronic recoils. The two calibration peaks are part of the electronic recoil band. An event of the ER band with a recoil energy E_R is

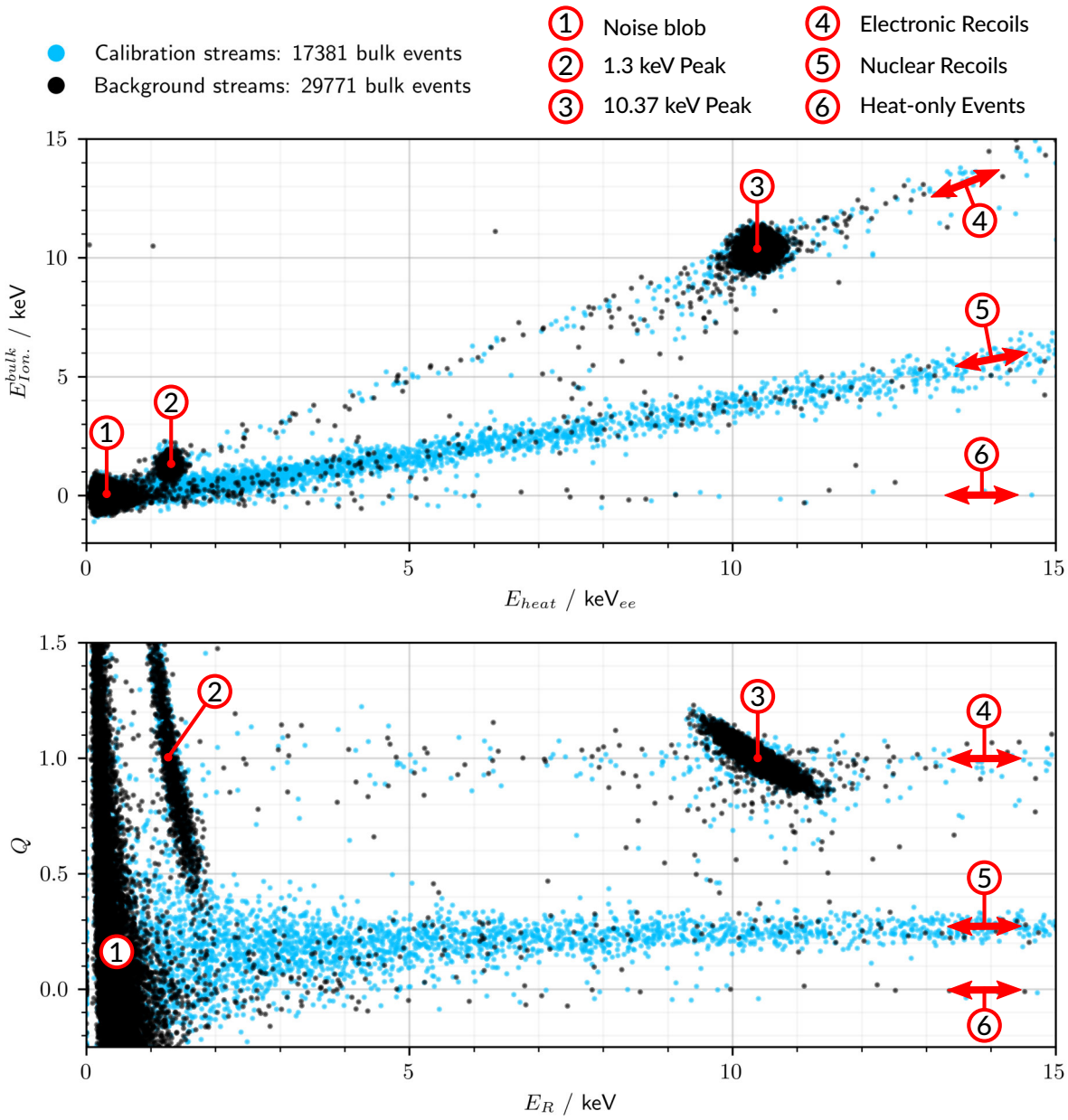

Figure 7.3: At the top, bulk ionization energy $E^{bulk}_{Ion.}$ of all bulk events versus their heat energy E_{heat}. At the bottom, quenching Q of all the bulk events versus their recoil energy E_R. Events from Calibration streams are in blue. Events from the Background streams are in black.

characterized by the following quantities:

$$\text{Gamme ER band:} \begin{cases} Q = Q_{ER} = 1 \\ E_{Ion.}^{bulk} = Q \cdot E_R = E_R \\ E_{heat} = E_R \end{cases} \tag{7.10}$$

The nuclear recoil band, or NR band, is annotated by the number 5. This band is densely populated for the Calibration streams. This confirm that the neutron source is well placed so that the majority of the triggering events are nuclear recoils. These events are also present in the Background streams although with much less statistics. These events are characterized with:

$$\text{Neutron NR band:} \begin{cases} Q = Q_{NR}\left(E_R\right) \\ E_{Ion.}^{bulk} = Q_{NR}\left(E_R\right) \cdot E_R \\ E_{heat} = E_R \cdot \frac{1+Q_{NR}(E_R)\frac{V_{bias}}{\epsilon_{e^- - h^+}}}{1+\frac{V_{bias}}{\epsilon_{e^- - h^+}}} \end{cases} \tag{7.11}$$

The quenching factor Q_{NR} associated with the nuclear recoils is a function of the recoil energy E_R. The nuclear recoils from the Background streams are precisely what corresponds to the IP2I neutron background and consist in the intrinsic limit to the measurement of the CENNS process.

The number 6 indicated a much less populated band of events displaying a quenching of $Q = 0$. These events are known as "Heat-only" events, HO events. This population is infamously known in all dark matter experiments (EDELWEISS, CDMS and CRESST) using cryogenic crystalline detectors. These events produce a signal solely on the heat channel. They are characterized by the quantities:

$$\text{Heat-only band:} \begin{cases} Q = Q_{HO} = 0 \\ E_{Ion.}^{bulk} = 0\,\text{keV} \\ E_{heat} = E_R \cdot \frac{1}{1+\frac{V_{bias}}{\epsilon_{e^- - h^+}}} \end{cases} \tag{7.12}$$

They could correspond to electronic and nuclear events with no charge collection due to all charges being trapped or recombining on the electrodes, as discussed in section 4.1.4. However, this is not compatible with the lower counts of inter-band events with an incomplete charge collection. Moreover, the HO events are present in all the streams with an apparent independence from the Background and Calibration configurations, and the calibration peaks. At this moment, their origin is unknown and is still under investigation.

The presence of the three ER, NR and HO bands in this plot demonstrate the discriminating ability of the double heat and ionization energy measurement. One can note that although the bands are well separated at high energy, they are merging at low energy due to their width which is fixed by the energy resolution of the heat and ionization channel. The merging phenomenon of the bands at low energy is also more visible in the bottom graph Q versus E_R. We can even visually witness that the lower part of the 1.3 keV event blob is leaking into the higher part of the nuclear band.

7.3.5 Band cuts and Unnormalized Energy Spectra

The objective of this analysis is to extract the energy spectrum of events associated to the nuclear recoils. In order to attribute each event to a recoil type, the so-called "Band Cuts" are defined. There are three cuts, each corresponding to the three electronic recoils, nuclear recoils and heat-only event bands. An event is attributed to a band if it is passing the associated cut. A band

cut is base on the comparison between the experimental bulk ionization energy $E_{Ion.}^{bulk}$ and the theoretical ionization energy $E_{Ion.}^{theory}(band)$ expected from an event belonging to the band. This theoretical energy is calculated using the characterization of the bands introduced in the previous section 7.3.4. The tolerance is chosen to be two standard deviation of the bulk ionization energy $\sigma_{E_{Ion.}^{bulk}}$ at the considered heat energy E_{heat}. The cut are therefore expressed mathematically with the inequality:

$$|E_{Ion.}^{bulk} - E_{Ion.}^{theory}(band)| < 2 \cdot \sigma_{E_{Ion.}^{bulk}}(E_{heat}) \tag{7.13}$$

One should note that the band cuts are defined using only the uncertainty on the ionization channel with the $2 \cdot \sigma_{E_{Ion.}^{bulk}}$ tolerance. Indeed, the resolution of the ionization channel is greater than the resolution of the heat channel. Thus, the analysis is simplified by assuming the measurement of the heat energy E_{heat} to be error free.

The "ER band cut" selects the events attributed to the electronic recoil band. The cut parametrization is based on the theoretical characterization of the electronic recoils presented in the system of equations 7.10. Passing events, deemed "ER events" satisfy the inequality:

$$|E_{Ion.}^{bulk} - E_{heat}| < 2 \cdot \sigma_{E_{Ion.}^{bulk}}(E_{heat}) \tag{7.14}$$

The "NR band cut" is associated with the nuclear recoil band. Its parametrization uses the theoretical characterization of the nuclear recoils presented in the system 7.11. The quenching factor Q_{NR} is evaluated with the Linhard model (eq. 4.4). Thus the "NR events" satisfies the inequality:

$$|E_{Ion.}^{bulk} - Q_{NR}(E_R) \cdot E_{heat}| < 2 \cdot \sigma_{E_{Ion.}^{bulk}}(E_{heat}) \tag{7.15}$$

with the recoil energy E_R calculated from $E_{Ion.}^{bulk}$ and E_{heat} with the equation 7.5.

The "HO band cut" attributes events to the heat-only band. Using their characterization in the system of equations 7.12, the "HO events" passing this cut satisfies:

$$|E_{Ion.}^{bulk}| < 2 \cdot \sigma_{E_{Ion.}^{bulk}}(E_{heat}) \tag{7.16}$$

The figure 7.4 illustrates the application of the band cuts on the bulk events originating from the Calibration streams. At the top are the bulk ionization energies $E_{Ion.}^{bulk}$ versus the heat energies E_{heat}. At the bottom is the quenching factor Q versus the recoil energy E_R. Each band cut is represented with the tolerance of $2 \cdot \sigma_{E_{Ion.}^{bulk}}(E_{heat})$ on the ionization energy. Each band is centered on the line drawn by their theoretical characterization $E_{Ion.}^{theory}(band)$. One should note that according to the expressions 7.11, there is no analytical expression of the ionization energy $E_{Ion.}^{theory}(\mathrm{NR\ band})$ as a function of the heat energy. To bypass this issue, the ionization energy is computed over a fine array of heat energy from 0 keV to 50 keV. Then, the plotted theoretical line is obtained by linear interpolation.

We see that for $E_R \lesssim 5.5$ keV, the different bands are merging into each other, starting with the NR and HO bands. As bands overlap, some events are attributed to multiple bands, particularly at the lowest energies. The lower parts of the 1.3 keV calibration peak is even leaking into the NR band. This effect is detrimental to the counting of the number of events of each type. A compensation of this effect applied later in the analysis and is described in the dedicated section 7.7.

At this point of the analysis, the selection of the nuclear recoils event is made with the NR band cut. A convenient review of the analysis cuts used to prune all the events is to compute the energy spectra. The figure 7.5 displays the recoil energy E_R spectra associated with the Background streams, on the top plot, and the Calibration streams, on the bottom plot. The histograms are calculated with bins of 1 keV width.

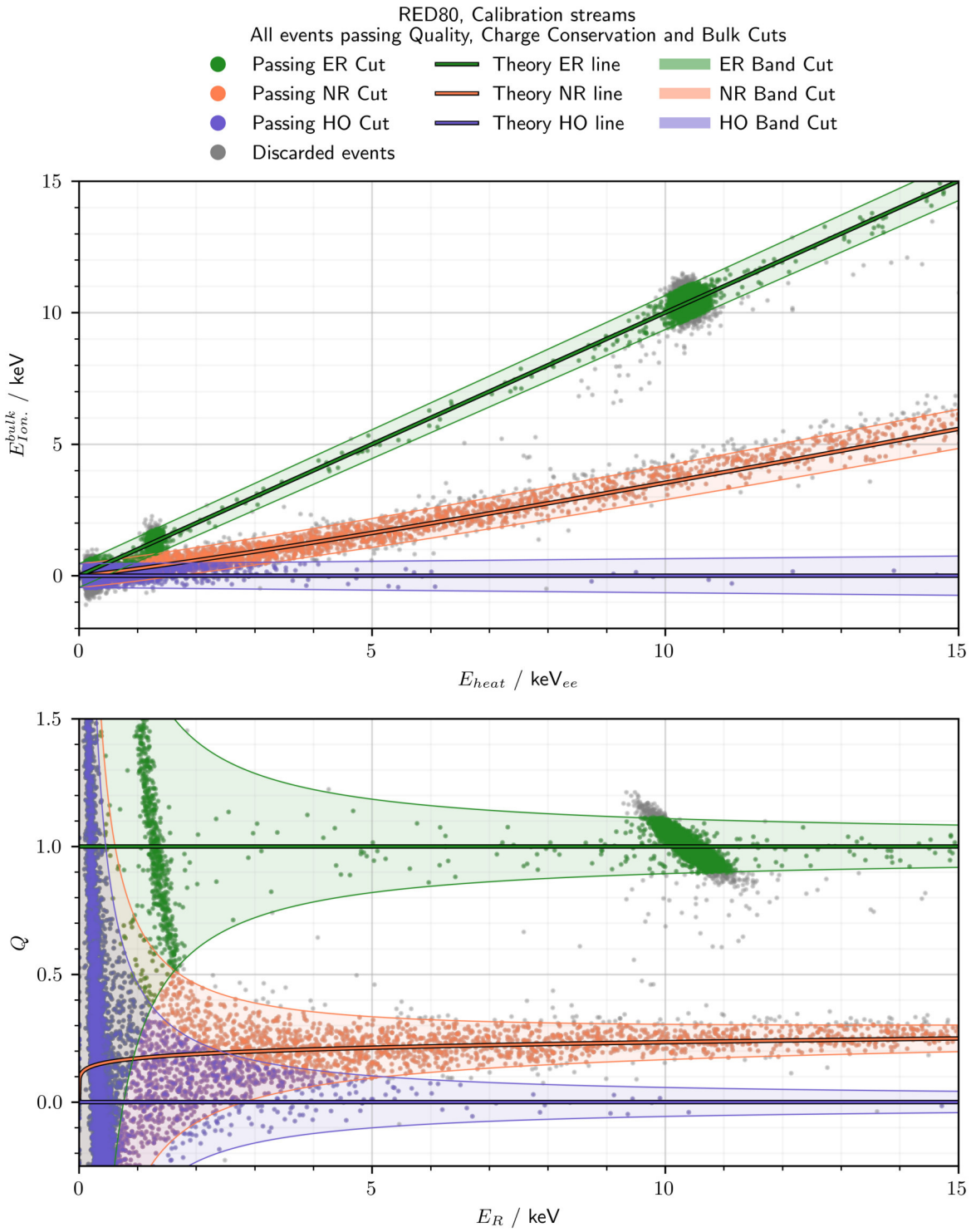

Figure 7.4: Illustration of the Band cuts on the bulk events originating from the Calibration events. The top plot represents the bulk ionization energy $E^{bulk}_{Ion.}$ versus the heat energy E_{heat}. The bottom plot displays the quenching factor Q versus the recoil energy E_R. The electronic recoil (ER), nuclear recoil (NR) and heat-only (HO) bands are plotted with the $2 \cdot \sigma_{E^{bulk}_{Ion.}}$ tolerance.

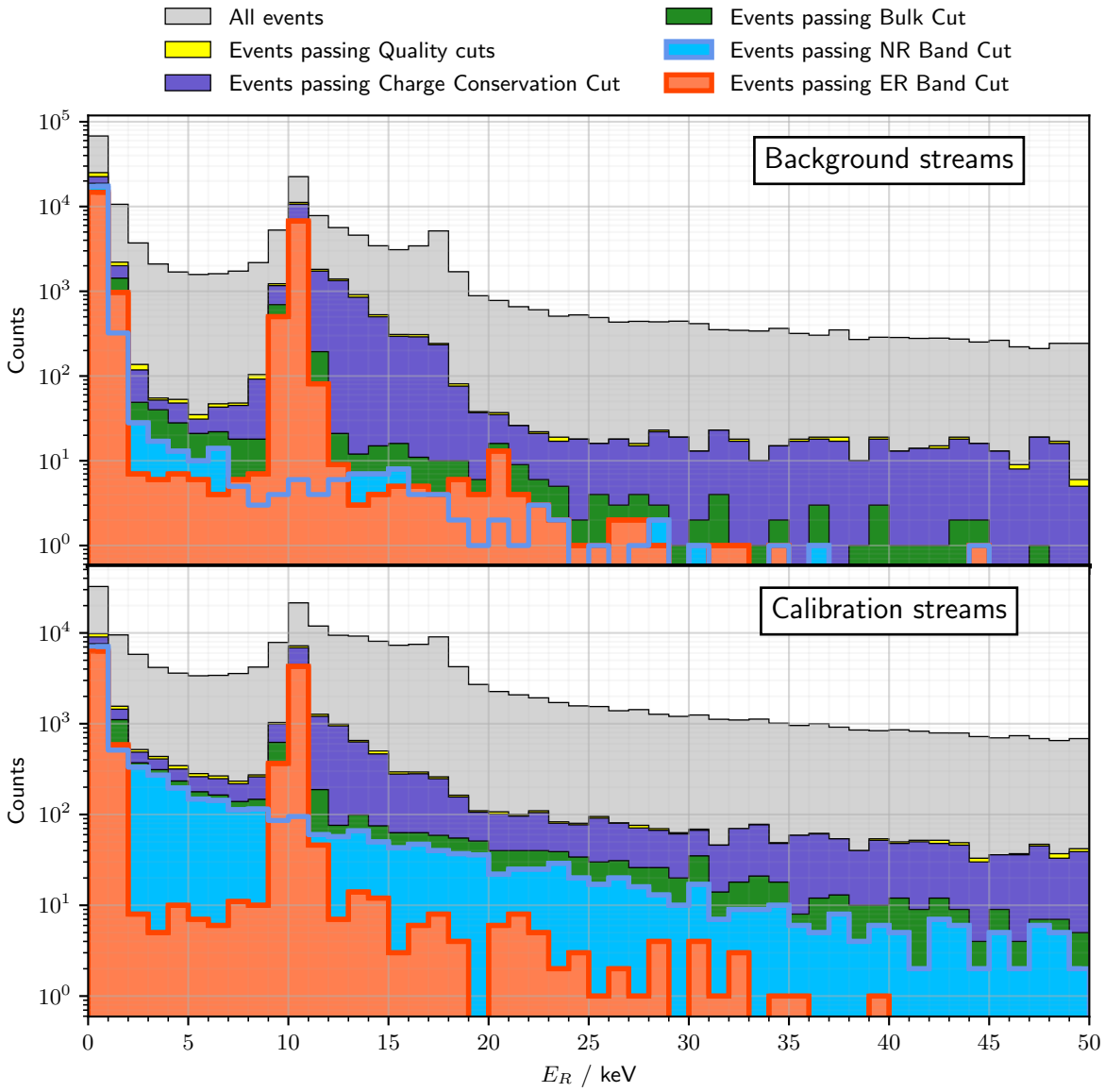

Figure 7.5: Recoil energy E_R Spectra of the events originating from the Background streams (top plot) and the Calibration streams (bottom plots). Each overlapping histogram is associated with an analysis cut. The width of all the bins is 1 keV.

The overlapping histograms let us appreciate the amount of discarded events by each analysis cut depending on their recoil energy. We can note some usual features in this histogram like the noise blob at the lowest energies and 10.37 keV calibration peaks. A visible consequence of the band overlapping at low energy is the attribution of the noise blob events to both the ER and NR band. The contribution of the 1.3 keV calibration events to the spectra is only perceptible in the second bin of the Background plot. The comparison of the Background and Calibration energy spectra levels should be made relative to the total number of events. Indeed, the two configurations have different live time calculated in the table 7.2. Here, we confirm that the Calibration streams, with a cumulative live time of 75.6 h, recorded more events than the Background streams, with the lower live time of 35.93 h. The major difference between the Background and Calibration is the relative levels of the ER band and NR spectra. For the Background configuration, the NR band spectrum has a similar level to the ER band spectrum, excepting the calibration peaks. In the case of the Calibration configuration, the NR band level is an order or two greater than the ER band background spectrum. This is consistent with the higher neutron flux induced by the neutron source.

Until now, the recoil energy was calculated from the heat energy E_{heat} and the bulk ionization energy $E_{Ion.}^{bulk}$ using the equation 7.5. While unbiased, the precision of the recoil energy calculation is limited by the relatively high error on the ionization energy measurement compared to the heat channel. Now that the events passing the NR and ER band cuts are considered as being generated from nuclear and electronic recoils respectively, it is possible to boost the resolution of the recoil energy E_R using their theoretical quenching factor. For the ER events, the quenching is $Q_{ER} = 1$ while for the NR events, the quenching $Q_{NR}(E_R)$ is derived from the Lindhard model in equation 4.4. As this quenching is in itself a function of the recoil E_R, it is necessary to numerically solve the following equation:

$$E_R = E_{Heat} \cdot \frac{1 + \frac{V_{bias}}{\epsilon_{e^- - h^+}}}{1 + Q_{NR}\left(E_R\right) \frac{V_{bias}}{\epsilon_{e^- - h^+}}} \tag{7.17}$$

With this calculation of the recoil energy, the ionization measurement is not used. The precision on the estimation of the recoil energy is now only limited by the error of the heat energy measurement.

In order to translate the recoil energy spectrum of the NR band into a measurement of the IP2I neutron background, it is necessary to estimate the nuclear recoil rate rather than their count. Once done, it is possible to compare directly Background and Calibration configurations. This part of the analysis is thoroughly explained in the next section.

7.4 Translating the Nuclear Recoil Counts to Rate

The objective of the analysis presented in the previous section 7.3 is to count the number of nuclear recoils recorded in the data streams in the Background and Calibration configurations. This eventually resulted in the recoil energy spectra presented in the figure 7.4. In this state, this result do not represent the neutron flux at the IP2I cryostat facility. Indeed they consist in an event count which is an extensive quantity depending on the experimental setup and analysis pipeline. The number of recorded events is proportional to the detector exposure, its triggering threshold and the analysis cut efficiencies. The final nuclear recoils count is dependent from the parametrization of the analysis cuts, in particular the tolerance of the analysis cuts. The $2 \cdot \sigma$ tolerance chosen for the analysis cuts yields a selection of well-reconstructed events at the cost of discarding a massive fraction of all the triggering events.

The neutron flux should be quantified with an intensive quantity which is the event rate. This section explains how the nuclear recoil spectra are translated into nuclear recoil rates. Most

of the efforts are focused on estimating the actual number of interactions which resulted in a nuclear recoil in the RED80 crystal during the data acquisition. This estimation is described in the next section 7.4.1 using the technique of pulse simulation. This is followed by the normalization of the interaction counts described in the sectionpar:normalization.

7.4.1 Pulse simulation

This section presents the "pulse simulation" technique. It is used to estimate the real number of events that did happen in the RED80 detector from the count of the events passing the band cuts presented in the figure 7.5. The pulse simulation is used to correct the counts in two ways. Firstly, it allows the calculation of the efficiencies associated with the trigger and the data cut. Secondly, it permits the correction of the band contaminations due to the ER, NR and HO bands overlapping at the lowest energies. The pulse simulation is based on simulating pulses of known recoil energy E_R and quenching Q. A pulse designates the signal generated by an event on the five measurement channels being the heat and the ionization A through D.

The simulation of a 0.5 s pulse window comes from scaling a pulse template. The heat and ionization signals of the template are the analytical models presented in the section 6.2.2. The ionization signal is simply modeled by a Heaviside function of the time (eq. 6.21). The heat signal is modeled by the 3-decaying exponential model presented in equation 6.20 with multiples parameters depending on the thermodynamic properties of the RED80 detector. As explained in the section 6.2.3, the parameters are adjusted from the 10.37 keV calibration events passing the bulk cuts. One should note that due to the non-linearity in the heat response discussed in chapter 3, the template shape deviates from the pulse shape of measured events at energies higher than 10.37 keV. This induces a loss of accuracy for the pulse simulation. Therefore, from now on, the analysis is limited to the recoil energy range $[0,\ 50]$ keV. This limited energy range should pose no threat to the measurement of the neutron background as it is expected to be observed at low energy thanks to kinematics considerations and confirmed by the uncorrected energy spectra associated to the NR band presented in the figure 7.5.

In order to simulate an event, each channel of the normalized template is scaled to a scaling energy $E_{heat}^{scaling}$ for the heat channel and $E_X^{scaling}$ for the ionization channel A through D. These scaling energies are derived from the heat energy E_{heat} and ionization energy E_X from a bank of reference events. These bank of reference events corresponds to the 10.37 keV calibration events passing the quality cuts. As such, this bank of event should be representative of all the events also featured event with incomplete charge collection. As to facilitate the reading of the scaling energies, the energies of the reference 10.37 keV calibration events in this reference bank are noted E_{heat}^{bank} and E_X^{bank} for the heat and ionization channels respectively.

For this work, the pulse simulation is operated for four different population of events. The most readily available population are the electronic recoils with a recoil energy of $E_R = 10.37$ keV. As simulated events, they are denominated the 10.37 keV line and are emulating the 10.37 keV calibration peak. The scaling energies are simply:

$$\begin{cases} E_{heat}^{scaling} = E_{heat}^{ref.} \\ E_X^{scaling} = E_X^{ref.} \end{cases} \quad \text{with} \quad X \in \{A, B, C, D\} \tag{7.18}$$

The second simulated population are the electronic recoils with a recoil energy of $E_R = 1.3$ keV. This simulated population is deemed the 1.3 keV line and is emulating the other calibration peak at 1.3 keV. The scaling energies are now:

$$\begin{cases} E_{heat}^{scaling} = E_{heat}^{ref.} \cdot \dfrac{1.3}{10.37} \\ E_X^{scaling} = E_X^{ref.} \cdot \dfrac{1.3}{10.37} \end{cases} \quad \text{with} \quad X \in \{A, B, C, D\} \tag{7.19}$$

The next simulated population corresponds to the electronic recoil band. These simulated events form the so called "flat ER" population. This denomination comes from the uniform distribution $\mathcal{U}(0,50)$ of input recoil energy E_R^{input} on the $[0,\ 50]$ keV analysis range of these events. For each event of the flat ER line, the scaling energies are:

$$\begin{cases} E_R^{input} \sim \mathcal{U}(0,50) \\ E_{heat}^{scaling} = E_{heat}^{ref.} \cdot \dfrac{E_R^{input}}{10.37} \\ E_X^{scaling} = E_X^{ref.} \cdot \dfrac{E_R^{input}}{10.37} \quad \text{with} \quad X \in \{A,B,C,D\} \end{cases} \tag{7.20}$$

The last simulated population corresponds to the nuclear recoil band. This population is denominated the "flat NR" population. As for the previous population, the recoil energy is sampled from the uniform distribution $\mathcal{U}(0,50)$. In order to simulate the characteristics of nuclear recoils presented in the system of equations 7.11, the scaling ionization energies are obtained from the quenching factor associated with nuclear recoils Q_{NR} derived from the Lindhard model. To first order, the scaling energies of the events belonging to the flat NR line are:

$$\begin{cases} E_R^{input} \sim \mathcal{U}(0,50) \\ E_{heat}^{scaling} = E_{heat}^{ref.} \cdot \dfrac{E_R^{input}}{10.37} \\ E_X^{scaling} = E_X^{ref.} \cdot \dfrac{E_R^{input}}{10.37} \cdot Q_{NR}\left(E_R^{input}\right) \quad \text{with} \quad X \in \{A,B,C,D\} \end{cases} \tag{7.21}$$

Once the pulses are simulated, they are injected into the experimental data streams. This injection consists in adding the 1 s signal at known randomized time t_0^{input}. As such, the pulse simulation technique is only valid when the whole stream of data is saved as described in section 6.2.2. In order to keep this probing technique from altering too much the characteristics of the analysis, it is decided to inject a maximum of 60 pulses per hour of streams. This process is repeated multiple times with different t_0 and for the four simulated population independently. In the end, it is a total of 1 million of each population that are simulated. Just as for the real measured data streams, the newly created streams with injected pulses are processed using the same pre-processing and analysis pipeline. The figure 7.6 presents the simulated events passing the quality and bulk cuts. At the top is the scatter of the bulk ionization energy $E_{Ion.}^{bulk}$ versus the heat energy E_{heat}. At the bottom is the graph of the estimated quenching Q and estimated recoil energy E_R of each event. Each simulated population has its own color.

These simulated pulses are excellent facsimiles of the real pulses, especially at the lowest energies, with the major advantage that we know their input recoil energy E_R^{input}, their injection time t_0^{input} and the type of recoil they emulate. We can thus proceed with the estimation of the efficiency of the pre-processing trigger and the analysis cuts.

7.5 Trigger Cut

The trigger is a pre-processing step described in section 6.2.3. Its role is to detect and create the 1 s pulse windows, that is to say triggering event, from a data stream. The objective of this section is to decide whether a simulated event injected at a time t_0^{input} has triggered in the pre-processing. As discussed in section 6.2.3, there are two conditions necessary to trigger. First, a triggering event shows an amplitude greater than the trigger threshold. And then, triggering events should be spaced in time by no less than 5 ms as to avoid the pile-up effect.

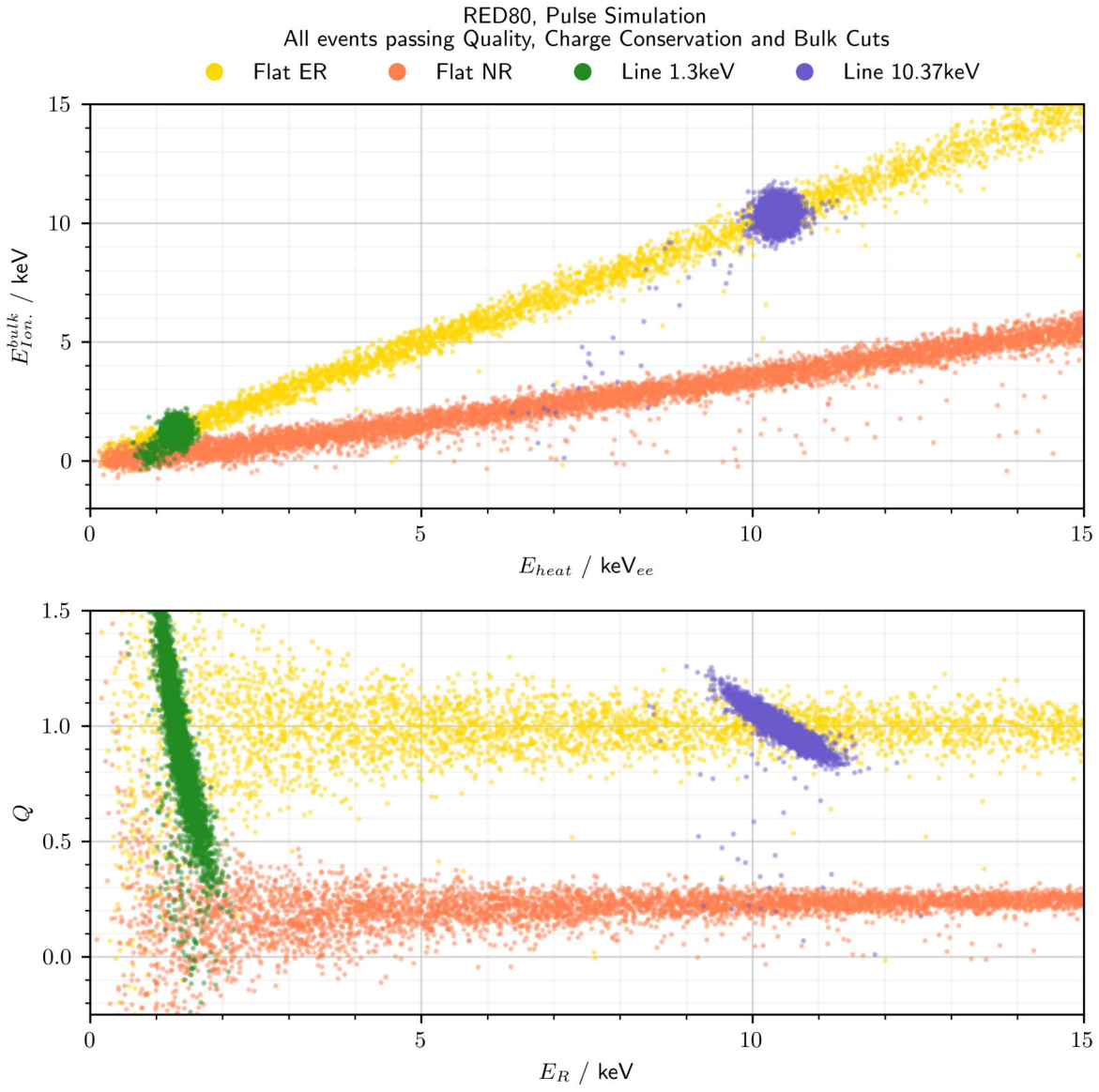

Figure 7.6: Illustration of the Pulse Simulation of the four population of events. The top plot represents the bulk ionization energy $E^{bulk}_{Ion.}$ versus the heat energy E_{heat}. The bottom plot displays the estimated quenching factor Q versus the estimated recoil energy E_R.

		Actual Condition of the Event	
		Condition Positive	Condition Negative
Classification of the Event from the Analysis Cut	Test outcome positive	True Positive (TP)	False Positive (FP)
	Test outcome negative	False Negative (FN)	True Negative (TN)

Table 7.4: Table of the four combinations of actual event condition and assigned condition by an analysis cut.

In the case of simulated events of known input time t_0^{input}, there is a supplementary condition that should be fulfilled for the simulated event to properly trigger. This condition is tied to the difference between the input time and the time reconstructed by the pre-processing process. Its role is to prevent a simulated pulse of low energy which could not have reached the trigger threshold on its own to have trigger by being injected close to an existing experimental pulse of sufficient amplitude energy. This condition is enforced by comparing the input time t_0^{input} of the simulated pulse to the measured time t_0 of all the triggering events in the considered stream. A maximum tolerance of 5 ms between the injection time t_0^{input} and the reconstructed time t_0 of a simulated pulse. This condition is represented by the inequality:

$$|t_0^{input} - t_0| \leq 5\text{ms} \tag{7.22}$$

Simulated events which triggers in the pre-processing and satisfies this additional condition are considered as having properly triggered. For the sake of denomination, these events are called "triggering events" having successfully passed the "Trigger cut". It is important to note that this trigger cut is specific to simulated pulses.

Reproducing this trigger cut with real pulses can only be done if we know the exact time of the energy deposit in the crystal. Access to this piece of information is impossible in this work using either the neutron source or the intrinsic calibration peaks of the germanium as in both cases they follow intrinsically stochastic process of radioactive decay. However, the use of controlled source of particles, such as a controlled pulsing LED or a pulsed neutron source are envisioned.

7.6 Efficiency correction

The objective of all the analysis cuts is to prune any events with bad energy reconstruction. However, in this process, the majority of the initial experimental events are discarded. This observation is also applicable to the pre-processing trigger. In the end, only a fraction of all the recoils in the germanium crystal do trigger and satisfy the analysis cuts. These remaining are counted and presented as the recoil energy spectra of the neutron background displayed in the figure 7.5. As to estimate the NR and ER background, it is necessary to estimate the initial number of recoils. This estimation is calculated by correcting the measured counts of NR and ER with the efficiency of the trigger and analysis cuts.

In the presented analysis, a cut is essentially a binary classification. This means that a cut classifies a given set of events into two groups. For example, the quality cut is a test which discriminates the events with evidences of good energy reconstruction from others. However, as all the cuts rely on estimators, the classification on an event by a analysis cut can differ from the actual status of the event. This leads to four possible combinations of the outcome of the cut and the actual condition on the tested event. The table 7.4 defines these four combinations.

The efficiency of a test is defined as the number of true positive events normalized by the number of tested events. However, the efficiency of an analysis cut shows a dependency with the recoil energy E_R and recoil type RT of the tested events. As such, the efficiency $\mathcal{F}$ is defined as a sequence with its kth element given by:

$$\mathcal{F}_k = \frac{N_k^{TP}(RT)}{N_k^{tot}(RT)} \tag{7.23}$$

with N_k^{TP}, the number of "True Positive" events in the kth bin in recoil energy E_R, and $N_k^{tot} = N_k^{TP} + N_k^{FP} + N_k^{FN} + N_k^{TN}$, the total number of events.

These counts of events are estimated with the pulse simulation. Indeed, contrary to the experimental events, the initial number of injected simulated events $N_k^{tot}(RT; simu.)$ is known for each of the recoil type RT: nuclear recoil are emulated with the "flat ER" population while the electronic recoils are emulated with the "flat ER" population. Similarly, with the application of the analysis cuts to the simulated events, the counts of true positive events $N_k^{TP}(RT; simu.)$ is measured.

One should note the important difference between the simulated pulses used to estimate the efficiency and the experimental pulses, with their counts corrected by this efficiency. For the experimental pulses, there is no direct access to the number of true positive events, but there rather is count $N_k^{cut}(RT; exp.)$ of all the events passing an analysis cut. As the data streams are long, the analysis is not limited by the statistic. Thus, the analysis cuts are parametrized with conservative 2σ tolerances. With this parametrization, it is expected to have a very low count of false positive events at the cost of having very high count of false negative. As a result, for this analysis, it is assumed that the count of false positive events is negligible:

$$N_k^{cut}(RT; exp.) = N_k^{TP}(RT; exp.) + N_k^{FP}(RT; exp.) \approx N_k^{TP}(RT; exp.) \tag{7.24}$$

Consequently, the measured count $N_k^{cut}(RT; exp.)$ is an excellent estimator of the number of experimental true positive events $N_k^{TP}(RT; exp.)$.

The efficiency of the analysis cuts $\mathcal{F}$ is therefore estimated from the pulse simulation and used to estimate the initial number of experimental recoils $N_k^{tot}(RT; exp.)$ from the measured counts illustrated by the recoil energy spectra in figure 7.5. Independently from the binning, the initial number of experimental recoils is calculated in each kth bin in recoil energy E_R as:

$$N_k^{tot}(RT; exp.) = \mathcal{F}_k(band) \cdot N_k^{bulk}(RT; exp.) = \frac{N_k^{TP,band}(RT; simu)}{N_k^{tot}(RT; simu)} \cdot N_k^{band}(RT; exp.) \tag{7.25}$$

The figure 7.7 presents the efficiency $\mathcal{F}$ of each analysis cut for the ER and NR types and the two Background and Calibration configurations. The binning in used is parametrized by the bins edges b_i:

$$\begin{cases} b_i & = b_{i-1} + 2 \cdot \max\left(\sigma^s_{E_{heat}}(b_i)\right)_{s \in streams} \\ b_0 & = 0\,\text{keV} \end{cases} \tag{7.26}$$

with $\left(\sigma^s_{E_{heat}}(b_i)\right)_{s \in streams}$ the heat resolution of each streams. With this parametrization of the binning, the width W_k of the kth bin is expressed:

$$W_k = b_{k+1} - b_k \tag{7.27}$$

The "No cut" is plotted as a reference cut accepting all the events and has an efficiency of $\mathcal{F} = 1$ in each bin by definition. The considered band cut depends on the recoil type of the

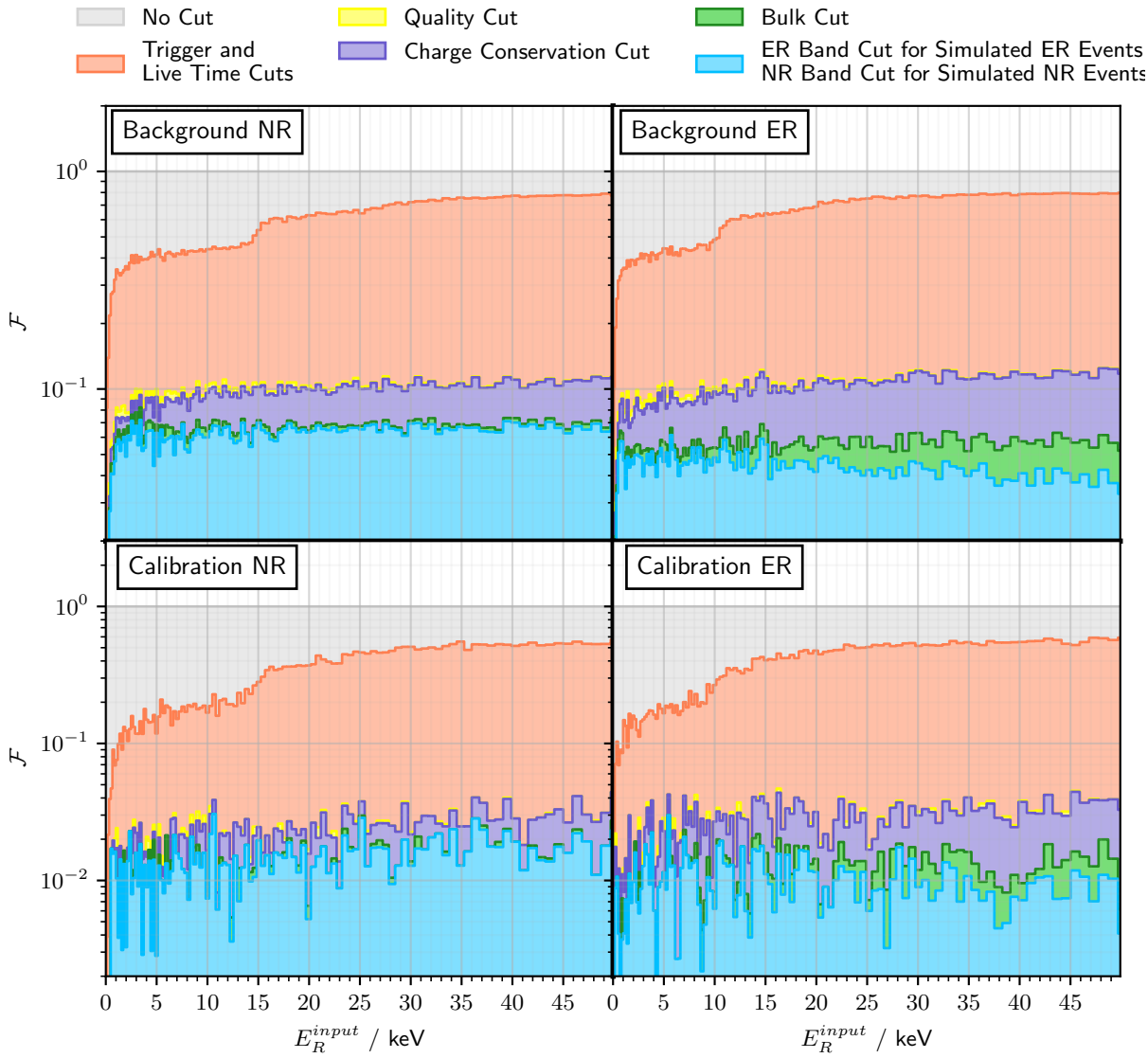

Figure 7.7: Efficiency $\mathcal{F}$ of the analysis cuts applied on the simulated events as functions of their input recoil energy E_R^{input}. Each subplot corresponds to one of the two Background and Calibration configurations and either the "flat NR" or "flat ER" simulated events. For the "flat NR" events, the NR band cut is drawn. For the "flat ER" events, the ER band cut is displayed.

events: the counts of ER is estimated with the ER band cut while the counts of NR recoils is estimated using the NR band cut. While the efficiencies associated with all the analysis cuts are plotted, the main efficiency used in the efficiency correction equation 7.25 is the efficiency of the band cut $\mathcal{F}_k(band)$.

The Background configuration displays higher band cut efficiency $\mathcal{F}_k(band)$ than the Calibration configuration for both the ER and NR. The Background configuration features an efficiency of about 6 % for the nuclear recoils and about 4 % for the electronic recoils. For the Calibration, the efficiencies are about 1 % for the NR events and 0.8 % for the ER events. This means that this few percent of the initial recoils in the crystal of RED80 induced an event that triggered and passed all the analysis cuts. We can diagnose the successive pruning of the events by studying the efficiency of the previous cuts.

The trigger cut is presented in section 7.5. The efficiency drop of the trigger cut at the lowest energies $\mathcal{O}(1\,\text{keV})$ is explained mainly by events not reaching the amplitude threshold. However, with few tens of percent of discarded events on the whole energy range, the trigger cut prove that a sufficient amplitude is not enough to triggered upon. Event discarded by the trigger cut can be explained by the screening of the low energy events by events of higher energies. Indeed, the pre-processing parametrization imposes that for events closer than 0.5 s, only the event of higher amplitude is triggered upon. This observation holds on the whole energy range as the trigger cut efficiency is monotonically increasing. Additionally, one can note the sudden increase in efficiency at about 10 keV for the ER and 15 keV for the NR. This feature can be linked to 10.37 keV calibration peak of the germanium crystal. Indeed, the crystal of RED80 is neutron-activated resulting in a high rate of 10.37 keV electronic recoils. These events are screening the events of heat energy $E_{heat} < 10.37\,\text{keV}_{ee}$. This heat energy readily corresponds to a recoil energy of $E_R = 10.37\,\text{keV}$ for the ER events. For the NR events, the corresponding energy is obtained through the expression of the heat energy E_{heat} as a function of the recoil energy E_R and the quenching Q_{NR} for a nuclear recoil in the equation 7.11:

$$E_{heat} = 10.37\,\text{keV}_{ee} = E_R \cdot \frac{1 + Q_{NR}\left(E_R\right)\frac{V_{bias}}{\epsilon_{e^- - h^+}}}{1 + \frac{V_{bias}}{\epsilon_{e^- - h^+}}} \cdot E_R \quad \Rightarrow \quad E_R = 14.82\,\text{keV} \tag{7.28}$$

The Lindhard quenching model is applied to estimate the value of Q_{NR}. The equation is numerically resolved, yielding the recoil energy $E_R = 14.82\,\text{keV}$. This value is indeed consistent with the energy of the sudden increase in efficiency.

All-in-all, the asymptotic efficiency of the trigger cut is about 80 % for the Background configuration. This observation is symptomatic from an above-ground experiment with reduced shielding and subject to the natural radioactivity and cosmic rays inducing a relatively high rate of event in the detectors. As for the Calibration configuration, this asymptotic efficiency is even lower 50 %. Indeed, with the neutron source facing the detector, the event rate is boosted by the intense rate of nuclear recoils.

The quality cut, defined in section 6.2.5, discards the events showing evidence of problematic energy reconstruction. The efficiency drops to approximately 10 % for the Background configuration and 10 % for the Calibration configuration. We also note that the increasing step for the trigger cut efficiency caused by the 10.37 keV calibration events has vanished. This is explained by considering that all the events presenting a pile-up effect (usually with a 10.37 keV calibration ER event) were discarded by the quality cuts. As the total event rate is higher for the Calibration configuration, the pile-up effect is affecting more events and thus the quality cuts are pruning more than for the Background configuration.

The charge conservation cut effect seems marginal for both recoil types and the two neutron source configurations. As discussed in section 6.2.8, there is no concrete evidence of event population not satisfying the electric charge conservation. As such, only events with outlying charge

conservation energy E_{CC} are discarded.

The bulk cut then comes into play and have a significant effect on all the energy range for each combination of recoil type and configuration. As defined in section 6.2.9, this cut selects the events not generating a signal on the guard electrodes A and C with inducing recoil in the bulk region of RED80 crystal. As such, the efficiency of the bulk cut should be proportional to the fiducial volume of RED80. This assumption could be verified by running a scan on the voltage bias V_{bias} of RED80, this affecting the fiducial volume as demonstrated in Chapter 5, and computing the efficiency for each point.

Finally, the band cut, defined in section 7.3.5, seems to discard a negligible fraction of the events. This is to be associated with the figure 7.4: a majority of the events are allocated to either the ER or NR bands, with only a few events kept out.

7.7 Band Contamination Correction

The objective of this section is to correct the counting issue induced by the ER, NR and HO bands overlapping at low energy. This phenomenon is visible on the plots displayed in the figure 7.4. Events in these overlapping areas are attributed to multiple bands and are counted multiple times, hence introducing a significant bias on the recoil energy spectra $N_k^{band}(RT; exp.)$ and the initial number of recoils $N_k^{tot}(RT; exp.)$. With the use of the pulse simulation, it is possible to estimate the contamination rate of the bands into one another.

The most rigorous but resource-intensive method would be to model the distribution of the ER, NR and HO events in term of ionization and heat energy and compute the likelihood function associated to each event. However, given the short time frame induced by the advancement of the RICOCHET experiment proposal, it was decided to correct the measurements using quicker binned statistics on the recoil energy spectra. While this latter method effectiveness is heavily affected by the choice of the binning, the induced biases are small and so it constitutes a very good approximation of the more rigorous likelihood method. The binning in use for this correction is the same as previously defined from its bin edges in equation 7.26.

This binned analysis is based on the knowledge of the shape of electronic recoil background affecting the detector RED80. Indeed, at the considered energy range, the germanium crystal is only subject to three possible sources of electronic recoils. Two of these sources corresponds to the 1.3 keV and 10.37 keV calibration peaks. The other source comes from the Compton scattering processes which is modeled by electronic recoils of uniform distribution in recoil energy, such as the simulated "flat ER" events. It is now possible to produce an empirical model of the recoil energy spectrum created by the electronic recoils. Its value in the kth bin for events passing analysis cut is noted $N_k^{cut}(Config.; ERmodel)$ for the two $Config.$ being Background or Calibration. This model has three empirical components based on the energy spectra of the simulated ER events: the flat ER events $N_k^{cut}(Config.; flatER)$, the 1.3 keV line events $N_k^{cut}(Config.; 1.3\,\text{keV}line)$ and the 10.37 keV line events $N_k^{cut}(Config.; 10.37\,\text{keV}line)$. Each model components $H_k^{cut}(Config.; simu.)$ is the recoil energy spectrum $N_k^{cut}(Config.; simu.)$ of a simulated population $simu. \in \{flatER, 1.3\,\text{keV}line, 10.37\,\text{keV}line\}$ normalized by the total number of simulated events $N_{tot}(simu.)$ of the population.

The ER background model $N_k^{cut}(Config.; ERmodel)$ is a linear combination of the three components $H_k^{cut}(Config.; simu.)$. For a configuration $Config.$, in the kth bin in recoil energy, the counts of events attributed to the ER background model and passing an analysis cut is expressed

		Model Component Factors $N(Config.;simu.)$		
		Compton Scattering, Flat ER events	1.3 keV peak	10.37 keV peak
Configuration	Background	9808	25289	214840
	Calibration	65943	65158	535453

Table 7.5: Best fitting parameters $N(Config.;simu.)$ for the adjustment of the ER Background model for the neutron source configuration. The graphical representation of the adjustment is presented in figure 7.8.

as:

$$\begin{aligned} N_k^{cut}(Config.;ERmodel) = & N(Config.;flatER)\cdot H_k^{cut}(Config.;flatER) \\ & + N(Config.;1.3\,\text{keV}line)\cdot H_k^{cut}(Config.;1.3\,\text{keV}line) \\ & + N(Config.;10.37\,\text{keV}line)\cdot H_k^{cut}(Config.;10.37\,\text{keV}line) \end{aligned} \quad (7.29)$$

with each factor $N(Config.;simu.)$ being a constant. With the chosen normalization of the components, the factors $N(Config.;simu.)$ are interpreted as the initial number of electronic recoils generated by the $simu.$ source, with $flatER$ corresponding to the Compton scattering processes.

These factors are unknown and are estimated by adjusting the ER background model to the experimental estimation of the ER background. These experimental data consist in the recoil energy spectra $N_k^{ERband}(Config.;exp.)$ of the events passing the ER band cut presented in the figure 7.5. An issue with this experimental estimation is the overlapping of the ER band cut with the NR and HO band cuts at low energy. This overlapping induces counting of nuclear and heat-only events thus biasing the estimation of the ER background. Moreover, at the lowest energies, the noise blob is passing the ER band cut. This noise blob feature is not taken into account in the ER background model and should not be used for the adjustment. The counter is to consider the events which satisfy only the ER band cut and that are discarded by the NR and HO band cuts. This condition is denominated "ER Band only" and expressed mathematically as:

$$(\text{ER Band only}) = (\text{ER Band Cut}) \text{ and not } (\text{NR Band Cut}) \text{ and not } (\text{HO Band Cut}) \quad (7.30)$$

The energy spectra formed by the experimental "ER Band only" events does not count the noise blob and has minimal contamination from nuclear recoils and heat-only events.

For each configuration, the ER background model satisfying the "ER Band Only" condition $N_k^{(\text{ER Band only})}(Config.;ERmodel)$ is adjusted to the experimental energy spectra$N_k^{(\text{ER Band only})}(Config.;exp.)$ using a minimization of the χ^2 between these functions of the recoil energy E_R. The best fitting parameters $N(Config.;simu.)$ are listed in the table 7.5.

This adjustment is graphically presented by the left subplots of the figure 7.8. The top plots corresponds to the Background configuration while the bottom plots corresponds to the Calibration configuration. Each of the left subplots display the experimental histogram, the adjusted histogram from the ER background model and the three components of this model as illustration.

The two right subplots display the two recoil energy spectra. The histograms denominated "NR band contamination" are formed by counting the events from the ER background model which passed the NR band cut $N_k^{\text{NR Band}}(\text{Config.};\text{ER model})$. As such, it is an estimation of the bias affecting the measurement of recoil energy spectra of the nuclear background presented in the figure 7.5. The terms of the corrected energy spectra associated with the NR and ER are

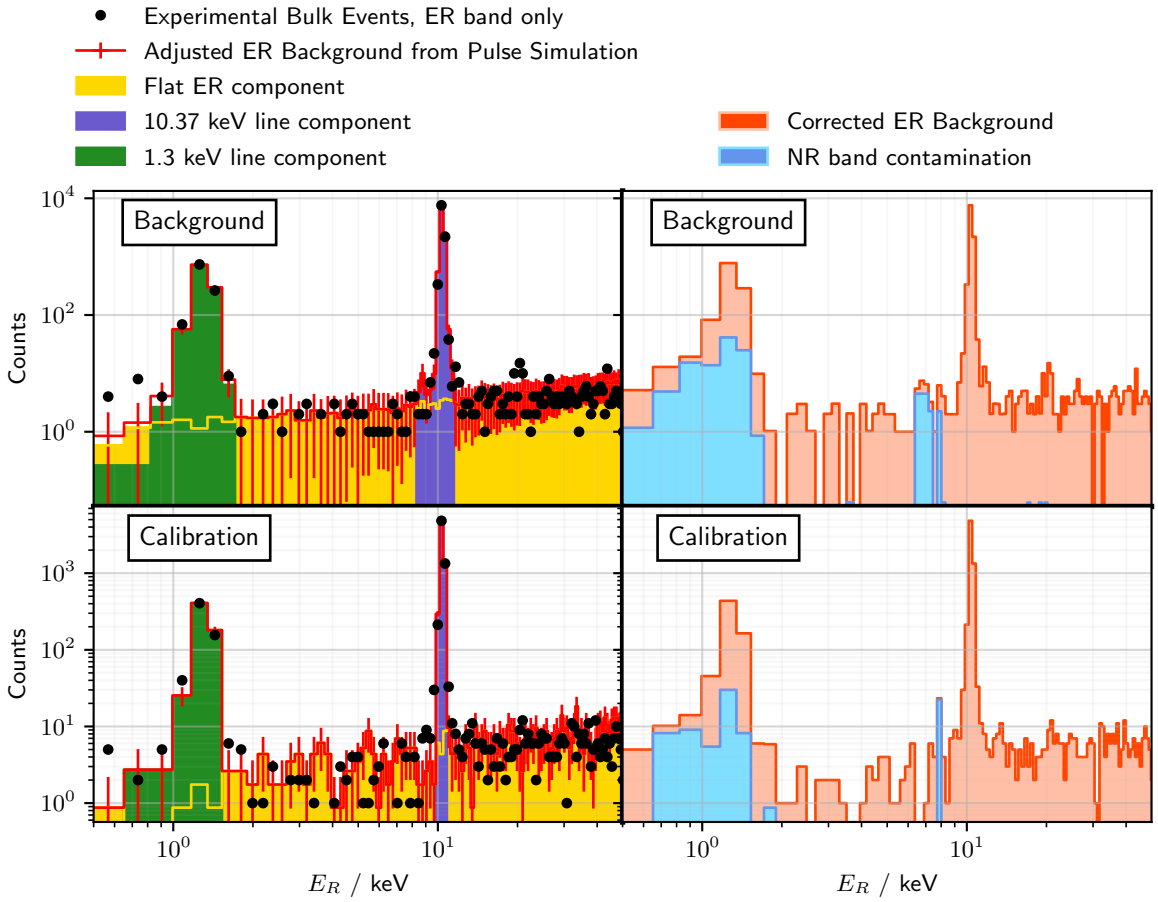

Figure 7.8: Adjustment of the ER background with the pulse simulation for the Background and Calibration configurations. The left subplots compares the histogram of experimental bulk events passing the ER band cut only with the simulated ER background model and its three components. The best fitting parameters are listed in the table 7.5. The right subplots display the counts of ER events contaminating the NR band and the corrected ER background corrected from the contamination.

expressed in the kth bin as:

$$N_k^{\text{NR band, corr.}}(\text{Config.}; exp.) = N_k^{\text{NR band}}(\text{Config.}; exp.) - N_k^{\text{NR Band}}(\text{Config.}; \text{ER model}) \quad (7.31)$$

$$N_k^{\text{ER band, corr.}}(\text{Config.}; exp.) = N_k^{\text{ER band only}}(\text{Config.}; exp.) + N_k^{\text{NR Band}}(\text{Config.}; \text{ER model}) \quad (7.32)$$

The correction of the experimental ER Background $N_k^{\text{ER band, corr.}}(\text{Config.}; exp.)$ is illustrated as the other histogram.

It appears that the contamination of the neutron band occurs mainly near the calibration peaks. The contamination at recoil energy $E_R \approx 8\,\text{keV}$ can be explained by 10.37 keV calibration electronic recoils with incomplete charge collection. The contamination at lower energy range corresponds to some 1.3 keV event population satisfying the NR band cut. This is consistent with and was expected from the observation of the Q versus E_R plots of figure 7.4 for the experimental data and figure 7.6 for the pulse simulation.

Following the discussion on the calibration peaks of the germanium presented in the section 2.3.4, we can actually estimate the electron capture ratio P_L/P_K associated with the 1.3 keV and 10.37 keV peaks, from the and K shells of ^{71}Ge respectively. The number of recoils produced by these peaks in the crystal of RED80 is estimated by to the best fitting parameters $N(Config.; simu.)$ presented in the table 7.5. The ratios $R_{calib.}(\text{Config.})$ between the two peak are:

$$\frac{P_L}{P_K}(\text{Background}) = \frac{N(\text{Background; 1.3 keV line})}{N(\text{Background; 10.37 keV line})} = \frac{25289}{214840} = 0.1177 \pm 0.0008 \quad (7.33)$$

$$\frac{P_L}{P_K}(\text{Calibration}) = \frac{N(\text{Calibration; 1.3 keV line})}{N(\text{Calibration; 10.37 keV line})} = \frac{65158}{535453} = 0.1217 \pm 0.0005 \quad (7.34)$$

with the 1σ statistical uncertainty assuming a Poisson statistic for the parameters $N(Config.; simu.)$. The most up-to-date measurement of the electron capture ratio is $P_L/P_K = 0.117 \pm 0.001$ [11]. The difference between this reference value and the two estimation can be explained by systematic uncertainties. As such, the agreement with our measurement is excellent. The replication of this result validates our methodology for the measurement of the electronic and neutron backgrounds.

7.8 Normalization of the energy spectra

From experimental data taken with the detector RED80 over a time span of several days, and with a proper processing and analysis of this data, we were able to estimate the number of electronic recoils and nuclear recoils that happened in the detector. The amount of recoils does depend on the nuclear and electronic background associated with the experimental setup which we want to measure. Yet, it is also proportional to the exposure of the detector as well as the bin width considered for the analysis.

The exposure $\mathcal{E}(Config.)$ is expressed in kg · d. Its roles is to normalize the event counts in respect to the live time T_{live} and the mass $m_{Ge} = 0.038\,\text{kg}$ of the RED80 detector:

$$\mathcal{E}(Config.) = T_{live}(Config.) \cdot m_{Ge} \quad (7.35)$$

The live time T_{live} corresponds to the duration during which the detector is correctly operating and recording data. For both the Background and the Calibration configurations, the live times are calculated in the table 7.2.

The presentation of the measurement of the neutron and electronic backgrounds is done with the daily event rate $\mathcal{R}$. This quantity is expressed in events/kg/keV/d. Its value in the kth energy bin for the configuration $Config. \in \{\text{Background, Calibration}\}$ and the recoil type

$RT \in \{ER, NR\}$ is expressed as:

$$\mathcal{R}_k(Config., RT) = \frac{N_k^{tot}(Config., RT; exp.)}{\mathcal{E}(Config.) \cdot W_k} \tag{7.36}$$

$$= \frac{\mathcal{F}_k \cdot N_k^{band}(Config., RT; exp.)}{m_{Ge} \cdot T_{live}(Config.) \cdot W_k} \tag{7.37}$$

using the efficiency correction equation 7.25, the detector exposure in equation 7.35 and the bin width W_k expressed in equation 7.26;

The figure 7.9 presents the NR and ER backgrounds for the two neutron source configurations as daily event rate $\mathcal{R}_k(Config., RT)$. The main results of this section concern the estimation of the NR backgrounds. We see that the NR event rate of the Calibration is about 50 times higher than for the Background configuration. The reference value is the NR event rate level at the lowest energies, which is about 1×10^6 events/kg/keV/d for the Calibration and 1×10^4 for the Background. This is consistent with the presence of the neutron source facing the detector RED80 inducing a high neutron flux in the cryostat and creating a heightened nuclear recoil rate.

Both measured neutron backgrounds are adjusted with a background model derived from the kinematic recoil properties. The daily event rate histograms are modeled with the functions:

$$\mathcal{R}_k(\text{Background, NR model}) = \mathcal{R}_0(\text{Background}) \cdot \exp\left(-\frac{(b_{k+1} + b_k)}{2 \cdot E_{cap}}\right) \tag{7.38}$$

$$\mathcal{R}_k(\text{Calibration, NR model}) = \mathcal{R}_0(\text{Calibration}) \cdot \exp\left(-\frac{(b_{k+1} + b_k)}{2 \cdot E_{cap}}\right) \tag{7.39}$$

with the expression $(b_{k+1} - b_k)/2$ corresponding to the center of the kth bin in recoil energy. This model of the NR background is parametrized with the three unknown $\mathcal{R}_0(\text{Background})$, $\mathcal{R}_0(\text{Calibration})$ and E_{cap}. The model is adjusted to the experimental NR backgrounds with χ^2 minimization considering a Poisson error on each points. The best fitting parameters are:

$$\begin{cases} \mathcal{R}_0(\text{Background}) & = 1.22 \times 10^4 \,\text{events/kg/keV/d} \\ \mathcal{R}_0(\text{Calibration}) & = 5.58 \times 10^5 \,\text{events/kg/keV/d} \\ E_{cap} & = 6.88 \,\text{keV} \end{cases} \tag{7.40}$$

Both event rates distributions seems to corresponds to the kinematic recoil distribution expected from MeV-scale fast neutrons.

The ER backgrounds are plotted for illustration and crosscheck. Indeed, we see that the amplitude of the calibration peaks is approximately the same for both configurations. This means that the rate of two calibration electronic recoil peaks is the same between the Background and Calibration configuration. As such, it confirms that the entire analysis processed the Background and the Calibration streams similarly.

We can note that the flat Compton background is globally higher for the Calibration compared to the Background. This can be explained by the higher neutron flux which produces gamma rays by interacting with the lead shield of the cryostat, and the gammas emitted by the AmBe source.

Comparing the nuclear recoil background and the electronic recoil background, we see that the NR background is predominant over the Compton background from $\mathcal{O}(10\,\text{keV})$ in the Background configuration. This means that at higher energies, the main component of the energy spectrum is the Compton background, which is typically observed in the past Direct Dark Matter searches. However, the neutron background is becoming the main component of the energy spectrum at lower energy. This means that by improving their energy resolution, the Direct

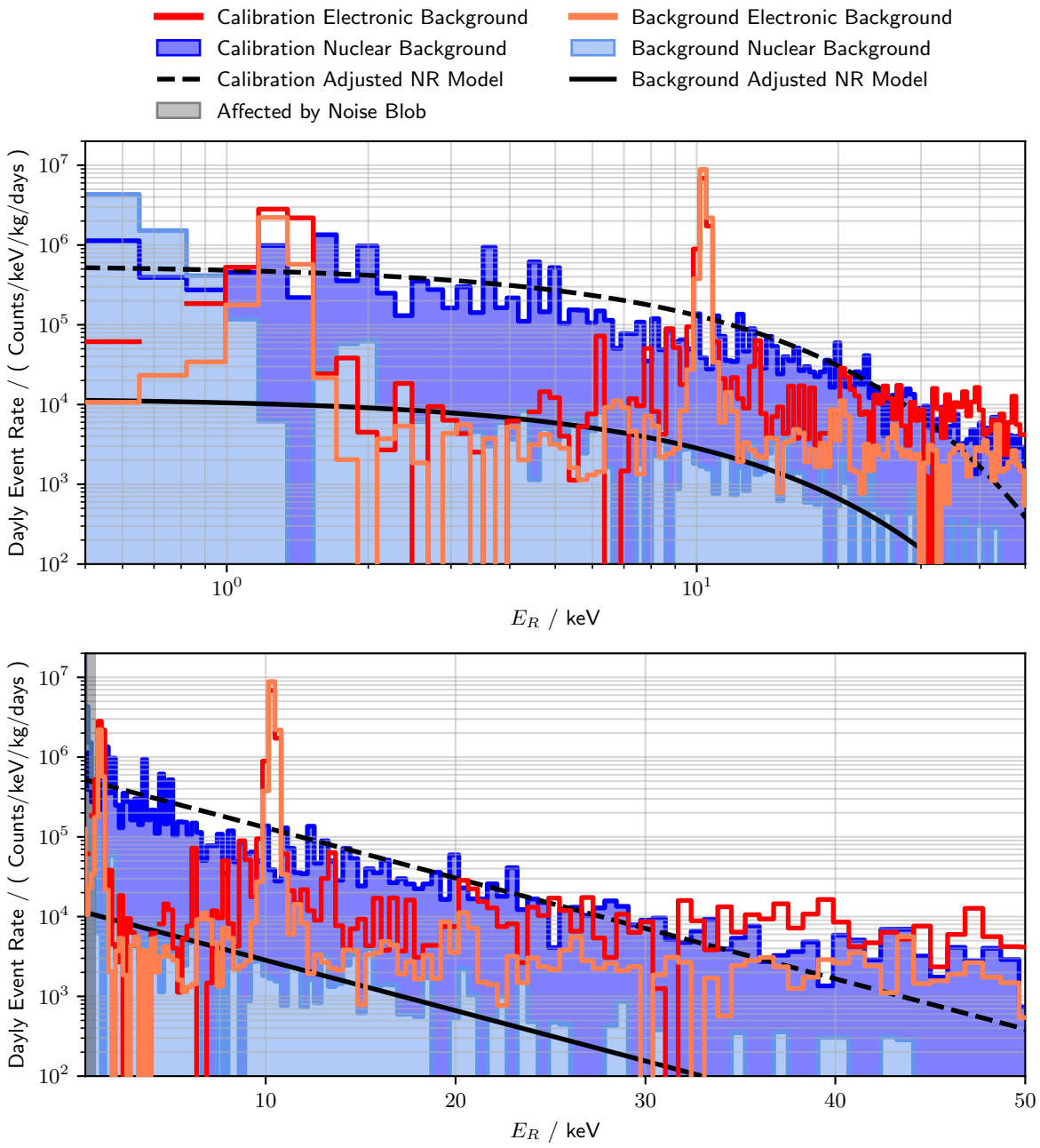

Figure 7.9: Neutron and electronic recoil backgrounds expressed as daily event rate $\mathcal{R}_k(Config., RT)$ for the Background and Calibration configurations. Both plots displays the same curves with a logarithmic energy scale on top and a linear energy scale at the bottom. The shaded energy range for $E_R < 1$ keV is discarded from integration as being affected by the noise blob.

Dark Matter experiments should now be prepared for this new NR background and adapt their shielding.

7.9 Measurement of the ILL neutron background

The neutron background measurements at the IP2I cryostat with the RED80 germanium detector are used to extrapolate the neutron background that will affect the CryoCube array of germanium detectors in the RICOCHET cryostat next to the nuclear reactor of the ILL. The observation of the measured neutron and ER background in figure 7.9 confirms that neutron is the most detrimental for the measure of the CENNS done at low energy. As such, an estimation of this neutron background at the ILL site is vital for the RICOCHET experiment.

While the neutron background was measured at the ILL with helium tube detectors with multiple nuclear reactor activities, this technology is only sensitive to energies higher than $\mathcal{O}(100\,\text{keV})$. A way to link the neutron background at high energy with the neutron background at low energy is to measure the same neutron background with the two technologies of detectors. This reference neutron background measurement is made at the IP2I cryostat facility with RED80 and is displayed in the figure 7.9. Measurements at high energies were taken with the helium tube detector in place of the cryostat, with the two same position of the neutron source, leading to the two Calibration and Background configuration. The comparison of the high and low energy spectra should be relative between the Calibration and the Background configurations. For this, we use the nuclear recoil event rate of both configurations integrated over an energy span. The ratio $\mathcal{R}_{Ge}$ of the integration in the interval $[1-50]$ keV of the nuclear recoil energy spectra in Calibration and Background is:

$$\begin{cases} k_0 = \min\{k; b_k \leq 1\,\text{keV}\} \\ K = \max\{k; b_{k+1} \leq 50\,\text{keV}\} \\ \mathcal{R}_{Ge}^{exp.} = \sum_{k=k_0}^{K} \dfrac{\mathcal{R}_k(\text{Calibration, NR background})}{\mathcal{R}_k(\text{Background, NR background})} = \dfrac{2897511}{79546} = 36.4 \pm 0.2 \end{cases} \tag{7.41}$$

with b_k the left bin edge of the kth bin as defined in the system of equations 7.26, and calculating the 1σ statistical uncertainty assuming a Poisson statistic for each integrated rate. As the systematic uncertainties are not considered, the error on the ratio $\mathcal{R}_{Ge}^{exp.}$ is underestimated. In comparison, the ratio obtained by the helium tube detectors were:

$$\begin{aligned} \mathcal{R}_{Dubna3-He} &= 26.5 \pm 4.8 \\ \mathcal{R}_{Grenoble3-He} &= 34.5 \pm 0.5 \end{aligned} \tag{7.42}$$

As such, the fast background measurement between the cryogenic detector RED80 and the ^{3}He detector are compatible with the measurement at high energies. The STEREO experiment located at the future RICOCHET site has been removed in December 2020, hence opening the possibility to accurately estimate the expected fast neutron background in RICOCHET with the same ^{3}He detectors.

Conclusion and Prospects

This thesis is inscribed in the R&D program of the RICOCHET experiment for the precision measurement of the CENNS near the research nuclear reactor of the ILL. Its main goal was to develop a new generation of low-threshold cryogenic germanium detectors satisfying the specifications of the CryoCube detector array for RICOCHET. For this purpose, the heat and ionization channels of these cryogenic detectors were modeled and optimized based on experimental data collected from prototype detectors operated at the IP2I cryogenic facility.

This work first started with the study of the heat channel. An electro-thermal model of simple RED detectors was built. Its adjustment to experimental data is excellent and permitted the adoption of a new methodology for the characterization of new detectors. The study of their steady-state and heat response to a scattering particle can be reproduced with this model, thus constraining the thermal properties of the detector components, and in particular the GeNTD thermal sensor. Interestingly, the prototype detector RED10 showed a high 20 % proportion of athermal phonons, greatly contributing to the sensitivity of the detector and motivating further studies on the relaxation of phonons in the detector. The modelization of the heat channel helped to understand the propagation of the signal into the detector and highlighted the existence of an optimal polarization current for the NTD thermal sensor. The noise PSDs of two different readout electronics were also fitted with the electro-thermal model, hinting towards a low-frequency noise component limiting their performance. We also confirmed that the EDELWEISS electronics with cold electronics is affected by a lower noise level and should be used for the characterization of detectors and data collection. The projected energy resolution calculated from the electro-thermal model motivated the optimization of the heat channel with a lower germanium crystal mass. The most recent prototype detectors operated in the IP2I cryostat weights between 32 g and 38 g and can reliably reach heat energy resolutions inferior to 30 eV.

This thesis then greatly furthered the knowledge on the ionization channel of the cryogenic detectors. The modelization of the signal generation by the drift of the electric charge carriers in the semiconductor germanium crystal was built. Thanks to its matrix formalism, this model brought attention to the influence of the cabling capacitance of the ionization polarization and readout electronics. Indeed, in the current situation, with a dominating high cabling capacitance, the sensitivities of the electrodes are almost equals and are limited by their common high cabling capacitance of their electronics. With the new low-noise HEMT-based electronics which will be installed closer to the detectors at the 1 K stage, inside the RICOCHET cryostat, the cabling capacitance will no more dominate the capacitance of the detector electrodes and the ionization signal signatures will drastically change. This model of the ionization channel was validated and is now coupled to the electrostatic simulation of the detectors within the finite element calculation software COMSOL®. These simulations yield a precise estimation of the fiducial volume of the detectors and the electric capacitance of their electrodes. The optimization of the two detector designs PL38 and FID38 was realized by scanning over the various parameters within the simulation. The comparison between simulated performance and experimental results highlighted the limitations of the electrostatic simulation, which does not take into account the oblique propagation of the electrons in the germanium crystal or the charge trapping processes.

This final result of this work is the characterization of the neutron background at the IP2I cryogenic laboratory. Benefiting from the good heat and ionization performances of the detector RED80, a data collection lasting more than five days with intermittent calibration using a

neutron source was realized. The in-depth analysis of the data streams permitted to exploit the intrinsic discrimination between nuclear and electronic recoils within the semiconducting germanium crystal thanks to the double-energy measurement of the detector. Indeed, the electronic and neutronic components of the background were isolated which allowed to compute their associated event rate spectra. This measurement of the fast neutron background in the IP2I cryostat will be used to estimate the expected neutron background at ILL site. Being one of the major obstacle to the CENNS precision measurement, knowledge of the neutron background is invaluable to adapt the RICOCHET strategy.

In the end, this thesis positions itself as a solid foundation for the development of low-threshold cryogenic germanium detectors. The R&D program at the IP2I cryogenic facility is in continuation of this work with:

- the upgrade of the suspended tower for the mechanical decoupling solution of the CryoCube within the RICOCHET cryostat, soon to be tested at the IP2I laboratory,
- the study of the new low-noise HEMT-based electronics with low cabling capacitance,
- the characterization of the two new prototype detectors RED130 and RED140, assembled following the PL38 and FID38 designs, with first experimental results pointing towards excellent performance.

The RICOCHET collaboration is on the right tracks to build the CryoCube according to specifications, to measure with high accuracy the low-energy CENNS process at the ILL by 2024, and perhaps help to go beyond the Standard Model with new exotic physics.

Bibliography

[1] A. H. Abdelhameed et al. "First results from the CRESST-III low-mass dark matter program". In: *Phys. Rev.* D100.10 (2019), p. 102002. DOI: 10.1103/PhysRevD.100.102002. arXiv: 1904.00498 [astro-ph.CO].

[2] Khalifeh Abusaleem and Balraj Singh. "Nuclear Data Sheets for A = 71". In: *Nuclear Data Sheets* 112.1 (2011), pp. 133 –273. ISSN: 0090-3752. DOI: https://doi.org/10.1016/j.nds.2010.12.002. URL: http://www.sciencedirect.com/science/article/pii/S0090375210001213.

[3] R. Agnese et al. "Demonstration of Surface Electron Rejection with Interleaved Germanium Detectors for Dark Matter Searches". In: *Appl. Phys. Lett.* 103 (2013), p. 164105. DOI: 10.1063/1.4819835,10.1063/1.4826093. arXiv: 1305.2405 [physics.ins-det].

[4] G. Agnolet et al. "Background Studies for the MINER Coherent Neutrino Scattering Reactor Experiment". In: *Nucl. Instrum. Meth. A* 853 (2017), pp. 53–60. DOI: 10.1016/j.nima.2017.02.024. arXiv: 1609.02066 [physics.ins-det].

[5] M. Agostini et al. "Comprehensive geoneutrino analysis with Borexino". In: *Phys. Rev. D* 101 (1 2020), p. 012009. DOI: 10.1103/PhysRevD.101.012009. URL: https://link.aps.org/doi/10.1103/PhysRevD.101.012009.

[6] A. Aguilar-Arevalo et al. "Results of the engineering run of the Coherent Neutrino Nucleus Interaction Experiment (CONNIE)". In: *Journal of Instrumentation* 11.07 (2016), P07024–P07024. DOI: 10.1088/1748-0221/11/07/p07024. URL: https://doi.org/10.1088/1748-0221/11/07/p07024.

[7] D. Akimov et al. "Observation of coherent elastic neutrino-nucleus scattering". English. In: *Science* 357.6356 (Aug. 2017), pp. 1123–1126. DOI: 10.1126/science.aao0990. URL: http://www.sciencemag.org/lookup/doi/10.1126/science.aao0990.

[8] D.Yu. Akimov et al. "Status of the RED-100 experiment". In: *Journal of Instrumentation* 12.06 (2017), pp. C06018–C06018. DOI: 10.1088/1748-0221/12/06/c06018. URL: https://doi.org/10.1088/1748-0221/12/06/c06018.

[9] E. Armengaud et al. "Performance of the EDELWEISS-III experiment for direct dark matter searches". In: *JINST* 12.08 (2017), P08010. DOI: 10.1088/1748-0221/12/08/P08010. arXiv: 1706.01070 [physics.ins-det].

[10] E. Armengaud et al. "Searching for low-mass dark matter particles with a massive Ge bolometer operated above ground". In: *Phys. Rev. D* 99 (8 2019), p. 082003. DOI: 10.1103/PhysRevD.99.082003. URL: https://link.aps.org/doi/10.1103/PhysRevD.99.082003.

[11] W. Bambynek et al. "Orbital electron capture by the nucleus". In: *Rev. Mod. Phys.* 49 (1 1977), pp. 77–221. DOI: 10.1103/RevModPhys.49.77. URL: https://link.aps.org/doi/10.1103/RevModPhys.49.77.

[12] Randall F. Barron. "Cryogenic Systems, 2nd Edition, 1985". In: ().

[13] A. Bellerive et al. "The Sudbury Neutrino Observatory". In: *Nuclear Physics B* 908 (2016). Neutrino Oscillations: Celebrating the Nobel Prize in Physics 2015, pp. 30 –51. ISSN: 0550-3213. DOI: https://doi.org/10.1016/j.nuclphysb.2016.04.035. URL: http://www.sciencedirect.com/science/article/pii/S0550321316300736.

[14] G. Bellini et al. "Geo-neutrinos". In: *Progress in Particle and Nuclear Physics* 73 (2013), pp. 1 –34. ISSN: 0146-6410. DOI: https://doi.org/10.1016/j.ppnp.2013.07.001. URL: http://www.sciencedirect.com/science/article/pii/S0146641013000732.

[15] V. Belov et al. "The νGeN experiment at the Kalinin Nuclear Power Plant". In: *JINST* 10.12 (2015), P12011. DOI: 10.1088/1748-0221/10/12/P12011.

[16] A. Benoit et al. "Measurement of the response of heat-and-ionization germanium detectors to nuclear recoils". In: *Nucl. Instrum. Meth. A* 577 (2007), pp. 558–568. DOI: 10.1016/j.nima.2007.04.118. arXiv: astro-ph/0607502.

[17] J. Billard et al. "Characterization and Optimization of EDELWEISS-III FID800 Heat Signals". In: *J. Low Temp. Phys.* 184.1-2 (2016). Ed. by Philippe Camus, Alexandre Juillard, and Alessandro Monfardini, pp. 299–307. DOI: 10.1007/s10909-016-1500-5.

[18] J. Billard et al. "Coherent Neutrino Scattering with Low Temperature Bolometers at Chooz Reactor Complex". In: *J. Phys. G* 44.10 (2017), p. 105101. DOI: 10.1088/1361-6471/aa83d0. arXiv: 1612.09035 [physics.ins-det].

[19] Julien Billard. "Détection directionnelle de matière sombre avec MIMAC". Thèse de doctorat dirigée par Mayet, Frédéric Physique Grenoble 2012. PhD thesis. 2012. URL: http://www.theses.fr/2012GRENY036.

[20] Julien Billard. "Searching for Dark Matter and New Physics in the Neutrino sector with Cryogenic detectors". PhD thesis. Université Lyon 1, 2020.

[21] Julien Billard, Joseph Johnston, and Bradley J. Kavanagh. "Prospects for exploring New Physics in Coherent Elastic Neutrino-Nucleus Scattering". In: *JCAP* 11 (2018), p. 016. DOI: 10.1088/1475-7516/2018/11/016. arXiv: 1805.01798 [hep-ph].

[22] A. Broniatowski. "Intervalley Scattering of Hot Electrons in Germanium at Millikelvin Temperatures". In: *Journal of Low Temperature Physics* 176.5 (2014), pp. 860–869. ISSN: 1573-7357. DOI: 10.1007/s10909-014-1091-y. URL: https://doi.org/10.1007/s10909-014-1091-y.

[23] Matteo Cadeddu and Francesca Dordei. "Reinterpreting the weak mixing angle from atomic parity violation in view of the Cs neutron rms radius measurement from COHERENT". In: *Phys. Rev. D* 99.3 (2019), p. 033010. DOI: 10.1103/PhysRevD.99.033010. arXiv: 1808.10202 [hep-ph].

[24] D. B. Chitwood et al. "Improved Measurement of the Positive-Muon Lifetime and Determination of the Fermi Constant". In: *Phys. Rev. Lett.* 99 (3 2007), p. 032001. DOI: 10.1103/PhysRevLett.99.032001. URL: https://link.aps.org/doi/10.1103/PhysRevLett.99.032001.

[25] D. D'Angelo et al. "Recent Borexino results and prospects for the near future". In: *EPJ Web Conf.* 126 (2016). Ed. by Larisa Bravina, Yiota Foka, and Sonja Kabana, p. 02008. DOI: 10.1051/epjconf/201612602008. arXiv: 1405.7919 [hep-ex].

[26] C. Enss, ed. *Cryogenic particle detection*. Vol. 99. Topics in applied physics. Berlin, Germany: Springer, 2005.

[27] Enectali Figueroa-Feliciano. "Complex microcalorimeter models and their application to position-sensitive detectors". In: *Journal of Applied Physics* 99 (2006), pp. 114513 –114513. DOI: 10.1063/1.2191449.

[28] Daniel Foreman-Mackey et al. "emcee: The MCMC Hammer". In: *Publications of the Astronomical Society of the Pacific* 125.925 (2013), p. 306. DOI: 10.1086/670067. arXiv: 1202.3665 [astro-ph.IM].

[29] Daniel Z. Freedman. "Coherent Neutrino Nucleus Scattering as a Probe of the Weak Neutral Current". In: *Phys. Rev. D* 9 (1974), pp. 1389–1392. DOI: 10.1103/PhysRevD.9.1389.

[30] M. Galeazzi and D. McCammon. "A microcalorimeter and bolometer model". In: *J. Appl. Phys.* 93 (2003), p. 4856. DOI: 10.1063/1.1559000. arXiv: astro-ph/0304397.

[31] Michael Hayes. *Lcapy*. 2020. URL: https://github.com/mph-/lcapy.

[32] COMSOL Inc. *COMSOL*. 2020. URL: http://www.comsol.com/products/multiphysics/.

[33] Ioffe Physico-Technical Institute. *New Semiconductor Materials. Characteristics and Properties*. [Online; accessed 19-December-2020]. 2020. URL: http://www.ioffe.ru/SVA/.

[34] M Scharff J Lindhard V Nielsen. "INTEGRAL EQUATIONS GOVERNING RADIATION EFFECTS". In: *Mat. Fys. Medd. Dan. Vid. Selsk. 33,no. 10* (1963).

[35] A. Juillard et al. "Low-noise HEMTs for Coherent Elastic Neutrino Scattering and Low-Mass Dark Matter Cryogenic Semiconductor Detectors". In: *18th International Workshop on Low Temperature Detectors (LTD 18) Milano, Italy, July 22-26, 2019*. 2019. DOI: 10.1007/s10909-019-02269-5. arXiv: 1909.02879 [physics.ins-det].

[36] Alexandre Juillard. "Résolution dans des bolomètres équipés de couches minces d'isolant d'Anderson pour des événements impliquant des reculs de noyaux". Theses. Université Paris Sud - Paris XI, 1999. URL: https://tel.archives-ouvertes.fr/tel-00002707.

[37] Manfred Lindner, Werner Rodejohann, and Xun-Jie Xu. "Coherent neutrino-nucleus scattering and new neutrino interactions". In: *Journal of High Energy Physics* 2017.3 (2017), p. 97. ISSN: 1029-8479. DOI: 10.1007/JHEP03(2017)097. URL: https://doi.org/10.1007/JHEP03(2017)097.

[38] P. N. Luke. "Voltage-assisted calorimetric ionization detector". In: *J. Appl. Phys.* 64.6858 (1988), p. 6858. DOI: 10.1063/1.341976.

[39] R. Maisonobe et al. "Vibration decoupling system for massive bolometers in dry cryostats". In: *JINST* 13.08 (2018), T08009. DOI: 10.1088/1748-0221/13/08/T08009. arXiv: 1803.03463 [physics.ins-det].

[40] Stefanos Marnieros. "Détecteurs cryogéniques et leurs applications en Astrophysique et Astroparticules". PhD thesis. Université Paris Sud, 2014.

[41] John C. Mather. "Bolometer noise: nonequilibrium theory". In: *Appl. Opt.* 21.6 (1982), pp. 1125–1129. DOI: 10.1364/AO.21.001125. URL: http://ao.osa.org/abstract.cfm?URI=ao-21-6-1125.

[42] S. Mathimalar et al. "Characterization of neutron transmutation doped (NTD) Ge for low temperature sensor development". In: *Nucl. Instrum. Meth.* B345 (2015), pp. 33–36. DOI: 10.1016/j.nimb.2014.12.020. arXiv: 1410.3934 [physics.ins-det].

[43] C.D. Motchenbacher, I.A. Connelly, and J.A. Connelly. *Low-Noise Electronic System Design*. A Wiley-Interscience publication. Wiley, 1993. ISBN: 9780471577423. URL: https://books.google.fr/books?id=VhkoAQAAMAAJ.

[44] B.S. Neganov and V.N. Trofimov. "Colorimetric method measuring ionizing radiation". In: *Otkryt. Izobret.* 146 (1985), p. 215.

[45] E. Olivieri et al. "Vibrations on pulse tube based Dry Dilution Refrigerators for low noise measurements". In: *Nucl. Instrum. Meth. A* 858 (2017), pp. 73–79. DOI: 10.1016/j.nima.2017.03.045. arXiv: 1703.08957 [physics.ins-det].

[46] C. Patrignani et al. "Review of Particle Physics". In: *Chin. Phys. C* 40.10 (2016), p. 100001. DOI: 10.1088/1674-1137/40/10/100001.

[47] Matt Pyle, Enectali Feliciano-Figueroa, and Bernard Sadoulet. "Optimized Designs for Very Low Temperature Massive Calorimeters". In: (Mar. 2015). arXiv: 1503.01200 [astro-ph.IM].

[48] Simon Ramo. "Currents induced by electron motion". In: *Proc. Ire.* 27 (1939), pp. 584–585. DOI: 10.1109/JRPROC.1939.228757.

[49] Mariia Redchuk et al. "Comprehensive measurement of pp-chain solar neutrinos with Borexino". In: *PoS* EPS-HEP2019 (2020), p. 400. DOI: 10.22323/1.364.0400.

[50] Marco Rovitto. "Electromigration Reliability Issue in Interconnects for Three-Dimensional Integration Technologies". PhD thesis. Technischen Universitat Wien, 2016. URL: https://www.iue.tuwien.ac.at/phd/rovitto/.

[51] Kate Scholberg. "Coherent elastic neutrino-nucleus scattering". In: *Journal of Physics: Conference Series* 606 (2015), p. 012010. DOI: 10.1088/1742-6596/606/1/012010. URL: https://doi.org/10.1088/1742-6596/606/1/012010.

[52] M. Schumann. "Direct Detection of WIMP Dark Matter: Concepts and Status". In: *J. Phys.* G46.10 (2019), p. 103003. DOI: 10.1088/1361-6471/ab2ea5. arXiv: 1903.03026 [astro-ph.CO].

[53] W. Shockley. "Currents to conductors induced by a moving point charge". In: *J. Appl. Phys.* 9.10 (1938), pp. 635–636. DOI: 10.1063/1.1710367.

[54] A.K. Soma et al. "Characterization and performance of germanium detectors with sub-keV sensitivities for neutrino and dark matter experiments". In: *Nuclear Instruments and Methods in Physics Research Section A: Accelerators, Spectrometers, Detectors and Associated Equipment* 836 (2016), pp. 67 –82. ISSN: 0168-9002. DOI: https://doi.org/10.1016/j.nima.2016.08.044. URL: http://www.sciencedirect.com/science/article/pii/S0168900216308622.

[55] R. Strauss et al. "The ν-cleus experiment: a gram-scale fiducial-volume cryogenic detector for the first detection of coherent neutrino–nucleus scattering". In: *Eur. Phys. J. C* 77.8 (2017). ISSN: 1434-6052. DOI: 10.1140/epjc/s10052-017-5068-2. eprint: 1704.04320. URL: http://dx.doi.org/10.1140/epjc/s10052-017-5068-2.

[56] A.C. Thompson. *X-ray Data Booklet*. Lawrence Berkeley National Laboratory, University of California, 2001. URL: https://books.google.fr/books?id=WV05HAAACAAJ.

[57] A.N. W et al. *Solid State Physics*. HRW international editions. Holt, Rinehart and Winston, 1976. ISBN: 9780030839931. URL: https://books.google.fr/books?id=oXIfAQAAMAAJ.